UNIVERSITY OF SOUTHAMPTON

AN INVESTIGATION OF THE FLOW AROUND A TRUNCATED CYLINDER

By

Richard John Pattenden

Thesis submitted for the degree of Doctor of Philosophy

FACULTY OF ENGINEERING AND APPLIED SCIENCE
SCHOOL OF ENGINEERING SCIENCES
FLUID-STRUCTURE INTERACTION RESEARCH GROUP

April 2004

UNIVERSITY OF SOUTHAMPTON

ABSTRACT

FACULTY OF ENGINEERING AND APPLIED SCIENCE
SCHOOL OF ENGINEERING SCIENCES
FLUID-STRUCTURE INTERACTION RESEARCH GROUP

Doctor of Philosophy

AN INVESTIGATION OF THE FLOW AROUND A TRUNCATED CYLINDER

Richard John Pattenden

The flow over a finite-height cylinder of height/diameter ratio of 1, with one end mounted on a ground plane, and the other end free, is studied experimentally and numerically. The context of the work is the investigation of numerical simulation methods for marine hydrodynamics, the aims being to test various simulation methods on a complex three-dimensional separated flow.

The experiments add to the sparse knowledge of this flow, particularly through the particle-image velocimetry (PIV) measurements which provide more detailed measurements of the flow. The surface flow visualisation images illustrate many features of the flow. Other measurements taken include hot-wire anemometry of the velocity fluctuations in the wake, surface pressure measurements, and force measurements.

A logical progression through different simulation techniques has been followed, starting with a basic Reynolds-Averaged Navier-Stokes (RANS) solution of the flow, using the k-ε model, which gave a poor prediction of the flow. Large-eddy simulations (LES) were performed which give better agreement with the experiments but fail in the modelling of the boundary layer flow on the ground plane. The next step was a detached-eddy (DES) simulation, which is hybrid RANS/LES model. This gives a better prediction of the flow near the wall, while retaining the benefits of an LES simulation away from the wall. These are believed to be the first LES and DES simulations of this flow.

In the context of marine hydrodynamics, which typically involves high Reynolds number flows, the DES methodology appears to offer a promising way forward. Particular attention has been focussed on the flow around a typical tanker hullform where the flow in the propeller plane is highly turbulent. It is proposed that DES would be useful in this situation to obtain information about the turbulent flow here.

The synthesis of experiments and simulations has shed new light on some of the key flow features around the truncated cylinder. In particular the horseshoe vortex system has been shown to consist of four vortices although they are not all visible in some experimental measurements. The flow over the free-end which was the subject of some debate has been shown to consist of a single vortex arching over the free-end rising from two swirl patterns on the surface. The wake is seen to consist of chaotic eddies with no dominant shedding frequency.

Table of Contents

List of Tables

List of Figures

Acknowledgements

During the course of this research, many people have offered advice and assistance. In particular I would like to thank my supervisors Dr. Stephen Turnock and Prof. Xin Zhang for their constant support. I would also like to thank Dr. Neil Bressloff for generously allowing me to use and modify his flow solver code, and for his help with problem solving.

The wind tunnel experiments would not have been possible without the support of all the staff of the wind tunnels, in particular Geoff Baldwin, who helped to set up the PIV apparatus, and Mike Tudor-Pole for responding to my requests for various equipment. I would like to thank Prof. Ian Castro for providing the hot-wire anemometry equipment and for his assistance with using it. Stephen Webb was also of great assistance in this respect. I greatly appreciate the efforts of the staff of EDMC and the model-maker, David Goldsworthy, without whom there would have been no models to test.

My thanks go to my friends and colleagues, William Batten and Ravi Arkalguld, for many fruitful discussions and diversions, and to Richard Pemberton for sharing many ideas and for his assistance with some of the work. Finally, I would like to thank my parents Valerie and John Pattenden for their continual support throughout the course of my research.

Nomenclature

Roman letters

A	frontal area of cylinder, hd (m^2)
B_l	Lateral blockage ratio, d/W_T
B_t	Total blockage ratio, $B_l B_v$
B_v	Vertical blockage ratio, h/H_T
C_D	drag coefficient, $D/(\frac{1}{2}\rho U_\infty^2 A)$
C_{DES}	constant used in DES length scale calculation
C_{Df}	drag coefficient due to friction
C_P	pressure coefficient, $p/(\frac{1}{2}\rho U_\infty^2)$
C_{Pb}	base pressure coefficient
C_{Pmin}	minimum pressure coefficient
D	drag (force on cylinder in streamwise direction) (N)
d	diameter of cylinder (m)
f	frequency (Hz)
H_T	height of wind tunnel (m)
h	height of cylinder (m)
k	turbulent kinetic energy, $\frac{1}{2}(\overline{u'^2}+\overline{v'^2}+\overline{w'^2})$
l_{SA}	length scale in SA model
$\tilde{l}_{SA}$	modified length scale in DES based on SA model
$l_{k\omega}$	length scale in k-ω - SST model
$\tilde{l}_{k\omega}$	modified length scale in DES based on k-ω - SST model
N_c	number of cells around circumference of cylinder
N_r	number of cells in radial direction
N_h	number of cells along span of cylinder
P	pressure (N/m^2)
P_∞	tunnel static pressure (N/m^2)
Re	Reynolds number based on cylinder diameter, $U_\infty d/\nu$
Re_d	Reynolds number based on cylinder diameter $(\equiv Re)$

Re_δ	Reynolds number based on boundary layer thickness, δ, $U_\infty \delta / \nu$
Re_{δ^*}	Reynolds number based on displacement thickness, δ^*, $U_\infty \delta^* / \nu$
Re_θ	Reynolds number based on momentum thickness, $U_\infty \theta / \nu$
S_c	size of cell in azimuthal direction on wall of cylinder
S_r	first cell size normal to wall of cylinder
S_h	first cell size normal to ground plane
S_{ij}	strain-rate tensor
Str	Strouhal number, fd/U_∞
t	time (*seconds*)
$\mathbf{U}$	velocity vector
U	x component of velocity (m/s)
$\mathbf{u}'$	fluctuating velocity vector (m/s)
u'	fluctuating streamwise velocity (m/s)
U_∞	Free stream velocity (m/s)
V	y component of velocity (m/s)
v'	r.m.s. of v velocity (m/s)
W	z component of velocity (m/s)
W_T	width of wind tunnel (m)
w'	r.m.s. of w velocity (m/s)
x	coordinate in streamwise direction (m)
x^+	normalised distance in direction parallel to wall (streamwise)
X_{S1}	x-coordinate of primary separation point, S_1
X_{S2}	x-coordinate of secondary separation point, S_2
X_{RF}	x-coordinate of attachment on floor, R_F
X_{RT}	x-coordinate of attachment on free-end, R_T
y	coordinate in lateral direction (m)
y^+	normalised distance in direction normal to wall
z	coordinate in vertical direction (m)
z^+	normalised distance in direction parallel to wall (cross-stream)

Greek letters

Δ	cell size
Δ_{PIV}	resolution of PIV data (interrogation area size) (mm)
δ	thickness of boundary layer (m)
δ^*	displacement thickness of boundary layer (m)

ε	turbulence dissipation rate (m^2/s^3)
η	shape factor of boundary layer profile, δ^*/θ
θ	momentum thickness of boundary layer (m)
μ	dynamic viscosity (Ns/m^2)
μ_t	turbulent viscosity (Ns/m^2)
ν	kinematic viscosity, μ/ρ (m^2/s)
$\tilde{\nu}$	solved variable in SA model
ν_t	turbulent kinematic viscosity (m^2/s)
ρ	density (kg/m^3)
σ	standard deviation
ϕ	angle from forward stagnation point $(degrees)$
ϕ_s	angular position of separation from side of cylinder $(degrees)$
Ω_{ij}	rate of rotation tensor
ω	turbulence frequency, ε/k

Glossary

CFD	Computational fluid dynamics
PC	Personal computer
RANS	Reynolds-averaged Navier-Stokes
LES	Large-eddy simulation
DES	Detached-eddy simulation
PIV	Particle image velocimetry
LDA	Laser Doppler anemometry
URANS	Unsteady Reynolds-averaged Navier-Stokes
RSM	Reynolds stress model
CCD	Charge-coupled device
PSD	Power spectral density function
MPI	Message passing interface
SST	Shear stress transport
CLAM	Curved Line Advection Method
PISO	Pressure implicit splitting of operators method
SIMPLE	Semi-implicit method for pressure-linked equations - consistent
TVD	Total variation diminishing
SIP	Strongly implicit procedure
SA	Spalart-Allmaras model

Chapter 1

Introduction

1.1 Motivation

In the marine environment there are many situations where a fluid, either water or air, flows around a solid body such as a ship or an offshore platform. Due to the large size of these bodies the Reynolds number of the flow is often large, resulting in turbulent flow. When these flows undergo separation the resulting wake consists of chaotic eddies, covering a wide range of length scales, which are continually evolving with time. Understanding this turbulent flow is of considerable engineering interest due to its effect on structural vibration, noise and drag. In the marine field such flows can occur at the sterns of ships such as tankers, around offshore structures, ship superstructures or submarine bridge fins.

Although the use of Computational Fluid Dynamics (CFD), which refers to the numerical simulation or modelling of fluid flows, is now widely used in industry as well as in academia, its performance is still poor when dealing with three-dimensional, separated, turbulent flows. Normally these flows are treated by considering only the mean flow pattern, with statistical quantities used to describe the deviations from this mean flow. The equations solved in this case are known as the Reynolds-Averaged Navier Stokes (RANS) equations. This method can give good results for the mean flow quantities, which for many applications may be adequate. However, their ability to model a particular flow is dependent on how the model has been calibrated so that a model which works in one situation may not work in another case.

The alternative is therefore to simulate all (or nearly all) of the turbulent flow structures in a time-dependent computation. If all the structures are resolved it is known as a Direct Numerical Simulation (DNS). At high Reynolds numbers a DNS would require a very fine mesh, which would be beyond the capabilities of most computer systems. It is possible, however, to use a statistical model to account for the effect of the very small scale structures while resolving the larger, energy-containing scales. This is known as Large-Eddy Simulation (LES). It is this technique which appears to offer a viable alternative to RANS methods for the prediction of

turbulent separated flow.

While LES should give a better representation of the mean flow due to its lesser dependence on statistical models, it also has the advantage of providing information on the unsteady turbulent flow structures, which can be useful in many situations. A large-scale example of this is the weather - a turbulent flow system. Most individuals are not interested in the time-averaged flow pattern around the Earth, as it has little impact on what they experience day by day. The importance of knowing the characteristics of the instantaneous flow depends on the length and time scales of the situation under consideration and also on whether there is a particularly dominant frequency of vortex motion. A well known example is the Von-Karman vortex shedding that occurs in the wakes of high-aspect ratio cylinders. This generates fluctuating lift and drag forces which give rise to structural vibrations.

Two examples of turbulent flows around ships where the instantaneous flow may be important are the flow of exhaust gases from the funnel and the flow at the stern upstream of the propeller and rudder. On cruise ships the flow of exhaust gases from the funnel must be checked to ensure that no gases are swept down to the deck where the passengers are relaxing. In the mean flow the gas concentration at deck level may be very low but it is still possible that an occasional turbulence event may sweep a larger quantity of gas to the deck, which might cause momentary discomfort to passengers. It would therefore be desirable to conduct a simulation of the larger turbulent structures to ensure that this does not occur.

The nature of the inflow into the propeller is of vital importance to the efficiency and vibration of the propeller. Typically the mean flow is studied to minimise the variation of velocity across the propeller disc, in order to minimise the vibrations which occur when one blade experiences a different incident velocity than the other blades. This ignores the effects of turbulence on the incident velocity however. While this would be insignificant if the time scale of the velocity fluctuations was much smaller than the propeller frequency, if the time scale is of the same order of magnitude or larger than the propeller frequency the effects might be felt on the efficiency and vibration of the propeller. This possibility will be discussed later in the thesis.

The simulation of these real-life flows presents many hurdles such as the difficulty in generating the computational grid, but also the lack of comprehensive experimental data with which to compare. For the purposes of this study it was decided to look at a simpler geometry which still presents a complex three-dimensional flow. The case of a circular cylinder of height/diameter ratio equal to 1, with one end mounted on a ground plane and the other end free was selected. Despite its geometrical simplicity, the flow is complex and limited research has been carried out on this particular flow. This provided the opportunity to carry out simultaneous experiments and simulations to compare their results and to gain further understanding of this flow.

1.2 Aims and objectives

The purpose of this work is to investigate the use of numerical simulations in combination with experiments to study turbulent separated flows. To this end a relatively simple geometry was chosen, being a circular cylinder of height/diameter ratio (h/d) of 1, mounted on the floor.

The aims of this work can be summarised as follows.

1. To perform experiments to measure the turbulent flow around a low-aspect ratio cylinder mounted on a ground plane, which is representative of a complex three-dimensional flow with many different flow features. This data should be sufficiently comprehensive to enable an assessment of the accuracy of the numerical simulations and to provide as much information as possible on the flow physics. The boundary conditions must be known to give the best opportunity for the simulations to match the experiment.

2. To investigate simulation techniques which can be applied to this flow. This will include RANS and LES methods, to find their strengths and weaknesses for this type of flow. The simulations will be set up to match the experimental conditions as closely as possible. The results of these simulations will be compared to the experimental results to assess their reliability.

3. To use the simulations in conjunction with the experiments to gain a deeper understanding of the flow physics. This will demonstrate the usefulness of numerical simulations in providing insight into phenomena which are difficult to observe experimentally. To do this the simulations must demonstrate at least qualitative agreement with the experiments if not quantitative.

4. To draw conclusions on the use of the simulation techniques employed here in aero- or hydrodynamics of ships. Similarities between the cylinder flow and the flow around ships will be identified and the ability of the simulation methods to predict these features will be discussed.

1.3 Outline of the work

The geometry chosen for this study is that of a truncated cylinder, of $h/d = 1$, mounted on a ground plane. This is representative of a complex three-dimensional separated flow, with a highly turbulent recirculation region and some pronounced vortical structures being formed. The geometry was chosen because although it is geometrically simple to model both computationally and experimentally, it represents a considerable challenge for numerical methods to accurately predict the flow field. The Reynolds number at which the measurements were made

was 2×10^5 which is just below the critical value at which transition occurs in the boundary layer on the cylinder. This Re was chosen because it allowed a reasonably large model ($150mm$ diameter) which makes the measurements easier. All previous work has been at subcritical Re so the data can be compared with other authors.

In order to obtain a comprehensive set of data to validate the computational models a series of experiments were carried out in a newly commissioned wind tunnel. This approach ensures that the computational boundary conditions can be matched to the measured tunnel flow. Various types of measurement have been taken including unsteady pressures, forces and particle image velocimetry. The data obtained adds to the limited amount of literature on the flow over low-aspect ratio cylinders and helps in the understanding of this flow.

In addition to the experiments a series of numerical studies were carried out with the aim of investigating the ability of various approaches to predict the flow. Initially a Reynolds-Averaged Navier-Stokes method was used as this is widely implemented and provides a benchmark of current capabilities. The results of this were restricted by the limitations of the turbulence model. It was considered that a Large-Eddy Simulation would capture the flow in the separated wake better as it resolves all the large-scale vortices. The results of this were better than the RANS with certain features being captured very well. The main problem with the LES is in the difficulty in capturing the turbulent boundary layer on the floor of the tunnel which affects the horseshoe vortex system in front of the cylinder.

The hybrid RANS/LES approach of Detached-Eddy Simulation offers a possible means of overcoming the difficulties with the turbulent boundary layers by acting as a RANS model in these regions. It was decided to try to implement this method in the flow-solver, which entailed the modification of the code to allow the existing Spalart-Allmaras RANS model to operate in DES mode. This took a long time due to various errors in the existing code which had to be resolved, however the results are encouraging.

The experimental data on the cylinder flow was analysed with respect to previous studies of this flow, but it is difficult to obtain a full understanding of this complex flow from experiments alone. The numerical simulations were used to study the whole flow-field and to help with the interpretation of the experimental measurements.

Part of the motivation behind the numerical studies was to understand how these methods might be used to simulate the flow around full-bodied ships such as tankers, as the author and colleagues were involved with a workshop looking at the use of CFD in ship hydrodynamics. This flow contains a region of turbulent flow near the stern of the ship which affects the performance of the propeller. It is therefore important to understand this flow. An LES simulation would be desirable to gain deeper insight into the physics of the flow in this region, but the long length of turbulent boundary layer upstream makes this difficult. DES therefore appears to offer the possibility of simulating this flow. In order to study the flow features in this region

some PIV measurements on a tanker model were carried out in the wind tunnel, but time did not permit the simulation of this flow.

1.4 Structure of the thesis

The structure of this thesis follows the progress of the work that was carried out. Firstly a detailed review of the existing literature on finite-height cylinder flows will be given, along with a discussion of the numerical simulations which have been performed on similar geometries (Chapter 2). The experiments carried out as part of the current research will be presented in Chapter 3. This will give details of the experimental techniques as well as the results obtained. The work then moves on to the numerical simulations. In Chapter 4 the governing equations will be given, along with the various turbulence models used herein. The developments made to a CFD code and the simple validation cases used to test this code will then be presented.

The following three chapters (Chapters 5 to 7) give details of the RANS, LES and DES simulations respectively. These three chapters are each written along similar lines to allow comparison between the different cases. They consist of details of the computational models, followed by a comparison of the results to the experimental results. The results of all the simulations will be summarised and compared in the discussion in Chapter 8. This chapter discusses the flow physics which is revealed from the synthesis of numerical simulations and experiments, and will explore the relevance of these findings to marine hydrodynamics. In particular the flow in the stern region of tanker hulls will be considered with reference to preliminary experiments carried out by the author, presented in Appendix F. Finally the conclusions will be summarised in Chapter 9.

The appendices contain drawings of the cylinder model, further figures from the experiments on the cylinder flow, details of the modifications made to the CFD code, a report on the development of a computing cluster, details of the computational grids used in the simulations, and finally a presentation of the PIV measurements of the flow around a tanker hull.

Chapter 2

Review of previous work

2.1 Introduction

The circular cylinder has proved a fruitful area of fluid dynamics research, due to the combination of a simple geometry with complex flow features. Most of the work has concentrated on the two-dimensional cross flow over cylinders of infinite aspect ratio. This exhibits the well known von Karman vortex shedding pattern in which vortices are shed alternately from each side of the cylinder at a particular frequency. The situation where the cylinder is of finite length with a free-end has received much less interest. Most of the research on finite cylinders has dealt with cylinders of large aspect ratios where most of the length behaves like a two-dimensional cylinder and the three-dimensional effects only become apparent near the free end. The extreme case is where $h/d \approx 1$ at which point the wake becomes completely three-dimensional. On the experimental side some researchers have looked at finite length cylinders and these are described below. On the computational side, however, relatively little investigation seems to have been carried out on this geometry.

This chapter will begin by describing the flow around infinite cylinders. It will then go on to summarise the existing literature on experimental investigations on finite-height cylinders. This is summarised in Table 2.1 which shows the range of h/d ratios and Re (based on diameter) tested along with the types of experiments carried out. The next section will look at the numerical studies into this type of flow. Finally a brief description of the related case of the surface mounted cube will be given.

2.2 Vortex shedding from infinitely long cylinders

The wake behind an infinitely long circular cylinder is dominated by the regular asymmetric vortex shedding pattern which varies in nature with Reynolds number. The effects of vortex shedding from cylindrical structures are felt through oscillating lift and drag loads which induce

vibrations in the structure. Much research has been carried out on this flow, reviews of which have been written by Williamson [1] and Zdravkovich [2].

At very low Re the flow forms two symmetric recirculation bubbles in the wake which are stable. This stable state is maintained up to $Re \approx 45$ at which point the wake becomes unstable to infinitesimal disturbances. Periodic oscillations develop in the wake, forming the typical von-Karman vortex sheet at $Re \approx 100$. In this state the flow is still laminar and the vortices are shed periodically from each side of the cylinder. As Re is increased further the vortices in the wake far downstream become unstable, becoming turbulent. This regime is referred to as the transition-in-wake state [2] and commences at $Re \approx 200$. As Re increases the turbulence moves upstream along the wake.

At Re between 400 and 200000 transition occurs in the free shear layers emanating from the side of the cylinder. This transition begins downstream with the formation of waves, which later become eddies and finally become fully turbulent. This turbulence moves upstream along the shear layers until at $Re = 100000 - 200000$ the entire shear layer beyond separation is turbulent. Up to this stage the vortex shedding is always periodic with a Strouhal number of around 0.2.

At higher Re transition spreads into the boundary layers on the side of the cylinder, resulting in delayed separation and hence reduced drag and higher frequency of shedding. The behaviour of the flow around this point is very sensitive to disturbances, with a number of flow patterns occurring. Around the critical regime at $300000 < Re < 500000$, the shear layers are sufficiently turbulent to reattach after a laminar separation. This occurs first on one side and then on both sides with resultant reductions in drag. As Re increases further the boundary layers on the cylinder become fully turbulent so that the separation is turbulent. During the transition regime the three-dimensionality caused by different transitions along the span causes the periodic shedding to break down. Once the flow is fully turbulent however regular shedding reappears.

2.3 Previous experimental studies on finite-height cylinders

2.3.1 Vortex shedding behaviour

Farivar [4] conducted experiments on cylinders of h/d ratios from 2.78 to 15, at a Reynolds number of 7×10^4, in which he showed the effect of the free end on the mean and fluctuating pressures and the mean forces. He identified three layers of vortex shedding with shedding frequency increasing toward the base. This lower region had a Strouhal number of similar value to the two-dimensional case. Ayoub and Karemcheti [9] performed measurements of the surface pressures and wake velocity fluctuations which show that a shedding regime exists in

Author(s)	Year	h/d	Re	Measurements					
				P	F	HW	LDA	OFV	SFV
Okamoto & Yagita [3]	1973	$1 \rightarrow 12.5$	13000	✓					✓
Farivar, Dj [4]	1981	$2.78 \rightarrow 15$	70000	✓	✓				
Sarode et al. [5]	1981	$1.1 \rightarrow 10$	22000	✓	✓				
Slaouti & Gerrard [6]	1981	$25 \rightarrow 30$	$60 \rightarrow 220$	✓	✓				
Taniguchi et al. [7]	1981	$0.75 \rightarrow 5$	21000	✓				✓	✓
Taniguchi et al. [8]	1981	1	50000	✓					
Ayoub & Karemcheti [9]	1982	12	$85000 \rightarrow 770000$	✓		✓			
Okamoto [10]	1982	1	47400	✓		✓			✓
Sakamoto & Arie [11]	1983	$1 \rightarrow 8$	$270 \rightarrow 920$			✓			✓
Kawamura et al. [12]	1984	$1 \rightarrow 8$	32000	✓				✓	✓
Sin & So [13]	1987	$0.5 \rightarrow 2.5$	48000	✓	✓				
Baban & So [14, 15]	1991	$1 \rightarrow 2$	46000		✓		✓		
Okamoto & Sunabashiri [16]	1992	$0.5 \rightarrow 24$	$25000 \rightarrow 47000$	✓		✓		✓	✓
Luo et al. [17]	1996	$4 \rightarrow 8$	33300	✓					
Kappler [18]	2000	$2 \rightarrow 5$	$22000 \rightarrow 54000$				✓		✓
Park & Lee [19, 20]	2000	$6 \rightarrow 13$	20000	✓		✓			✓
Roh & Park [21]	2003	1.25, 4.25	6000, 148000					✓	✓

Table 2.1: Summary of previous experiments on cylinders with a free-end mounted on a ground plane. Key to measurement types: P - surface pressures, F - force measurements, HW - hot-wire anemometry, W - windmill type anemometer, LDA - laser doppler anemometry, OFV - oil flow visualisation, SFV - smoke flow visualisation

the tip region that is distinct to that over the rest of the length. Slaouti and Gerrard [6] showed the effect of varying the end conditions on the form of the vortex shedding pattern on a high aspect ratio cylinder at low Reynolds numbers.

Experiments on low aspect ratio cylinders are less common. Okamoto and Yagita [3], took surface pressure measurements on cylinders with aspect ratios varying from 1 to 12.5 to find the drag coefficients as a function of aspect ratio. The drag coefficient was found to decrease with decreasing aspect ratio. They also noted that the vortex shedding pattern does not exist at $h/d \leq 6$ as the effects of the free end reach the base.

Taniguchi et al. [7, 8] measured surface pressures on cylinders of aspect ratios between 0.75 and 5. The cylinders were placed in turbulent boundary layers of different thicknesses relative to the cylinder height. The relationship of the surface pressures to the boundary layer velocity was investigated. Taniguchi's coworkers, Sakamoto and Arie [11], investigated the effects of aspect ratio and boundary layer thickness on the vortex shedding frequency behind the cylinders. They found that the shedding frequency is related to the aspect ratio by a power law, and that the shedding changes from Karman type to symmetric arch type at an aspect ratio of 2.5.

Okamoto [10] studied the flow over a cylinder of aspect ratio 1 and a hemisphere capped cylinder. It was found that the vortices shed from the cylinder were symmetric arch vortices which shed at a Strouhal number of 0.225. Measurements were made of surface pressures and turbulence in the wake. Okamoto and Sunabashiri [16] studied the changes in vortex formation with varying aspect ratio. It was found that the vortex shedding pattern changed from symmetric "arch" to antisymmetric "Karman" vortices above $h/d = 4$.

Kawamura et al. [12] tested cylinders of $h/d = 1 \sim 8$, performing flow visualisation, hot-wire measurements and pressure measurements. They attributed the reduced drag coefficient, relative to an infinite cylinder, to the reduced separation velocity, due to separation occurring earlier. This earlier separation is attributed to the increased base pressure due to the downwash from the free end. Using a small "windmill" they demonstrated the presence of longitudinal vortices coming off the sides of the free-end. They found that below a certain h/d ratio, which depends on the oncoming boundary layer height, no periodic vortex shedding occurs. Typically they found the critical value of h/d to be around 6.

Sin and So [13] measured local unsteady forces on a part of the span for different aspect ratios down to 1. They found that there was no suppressed two-dimensional region for the low aspect ratio cylinders and the strength of the force fluctuations was very small at $h/d < 1.5$. The band width of the shedding frequency was also much greater, due to the interference of the tip flow on the transverse shedding. This agrees with Luo et al. [17] who only detected vortex shedding at $h/d = 8$. Baban and So [14, 15] used a similar setup to Sin and So to investigate further the unsteady forces on low-aspect ratio cylinders. They found two flow

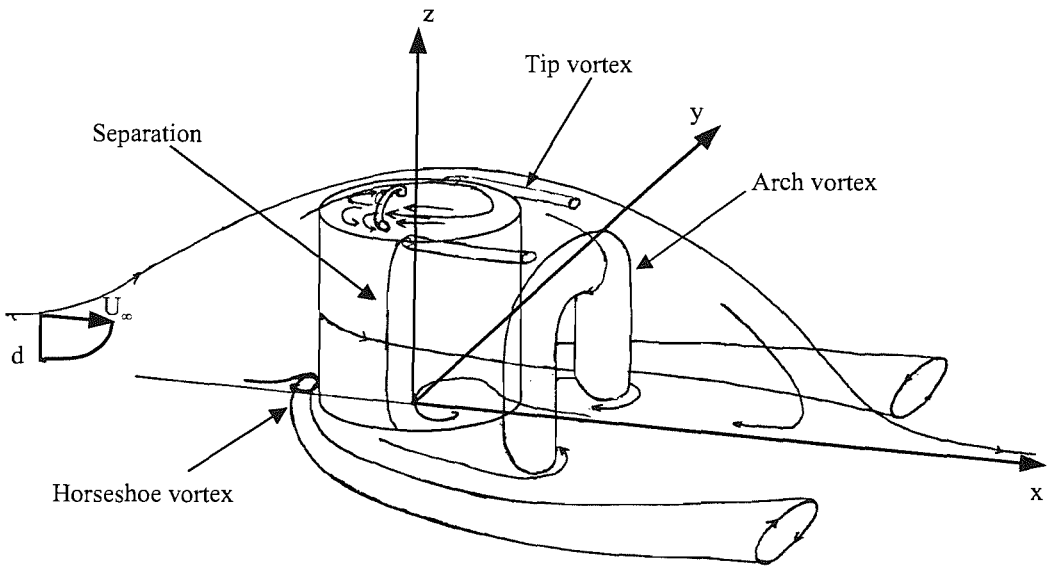

Figure 2.1: Schematic diagram of flow over truncated cylinder

mechanisms which were responsible for the unsteady lift and drag. The lift fluctuations were caused by vortex shedding from the cylinder sides, while the drag fluctuations were caused by oscillations of the entire recirculation region. They also measured mean and fluctuating velocities in the wake using laser-doppler anemometry (LDA). They noted that the fluctuations in the drag coefficient were up to 3 times larger than in the lift coefficient.

Figure 2.1 is a sketch of the time-averaged flow topology inferred from the review of the available literature, inspired by the sketch of the flow over a cube by Martinuzzi and Tropea [22]. The arch vortex structure as described above is shown behind the cylinder.

2.3.2 Horseshoe vortices

The flow on a surface approaching an obstacle experiences an adverse pressure gradient upstream of the stagnation point. This pressure gradient causes the boundary layer to separate from the ground plane forming a region of reversed flow upstream of the obstacle. The vortex formed here then trails downstream around the body. This vortex is commonly referred to as the horseshoe vortex (also sometimes called a necklace vortex), due to the way it wraps around the body. Cylinders mounted on a ground plane are a particularly good example of such a flow and have been extensively studied.

Simpson [23] published a review of the previous research into horseshoe vortices. This describes the key features of the laminar and turbulent horseshoe vortex systems formed around

both blunt and streamlined bodies. At low Reynolds numbers based on the displacement thickness of the oncoming boundary layer, up to $Re_{\delta^*} \approx 1000$, the vortex system is laminar. This regime is described by Visbal [24] and Baker [25]. The number of vortices increases with Reynolds number due to the instability of the system [26]. At higher Reynolds numbers the horseshoe vortex system becomes turbulent. This has been studied by a number of authors. Notably Baker [27] proposed a four-vortex topology for this regime based on surface flow visualisation as reproduced in Figure 2.2. This system consists of a primary separation (S) from which vortex 2 originates. There is a reattachment behind this followed by a small recirculation (1') close to the ground caused by separation of the flow under the primary vortex (1). A small corner vortex exists at the base of the cylinder (0). Details of the variation of the vortex dimensions with the boundary layer characteristics were presented.

An analysis of published data on horseshoe vortex size and position has been published by Ballio et al. [28]. They report that turbulent horseshoe vortices are mainly dependent on the diameter of the body and are not strongly correlated with any flow parameter. While many authors have presented surface flow patterns similar to Baker's, few measurements of velocities in the symmetry plane have been made. Devenport and Simpson [29] made LDA measurements on this plane which appear only to show a single vortex system, although their surface flow is similar to Figure 2.2. Pierce and Tree [30] also made LDA measurements which also show only one vortex. There seems to be some uncertainty over the relationship between these velocity fields and the visualised surface flow. Eckerle and Langston [31] also presented measurements of a turbulent horseshoe vortex. They also reported a single vortex although they report that the vortex was weaker on the symmetry plane than at 15 degrees.

The unsteady behaviour of the turbulent horseshoe vortex has been studied by Devenport and Simpson [29] and Baker [27]. They report a bimodal distribution of velocity in the region of the primary vortex core, due to the vortex switching between two positions. They suggest that this is responsible for the high shear stresses under the vortex. Measurements of the shear stress on the ground under a vortex produced by an oscillating flow were made by Sumer et al. [32].

2.3.3 Free-end flow

For a low h/d ratio, as is being considered in this work, the flow pattern is likely to be dominated by both the flow on the ground plane as described above and the flow over the free-end. While the horseshoe vortex has received a great deal of attention due to its applicability to such a wide range of flows, the flow over the free-end of a cylinder has not been studied as extensively. Most of the papers on finite-height cylinders mentioned above have investigated the behaviour of the vortex shedding in the vicinity of the free-end but have not studied the

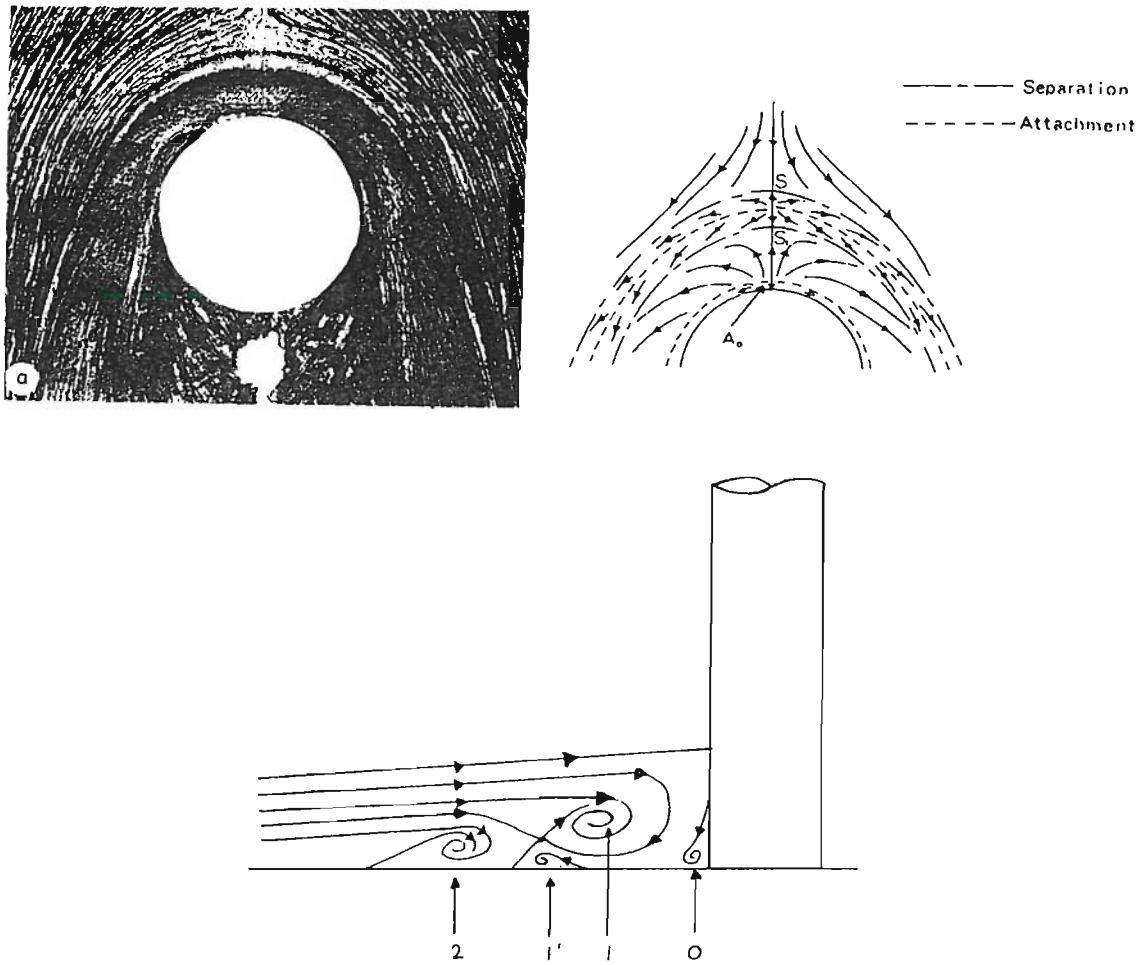

Figure 2.2: Topology of turbulent horseshoe vortex according to Baker. *Reprinted from [27], Figures 2 and 3, with permission from Elsevier*

structure of this part of the flow. It is generally acknowledged that the antisymmetric vortex shedding is suppressed near the free-end as reported in Section 2.3.1.

The effects of the free end on the near wake were investigated by Park and Lee [19], who discussed the effect of the counter rotating vortices formed at the free end. They attributed the three dimensionality to the downwash caused by these vortices. Their tests were carried out on cylinders of $30mm$ diameter in a free-stream velocity of $10m/s$ in a wind tunnel, giving a Reynolds number based on diameter of 20000. Aspect ratios varied from 6 to 13. They present particle visualisations which show the pair of tip vortices downstream of the free-end. They noted a particular flow feature having a broad peak at $24Hz$, corresponding to a Strouhal number of 0.07, near the free end, which they found to be related to the counter rotating vortices.

The flow patterns on top of the cylinder were discussed by Kawamura et al. [12]. They noted that the flow which separates from the leading edge reattaches to the free-end when $h/d = 8$ but not at $h/d = 4$. This produces a different flow pattern on the free-end corresponding to a different pressure distribution. At $h/d = 1$ the flow reattaches on the top. The attachment line is visible across the rear of the surface. All of these visualisations show the two swirl patterns in the forward half of the cylinder. They attribute this to the reversed flow along the centre being entrained by the obliquely separated flow from the leading edge. They describe the vortex structure on the free-end as being similar to the "mushroom" vortex seen by Winkelman and Barlow [33] on an aerofoil after stall.

Roh and Park [21] performed a flow visualisation study of the flow on the free-end surface of a finite height cylinder mounted on a flat plate. Their experiments were made at Reynolds numbers of 5.92×10^3 and 1.48×10^5, with aspect ratios of 1.25 and 4.25. Oil flow visualisations of the flow on the free-end surface show an "owl-face" configuration, characterised by a pair of swirl patterns on the forward half of the top surface. They suggest that these swirls form the base of a pair of trailing vortices, shown by smoke visualisation, which develop along the top of the cylinder alongside the tip vortices formed at the edge of the cylinder. They observed little difference in the flow pattern with the different Reynolds numbers and aspect ratios.

Figure 2.1 depicts the flow as proposed by Kawamura with the mushroom vortex over the tip and the trailing tip vortices from the edges. This can be compared with the topology according to Roh and Park in Figure 2.3 which shows the four streamwise trailing vortices which they propose.

2.4 Numerical investigations of finite-height cylinder flows

Flows around bluff bodies occur in a wide range of situations in nature and in engineering. The ability to predict these flows is therefore of great importance in order to improve the design of such structures. However, the problem of predicting unsteady flows around bluff bodies

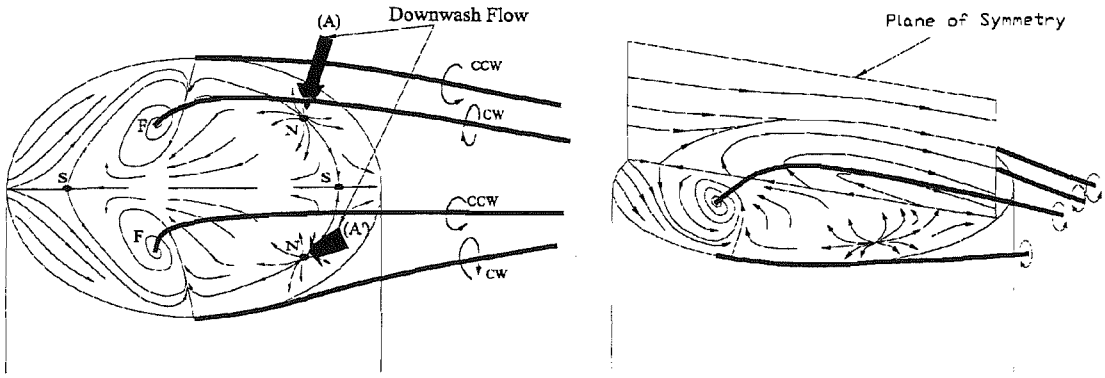

Figure 2.3: Topology of free-end flow according to Roh and Park. *Reprinted from [21], Figures 5 and 6, with permission from Springer*

is a difficult one, due mainly to the complex turbulent flow in the wake region. While many calculations have been performed on complex geometries, both in industry and in academia, the majority use Reynolds-averaged Navier-Stokes (RANS) solvers with statistical turbulence models. Such models will not capture all the complex flow features which occur behind bluff bodies. A steady-state RANS solver will only resolve the mean flow pattern with all the turbulent scales being modelled. Even an unsteady RANS (URANS) code will only resolve the largest scale fluctuations such as periodic vortex shedding. Although these types of solvers will be able to approach the correct mean forces and velocity field, and the turbulent kinetic energy may be correct, there will be no detail of the structure of the turbulence [34].

In order to overcome this, large-eddy simulations (LES) can be used. These differ from the RANS methods in that all the turbulent structures are resolved down to the grid scale, while only the turbulence smaller than this scale is modelled. LES should therefore be able to predict the global flow parameters better than a RANS model because it is less dependent on empirical, statistical turbulence closures.

To the author's knowledge only one other LES simulation of the flow around a finite-height cylinder has been published, by Fröhlich et al.[35]. They performed LES simulations at a Reynolds number of 43000 and $h/d = 2.5$, corresponding to experiments carried out by Kappler and Rodi [18, 36]. Their model ignored the effects of the boundary layer on the ground plane by imposing a free-slip condition on this boundary. This was shown to give rise to von-Karman shedding in the lower half of the wake which are suppressed in the experiment. The arch vortex near the free-end and the longitudinal tip vortices are visible. They found that the grid resolution was critical to the prediction of the transition in the shear layers just after separation.

One of the main problems with LES for this type of flow is the grid resolution required to resolve the boundary layer correctly, particularly at higher Reynolds numbers. One approach

that has been proposed for such situations is a hybrid RANS/LES model. The method developed by Spalart [34] and Travin [37] is known as detached-eddy simulation (DES). This is based on the Spalart-Allmaras turbulence model [38] with a simple adjustment to the length scale dependent on the distance to the wall and the cell size. If the cell is close to the wall and is too large for an LES solution the model behaves as the conventional RANS model. Away from the wall, however, the model behaves as a subgrid-scale model and resolves all the energy cascade down to length scales similar to the grid scale. This model has been used successfully to model a variety of flows from cylinders to stalling aerofoils [37, 39, 40, 41, 42, 43]. More detail on this method will be presented in Chapter 4.

2.5 The flow over a surface-mounted cube

While low-aspect ratio cylinders mounted on a ground plane have not been widely studied, particularly numerically, the similar case of a surface-mounted cube has received a lot of attention. The key experiments are those of Castro and Robins [44], who made pulsed-wire anemometer measurements in the wake of the cube and surface pressure measurements, and Martinuzzi and Tropea [22] who performed flow visualisations and surface pressure measurements.

The cube has been studied numerically as it is a simple geometry and the separation points are fixed by the sharp edges. The experiments of Martinuzzi and Tropea were used as a benchmark for a recent workshop on large-eddy simulation [45, 46], along with the related case of a square infinite cylinder. Rodi [45] performed a comparison between LES and RANS for the flow around these two geometries. He found that the standard $k-\varepsilon$ model over-predicts the turbulence production in the stagnation region. There are modifications to this model which can better calibrate the model to this flow. The turbulence fluctuations were under-predicted by the RANS models. LES was able to predict the turbulent fluctuations, and generally predicted the overall flow much better than the RANS.

Murakami [47] also looked at the surface mounted cube, with broadly similar results. He also found that the standard $k-\varepsilon$ model over-predicted the turbulence production but a modified version corrected this. He used a Reynolds stress model (RSM) which gave quite poor results. He concluded that this type of model would need some refinement to work well on this type of flow. The LES results were promising, particularly with the use of a dynamic subgrid-scale model, where the Smagorinsky constant is replaced by a calculated value dependent on the flow field. This overcomes the problem of having to select a value for the Smagorinsky constant which will not be correct for the whole flow-field.

2.6 Conclusions from the literature review

The choice of the low-aspect ratio, finite-height cylinder for this research is justified by this review of the available literature. It seems that while many studies have been made of the flow around higher-aspect ratio cylinders, with clearly defined two-dimensional vortex shedding patterns, with a few exceptions this particular case has been largely overlooked. From the available information the flow around the low-aspect ratio cylinder seems a complex one with the trailing vortices from the tip and the base merging and enclosing a turbulent recirculation region in the wake. This type of flow is likely to prove difficult for many turbulence models in common usage to predict, and is therefore a challenging test-case for CFD codes intended for the prediction of three-dimensional turbulent flows. The key flow features found from the above review are summarised below.

- The antisymmetric vortex shedding pattern typically seen on higher aspect ratio cylinders has been observed to change to a weaker symmetric shedding pattern at aspect ratios between 2.5 and 8.
- A horseshoe vortex is formed on the ground due to the adverse pressure gradient upstream of the cylinder. This vortex trails downstream where it may interact with the transverse vortices and also the tip vortices.
- At the free end a pair of counter-rotating longitudinal tip vortices is formed, originating from the forward half of the free end. These trail downstream and descend towards the ground plate. This downwash may contribute to the suppression of the transverse vortex shedding.

From the review above it appears that while much experimentation has been carried out on truncated cylinders, the range of different measurements and test conditions is quite wide. It is difficult to draw definite conclusions on the details of the flow as each investigator has focused on different aspects of the flow with no consistency between experiments. It would be difficult to use this data for validation of CFD codes due to the difficulty in comparing like for like. One of the first aims of this work is therefore to gather a set of experimental data which can be used to gain confidence in the numerical simulations. These simulations can then be used to gather more information about the flow features. The experiments are reported in the next chapter.

The choice of numerical method is not simple however as this type of bluff body flow is difficult for the majority of commonly used models. Most RANS models are formulated for isotropic turbulence and therefore fail when the flow is anisotropic as in this case. Large-eddy simulation methods perform better for predicting the wake structure and give more detail of the turbulence. However, they have some difficulty with boundary layer flows. The detached-eddy

simulation method offers a potential improvement over LES in being able to model turbulent boundary layers at much less cost. This seems to be a promising method for the truncated cylinder on a ground plate and so will be investigated further.

Chapter 3

Experiments on the truncated cylinder

3.1 Introduction

The review of the literature on the subject of finite-height cylinders has shown that, while some studies have been made, none are sufficiently comprehensive to validate a computational model. The differences between the cases would prevent meaningful comparisons. The aim of the present study is to perform a set of experiments which will complement concurrent numerical studies. This will allow sensible comparisons to be made between experimental and computational results. The computational simulations, if successful, can then be used to investigate the flow further, while also providing valuable insight into the capabilities of the models used.

The start of this work coincided with the construction of a new $0.9m \times 0.6m$ wind tunnel in the School of Engineering Sciences [48, 49]. This work was therefore the first to be done in this new tunnel and so the various data acquisition and measurement systems were untried in this tunnel.

In order to get a complete picture of the flow, a number of different types of measurement were made. Surface pressures were measured using pressure transducers to give the mean and unsteady pressure distribution. A strain-gauge dynamometer was used to measure total drag forces. Surface flow visualisation was performed to give a clear picture of the flow pattern on the surfaces. Finally the velocity field in the wake of the cylinder was measured using hot-wire anemometry and particle image velocimetry (PIV). The upstream flow was also measured using pitot-static tubes and hot-wire anemometry.

Details of the experiments will be presented below, starting with the experimental arrangement and upstream flow conditions. Each set of measurements will be described individually, and their relationship to the other results will be discussed. Further analysis of the flow will be described in Chapter 8 where the results of the numerical simulations will also be used to help to understand the flow physics.

3.2 Details of experimental arrangement

The experiments were carried out in the new $0.9m \times 0.6m$ wind tunnel, a schematic diagram of which is shown in Figure 3.1. It is an open circuit suction wind tunnel, driven by an axial flow fan discharging into the laboratory, with a working section measuring $0.9m$ wide by $0.6m$ high and $2.4m$ long. It is fitted with meshes of various sizes at the intake to control the turbulence in the tunnel. The free-stream turbulence level was found to be 0.3% as shown in section 3.5.2.

The cylinder model had an aspect ratio, $h/d = 1$, with $150mm$ height and diameter. These dimensions give a Reynolds number based on the cylinder diameter of 1.96×10^5 at a tunnel speed of $20m/s$. It was located $1.2m$ from the start of the working section. The model was made of hollow aluminium tube of $10mm$ wall thickness to allow the fitting of the pressure transducers. These are placed in five $2.5mm$ holes drilled at $25mm$ spacing along a vertical line on the cylinder side. The location of these holes can be seen in the drawings of the cylinder model given in Appendix A. The model had a removable base which could be attached either directly to the dynamometer below the tunnel or clamped to the floor of the tunnel. The former arrangement was used for the measurement of forces and also for pressure measurements as the dynamometer incorporated a turntable which was used to rotate the model to align the pressure transducers at the required angle. The latter arrangement eliminated the gap between the model and the ground plate.

One of the problems of mounting a model directly on the floor of the wind tunnel is that the boundary layer will have had a long length in which to develop and will therefore be relatively thick. This has been measured at $25mm$ or $h/6$ at the model position at the speed of these tests. It is usual in this situation to employ a ground plate mounted above the tunnel boundary layer, on which a thinner boundary layer is allowed to develop, such that it has reached a fully developed state at the location of the model. However, when simulating such situations numerically it is important to know the boundary layer characteristics at the upstream end of the computational domain. The computation would be easier if this were either a fully-developed boundary layer, which would require a long ground plate upstream of this point, or if it were a uniform flow with no boundary layer, equivalent to the leading edge of the ground plate. Due to space restrictions in the tunnel the latter method was adopted. The ground plate had the added benefit of making photography for flow visualisation and PIV easier by raising the model to the level of the side window.

The ground plate was constructed of $5mm$ MDF board screwed onto blocks to raise it $55mm$ above the tunnel floor. It was important to ensure that it was secured well enough not to flex upwards due to the flow over it. The leading edge was given an elliptic profile to avoid separation, which would affect the flow at the model. The model can be screwed either on to the top of a post on top of the dynamometer or directly to the ground plate. When attached

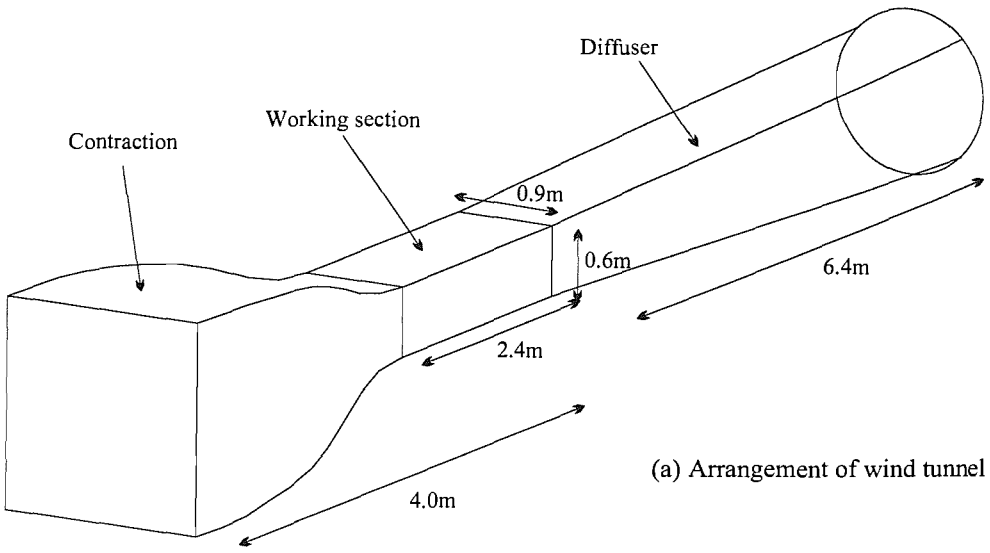

(a) Arrangement of wind tunnel

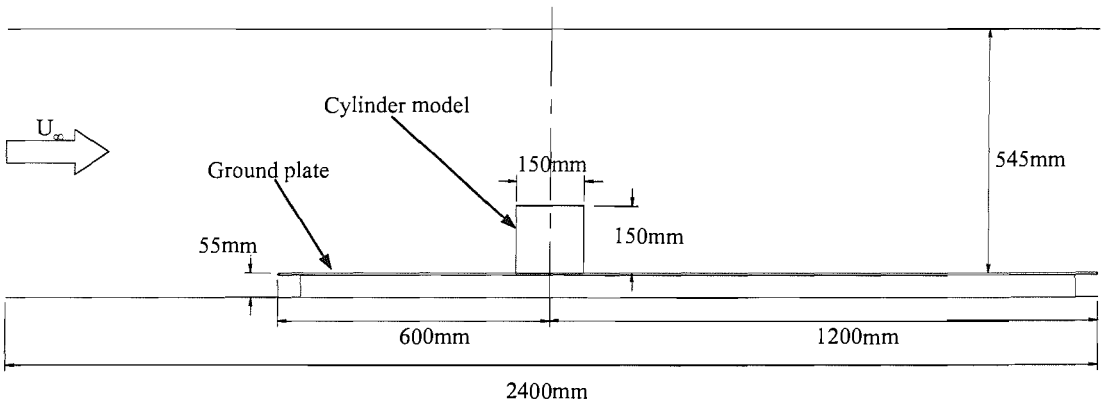

(b) Side view of model in working section

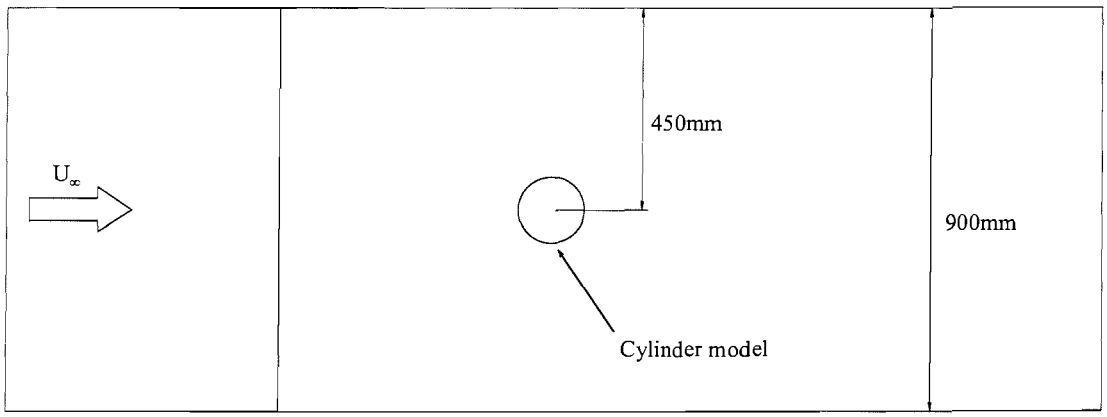

(c) Plan view of model in working section

Figure 3.1: Diagram showing location of cylinder model and ground plate in wind tunnel working section

to the dynamometer it is important to ensure that the base of the model is not touching the floor, as this would restrict its movement, but at the same time as much as possible of the gap underneath is sealed with tape, leaving $\sim 0.5mm$ to minimise flow leakage under the model. The arrangement of the model in the working section of the wind tunnel is shown in Figure 3.1.

3.3 Blockage considerations

An important consideration when performing wind tunnel experiments is the effect of the proximity of the wind tunnel walls to the model on the flow characteristics and forces acting on the model. For aerofoils and similar bodies there are accepted techniques for assessing the magnitude of this effect such as that proposed by Lock [50] and Allen and Vincenti [51]. These methods have been shown to be inadequate for bluff body flows, particularly three-dimensional ones. West et al. [52] carried out a series of experiments on cylinders spanning a wind tunnel, with varying blockage ratio and aspect ratio. He found that although the blockage correction was valid for the flow on the forward part of the cylinder, the separation point varied with blockage, which cannot be accounted for by the correction methods. Farell et al. [53] published results of blockage ratio tests on cylinders spanning a wind tunnel, and also on cooling tower models. The blockage correction procedures were found not to be applicable to the cooling tower models. One of the main problems appears to be the fact that there is a blockage factor in both lateral and vertical dimensions and the interaction between these is difficult to assess.

For a three-dimensional body there are three blockage ratios which need to be considered: the lateral blockage ratio $B_l = d/W_T$, the vertical blockage ratio $B_v = h/H_T$, and the total blockage ratio $B_t = B_l B_v$. The ratios for the truncated cylinder model considered here are $B_l = 0.167$, $B_v = 0.25$ and $B_t = 0.042$. According to the results of Farell et al. for the cooling tower models this would lead to an increase in base pressure coefficient C_{Pb} of 35%. Base pressure coefficient here is the pressure coefficient on the centreline on the downstream face of the cylinder.

This effect must be taken into consideration when comparing data to other experiments which may have different blockage ratios. For the purposes of the current work however, the computational model is set up to model the effect of the tunnel walls on the flow and so a direct comparison can be made with the experiment. Indeed restricting the domain reduces the uncertainty in the computations, as the placement of the boundaries in a computational model can cause problems when trying to simulate external flows.

3.4 Details of measurement methods

3.4.1 Tunnel flow speed control

The speed was measured by a pitot-static tube mounted in the working section. This tube was located $200mm$ below the roof of the tunnel and $550mm$ downstream of the start of the working section. The pressure differential was measured by a Furness Controls FC012 digital micromanometer which had a range of $1999N/m^2$, with a quoted accuracy of $\pm 0.5\%$. The flow speed within the wind tunnel was set by a frequency controller on the power supply to the fan. The fan speed was set to give a constant pressure differential.

3.4.2 Surface-flow visualisation

In order to aid the understanding of the flow topology surface flow visualisation was performed. In order to do this a mixture of titanium dioxide, paraffin and oleic acid was applied to all the relevant surfaces. The cylinder and floor had previously been covered with black self-adhesive plastic. The tunnel was run for 30 to 60 minutes depending on flow speed to allow the paraffin to evaporate leaving the flow pattern visible. While the high speed regions on the floor and the front of the cylinder dried quickly the low speed regions in the wake took longer to dry and in some cases had to be left overnight to dry before the pattern was visible. The flow pattern was photographed, using a standard $35mm$ camera, with the model still in the tunnel as it was impossible to remove it without disturbing the flow pattern.

3.4.3 Particle image velocimetry

Particle image velocimetry (PIV) is a technique which is rapidly gaining in popularity in experimental fluid dynamics due to its ability to capture flow velocities in an entire plane simultaneously. This is particularly relevant when comparisons are being made with computational results which contain flow information for the entire domain. The method consists of taking two consecutive images of particles in a plane of the flow in order to calculate their velocity. The plane is illuminated by two high intensity lasers, arranged to produce a thin sheet of light, which fire in quick succession (up to around $100\mu s$ in typical experiments). The images are then captured by a charge-coupled device (CCD) camera mounted perpendicular to the plane. The system is driven by a control unit linked to PC software where the data processing is carried out. The algorithm performs a cross-correlation of the two images to determine the motion of the particles [54].

PIV as described here can only be used to obtain the two components of the velocity vector

in the plane of the light sheet. There are variations on this method which allow more information to be obtained. These include stereoscopic PIV which uses two cameras viewing a thick light sheet from different angles to obtain the three velocity components.

PIV apparatus

The PIV system used was supplied to the School of Engineering Sciences by Dantec Dynamics. The heart of the system is a FlowMap controller which controls the camera and the laser, and also performs the processing of the images. The user interface to this is the FlowManager software which runs on an adjacent PC, which also stores the data after acquisition. This software is used to set up the parameters for the camera and laser and is also used to perform post-processing and visualisation of the data.

The laser used was a New Wave Gemini $120mJ$ Nd:Yag dual laser system. This consists of two laser heads mounted in a single casing with a rotating mirror to direct one beam at a time to the lens. Each laser head flashes at $4Hz$ with a variable offset time between the two. The laser heads were mounted on top of the wind tunnel above a narrow slot in the roof for the beam to pass through. This allowed measurement in either the longitudinal, xz, plane or the transverse, yz, plane. In the longitudinal planes U and W were obtained at each instant, while in the transverse planes V and W were measured. The beam thickness was approximately $1mm$.

An 80C60 HiSense CCD camera with a resolution of 1280 by 1024 pixels was used to capture the images. In these tests a $60mm$ lens was used. For measurements in the longitudinal, xz plane, the camera was mounted on a tripod to the side of the tunnel, viewing through one of the side windows. This window was a glass one instead of the usual Perspex window. The image size in this plane was $292 \times 233mm$ or $1.95d \times 1.55d$. It was necessary to take three images from the front of the cylinder to two diameters downstream. Table 3.1 lists the locations of the planes in which measurements were taken, along with the number of samples. Some later tests used a $105mm$ lens to obtain higher resolution views of certain features. The image areas and resolutions are shown in Table 3.1.

For measurements in the transverse plane it was necessary to mount the camera inside the tunnel downstream of the measurement plane. In order to measure different x-planes it was decided to move the model along the floor of the tunnel rather than moving the laser and the camera, due to the difficulty in moving the latter two. This had the disadvantage of the model not having a constant inflow condition, but as it was only moved by two diameters upstream the effect of this should be small. The image size in this plane was $225 \times 180mm$ or $1.5d \times 1.2d$, which was sufficient to cover the entire wake region near the model.

The seeding was provided by a water-based fog generator. Initially this was placed immediately outside the contraction inlet but it was found that the fog did not diffuse sufficiently

Table 3.1: Details of PIV planes

Plane	x/d	y/d	z/d	Δ_{PIV} (mm)	Samples	U_∞ (m/s)
L1	$-1.45 \rightarrow 0.50$	0	$0 \rightarrow 1.55$	7.3	1000	20
L2	$-0.71 \rightarrow 1.24$	0	$0 \rightarrow 1.55$	7.3	1000	20
L3	$0.66 \rightarrow 2.60$	0	$0 \rightarrow 1.55$	7.3	1000	20
L4	$0.46 \rightarrow 1.01$	0	$0 \rightarrow 0.44$	2.1	500	10,20
L5	$-0.60 \rightarrow 0.57$	0	$0.62 \rightarrow 1.56$	4.4	500	10,20
L6	$-1.28 \rightarrow -0.34$	0	$0 \rightarrow 0.75$	3.5	500	10,15,20
L7	$-1.03 \rightarrow -0.48$	0	$0 \rightarrow 0.44$	2.1	500	10,15,20
T0	0.50	$-0.75 \rightarrow 0.75$	$0 \rightarrow 1.20$	5.6	1000	20
T1	0.67	$-0.75 \rightarrow 0.75$	$0 \rightarrow 1.20$	5.6	1000	20
T2	0.83	$-0.75 \rightarrow 0.75$	$0 \rightarrow 1.20$	5.6	1000	20
T3	1.00	$-0.75 \rightarrow 0.75$	$0 \rightarrow 1.20$	5.6	1000	20
T4	1.50	$-0.75 \rightarrow 0.75$	$0 \rightarrow 1.20$	5.6	1000	20
T5	2.50	$-0.75 \rightarrow 0.75$	$0 \rightarrow 1.20$	5.6	1000	20

before reaching the working section. The fog generator was therefore placed at the other end of the laboratory, near the tunnel exit, so that it could diffuse around the laboratory before entering the tunnel. After some experimentation a suitable level of seeding was reached, determined by minimising the number of spurious vectors in the data.

One difficulty that was experienced was the reflection of the laser light off the cylinder and wind tunnel surfaces. This was a particular problem when trying to measure the flow very close to a horizontal surface when the bottom of image was too bright for the particles to be discernible. The model and ground plate were originally painted with matt black paint to minimise reflections. It was later found however, that a smooth black PVC self-adhesive coating was slightly better. This seemed to be due to the smoothness of the surface, as the painted finish was slightly rough and scattered the light more than the smooth plastic finish.

Image acquisition and processing

An important parameter is the timing between images with regard to the distance travelled by the particles. In the case of the FlowMap software the image is divided into interrogation areas in which the correlation is calculated. The particles should travel as far as possible without leaving the interrogation area. In this case the interrogation area was set to 32×32 pixels. The physical size of this square, which is the resolution of the PIV data, is shown as Δ_{PIV} in Table

3.1. In the streamwise direction the dominant velocity is parallel to the plane and of the same order of magnitude as the free-stream velocity. At a velocity of $20m/s$ the time for a particle to cross the interrogation area of the coarse longitudinal planes (L1, L2, L3) is $365\mu s$. In practice a timing of $60\mu s$ was found to give reliable measurements.

For the transverse planes the velocities in the plane are relatively low compared to the normal velocity. Also the thickness of the light sheet at around $1mm$ is much less than the width of the interrogation area, so the determining factor becomes the time for the particles to travel through the light sheet. At $20m/s$ this would take $50\mu s$. In reality the thickness of the light sheet is not known exactly and its intensity may vary away from the centre. Also the flow velocity in the turbulent recirculation region varies greatly across the plane. A time between images of $15\mu s$ was found to give the least erroneous measurements.

According to the spectra of the velocity signals in the wake, to be presented in section 3.5.6, the dominant structures in the flow have a characteristic frequency between 10 to 30 Hz. As the sampling frequency of the PIV system is only $4Hz$ no frequency information can be obtained from the PIV (a recent development in the technology, known as "time-resolved PIV", will allow sufficiently high sampling rates to obtain frequency information). All the statistical quantities can be derived though, as the data samples can be considered to be uncorrelated. A sufficient number of samples must therefore be obtained so that the statistical values are accurate. In these experiments 1000 samples were taken at each plane which was found to be sufficient.

The cross-correlation was performed using 32×32 pixel squares with a 50% overlap between areas. Erroneous points were removed from the data set using a range validation method. This means that any vectors with magnitudes greater than a certain value, typically $25m/s$ was chosen for a longitudinal plane, were discarded. The discarded vectors were substituted by interpolation.

Accuracy of PIV measurements

There are a number of factors which must be taken into account when carrying out a PIV measurement which have an impact on the accuracy of the results. Most of these are due to errors in the correlation of the two images, which contribute either a bias error or a random error [55]. These include the particle image diameter, which needs to be just over two pixels to allow interpolation between pixels. The density of particles affects the number of valid image pairs within each interrogation area and so a higher density increases the strength of the correlation peak. Displacement (or velocity) gradients across the interrogation area will introduce a bias error due to more particle image pairs on one side of the interrogation area than the other. Out-of-plane motion of the particles if the plane is normal to the main flow can

cause a loss of particle image pairs when the particle drops out of the plane between images.

Some of these have been addressed by Webb and Castro [56] at the University of Southampton, using the same apparatus as used in this work. In particular they looked at the effect of the timing between images and of the image size with regard to the spatial resolution of the flow. They studied a variety of flow conditions covering a range of turbulence intensities from homogeneous turbulence to a recirculation bubble. They found that in general the mean velocity profiles were in close agreement with hot-wire or laser-doppler anemometry measurements. In the low turbulence intensity flow ($\approx 5\%$) the normal Reynolds stresses measured by PIV were 30% less than the hot-wire measurements. This was due to poor sub-pixel interpolation which causes an effect known as "peak-locking" where the velocity tends towards certain values. In the higher turbulence intensity flows the agreement with other data sources was much better, for both the normal stresses and shear stresses.

In general the accuracy of the PIV method is of the order of 0.1 pixel, which corresponds to 1.25% of the maximum displacement if this is chosen to be 8 pixels (or 25% of the interrogation area size). In practice in these experiments a displacement of 0.1 pixel corresponded to a velocity error varying from 0.5%, in the closeup views of the horseshoe vortex, to 6% of the free-stream velocity in the transverse planes.

There is some overlap between the measurement planes which affords the opportunity to compare the values at certain points in each plane. Looking at the overlap between planes L2 and L3, the mean velocity is within 5%, while u' and v' are also within 5% in the high turbulence intensity region. Also looking at the velocity at a point upstream and above the cylinder in plane L1, where the turbulence intensity should be less than 1% the standard deviation is around 5% of the free-stream velocity. This would correspond to a particle displacement of 0.2 pixels. The error in the turbulence stresses can also be assumed to be no more than $5\%U_\infty$.

When calculating statistics of any sort it is important to ensure that sufficient samples have been taken. In most of the measurements made here 1000 instantaneous measurements were taken, although in some cases 500 was deemed sufficient. The convergence of the statistical values with the number of samples can be seen in Figure 3.2. This shows that the statistics have converged to within 1% of their final values after 600 samples.

3.4.4 Hot-wire anemometry

The velocity in the wake of the cylinder was measured using a single hot-wire anemometer, a Dantec single-sensor miniature, straight probe. The sensor is a $5\mu m$ diameter, $1.25mm$ long platinum-plated tungsten wire welded to the prongs of the probe. This is supported in a cylindrical body with a cable exiting at the end. The probe body was attached to a stiff metal rod which was attached to the traverse post.

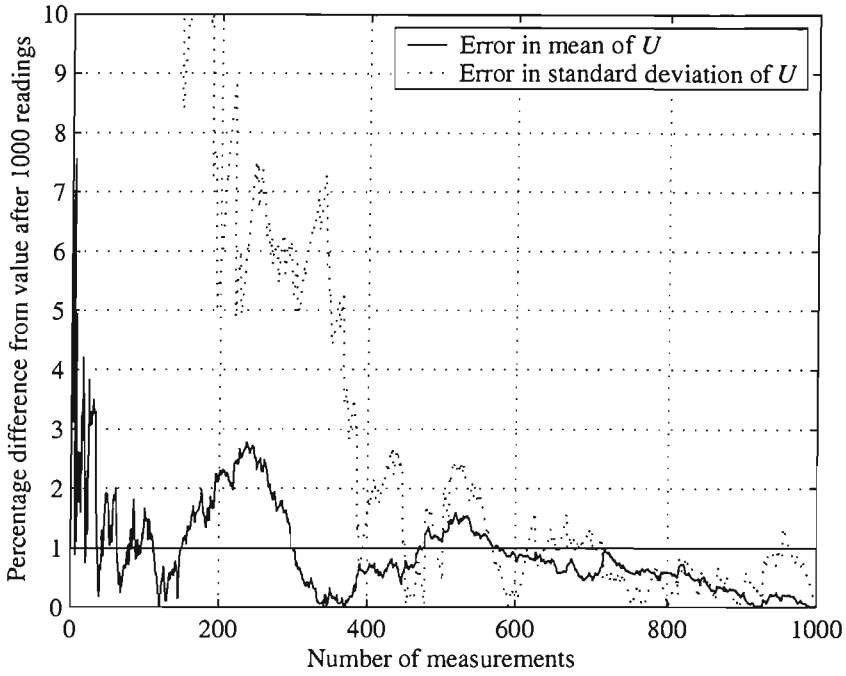

Figure 3.2: Examples of the convergence of statistical quantities in PIV measurements at $x/d = 1, y/d = 1$

The traverse system is permanently mounted above the working section, supported by a substantial framework. It can move in three degrees of freedom. A $25mm$ steel post, which is driven in the vertical direction by a stepper motor and leadscrew, enters the working section through a slot in the roof. This is moved in the lateral direction by another stepper motor and leadscrew. This whole assembly can be moved, manually, forward and backward on slides. The stepper motors driving the vertical and lateral motions are controlled by software on the data acquisition computer. The position of the hot wire was measured to an accuracy of $\pm 0.25mm$ with a repeatability of $\pm 0.07mm$.

The probe is connected to a constant-temperature anemometer bridge circuit, manufactured by the University of Newcastle, NSW, Australia [57]. This has to be allowed to warm up for a considerable period of time due to the rather low resistance of the $5\mu m$ wire, otherwise a significant amount of drift can be experienced. The output from this bridge is connected to an analogue to digital converter which is connected to an Apple PowerMac G4 computer. This runs the LabView data acquisition software for which a number of modules have been developed for hot-wire anemometry at the Universities of Southampton and Surrey. The calibration and analysis of the output signal is carried out in this software.

The probe measures the magnitude of velocity normal to the wire, that is $\sqrt{U^2 + W^2}$ when the wire is horizontal. This means that the output is only meaningful when the streamwise velocity component is dominant or when the flow angle is known. Single wire measurements

are therefore not reliable within recirculation regions. The probe was calibrated frequently during the tests by moving it into the free-stream and using the pitot-static tube as a reference velocity. The uncertainty in the velocity is $\pm 1\%$, taking into account the calibration errors and drift during the tests.

3.4.5 Surface pressure measurements

An important feature of the flow over a body is the pressure distribution generated by the flow on the surface. In an unsteady flow situation however these pressures will be fluctuating with the flow field and give rise to fluctuating forces. A knowledge of the unsteady pressure field can be important to the understanding of the flow. The pressure on the surface of the model was measured using a set of five pressure transducers set in the sides of the cylinder. The sensors used were piezoresistive gauge pressure transducers (Endevco Model 8507C-2) with a $2mm$ diameter silicon diaphragm and a range of 2psi ($1406mmH_2O$). The five transducers were equally spaced along a generator of the cylinder ($z/d = 0.17$ to 0.83 inclusive) and the cylinder was rotated on the dynamometer base through 360 degrees at 5 degree intervals so that a full picture of the surface pressures could be gathered.

Although calibration data for the transducers had been provided by the manufacturer, when the first measurements were made the results were clearly incorrect. Further investigation revealed that the sensitivity was affected quite significantly by the mounting method. It was found to be imperative that no radial load was applied to the barrel of the transducer as this distorts the diaphragm. The manufacturer's advice was sought and they recommended the use a flexible silicone adhesive. Tests with this showed that the sensitivity is closer to that stated by the manufacturer but it still had significant differences. The transducers therefore had to be calibrated in position in the model. This was achieved by measuring the surface pressures at two angles using pressure tappings in the transducer holes which were connected to a micromanometer.

As the transducers measure gauge pressure, that is the difference between the pressure at the front and the back of the transducer body, it was necessary to know the pressure inside the cylinder. A tube was attached inside the model which was connected to the micromanometer. The tunnel static pressure from the pitot-static tube was used as a reference so that the difference between the pressure on the cylinder surface and the tunnel static could be found. The voltages from the transducer output were calibrated using the values measured previously at $\theta = 0$ degrees and $\theta = 45$ degrees.

The errors in the pressure measurements were estimated using the method of Moffatt[58]. The fixed errors were estimated as follows: $\pm 0.20mmH_2O$ for the transducers, based on the manufacturers data and $\pm 0.05mmH_2O$ for the two micromanometers. Other sources of error

such as the analogue to digital converter were considered to be negligible. This leads to a fixed calibration error of $\pm 0.21 mmH_2O$, and a total measurement error of $\pm 0.30 mmH_2O$ or $\sim \pm 1.2\%$ at $25 mmH_2O$. The frequency response is flat up to 20% of the resonant frequency, $70000 Hz$, which covers the range of interest. The variable errors, i.e. the non-repeatability of the measurements has been estimated from a series of 30 readings at the same condition. This gives a standard deviation, σ, of $0.017 mmH_2O$ at a mean pressure of $-3.483 mmH_2O$. This corresponds to a variable error, $2\sigma = \pm 1\%$ of the mean. 95% of the samples will lie within this band. The total uncertainty is therefore $\pm 1.4\%$.

3.4.6 Force measurements

The forces acting on the model were to be measured using a dynamometer mounted underneath the tunnel. The original dynamometer that was used with this wind tunnel was a five-component strain-gauge dynamometer [59]. Initial tests with this showed that although the results were mostly sensible, the repeatability was not good. This was due to the sensitivity of the dynamometer being too large for the relatively small forces acting on the model. The sensitivity of the dynamometer was $3.96 \mu V/N$, giving only $19.8 \mu V$ at $5N$. For the channel used the design load of the strain gauge is $380N$.

In view of this, a smaller dynamometer was located which had a greater sensitivity of $74 \mu V/N$. This was used for all subsequent tests. This dynamometer was a three-channel dynamometer with lift, drag and torque channels. However, the lift and torque channels were giving non-linear readings with a large voltage offset, suggesting a broken connection. The technicians were unable to find the cause of this though, so only the drag channel was used. The dynamometer was simply rotated and the tests repeated to measure lift. Unfortunately this precluded the possibility of correlating simultaneous lift and drag measurements.

The dynamometer was connected to the Fylde bridge balance and power supply. The amplified signal was then processed by an analogue to digital converter and either the LabView measurement software or the Wolfson Unit TurboAD software was used to record the values. Calibration was achieved by attaching weights suspended over a pulley. This process was repeated for every set of measurements. A series of four weights were used up to $2.41 kg$.

The variable error in the force measurements is estimated by taking a series of 30 readings with a fixed load applied to the dynamometer. This gives a standard deviation of $0.0034N$ at a load of $0.73N$, or $\pm 0.5\%$. The fixed error is $\pm 0.01N$. The total uncertainty in the force measurements is $\pm 0.5\%$.

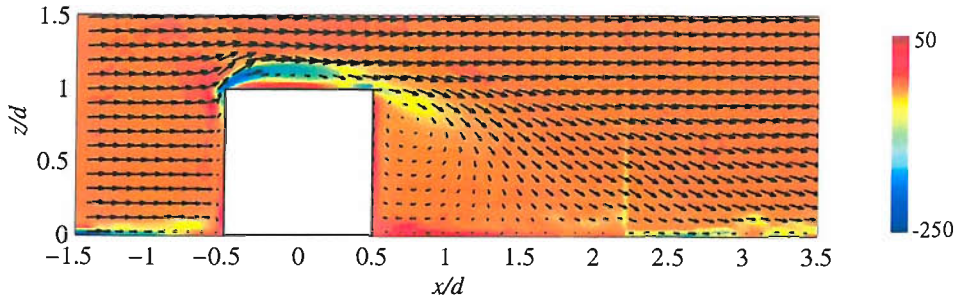

Figure 3.3: Velocity vectors with contours of vorticity ($y/d = 0$), measured by PIV

3.5 Results and discussion

3.5.1 Overview

As stated previously, the flow considered here is complex with a number of constituent features (Figure 2.1). Some of the measurements encompass all aspects of the flow, while others only represent certain parts of the flow. In the presentation of the results below an attempt has been made to identify the different flow features and to present the results in a way which demonstrates these features individually. It is felt that this is the most convenient way to examine the various datasets. First of all the overall flow structure will be presented using the flow visualisation and PIV results.

Figure 3.3 shows the overall structure of the flow in the longitudinal ($y/d = 0$) plane. The flow is seen to undergo separation at the leading edge of the free-end of the cylinder. This forms a recirculation bubble on the free-end which reattaches to the surface of the free-end at $x/d \approx 0.2$. At the trailing edge a shear-layer is formed enclosing a large recirculation region extending to $x/d \approx 1.5$. A pronounced vortex can be seen just behind the trailing edge at the end of the cylinder. This is the top of the so-called "arch vortex" which loops down to the ground plane. The bases of this vortex are seen as focal nodes in the flow visualisation image of the ground plane in Figure 3.4 marked as F_F. The flow features in the oil flow visualisation are interpreted according to Tobak and Peake [60] and Perry and Chong [61].

The horseshoe vortex which is formed at the juncture of the cylinder with the ground plane is just visible in Figure 3.3. The path of this vortex on the ground can also be seen in the flow visualisation picture in Figure 3.4. The primary separation point (S_1) is at $x/d = -1$. S_2 is the secondary separation point as defined by Baker (Figure 2.2), while line C is the line of converging streamlines at the upstream edge of the primary vortex. The streamlines inside this line are created by the outward flow under the primary vortex and are swept back by the spiral motion of the vortex. There is another line of diverging streamlines (D) inside this, extending from the leading edge of the cylinder. This is the inner edge of the horseshoe which moves away from the cylinder as it moves downstream. The inward facing streamlines inside this are

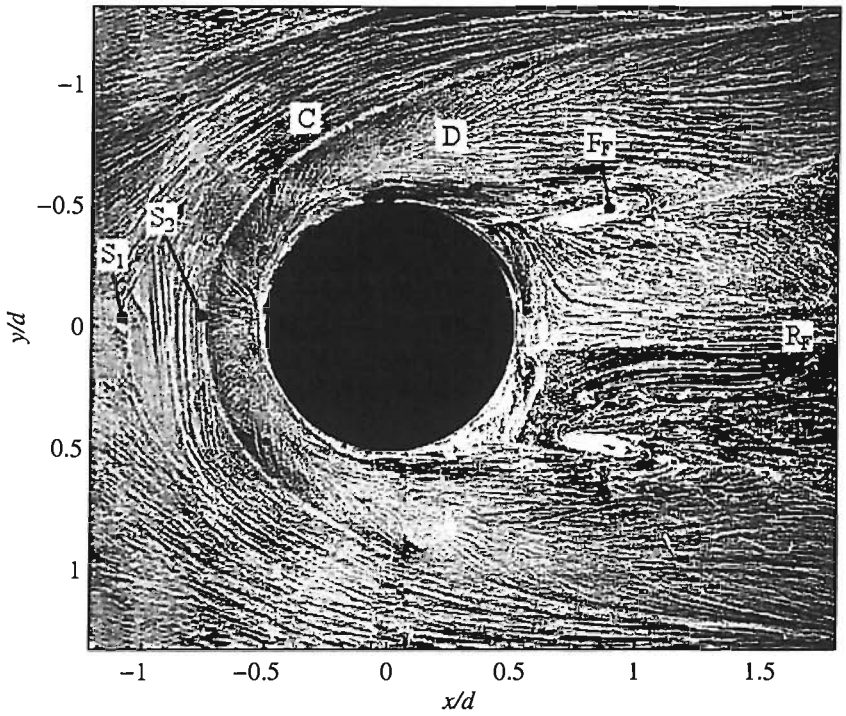

Figure 3.4: Surface flow visualisation - floor of tunnel (flow from left to right)

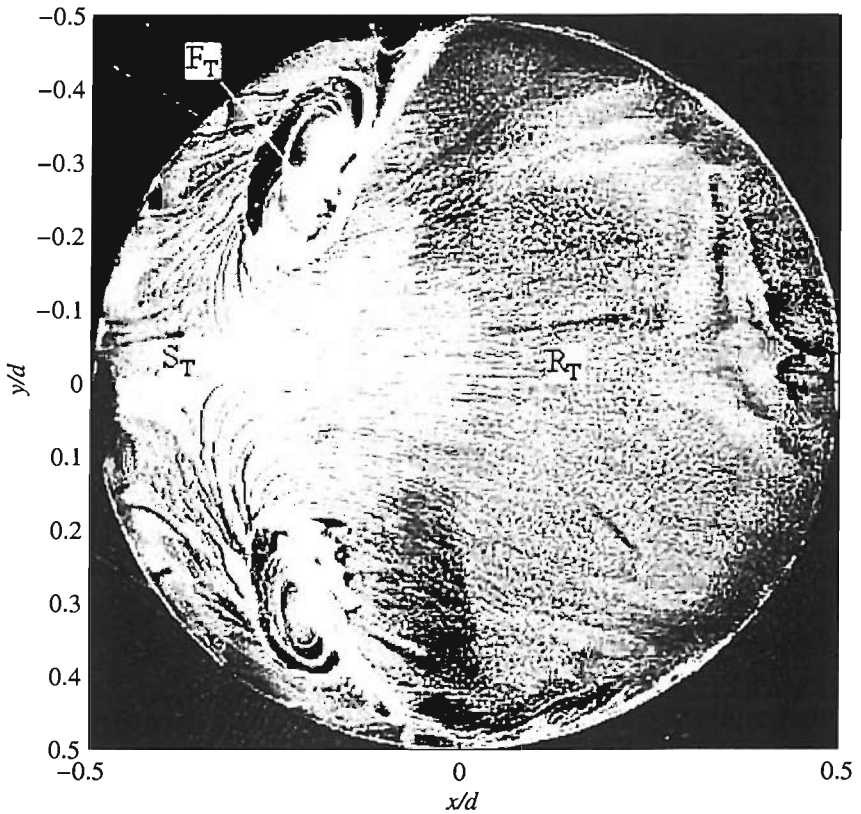

Figure 3.5: Surface flow visualisation - top of cylinder (flow from left to right)

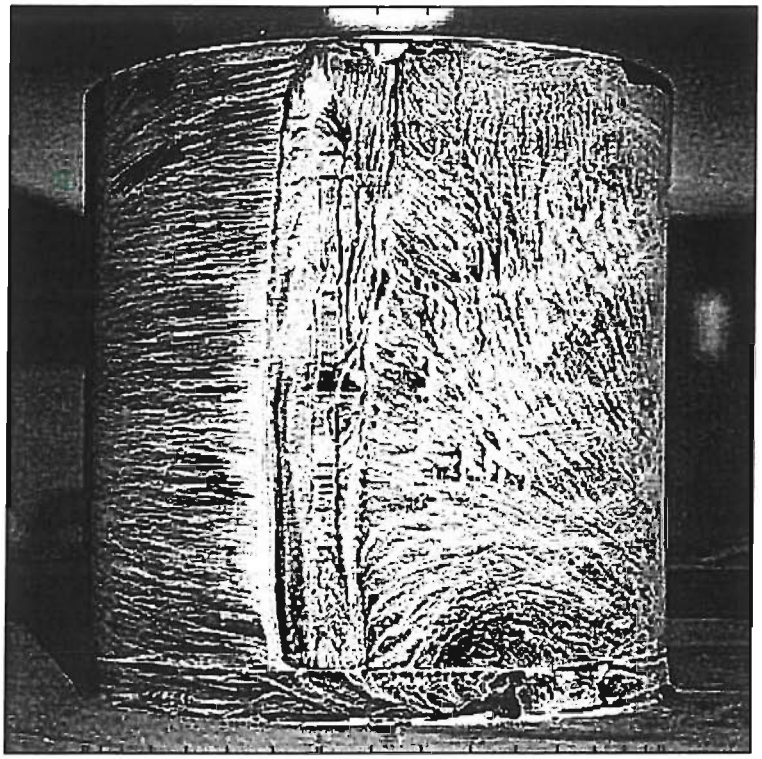

Figure 3.6: Surface flow visualisation - side of cylinder (flow from left to right)

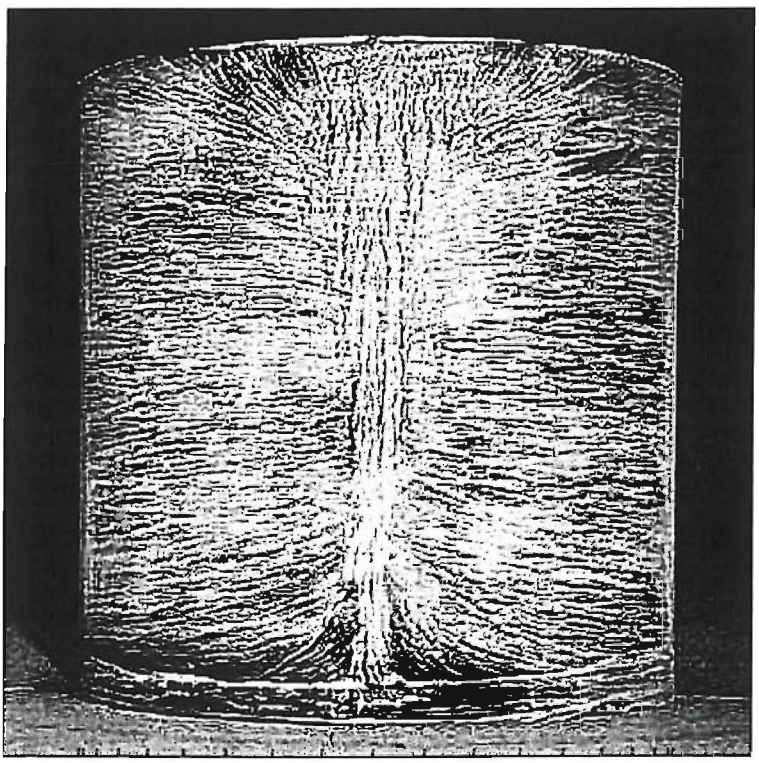

Figure 3.7: Surface flow visualisation - front of cylinder (flow into page)

due to a counter-rotating vortex formed in the corner. The reattachment of the wake to the ground plane is marked by R_T.

Figure 3.5 shows the flow on the surface of the free-end of the cylinder. The most prominent features are the two foci (F_T) at $x/d \approx -0.25$. There is a saddle point of separation (S_T) between them at $x/d = -0.4$. This is where the reversed flow along the centreline of the tip separates from the surface to form a small vortex near the leading edge. There is a saddle point of reattachment (R_T) at $x/d = -0.7$ where the flow reattaches to the free-end. The nature of this flow will be discussed further in Section 3.5.4.

The flow separates from the cylinder surface at an angle of 70 degrees from the leading edge. This can be seen from the flow visualisation in Figure 3.6 which shows a side view of the cylinder. The oil flow is clearly attached on the forward part of the cylinder before forming a vertical line where the flow separates. Figure 3.7 shows a view of the front of the cylinder showing the upwash near the free-end and the downwash near the ground.

Table 3.2 lists the key results obtained by previous authors on cylinders of $h/d = 1$ for comparison with the current work.

Table 3.2: Summary of previous experimental results on cylinders of $h/d = 1$ mounted on the ground (upstream boundary layers are turbulent unless otherwise stated)

Author(s)	Year	h/d	Re_d	δ/d	X_{s1}	X_{s2}	θ_s	X_{rt}	X_{rf}	C_{pmin}	C_{pb}	C_D
Okamoto and Yagita	1973	1	13000	0.16 (lam)	-	-	73	-	-	-0.6	-0.46	-
Taniguchi et al.	1981	1	21000	2.0	-	-	-	-	-	-0.4	-0.25	0.7
Okamoto	1982	1	47400	0.1 (lam)	-1.5	-	70	-	2.9	-0.65	-0.57	0.7
Kawamura et al.	1984	1	32000	0.10 (lam)	-	-	72	0.2	-	-0.65	-0.54	0.75
Sin and So	1987	1	48000	0.25	-	-	-	-	-	-0.85	-0.56	0.79
Okamoto and Sunabashiri	1992	1	30000	0.06	-	-	73	-	2.9	-0.65	-0.57	0.7
Roh and Park	2003	1.25	148000	0.06	-	-	-	0.4	-	-	-	-
Current work	2003	1	196000	0.10	-1.00	-0.78	70	0.17	1.6	-0.65	-0.57	0.79

Table 3.3: Details of the boundary layer on the ground plane at the model location (x/d=0, y/d=0)

U_∞ (m/s)	δ/d	δ^*/d	θ/d	Re_θ	η
10	0.20	0.022	0.018	1761	1.21
15	0.14	0.016	0.013	1942	1.25
20	0.10	0.013	0.010	2037	1.30

3.5.2 Upstream flow characteristics

It is important to understand the nature of the flow upstream of the model so that comparisons can be made between different cases. This information can also be applied to the inlet condition of the CFD model to give a more accurate representation of the flow. The particular features of interest are the free-stream turbulence level, the uniformity of the flow across the section and the thickness and nature of the boundary layer on the floor.

First, the velocity on a plane just downstream of the leading edge of the ground plate was measured to check for turbulence intensity and uniformity of the tunnel flow. Measurements were made at 7 transverse locations between $y = -150mm$ and $150mm$, and at heights z from $10mm$ to $300mm$ at intervals of $20mm$. The flow speed was found to be uniform to $\pm 0.5\%$. The turbulence intensity was 0.3%.

Profiles of the boundary layer were measured at the location of the front of the model, $x/d = -0.5$, without the model being there. Figure 3.8 shows the profiles at three locations across the tunnel which show that the boundary layer is symmetrical across the tunnel to within 3%.

Figure 3.9 shows the variation in floor boundary layer thickness with tunnel speed. The nature of the boundary layer can be described by the shape factor, η, where

$$\eta = \delta^*/\theta$$

with δ^* being the displacement thickness and θ being the momentum thickness. For the $U_\infty = 20m/s$ condition $\eta \approx 1.25$, which is close to that found by Klebanoff [62] for a turbulent boundary layer ($\eta \approx 1.3$), whereas for a laminar boundary layer as described by Blasius (1908) $\eta \approx 2.6$. The slightly smaller shape factor could be due to a favourable pressure gradient in the working section of the tunnel, also Re_θ, at 3000 is lower than the value (8000) used by Klebanoff. Figure 3.10 shows the profiles of streamwise turbulence intensity, u'/U_∞, at different tunnel speeds, compared to the data of Klebanoff. It can be seen that the turbulence intensities are slightly higher than those measured by Klebanoff.

Figure 3.11 shows the boundary layer profiles at $x/d = -1.0$ at different speeds measured

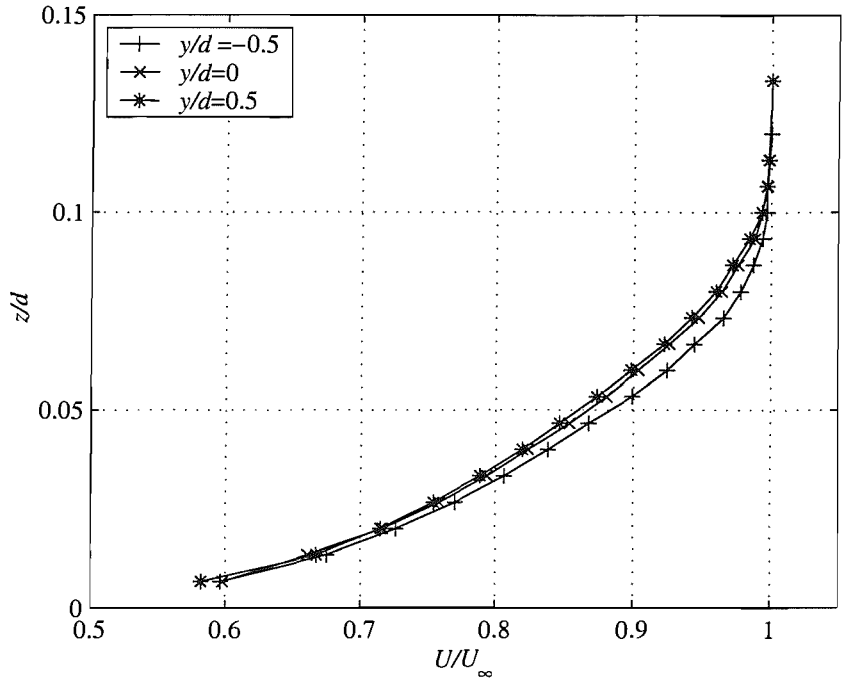

Figure 3.8: Plot of the normalised U velocity in the boundary layer across the tunnel ($x/d = -0.5$) at $U_\infty = 20m/s$ without the model

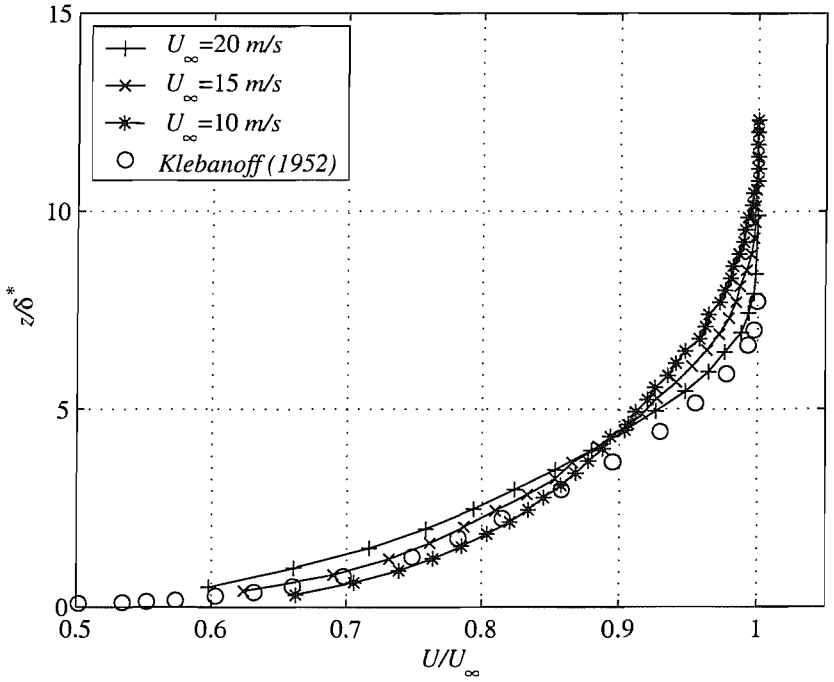

Figure 3.9: Plot of the normalised U velocity in the boundary layer at various speeds ($x/d = -0.5$) without the model

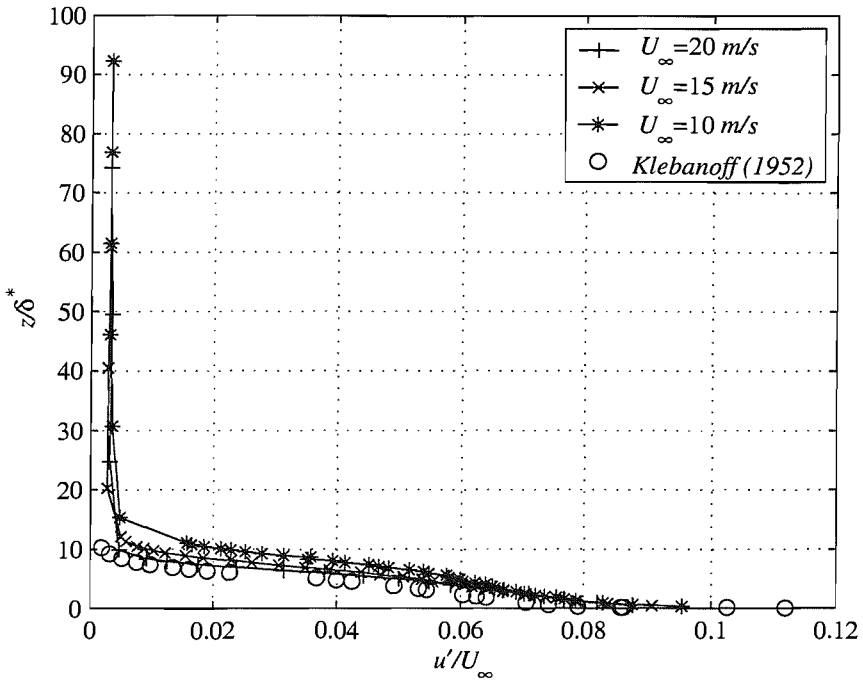

Figure 3.10: Plot of the fluctuations in U velocity, u' in the boundary layer at various speeds ($x/d = -0.5$) without the model

by PIV. These were taken in the presence of the cylinder and are $0.25d$ upstream of the front of the horseshoe vortex.

3.5.3 Horseshoe vortex

One of the dominant features of the flow around an obstacle on a ground plane is the presence of a horseshoe vortex. This is formed when the flow separates under the influence of the adverse pressure gradient upstream of the stagnation point and causes the flow to roll-up and convect downstream around the body.

Figure 3.12 shows the velocity vectors and vorticity contours of the symmetry plane in front of the cylinder showing the horseshoe vortex. The centre of the primary vortex shown here is at $x/d = -0.67$, $z/d = 0.04$. At first glance there appears to be a separation point on the ground plane in front of the horseshoe vortex, at $x/d = -0.76$ when $U_\infty = 20m/s$. This corresponds to the position of point S_2 in the oil flow visualisation (Figure 3.4) which was supposed to be a reattachment line according to the analysis of Baker [27] in Figure 2.2. According to this theory, and the flow visualisation, the separation point (S_1) should be further upstream around $x/d = -1$. On closer inspection of the vector plots (Figure 3.12(c)) it can be seen that the vectors closest to the ground are actually pointing downwards, indicating that this point is indeed a reattachment as proposed by Baker [27]. The implication of this is that there are

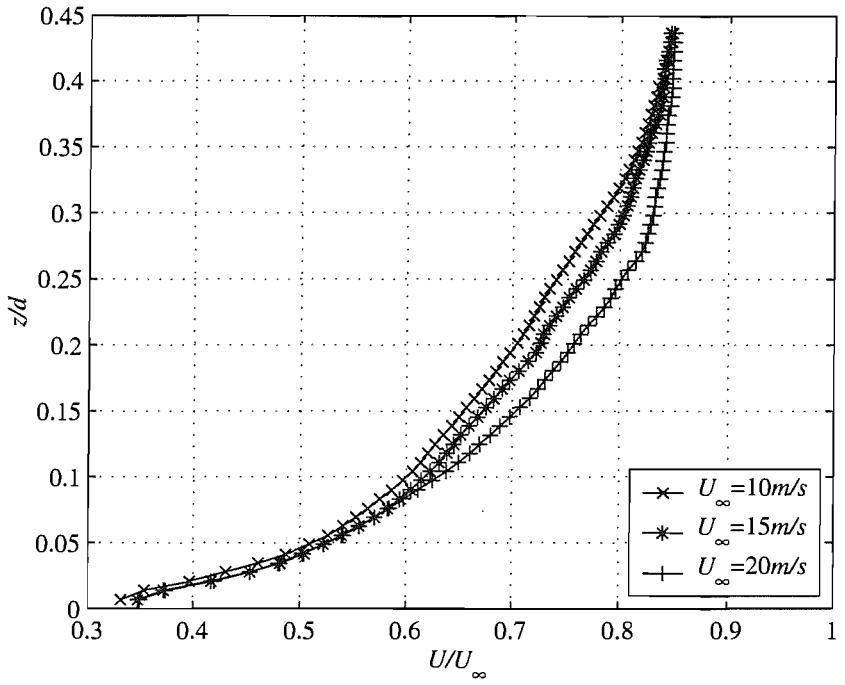

(a) Velocity

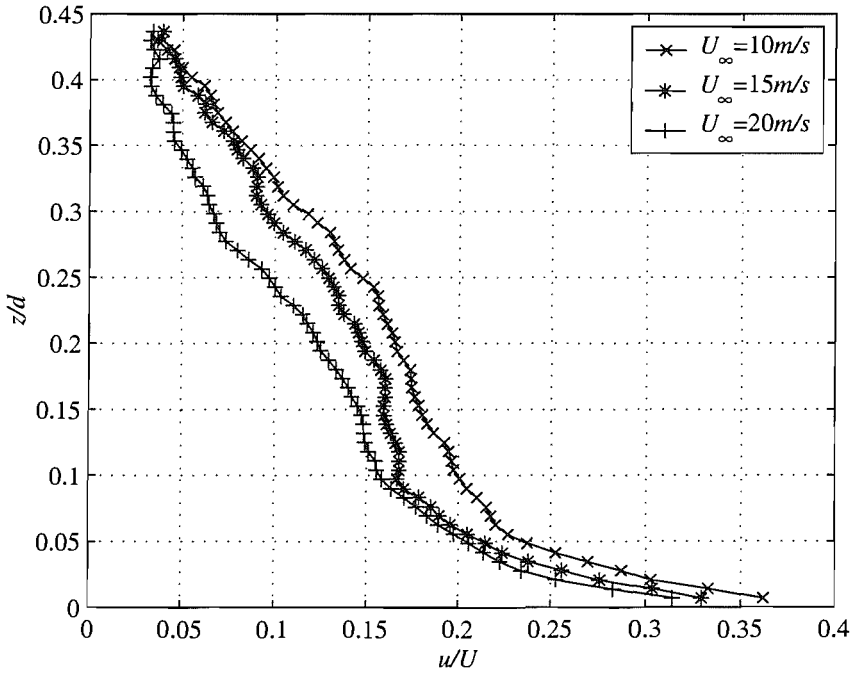

(b) Turbulence intensity

Figure 3.11: Boundary layer velocity and turbulence intensity profiles at $x/d = -1.0$ in the presence of the model, measured by PIV.

recirculating vortices either side of this point which are not visible in these measurements. The height of the saddle point between these vortices is $z/d = 0.02$ or 0.2δ. It should be noted that the resolution of the PIV measurements here is $0.013d$ so the position of this point cannot be stated precisely. Higher resolution measurements would be needed to be confident in this value. This feature will be discussed further in Chapter 8.

Figure 3.13 shows plots of the U-velocity through the centre of the vortex on the symmetry plane. This shows that there is little difference in the position of the centre of the vortex at the two different speeds. The centre of the vortex is at $x/d = -0.67$, $z/d = 0.04$. There is no evidence of the bi-modal behaviour as reported by Baker [26].

The horseshoe vortex displays considerable unsteadiness in its location as can be seen from the instantaneous PIV images. The location of the centre of vortex can be approximated by the maximum value of vorticity (actually the most negative value in this coordinate system) and can be found by locating the data point at which this occurs. These locations have been found from each of the 500 PIV images at the $20m/s$ tunnel speed, and are plotted in Figure 3.14. This motion appears to be a motion of the entire vortex as there is only one vortex core evident in each instantaneous image. The position has a standard deviation of 0.039 in the x direction and 0.012 in the z direction.

3.5.4 Free-end flow

The flow over the free-end is characterised by the separation from the sharp leading edge. This forms a complex three-dimensional recirculation region on top of the cylinder. The flow visualisation image in Figure 3.5 shows the swirl patterns on the forward half of the cylinder tip. There is a saddle point (S_T) just behind the leading edge at $x/d = -0.4$, where the streamlines from the rear of the cylinder return and turn out towards the swirls. The flow exits the swirls over the edge of the cylinder just behind the separation line. On the rear half of the free-end there is another saddle point (R_T) where the streamlines from the leading edge descend to the tip.

The PIV velocity vectors of the streamwise symmetry plane on top of the cylinder (Figure 3.15) show the region of recirculating flow. The resolution of this image is perhaps not sufficient to identify the details of the flow as there are only 10 points in the height of the vortex. Difficulties with the reflection of the laser light off the cylinder surface also masked the details of the flow close to the tip. Figure 3.16 shows the flow immediately behind the trailing edge of the cylinder. The tip vortices are clearly visible at the corners of the free-end.

One recent paper on the subject of the free-end flow by Roh and Park [21] proposed a flow topology consisting of two pairs of counter-rotating streamwise vortices, with the inner pair being rooted on the swirl patterns on the tip. These measurements were carried out at

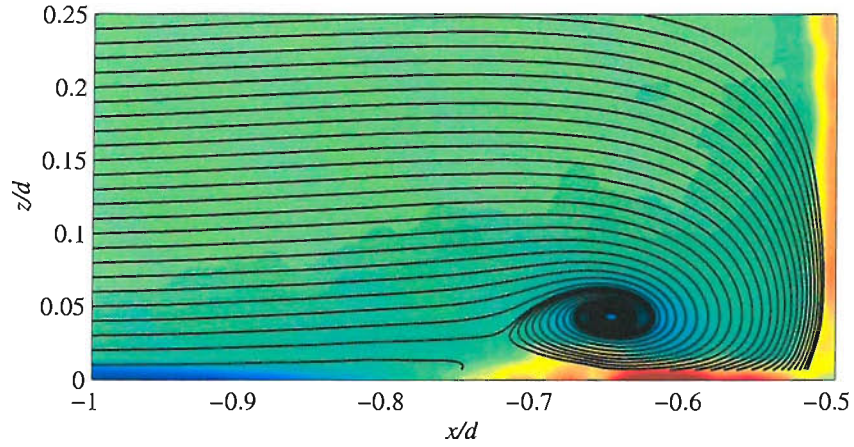

(a) $U_\infty = 10m/s$

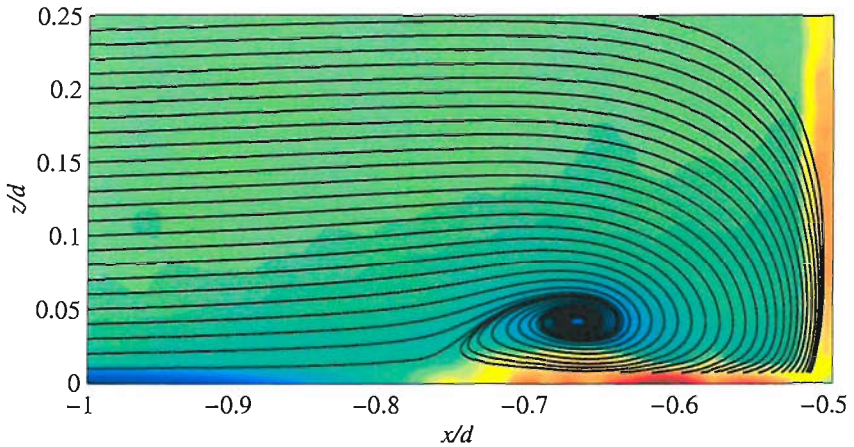

(b) $U_\infty = 20m/s$

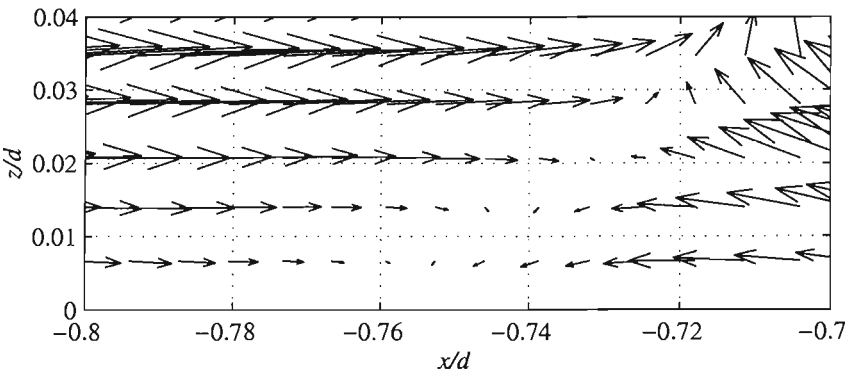

(c) $U_\infty = 10m/s$ - Exploded view of attachment

Figure 3.12: Velocity vectors and vorticity contours on centreline ($y/d = 0$) upstream of cylinder, showing the horseshoe vortex.

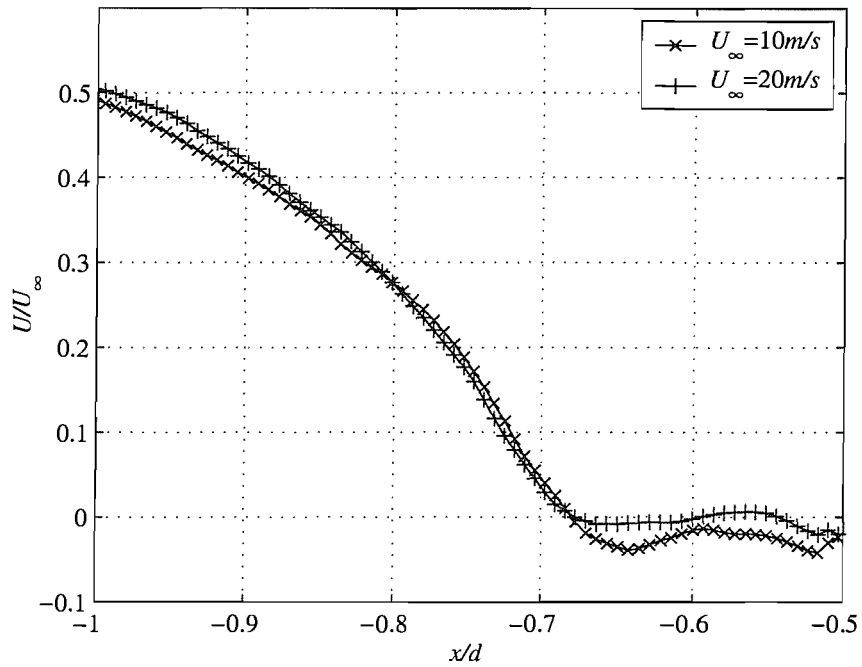

(a) $z/d = 0.04$

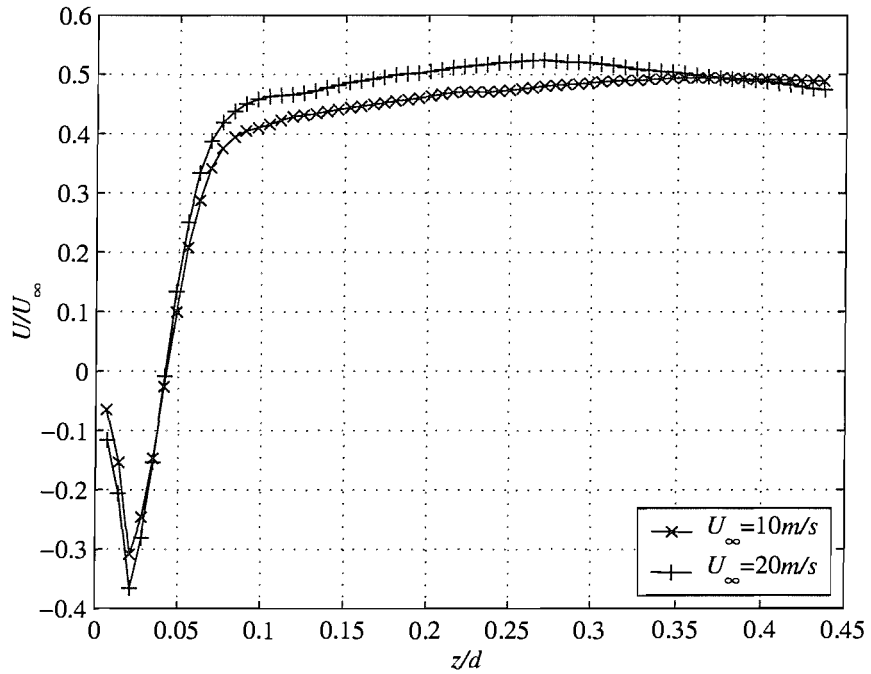

(b) $x/d = -0.66$

Figure 3.13: Normalised U velocities through centre of horseshoe vortex

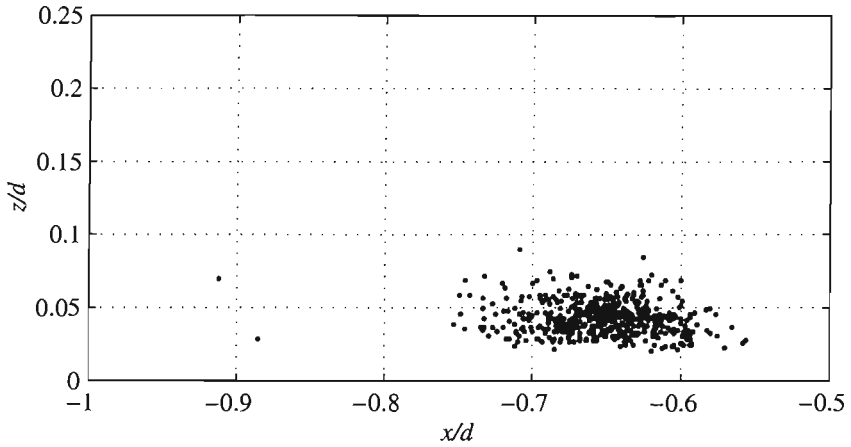

Figure 3.14: Plot showing locations of horseshoe vortex centre on $y/d = 0$ in each PIV image at $U_\infty = 20m/s$

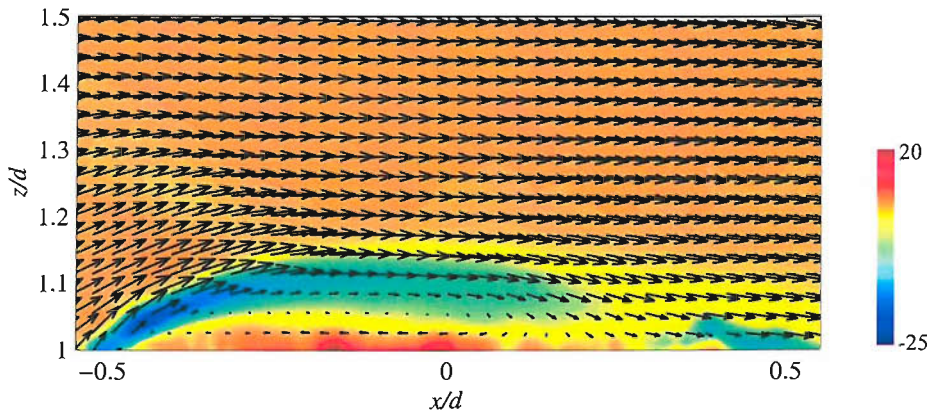

Figure 3.15: Vector plot with contours of vorticity on $y/d = 0$ on top of the cylinder ($U_\infty = 20m/s$)

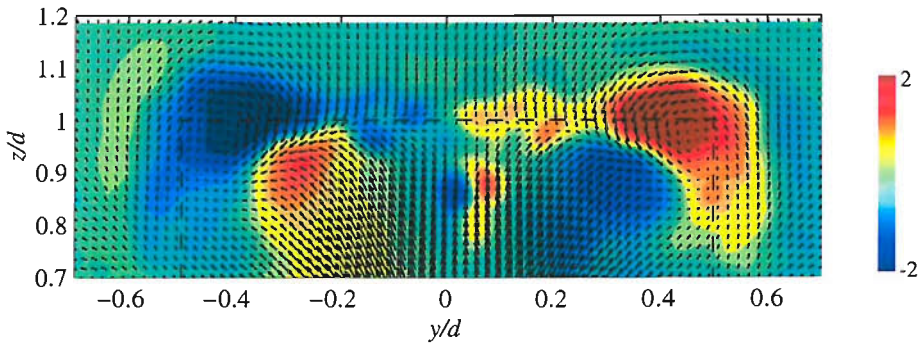

Figure 3.16: Vector plot with contours of vorticity on $x/d = 0.5$ ($U_\infty = 20m/s$)

Reynolds numbers of 5.92×10^3 and 1.48×10^5, with aspect ratios of 1.25 and 4.25; the high *Re*, low aspect ratio case should correspond quite closely to the present study. Their light-sheet visualisation appears to show these vortices inside the two tip vortices and trailing downstream of the cylinder. However there is no evidence of this inner pair of vortices in the current results. Indeed there appear to be some important differences between the topology as proposed by Roh and Park and the flow measured here.

In view of the discrepancies in the tip flow topologies reported in the literature, and in light of the current results, a fresh attempt at depicting the flow pattern has been made in Chapter 8. Here the numerical results will be used to support the theory that there is a single vortex wrapping over the free-end with its bases on the two foci.

3.5.5 Separation and mean flow structure of the wake

As has been seen in the flow visualisation in Figure 3.6 the flow separates from the side of the cylinder 70 degrees from the leading edge. Near the free-end separation is delayed by about 5 degrees due to the oblique flow over the end. At the sub-critical Reynolds number of 2×10^5, at which these experiments were carried out, the boundary layer is laminar with transition presumably occurring in the shear layer immediately after separation. This corresponds to the transition in shear layers regime reported by Zdravkovich [2] for the infinite cylinder case at Reynolds numbers up to 2×10^5. On an infinite cylinder separation would be expected at 80 degrees in this regime; the difference being attributed to the higher pressure behind the cylinder due to the flow over the free-end entering the recirculation region [3].

To see the effect of transition on the separation point the boundary layer was tripped to turbulence using a wire placed on the forward surface of the cylinder [63]. The size of the wire was selected using the equation,

$$\frac{U_\infty d_w}{\nu} > 36\left(\frac{U_\infty x}{\nu}\right)$$

where d_w is the diameter of the wire and x is the distance from the leading edge to the wire. For a wire at 10% of the diameter from the leading edge this gives a wire diameter of $0.44mm$. A $0.5mm$ wire was therefore used. Flow visualisation was carried out in this condition, and it can be seen from Figure 3.17 that separation is delayed until 80 degrees from the leading edge. This is further forward than the 100 degrees which would be expected for an infinite cylinder in the transition in boundary layers regime. The later separation point appeared to make little difference to the remainder of the flow and so other measurements were not repeated in this condition.

Downstream of separation the detached shear layer around the cylinder encloses a recirculation region. This extends to $x/d = 1.6$ where the flow descending from the free-end attaches

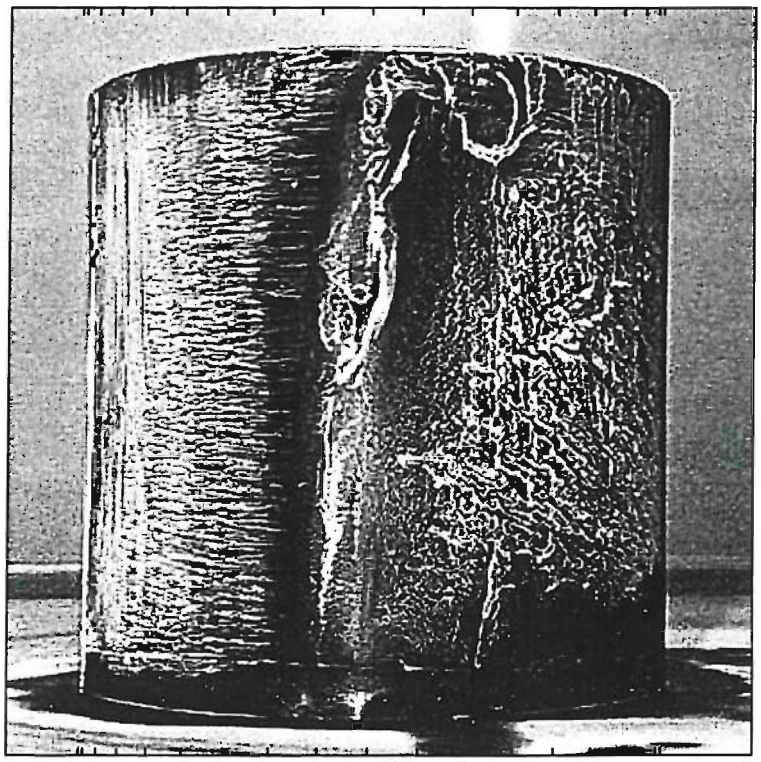

Figure 3.17: Surface flow visualisation on the side of the cylinder with tripped boundary layer, $U_\infty = 20m/s$ (Flow from left to right)

to the ground plane. Between this and the cylinder there is a region of backflow along the ground, which wraps into the arch vortex. The bases of this vortex can be seen in the flow visualisation in Figure 3.4. The shear layers at the sides and over the top interact and form a pair of vortices aligned in the streamwise direction. The development of these can be seen in the PIV measurement planes in Figure 3.18.

At the first plane ($x/d = 0.5$) two counter-rotating tip vortices can be seen at the free-end of the cylinder. They are most clearly shown by the area of high vorticity, rather than the velocity vectors, as these are influenced by the global flow around the back of the cylinder. These vortices remain at a similar location in the plane until $x/d = 1.0$ where they start to dilate and descend towards the ground plane. They appear to be pushed down by the downwash behind the cylinder. Moving downstream, the tip vortices expand as they descend to the ground. At $x/d = 2.5$ it appears that the tip vortices may have merged with the horseshoe vortex to create a much larger vortex.

At $x/d = 0.5$ two areas of high vorticity are observed either side at the base of the cylinder. These appear to be induced by the horseshoe vortex which rotates in the opposite sense. The main horseshoe vortex is likely to be outside the extents of these planes. As has been seen from the surface flow visualisation the horseshoe vortex extends to $y/d = \pm 1$ at $x/d = 0.5$. In fact the inside edge of the horseshoe is discernible from the velocity vectors at the sides of the plot, where the vectors at the outside lower corner are pointing downwards and outwards.

3.5.6 Velocity fluctuations in the wake

The structure described above only exists in the time-averaged flow. In an instantaneous view of the flow there are many vortices of various scales and orientations. An illustration of this can be seen in Figure 3.19 which shows an instantaneous vorticity field at $x/d = 1.5$. This is typical of a turbulent flow where larger vortices are unstable and break down into smaller ones. This continues until the vortices are small enough that the viscosity of the fluid is sufficient to dissipate the energy through heat. This scale is known as the Kolmogorov length scale [64]. Thus at any instant the flow consists of vortices with a wide range of length-scales. These vortices have characteristic frequencies of formation which are visible in a plot of the power spectral density function of a velocity signal.

The form of the wake within the recirculation bubble has been shown by Okamoto [10] to be an arch vortex, which is attached to the ground behind the cylinder and loops over to the other side. It has been suggested that this is shed at a certain Strouhal number in a symmetrical manner, as opposed to the antisymmetric shedding experienced behind a higher aspect ratio cylinder. In fact Okamoto and Sunabashiri [16] found that the peak in the frequency spectrum was very broad for the low aspect ratio cylinder, suggesting that the shedding was not strong. Other authors such as Park and Lee [19] while looking at higher aspect ratio cylinders found a

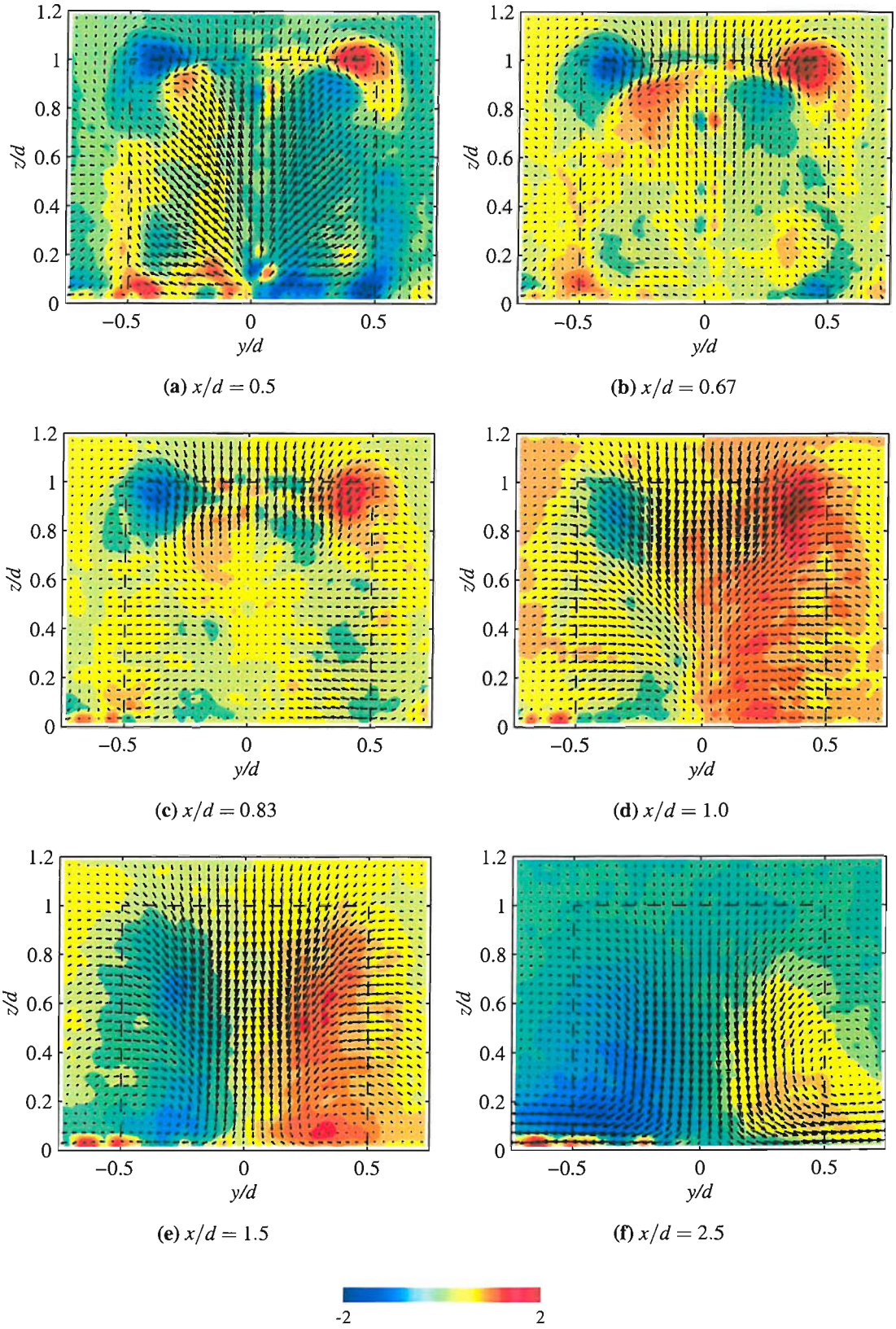

(a) $x/d = 0.5$

(b) $x/d = 0.67$

(c) $x/d = 0.83$

(d) $x/d = 1.0$

(e) $x/d = 1.5$

(f) $x/d = 2.5$

Figure 3.18: Time-averaged velocity vectors and contours of vorticity viewed from downstream, $U_\infty = 20m/s$

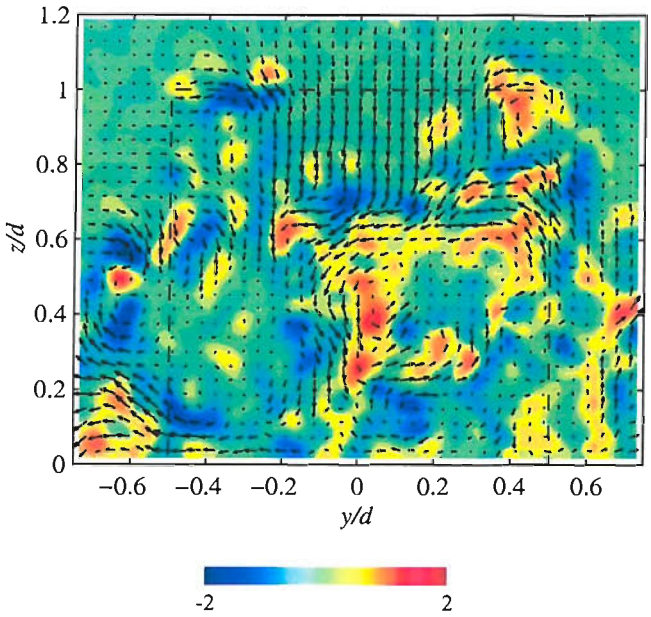

Figure 3.19: Instantaneous velocity vectors and contours of vorticity at $x/d = 1$ viewed from downstream, $U_\infty = 20m/s$

particular shedding pattern near the tip of the cylinder which they attributed to the tip vortex.

In this study the unsteady behaviour of the wake flow has been investigated using hot-wire anemometry. The existence of any dominant vortex shedding frequencies can be identified by plotting the power spectral density function of the velocity fluctuations. The power spectral density function is defined as,

$$E(f) = \lim_{\Delta f \to 0} \left(\lim_{T \to \infty} \left(\frac{1}{\Delta f T} \int_0^T u^2(t, f, \Delta f)\, dt \right) \right) \tag{3.1}$$

where $u(t, f, \Delta f)$ represents the part of $u(t)$ which lies within a band of frequency Δf wide, centred on f [65]. The spectra were measured on a plane at $x/d = 1.5$, near the back of the recirculation region. Measurements were made along the lines $y/d = 1$ and $z/d = 1$. Measurements inside this region would be less reliable due to the likelihood of reversed flow. The measurements were made at a sampling frequency of $1000Hz$, in 30 blocks of 4096 samples, corresponding to a measurement time of $123s$. These tests were carried out at tunnel speeds of $10m/s$ and $20m/s$.

Figure 3.20 shows the variation of the PSD with transverse location along $z/d = 1$ at $U_\infty = 10m/s$. There is a peak in the PSD at $f = 16Hz$ which becomes more pronounced moving away from the centreline. Similarly Figure 3.22, which plots the PSD along $y/d = 1$ at different heights, shows the $16Hz$ peak becoming clearer towards the top of the cylinder. This suggests that the flow feature causing this peak is related to the flow over the free end rather than von-Karman type shedding of the transverse vortices, as these should be more pronounced towards the middle or bottom of the cylinder. However, $16Hz$ corresponds to a Strouhal number of 0.24, which is the number found by Okamoto and Sunabashiri [16] for the transverse vortex

shedding from a cylinder of aspect ratio 1.

Looking at the $U_\infty = 20m/s$ case, the plots (Figures 3.21 and 3.23) appear to show the same trends, in so far as the peak in the PSD is strongest at $y/d = 1$, $z/d = 1$. However, what is surprising is that the dominant frequency is actually the same as for $U_\infty = 10m/s$, that is $f = 16Hz$ or a Strouhal number of 0.12. Closer inspection of the lower speed graphs reveals that there does appear to be some energy around this lower Strouhal number as well as the higher frequency peak. Similarly in the higher speed case there is some energy around the higher Strouhal number as well. This suggests that there are two shedding frequencies which are more or less dominant depending on the flow speed.

To investigate this further, the PSD was measured at $y/d = 1$, $z/d = 1$ at various speeds. The results are plotted in Figure 3.24. It is quite clear that there is a transition from the higher Strouhal number to the lower one around $U_\infty = 17.5m/s$, where the two peaks are approximately equal heights. It is possible that a change in the position of the shear layer results in a different part of the flow being measured, however further work would be needed to confirm this.

3.5.7 Forces and pressures on the cylinder

Figure 3.25 shows the mean surface pressure coefficient, C_P around the circumference of the cylinder at different heights above the floor, at $U_\infty = 20m/s$. The plot shows that the pressure coefficient starts at 1 at the stagnation point on the leading edge and then falls rapidly to a minimum point, $C_P = -0.65$ at around 65 degrees, before rising slightly and levelling out in the wake region. The base pressure coefficient is -0.57. At the stagnation point the highest C_P is at the mid-height position with the pressure dropping very slightly towards the base and more towards the tip. The minimum pressure is lowest at the top of the cylinder as well. These pressures agree closely with those measured by Okamoto [16] and Kawamura et al. [12] despite the higher Reynolds number as shown in Figure 3.26. The rise from the minimum is slightly quicker than the others suggesting that separation occurs a few degrees earlier than in the other experiments. It should be noted that these results are different from those presented in [66] as there was an error in the calibration in those results. The drag coefficient found by integrating the pressure distribution over the surface (Equation 3.2) is 0.79 compared to 0.7 for Okamoto's and 0.75 for Kawamura's data.

$$C_D = \int_0^\pi C_P \cos\theta d\theta \tag{3.2}$$

The plots of power spectral density function in Figure 3.27 show a peak in the energy spectrum of the pressure signals at $12Hz$ which corresponds to a Strouhal number of 0.09. This is lower than the frequencies seen in the hot-wire measurements, which may be because it is caused by larger scale structures in the wake.

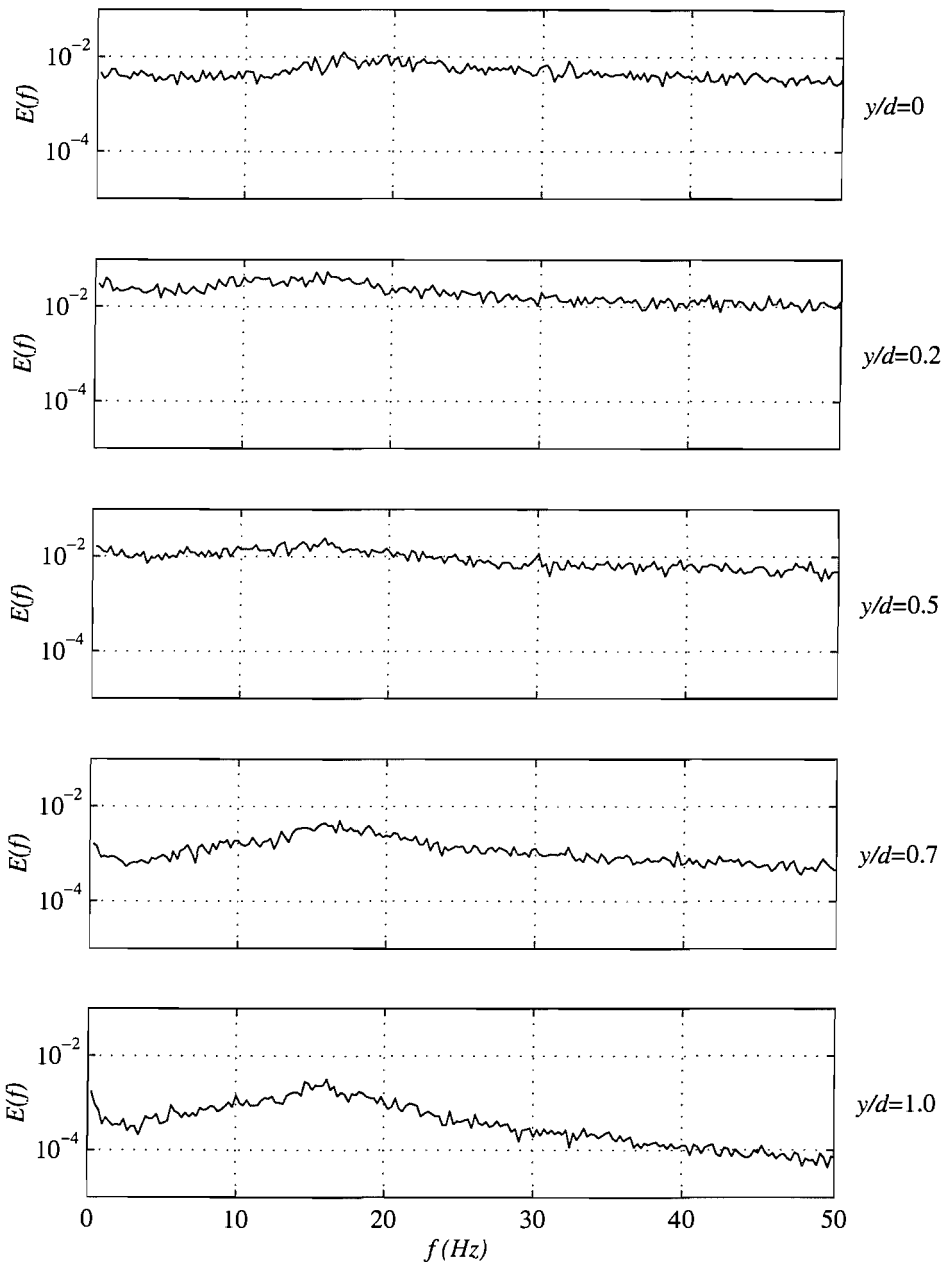

Figure 3.20: Power spectral density function of U velocity at $x/d = 1.5$, $z/d = 1$, $U_\infty = 10$

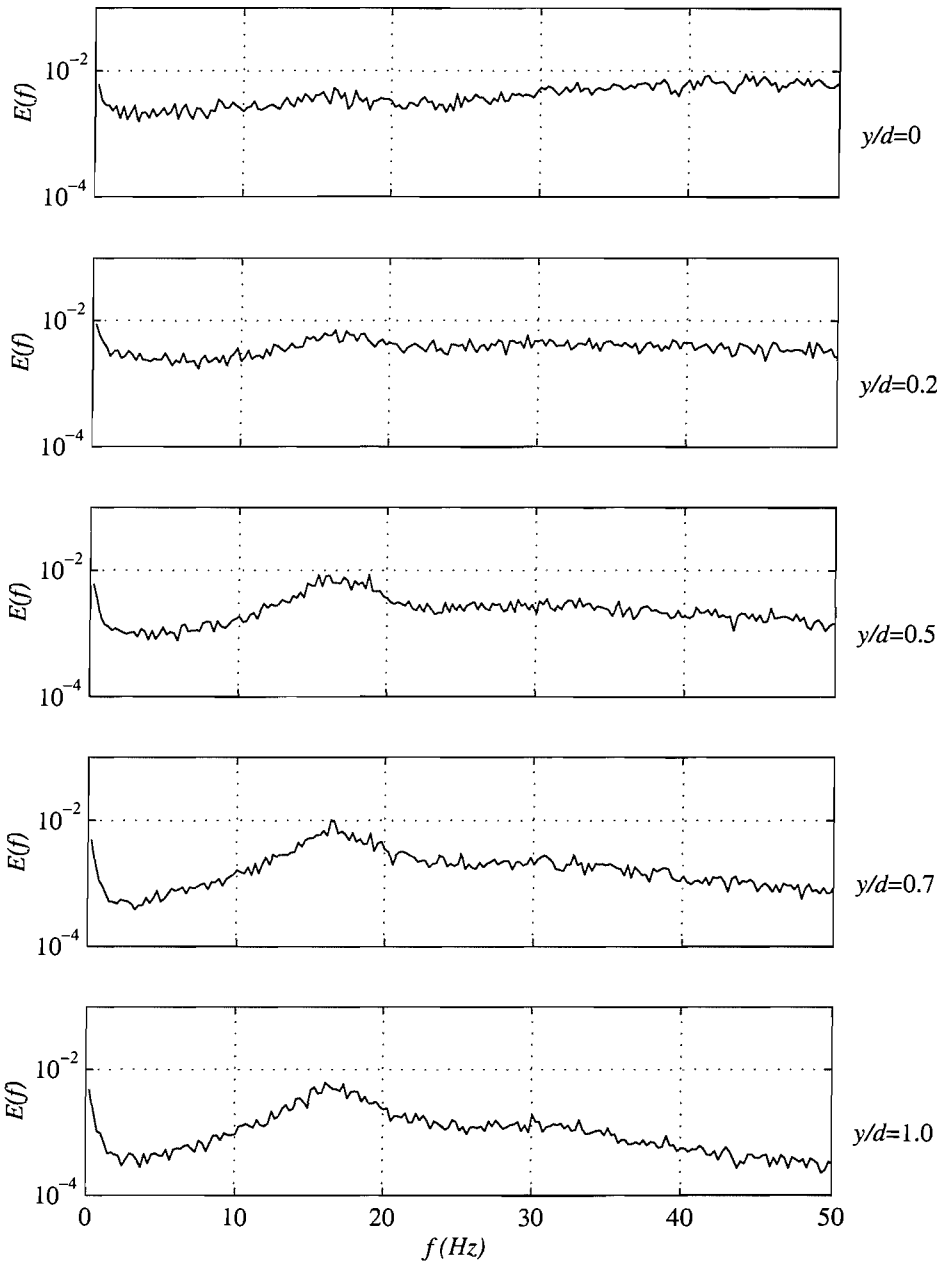

Figure 3.21: Power spectral density function of U velocity at $x/d = 1.5$, $z/d = 1$, $U_\infty = 20$

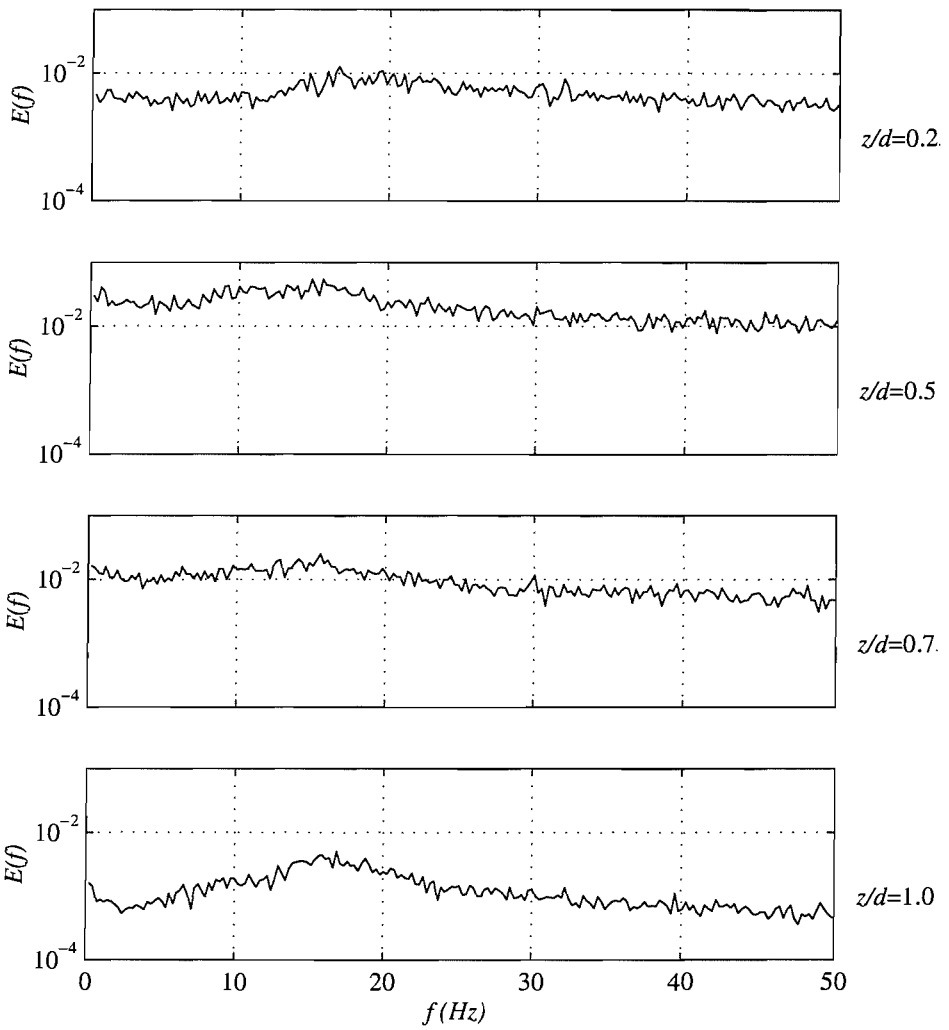

Figure 3.22: Power spectral density function of U velocity at $x/d = 1.5$, $y/d = 1$, $U_\infty = 10$

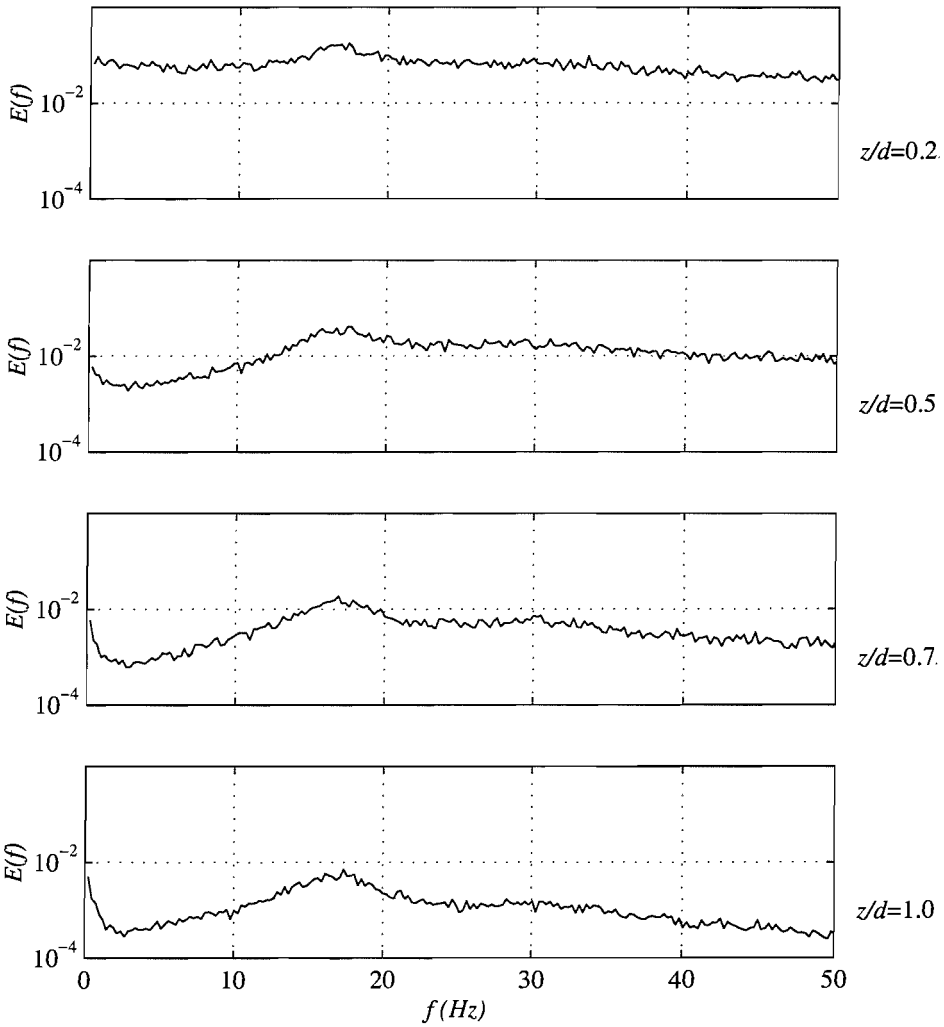

Figure 3.23: Power spectral density function of U velocity at $x/d = 1.5$, $y/d = 1$, $U_\infty = 20$

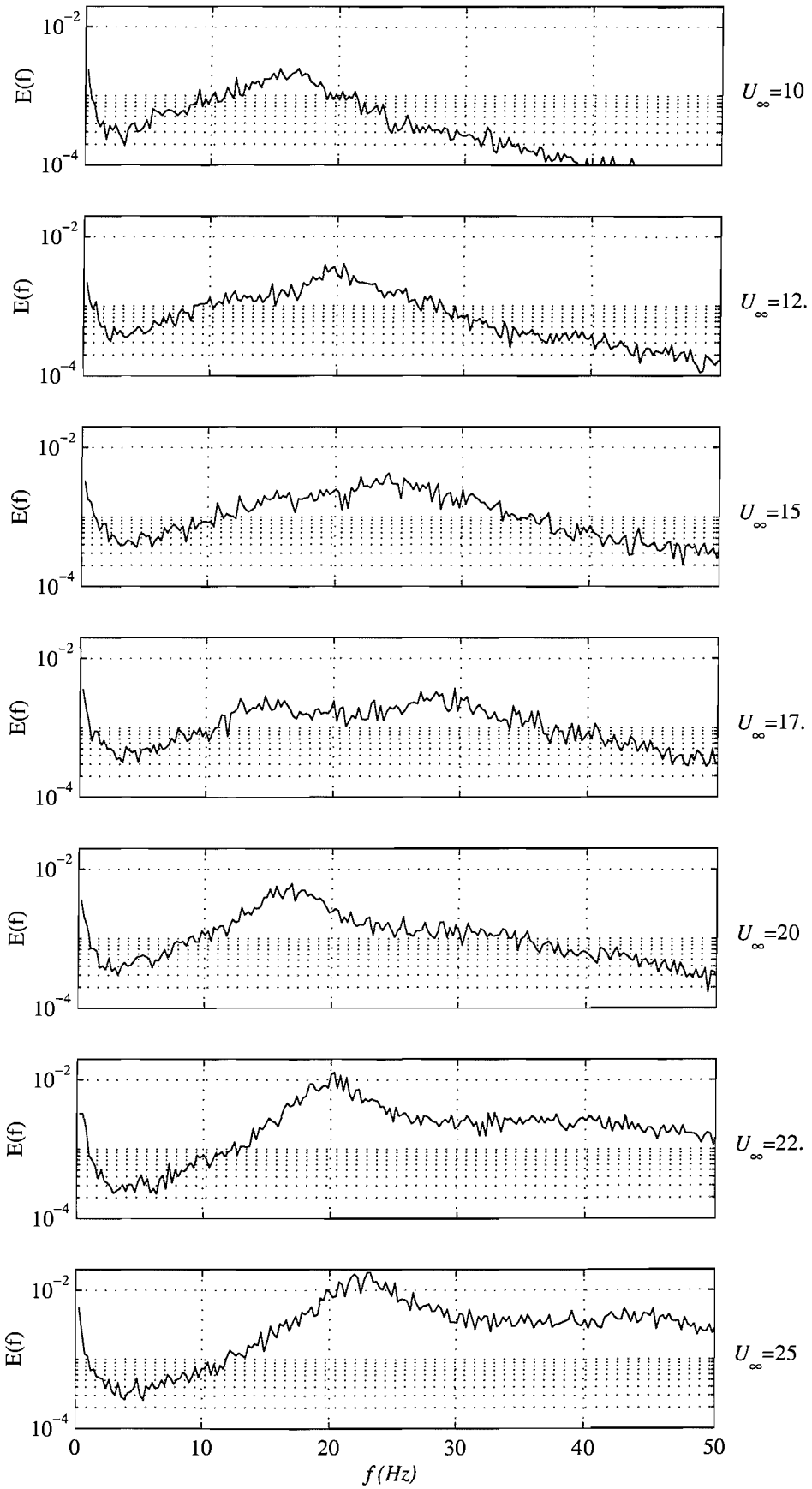

Figure 3.24: Power spectral density function of U velocity at $x/d = 1, y/d = 1, z/d = 1$

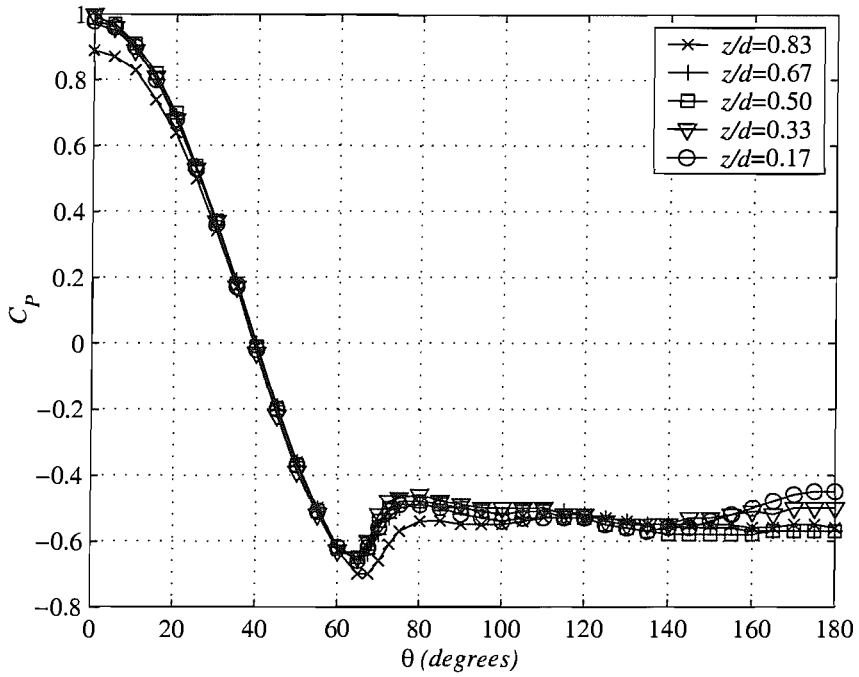

Figure 3.25: Distribution of pressure coefficient around cylinder at different spanwise locations, $U_\infty = 20m/s$

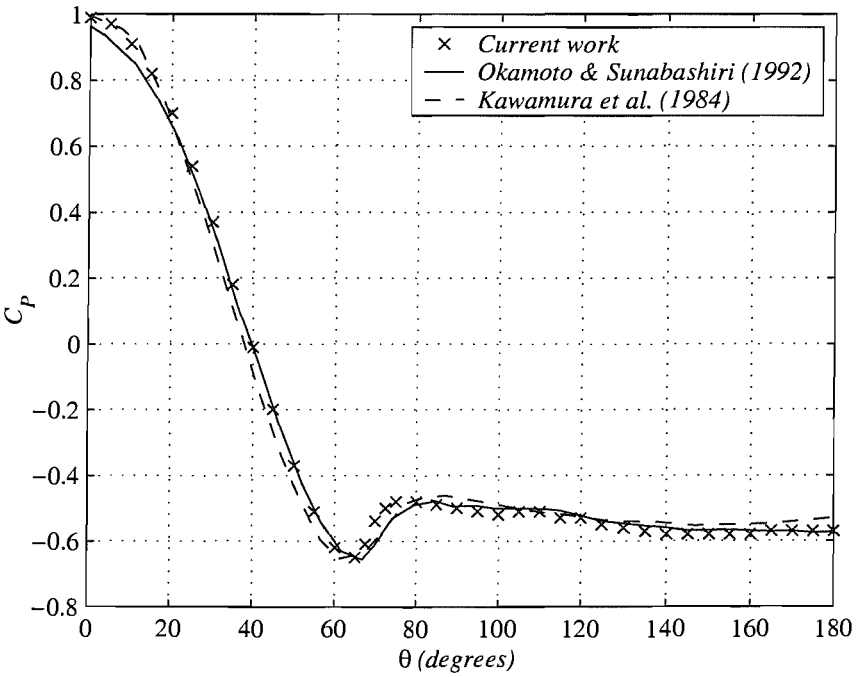

Figure 3.26: Distribution of pressure coefficient around cylinder at $z/d = 0.5$ compared to other authors, $U_\infty = 20m/s$

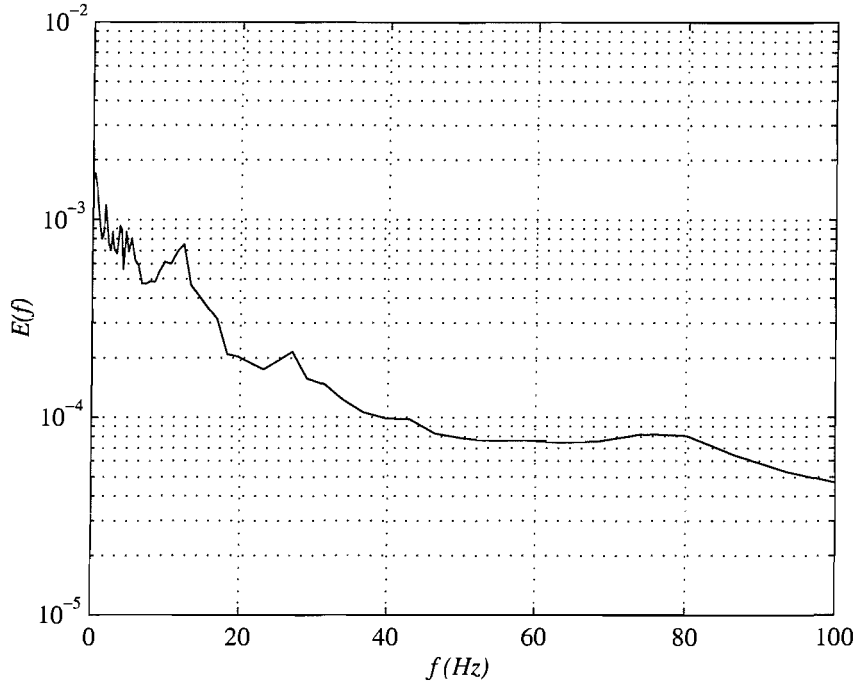

(a) $\theta = 135$ degrees

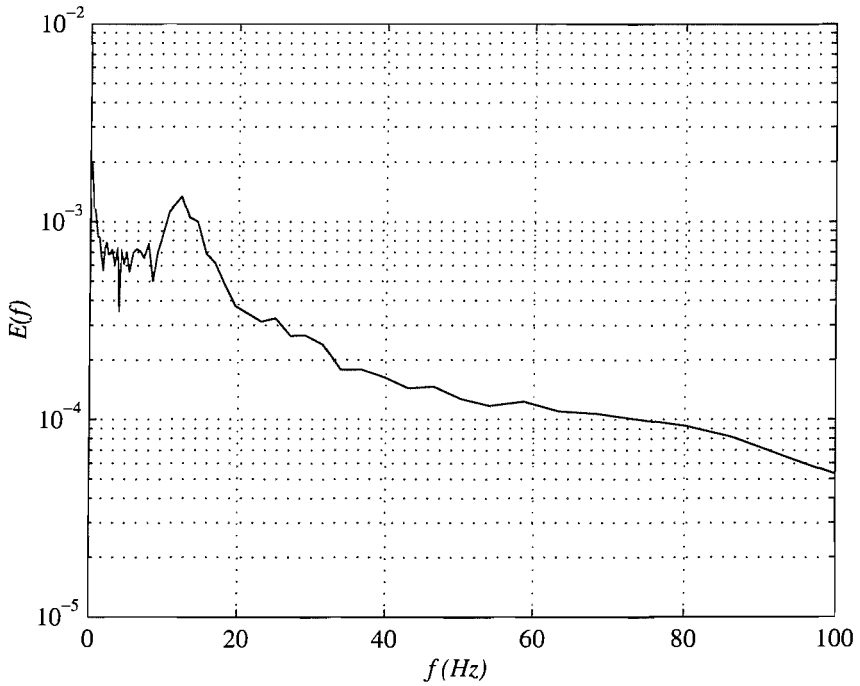

(b) $\theta = 180$ degrees

Figure 3.27: Power spectral density function of pressure measurements at $z/h = 0.5$

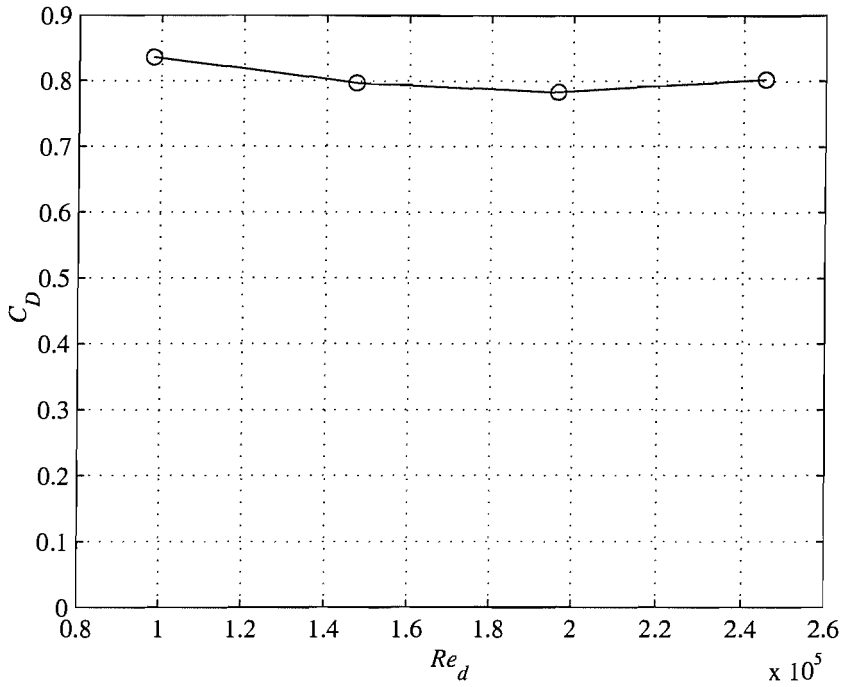

Figure 3.28: Mean drag coefficients

The mean drag coefficients were found at a range of speeds and are plotted in Figure 3.28. At $U_\infty = 20m/s$, $C_D = 0.78$ which agrees well with the C_D found from the pressure distribution above. This suggests that the pressure drag contributes the majority of the drag force with friction being insignificant. This is confirmed by the fact that the frictional drag coefficient $C_{Df} \propto kRe^{-1/2}$ [67], where k is a constant $O(1)$ and $Re^{-1/2} = 2 \times 10^{-3}$, which gives $C_{Df} \sim 10^{-3}$. The variation with Reynolds number is small, although at 6% should be outside the error bounds on these measurements. Normally on an infinite cylinder C_D would increase up to the transition point at $Re \approx 2 \times 10^5$ at which point there would be a large fall in drag. In this case the drag is decreasing up to $Re = 2 \times 10^5$ but then the final point is slightly higher. This is probably due to experimental error rather than a physical effect.

Plots of the power spectral density function of the signals are shown in Figure 3.29. The strong peaks at around $11Hz$ and $16Hz$ in the drag, and at $13Hz$ and $21Hz$ in the lift appear to be constant with tunnel speed and indeed occur when the dynamometer is physically tapped, consistent with their being natural frequencies of the system which are being excited by the vortex shedding. It seems strange however, that they should be different for lift and drag. The differences are likely to be due to changes in the stiffness of the mounting as the dynamometer was rotated. The more interesting characteristics are the next broadband peaks at $24Hz$, $36Hz$ and $48Hz$ at $10m/s$, $15m/s$ and $20m/s$ respectively. These occur at a constant Strouhal number of 0.36.

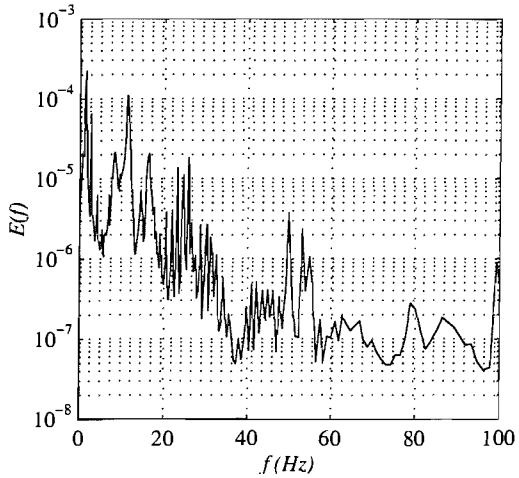

(a) Drag, $U_\infty = 10m/s$

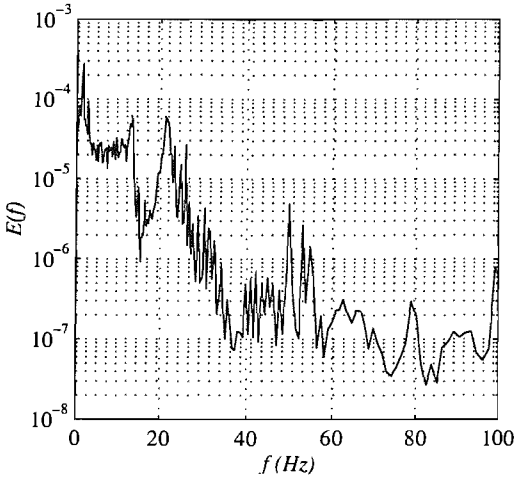

(b) Lift, $U_\infty = 10m/s$

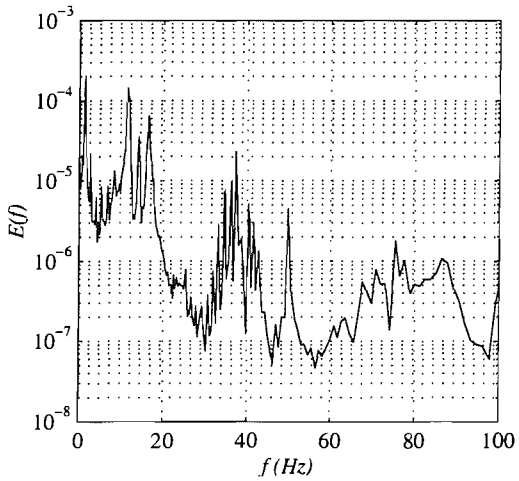

(c) Drag, $U_\infty = 15m/s$

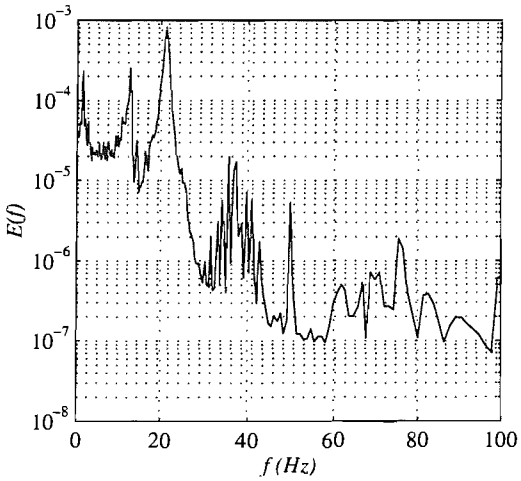

(d) Lift, $U_\infty = 15m/s$

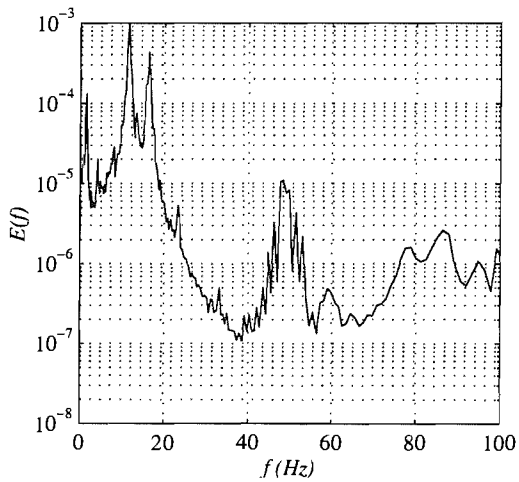

(e) Drag, $U_\infty = 20m/s$

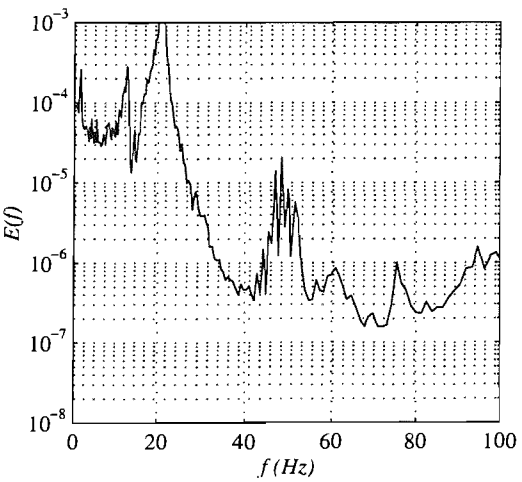

(f) Lift, $U_\infty = 20m/s$

Figure 3.29: Power spectral density function of force signals

3.6 Conclusions

This series of experiments has provided a large amount of data on the flow over a low aspect ratio cylinder. Surface flow visualisation has been carried out on all surfaces, showing clearly the footprints of the vortex structures found in the mean flow. Measurements have been made of the velocity field in a number of planes using PIV, which gives the mean and instantaneous flow as well as the turbulence statistics. Hot-wire anemometry has been used to measure the spectra of the velocity in the wake region. Force and pressure measurements have also been made. The principal features found are summarised below.

1. A turbulent boundary layer develops upstream of the cylinder model on the ground plane. At the normal test speed of $20m/s$, the boundary layer thickness is $0.1h$ at the cylinder location and it is fully developed.

2. A horseshoe vortex is formed at the junction of the cylinder with the ground plane. The secondary separation point, S_2, seen in both the PIV and flow visualisation is at $x/d = -0.78$, while the centre of the vortex is at $x/d = -0.68$, $z/d = 0.04$. The primary separation point, S_1, in the flow visualisation is at $x/d = -1$.

3. The flow undergoes laminar separation from the cylinder at 70 degrees from the leading edge as can be seen from both the flow visualisation and the pressure measurements. If the flow is tripped using a wire on the cylinder surface the separation point moves back to 80 degrees.

4. The flow over the free-end separates from the leading edge, and then attaches on the top of the cylinder at $x/d = 0.17$. Two swirls are visible on the surface of the free-end which appear to be the bases of vortices, although there is some debate about where these vortices go. The present findings appear not to support the hypothesis of Roh and Park.

5. The transverse PIV planes show longitudinal vortices originating from the sides of the free-end and at the base after separation. Moving downstream these vortices appear to merge and are enveloped by two large counter-rotating vortices which trail far downstream.

6. The hot-wire measurements show that there is weak peak in the frequency spectra at a Strouhal number of 0.12 at $U_0 = 20m/s$. At lower speeds a higher frequency component becomes more dominant. The pressure and force signals also show peaks but at slightly different values. This implies that there are a number of features of different frequency which affect different parts of the flow.

This set of data will form a good basis for validating the numerical code as it is comprehensive with constant conditions for all measurements, which will be easily reproduced computationally. The PIV measurements in particular will enable a comparison of full planes of data rather than single values. The next four chapters will present the development of the numerical simulations of this flow. Chapter 8 will then draw the experimental and numerical results together to develop a greater understanding of the flow physics.

Chapter 4

Numerical methods

4.1 Introduction

The measurements presented in the previous chapter show that the flow over a truncated cylinder consists of many components which interact with each other. They have also shown that the instantaneous flow contains many small scale features which do not appear in the mean flow. In order to gain a full picture of this flow field numerically it is necessary to simulate all the scales of motion which are seen in the instantaneous flow field. This requires the use of a time-dependent flow simulation technique such as LES which can resolve all the structures down to the grid scale.

The numerical simulations described in this thesis were carried out using Elmore, a code developed by Neil Bressloff [68] at the University of Southampton. It is a general purpose finite-volume Navier-Stokes solver capable of solving incompressible or compressible flows, steady or unsteady, and with a variety of schemes and turbulence models. It can run in parallel, using the MPI libraries, either on a multi-processor shared memory machine, or on a cluster of heterogeneous computers. This code was initially chosen in preference to the commercial codes CFX and Fluent due its unrestricted parallel capability, which was not available in the commercial packages at that time. The use of an in-house code also offered the opportunity to make modifications to the code which enabled the testing and use of a recently implemented LES model and the incorporation, by the author, of a DES capability into the code. The latest versions of the commercial codes would be suitable for these computations.

The focus of this work is on the simulation of turbulent flows, in particular using large-eddy simulation (LES) and detached-eddy simulation (DES). It is in this area that developments have been made to the code. While the code has previously been used for RANS turbulence modelling and contains a number of these models, it had not been used for LES or DES. An LES module had been implemented by another researcher shortly before this work began, but

it had not been fully tested. The version of DES used in this work is based on the Spalart-Allmaras RANS model which was already in the code, and so it was necessary for the author to make the necessary modifications to this model to enable operation in DES mode. More details of the changes made to the code can be found in Appendix C.

The following sections give an overview of the equations governing fluid motion and then the turbulence modelling and simulation techniques employed in this work are described. The RANS method, including details of the k-ε and Spalart-Allmaras models, will be described, followed by details of LES and finally a description of the DES method. A discussion of the method used in the code to solve these equations will be given followed by some comments on the use of parallel computing in this work. After this discussion of the techniques used, some basic validation studies will be presented. These include a channel flow, a flat plate boundary layer and the flow around an infinite length cylinder.

4.2 Governing equations and turbulence modelling

4.2.1 Navier-Stokes equations

The behaviour of a fluid is defined by the Navier-Stokes equations, which for an incompressible, Newtonian fluid can be written as [69]

$$\nabla \cdot \mathbf{U} = 0 \tag{4.1}$$

$$\frac{\partial (\rho U_i)}{\partial t} + \nabla \cdot (\rho U_i \mathbf{U}) = -\frac{\partial P}{\partial x_i} + \nabla \cdot (\mu \nabla U_i) + S_M \tag{4.2}$$

The first equation represents conservation of mass, while the second represents conservation of momentum. This is divided into a rate of change term describing the change with time, a convective term, a diffusion term and a source term, S_M.

4.2.2 RANS modelling

For a statistically steady flow the velocity components and other scalar quantities can be written as the sum of the mean plus a fluctuating component,

$$\mathbf{U}(t) = \bar{\mathbf{U}} + \mathbf{u}'(t) \tag{4.3}$$

Substituting into the continuity and momentum equations eventually leads to the Reynolds-averaged Navier-Stokes equations (RANS),

$$\nabla \cdot \bar{\mathbf{U}} = 0 \tag{4.4}$$

$$\frac{\partial (\rho \bar{U}_i)}{\partial t} + \nabla \cdot \left(\rho \bar{U}_i \bar{\mathbf{U}}\right) + \nabla \cdot \left(\rho \overline{u_i' \mathbf{u}'}\right) = -\frac{\partial P}{\partial x_i} + \nabla \cdot (\mu \nabla \bar{U}_i) + S_M \tag{4.5}$$

The viscous stresses are defined as,

$$\bar{\tau}_{ij} = \mu \left(\frac{\partial \bar{U}_i}{\partial x_j} + \frac{\partial \bar{U}_i}{\partial x_j} \right) \tag{4.6}$$

The process of time-averaging the equations has introduced six new unknowns, called the Reynolds stresses, $\rho\overline{u_i' u_j'}$. In order to solve the equations it is necessary to provide suitable approximations to these values. Most common methods apply the eddy-viscosity hypothesis which relates the Reynolds stresses to the mean rates of deformation.

$$-\rho\overline{u_i' u_j'} = \mu_t \left(\frac{\partial \bar{U}_i}{\partial x_j} + \frac{\partial \bar{U}_j}{\partial x_i} \right) - \frac{2}{3}\rho\delta_{ij}k \tag{4.7}$$

It can be seen that this is analogous to the viscous stresses in Equation 4.6, but with a turbulent viscosity, μ_t. k is the turbulent kinetic energy, $k = \frac{1}{2}\overline{u_i' u_i'}$.

There are many turbulence models in use, which use more or less complex equations to determine the turbulent viscosity. They range from the simple algebraic mixing length models, through the widely used two-equation models such as the $k-\varepsilon$ model, to the Reynolds stress models which solve transport equations for all six Reynolds stresses. With the exception of the Reynolds stress models all of these models assume that the turbulence is isotropic, which is not the case in many flows.

4.2.3 Spalart-Allmaras model

The Spalart-Allmaras model [38] is a one-equation turbulence model developed specifically for external aerodynamic type flows. It is based upon a transport equation for the turbulent kinematic viscosity, ν_t. It contains a destruction term based on the distance to the nearest walls, and an optional trip term to allow laminar to turbulent transition at a specified location. The equations of the model are as follows.

A transport equation is solved for $\tilde{\nu}$, given by

$$\tilde{\nu} = \frac{\nu_t}{f_{v1}}, \quad f_{v1} = \frac{\chi^3}{\chi^3 + c_{v1}^3}, \quad \chi = \frac{\tilde{\nu}}{\nu} \tag{4.8}$$

$$\begin{aligned} \frac{D\tilde{\nu}}{Dt} &= c_{b1}\left[1 - f_{t2}\right]\tilde{S}\tilde{\nu} + \frac{1}{\sigma}\left[\nabla\cdot\left(\left(\nu + \tilde{\nu}\right)\nabla\tilde{\nu}\right) + c_{b2}\left(\nabla\tilde{\nu}\right)^2\right] \\ &\quad - \left[c_{w1} f_w - \frac{c_{b1}}{\kappa^2} f_{t2}\right]\left[\frac{\tilde{\nu}}{l_{SA}}\right]^2 + f_{t1}\Delta U^2 \end{aligned} \tag{4.9}$$

where,

$$\tilde{S} \equiv S + \frac{\tilde{\nu}}{\kappa^2 l_{SA}^2} f_{v2} \tag{4.10}$$

$$f_{v2} = 1 - \frac{\chi}{1+\chi f_{v1}} \tag{4.11}$$

with S being the magnitude of vorticity and d the distance to the nearest wall.

$$f_w = g\left[\frac{1+c_{w3}^6}{g^6+c_{w3}^6}\right]^{1/6} \tag{4.12}$$

$$g = r + c_{w2}\left(r^6 - r\right), r \equiv \frac{\tilde{\nu}}{\tilde{S}\kappa^2 l_{SA}^2} \tag{4.13}$$

The optional trip terms are,

$$f_{t2} = c_{t3}\exp\left(-c_{t4}\chi^2\right) \tag{4.14}$$

$$f_{t1} = c_{t1}g_t\exp\left(-c_{t2}\frac{\omega_t^2}{\Delta U^2}\left[l_{SA}^2 + g_t^2 l_{SAt}^2\right]\right) \tag{4.15}$$

4.2.4 k-ε model

The k-ε model is one of the most commonly used two-equation models [70]. The same eddy-viscosity hypothesis is applied as above, but here instead of solving an equation for the turbulent viscosity directly, the following relation is employed:

$$\mu_t = \rho C_\mu \sqrt{k} L \tag{4.16}$$

The length scale of the turbulence, L, can be based on the dissipation rate, ε:

$$\varepsilon \approx \frac{k^{3/2}}{L} \tag{4.17}$$

which leads to:

$$\mu_t = \rho C_\mu \frac{k^2}{\varepsilon} \tag{4.18}$$

The turbulent kinetic energy, k, and the dissipation rate, ε, can be found by solving two partial differential equations as given below.

$$\frac{\partial(\rho k)}{\partial t} + \frac{\partial\left(\rho\bar{U}_j k\right)}{\partial x_j} = \frac{\partial}{\partial x_j}\left(\mu\frac{\partial k}{\partial x_j}\right) - \frac{\partial}{\partial x_j}\left(\frac{\rho}{2}\overline{u_j' u_i' u_i'} + \overline{p' u_j'}\right) - \rho\overline{u_i' u_j'}\frac{\partial \bar{U}_i}{\partial x_j} - \mu\overline{\frac{\partial u_i'}{\partial x_k}\frac{\partial u_i'}{\partial x_k}} \tag{4.19}$$

$$\frac{\partial(\rho\varepsilon)}{\partial t} + \frac{\partial\left(\rho\bar{U}_j\varepsilon\right)}{\partial x_j} = C_{\varepsilon 1}P_k\frac{\varepsilon}{k} - \rho C_{\varepsilon 2}\frac{\varepsilon^2}{k} + \frac{\partial}{\partial x_j}\left(\frac{\mu_t}{\sigma_\varepsilon}\frac{\partial\varepsilon}{\partial x_j}\right) \tag{4.20}$$

In the k-equation (Equation 4.19), two terms on the right-hand side cannot be computed and must be modelled. The second term on the right, which represents the turbulent diffusion of kinetic energy, is modelled by a gradient diffusion assumption:

$$-\left(\frac{\rho}{2}\overline{u'_j u'_i u'_i} + \overline{p' u'_j}\right) \approx \frac{\mu_t}{\sigma_k}\frac{\partial k}{\partial x_j} \tag{4.21}$$

where σ_k is a turbulent Prandtl number approximately equal to unity.

The third term on the right-hand side of Equation 4.19, which represents the rate of production of turbulent kinetic energy by the mean flow, can be approximated using the eddy-viscosity hypothesis:

$$P_k = -\rho\overline{u'_i u'_j}\frac{\partial \bar{U}_i}{\partial x_j} \approx \mu_t\left(\frac{\partial \bar{U}_i}{\partial x_j} + \frac{\partial \bar{U}_j}{\partial x_i}\right)\frac{\partial \bar{U}_i}{\partial x_j} \tag{4.22}$$

4.2.5 Large-eddy simulation

As its name implies a large-eddy simulation consists of a time-dependent computation in which the large scale eddies in a turbulent flow are fully resolved, while the smaller scale eddies are modelled. This can be justified as the large-scale motions are generally dependent on the geometry while the smaller scale structures are more universal in their nature and can be approximated quite well. Also the majority of the energy is contained within the larger scales and so the accuracy of the prediction of the smaller scales is less important.

In order to define the equations that are to be solved the flow field must be filtered to remove the smaller scales which are to be modelled. This operation is typically defined as follows:

$$\bar{U}_i(x) = \int G(x,x')u_i(x')dx' \tag{4.23}$$

where $G(x,x')$ describes the filter function. In the present studies a box filter is used of width, Δ, equal to the cell size. Any eddies smaller than the filter width are regarded as small eddies and are modelled.

The filtered Navier-Stokes equations are written as:

$$\frac{\partial(\rho\bar{U}_i)}{\partial x_i} = 0 \tag{4.24}$$

$$\frac{\partial(\rho\bar{U}_i)}{\partial t} + \frac{\partial\left(\rho\overline{\bar{U}_i\bar{U}_j}\right)}{\partial x_j} = -\frac{\partial \bar{P}}{\partial x_i} + \frac{\partial}{\partial x_j}\left[\mu\left(\frac{\partial \bar{U}_i}{\partial x_j} + \frac{\partial \bar{U}_j}{\partial x_i}\right)\right] \tag{4.25}$$

Since $\overline{U_i U_j} \neq \bar{U}_i\bar{U}_j$ and this quantity cannot be computed it is necessary to model the difference between the two sides of this inequality with the approximation:

$$\tau^s_{ij} = -\rho\left(\overline{U_i U_j} - \bar{U}_i\bar{U}_j\right) \tag{4.26}$$

The quantity τ_{ij}^s is called the subgrid scale Reynolds stress. In most LES methods this stress is approximated by an eddy-viscosity model:

$$\tau_{ij}^s - \frac{1}{3}\tau_{kk}^s \delta_{ij} = \mu_t \left(\frac{\partial \bar{U}_i}{\partial x_j} + \frac{\partial \bar{U}_j}{\partial x_i} \right) \tag{4.27}$$

There have been many models proposed for the calculation of μ_t in this equation. The one used in the simulations presented here is the structure-function model as proposed by Métais and Lesieur (1992). Here the eddy viscosity is given by,

$$\mu_t = 0.105 \rho C_K^{-3/2} \Delta x F_2^{1/2} \tag{4.28}$$

where,

$$F_2 = \langle \| \overline{U}(\mathbf{x},t) - \overline{U}(\mathbf{x}+\mathbf{r},t) \|^2 \rangle_{\|\mathbf{r}\|=\Delta x}$$

C_K is the Kolmogorov constant and Δx is the cell size.

This model has been shown to be less dissipative in isotropic flows than the commonly used Smagorinsky model. In this situation the inertial range is better predicted. In shear flows however it may be more dissipative than other models, which may make this model less suitable for the flows considered here [72].

4.2.6 Detached-eddy simulation

Detached-eddy simulation (DES) is a method proposed by Spalart et al. [73, 34], in order to overcome the considerable computational cost involved with full LES simulations. The basis of this method is that RANS models are quite capable of modelling boundary layer flows, but generally fail to predict the larger scale eddies in regions of separated flow. In these regions LES should be far better at capturing the flow physics. DES is therefore a hybrid of RANS and LES, where the model operates in RANS mode close to the walls and in LES mode away from the walls. The original DES method of Spalart is based on the Spalart-Allmaras (S-A) one equation turbulence model [38]. The standard S-A model uses the distance to the nearest wall as the length scale, l_{SA}. In DES the length scale is modified so that it depends on the grid spacing, Δ as follows:

$$\tilde{l}_{SA} \equiv \min(l_{SA}, C_{DES}\Delta) \tag{4.29}$$

where Δ is the largest dimension of the cell, not the cube root of their sum,

$$\Delta \equiv \max(\Delta x, \Delta y, \Delta z) \tag{4.30}$$

C_{DES} is a constant which defines the transition point between the DES and RANS modes. In isotropic turbulence it has been calibrated to $C_{DES} = 0.65$. This has also been found to be suitable for most other flows [40].

There is also an alternative form of detached-eddy simulation based on the $k-\omega$ SST model of Menter, proposed by Strelets [74]. In this version the length scale, $l_{k\omega}$, is replaced by

$$\tilde{l}_{k\omega} = \min(l_{k\omega}, C_{DES}\Delta) \tag{4.31}$$

The DES model was tested on turbulent channel flows by Nikitin and his co-workers [75]. They simulated flows with Reynolds numbers, based on friction velocity, Re_τ from 180 to 80000, on a variety of grids and with three different codes. The grids that they used were generally fine enough for a full LES simulation, and the "RANS" region was only around 0.1δ.

Calculations of the flow past circular cylinders using DES have been performed by Travin et al.[37]. The principle purpose of these tests was to validate the model for flows with smooth-surface separation, which impose an additional challenge to turbulence models. Simulations were carried out with both laminar and turbulent separation, at Reynolds numbers from 5×10^4 to 3×10^6. Most of the simulations were performed using three-dimensional grids with a z-dimension of $2d$. The purely two-dimensional simulations gave markedly worse results. The comparisons with experimental data are not particularly favourable, partly due to differences in the Reynolds numbers and other conditions, and also due to the discrepancies between different sets of experiments. However, the separation points and Strouhal numbers are well predicted in most of the simulations. The trip-less approach, presented in Shur et al. [76] and applied by Spalart and Strelets [39], was used for the laminar separation cases. The changes in the flow and drag between laminar and turbulent separation were reproduced well.

The importance of a sufficiently long averaging time for force coefficients is highlighted, due to the presence of long time-scale modulations in the amplitude of the forces. They suggest 50 shedding cycles as being sufficient.

Another application of detached-eddy simulation is for airfoils at high angles of attack, with massive separation as described by Shur et al. [40]. This paper presents some initial results of DES simulations of the flow behind a stalled airfoil at angles of attack up to 90 degrees. The lift and drag are predicted to within 10% of the experimental results.

Morton et al. [41] presented results of DES and RANS simulations of the vortical flow over a delta wing. This flow is characterised by the primary vortex generated behind the leading edge of a delta wing at an angle of attack. This vortex is influenced by viscous effects in the boundary layer of the airfoil, and suffers vortex breakdown at some distance downstream. The prediction of this breakdown is dependent on the ability of the turbulence model to calculate properly the turbulent kinetic energy in the vortex. RANS and DES simulations were performed using both the Spalart-Allmaras and $k-\omega$ SST models. The DES models were found to compare very well with the experimental data in their prediction of the vortex breakdown and the frequency components of the flow. The RANS models produce too much eddy viscosity in the vortex core

and so do not predict breakdown well. The rotation correction to the Spalart-Allmaras model was tested with good results in the breakdown region due to the reduction in eddy viscosity. A DES model with the rotation correction was not tried, but it was also thought likely to produce good results.

Constantinescu et al. [42] simulated the flow around a sphere using DES and LES at a subcritical Reynolds number of 10^4. They found good agreement with experimental data. A fifth-order upwind scheme was used for the discretisation of the convective terms which was found not to be too dissipative, whereas a second order scheme did have more effect on the results.

Constantinescu et al. [43] also carried out an investigation of the flow around a prolate spheroid using DES as well as RANS. The flow considered was that over a 6:1 prolate spheroid at a Reynolds number of 4.2×10^6, at angles of attack between 10 and 20 degrees. The advantages of a DES approach for this flow are not as pronounced as for the previous examples because the flow is not massively separated. The flow is characterised by longitudinal vortices which are quite stable and so the amount of unsteady, chaotic motion is less. The DES and RANS results were indeed found to give similar results. The rotation and streamline curvature correction of Spalart and Shur [77] was shown to improve the pressure prediction on the surface of the cylinder.

The modifications made to the code in order to implement the DES functionality into the flow solver are described in more detail in Appendix C.

4.3 Details of the flow solver

The flow solver [68] uses the finite volume method for discretising the equations. It is based on structured multi-block grids using a collocated variable arrangement. The convective fluxes are discretised in space using the second order, Curved Line Advection Method (CLAM) of Van Leer [78] which is a member of the high resolution TVD scheme family. The diffusive fluxes are discretised using second order central differences. The SIMPLEC pressure-correction scheme is used, and the matrices are solved using the Strongly-Implicit Procedure (SIP). All the simulations described here were performed as time-dependent problems, even for the steady-state RANS flows. A second-order, implicit three time level method was used for the discretisation in time.

The code was initially run on a cluster of workstations in the Ship Science design offices (see Appendix D). However, the installation by the University of a new large-scale compute cluster in 2002 provided a significant increase in the available resources and enabled the larger simulations presented here to be run. This facility comprises 292 dual 1GHz Pentium III nodes and 112 single 1.8Ghz Pentium 4 nodes. The nodes have 512Mb of memory and are connected

by 100Mbps Fast Ethernet connections. The largest simulations described here were run on a minimum of 6 dual-processor nodes. The truncated cylinder simulations required approximately 1 minute per time-step (precise values can be found in Chapters 5 to 7), which means one week for 10000 time steps. The LES and DES simulations were run for up to 50000 time steps to obtain converged statistics.

4.4 Basic validation studies

Before the code could be applied to the truncated cylinder geometry it was necessary to validate the models using simple test cases, because although many aspects of the code had been extensively used before [68, 79], the Spalart-Allmaras model (S-A) had not been tested sufficiently and the large- and detached-eddy simulation functions were new. Three basic geometries were chosen for the validation studies: the channel flow as investigated by Kim et al.[80], the boundary layer on the ground plate in the wind tunnel tunnel experiments performed here, and the classic infinitely long cylinder flow. The latter two flows can be seen as two of the basic components of the flow around the truncated cylinder in the wind-tunnel and so were felt to be suitable tests of the code. They also proved useful for the development of the code, enabling errors to be found more easily than on a more complex geometry.

4.4.1 Channel flow

The turbulent channel flow case was used to verify that the turbulence models were resolving the boundary layer correctly and to determine their sensitivity to grid resolution. The data used for comparison was that presented by Kim et al.[80] from their DNS simulations. In their simulations the Reynolds number based on the mean centreline velocity and the channel half-width, which is equal to the boundary layer thickness, δ, was 3300 ($Re_\tau = 180$). The grid size was $192 \times 129 \times 160$ in x, y and z, giving around 4×10^6 cells. The dimensions of the domain were $4\pi\delta \times 2\delta \times 2\pi\delta$ with periodic boundaries in the streamwise and spanwise directions. This size was shown to be sufficient based on two-point correlations.

This test-case was applied to the k-ε and S-A RANS models only. Large-eddy simulations of turbulent channel flows generally require a grid fine enough to resolve the buffer layer and the associated streaks. With such a fine grid the solution becomes very close to a direct numerical simulation as the subgrid-scale stresses are very small. The cost of these computations can be shown to scale as Re^3 and so they become unfeasible at high Re [72]. The purpose of detached-eddy simulation is to avoid the problem of resolving the boundary layer eddies by operating as a RANS model in boundary layer regions, while the LES mode reserved for regions of separated flow where larger scale structures will be found. From this point of view it did not

seem worthwhile to perform LES or DES simulations of the channel flow. In the case of DES, it will be working in RANS mode near the wall anyway and so the S-A validation will apply.

A two-dimensional grid was used with a length in the x-direction of 100δ to allow the boundary layer to fully develop. The number of cells in the streamwise direction was 128. In the y-direction the number of cells was varied from 8 to 128 using a non-uniform spacing according to the function [81],

$$\frac{y}{L} = \eta p + (1-p)\left(1 - \left(\frac{\tanh((1-\eta)q)}{\tanh(q)}\right)\right) \tag{4.32}$$

where,

$$\eta = \frac{n}{N}$$

Here n is the current node number and N is the total number of nodes on the edge. L is the edge length. In this case $p = 0.064668$ and $q = 1.479993$ giving a first cell size of $y/\delta = 0.0056$ on the finest mesh. This corresponds to $y^+ \approx 1$. For the purposes of this study the distribution was kept constant so that the wall spacing increased with decreasing grid resolution. The solver was run in time-stepping mode and run for 1.5 times the flow-through time. The PISO pressure-correction scheme [82] was used with the CLAM differencing scheme [78].

Figures 4.1 to 4.3 show the profiles of velocity and turbulent viscosity, ν_t, at $x/\delta = 100$. The flow at this point is fully developed and it can be seen that the agreement with the DNS data of Kim et al. is very good except for the two very coarse grids. The wall cell spacing in the 128×16 and 128×16 grids was outside the laminar sub-layer and so accuracy would be impaired despite the use of a wall-function.

4.4.2 Modelling the boundary layer on the ground plane

One of the key features of the truncated cylinder flow is the horseshoe vortex on the ground plane. The prediction of this is dependent on the oncoming boundary layer on the ground. It is therefore useful to assess the grid dependence of the boundary layer prediction for the various models employed in this study. To do this a simple grid was constructed with the same length and height as the target model, that is $10.67d$ long by $4d$ high. For the RANS cases a two-dimensional grid was used, while for the LES and DES models a three-dimensional grid was employed with a z-dimension of $0.05d$. Normally when performing an LES simulation of a boundary layer one would use a fine enough grid in all dimensions to resolve the small-scale structures within the boundary layer. In the case of the cylinder on a ground plane however this would necessitate an excessively large number of cells. The grid used is therefore not fine enough to resolve the boundary layer structures properly. It is therefore of interest to know how the boundary profile will be affected by this. For the DES case the problem is not so severe

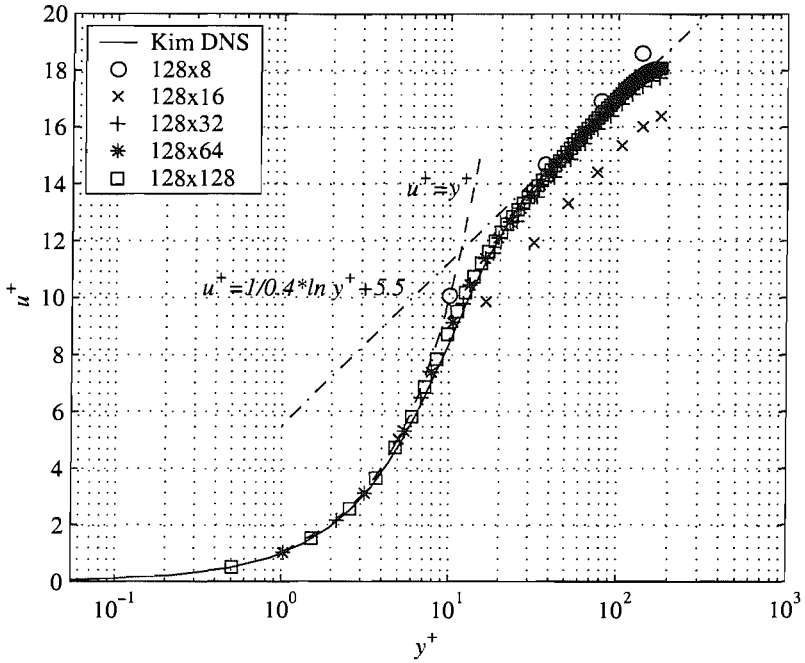

Figure 4.1: Velocity profile for channel flow for different grid resolutions

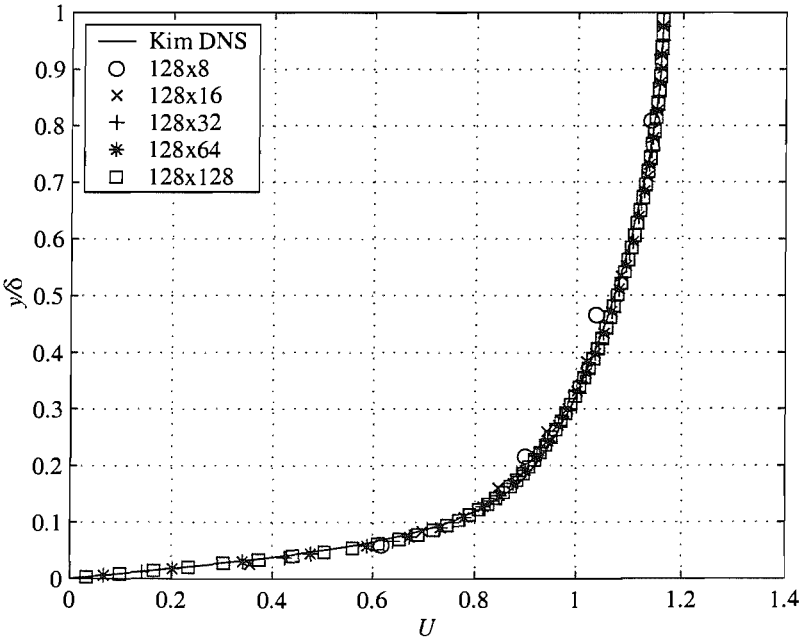

Figure 4.2: Velocity profile for channel flow for different grid resolutions

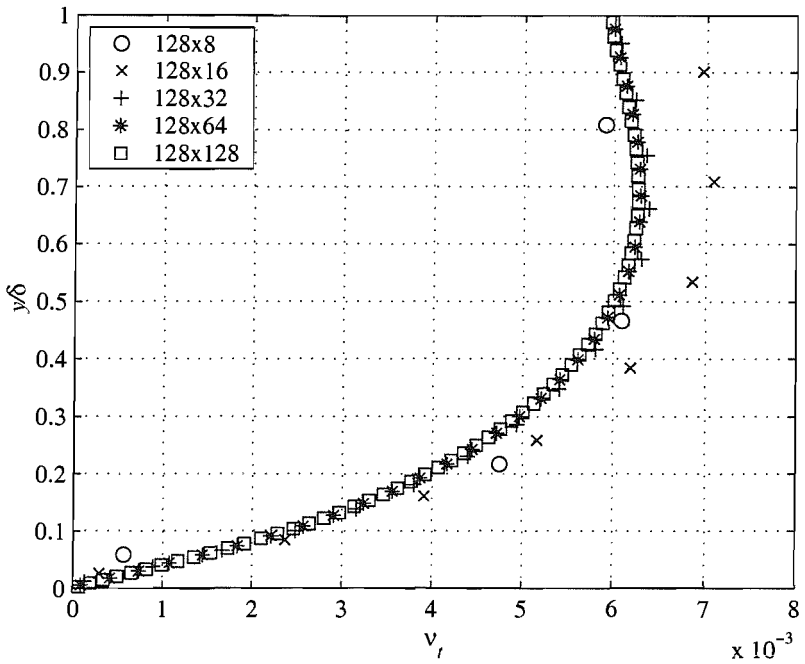

Figure 4.3: ν_t profile for channel flow for different grid resolutions

Table 4.1: Details of flat plate boundary layer grids

Grid No	N_x	N_y	N_z	S_x		S_y	S_z	Δx^+		Δy^+	Δz^+
				min	max			min	max		
1	66	37	5	0.0100	0.60	0.005	0.0100	54	3240	27	54
2	132	75	10	0.0050	0.30	0.002	0.0050	33	1980	13	33
3	264	150	20	0.0025	0.15	0.001	0.0025	18	1080	7	18

as the model will function as a RANS model where the grid is stretched. There will still be a region where the grid is refined around the base of the cylinder where the DES mode will be activated. It is of interest to see how the model behaves while switching from RANS to LES mode.

Figure 4.4 shows the boundary layer profiles produced by the Spalart-Allmaras RANS model at $x/d = -0.5$, which is the position at which the experimental measurements were made (see Figure 3.8 and 3.9). The coarsest grid is clearly not fine enough to resolve the boundary layer accurately. The two finer grids are much closer to the correct profile. The modelled boundary layer thickness is $3mm$ less than the experimental value. It is possible that this is due to the flow conditions not being correct at the inlet boundary. It would be desirable to have more experimental data on the flow at the leading edge of the ground plate to check that the uniform inflow is representative of the experiment.

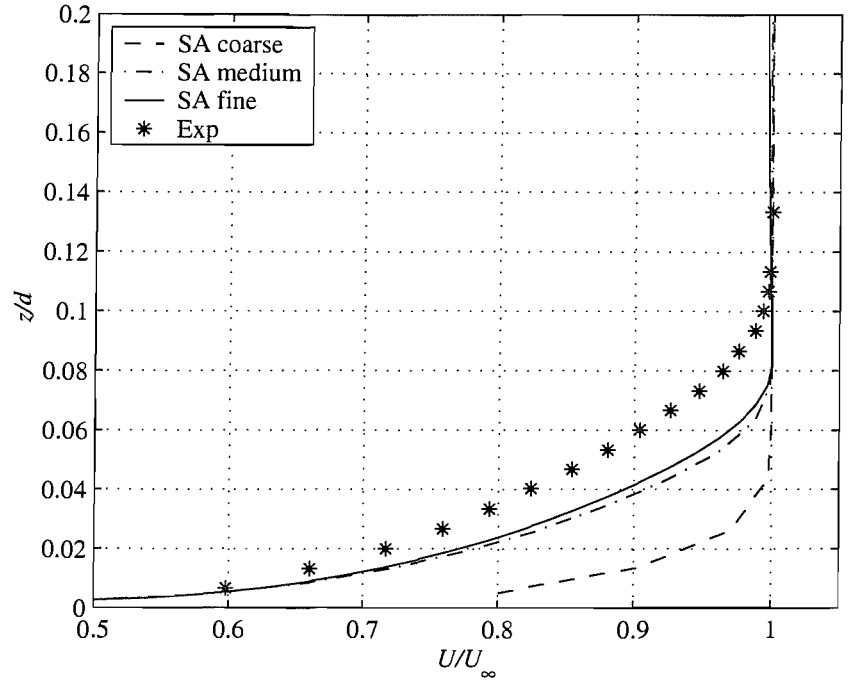

Figure 4.4: Flat plate boundary layer profiles for different grids using the SA model ($x/d = -0.5$)

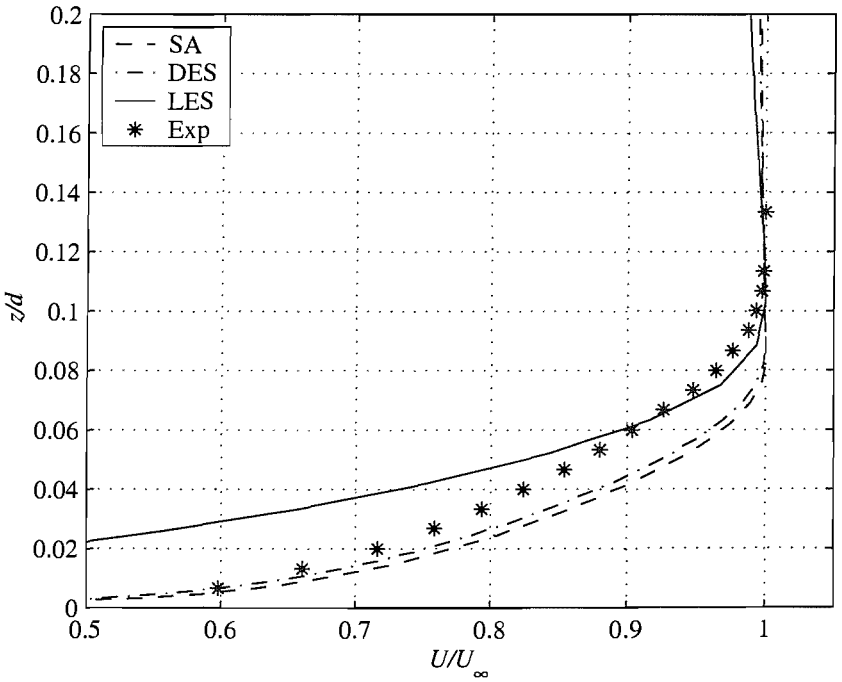

Figure 4.5: Flat plate boundary layer profiles for different models on the finest grid ($x/d = -0.5$)

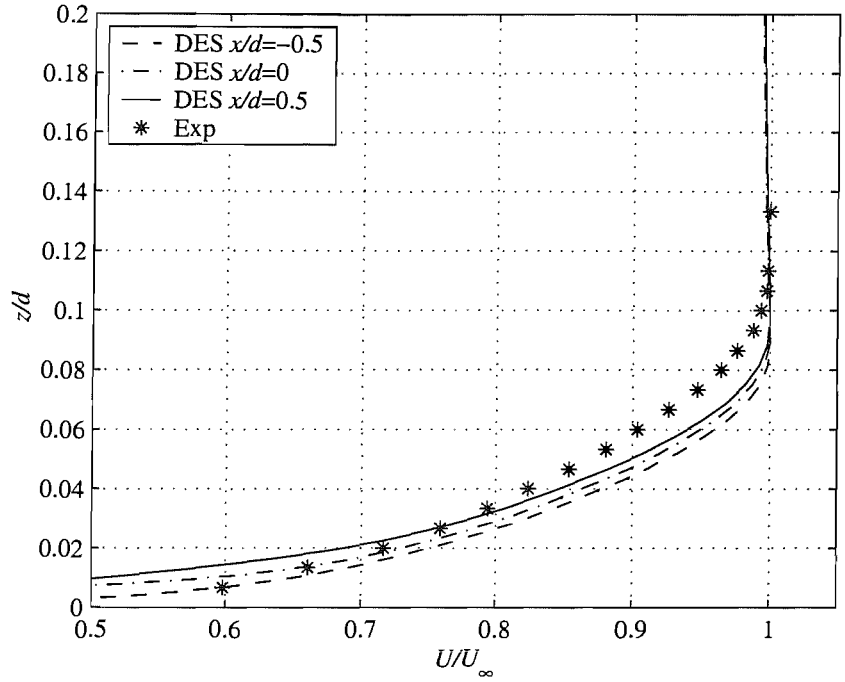

Figure 4.6: Flat plate boundary layer profiles at different x/d for the DES model on the finest grid

The performance of the different models is compared in Figure 4.5. It can be seen that the SA and DES results are very close as would be expected since the DES should be functioning in RANS mode upstream of this point. The LES profile is more like a laminar boundary layer although the thickness is about right. This is because the grid is not fine enough to resolve the turbulent structures and no wall-function is employed.

Figure 4.6 plots the boundary layer profiles of the DES model at different streamwise locations. The first curve at $x/d = -0.5$ is essentially the RANS solution. Beyond this point the grid is refined so that the model operates in LES mode. Here the turbulent viscosity is reduced due to the reduced length scale. If the turbulent fluctuations were simulated correctly in this zone the velocity profile should remain correct. However in this case the profile can be seen to straighten slightly. This suggests that the fluctuations are not being simulated fully. This is likely to be due to the lack of turbulent fluctuations entering this region from the RANS region upstream. This is an acknowledged weakness of DES and applies equally to areas of separation where the separated shear layer does not contain any turbulence from the boundary layer [37].

The LES simulation fails to predict a fully turbulent boundary layer. This is to be expected as no wall model was used and the grid resolution was not fine enough to resolve the momentum carrying scales in the viscous sublayer. This is perhaps exaggerated by the stretching of the grid up and downstream of the cylinder location.

Table 4.2: Details of flat plate boundary layer profiles for different models

Model	x/d	δ/d	δ^*/d	θ/d	Re_θ	η
SA	-0.5	0.087	0.011	0.007	1565	1.40
LES	-0.5	0.103	0.024	0.011	2207	2.15
DES	-0.5	0.088	0.012	0.009	1705	1.42
DES	0.0	0.095	0.015	0.009	1771	1.65
DES	0.5	0.102	0.016	0.010	1970	1.63
Exp	-0.5	0.10	0.013	0.010	2037	1.30

4.4.3 Infinite-height cylinder flow

The case of the infinitely long cylinder is an extensively researched flow, numerically and experimentally due to its geometrical simplicity, its common occurrence in real-world situations, and its periodic vortex shedding phenomena. Good reviews of this work have been published by Williamson [1] and Zdravkovich [2]. The abundance of data on this flow means that it is a good case for validating a code, although sometimes the discrepancies between different experiments may be large, particularly at high Reynolds numbers, making comparisons awkward.

Before attempting to solve the flow around a finite-height cylinder, the geometrically simpler case of a two-dimensional cylinder was used to gain experience of modelling a bluff-body flow with this code. The simulations reported here were two-dimensional RANS calculations using the Spalart-Allmaras model. This case will test the model's ability to predict separation from a curved surface and also the vortex shedding in the wake.

The model was run in time-stepping mode, but no vortex shedding was predicted. This is surprising as even a RANS model should predict the periodic vortex shedding pattern. In the turbulent regime however the vortex shedding is not strong. The mean flow parameters of pressure distribution and separation are still of interest however.

These simulations were run at $Re_d = 140000$ which is close to that used for the truncated cylinder experiments and corresponds to that presented by Travin et al. [37] who tested the DES and the Spalart-Allmaras model at this Re. For the turbulent separation case computed here they found $C_D = 0.56$ and $C_{Pb} = -0.59$. There is limited experimental data on the fully turbulent regime, but the consensus is that separation occurs between 90 and 100 degrees with C_D being between 0.6 and 0.7 [2].

The tests presented here include a study of the dependence of the solution on the grid resolution. Table 4.3 lists the five grids used for this test. Starting from grid 1, the mesh was refined twice, while keeping the same distribution, to give grids 2 and 3. The distribution of

Table 4.3: Details of 2-d cylinder grids

Grid No	N_c	N_r	S_c	S_r	No. cells	y^+ max	y^+ min	Cd	Sep.(deg)
1	280	88	0.0357	0.0011	25,550	9.3	0.06	0.26	101
2	352	111	0.0283	0.0008	40,392	7.6	0.02	0.49	101
3	440	140	0.0071	0.0007	63,690	6.2	0.05	0.59	103
4	440	140	0.0071	0.0021	63,690	9.2	0.15	0.57	103
5	440	140	0.0071	0.0042	63,690	18.2	0.40	1.43	99
Travin [37]	150	109			16,350			0.59	~ 100

points in the radial direction in grid 3 was then altered to give larger y^+ values in grids 4 and 5. The simulations were run for 10000 time steps of 0.005. It can be seen that the drag coefficient due to pressure varies considerably with grid resolution, with the largest y^+ of 18.2, which is outside the laminar sub-layer, giving very poor results. The finer grids seem to be converging towards the value of 0.59 of grid 3, which is close to that found by Travin et al. The base pressure coefficient, C_{Pb} is converging towards 0.57 compared to the 0.59 of Travin et al. This indicates that the code is working correctly as it matches the results of another code using the same model. It should be noted however that their grid had many fewer cells than the present computations but they were able to use non-matching interfaces to obtain a much finer density in the wake region than around the front of the cylinder.

Interestingly the separation point does not vary much with the grid resolution. Even with the largest y^+ value the separation point is within 2 degrees of the other grids. It seems that the pressure more dependent on the grid than the velocity field.

4.5 Conclusions

- All simulations were performed using a solver developed at the University. This is a parallel multi-block structured finite-volume solver. It is capable of running unsteady simulations using RANS turbulence models or LES.
- As part of the present work a detached-eddy simulation capability was incorporated in the code. This is a modification of the Spalart-Allmaras turbulence model. Other modifications to the code were made to facilitate running LES/DES problems, as detailed in Appendix C.
- A set of relatively simple validation cases were performed with particular emphasis on

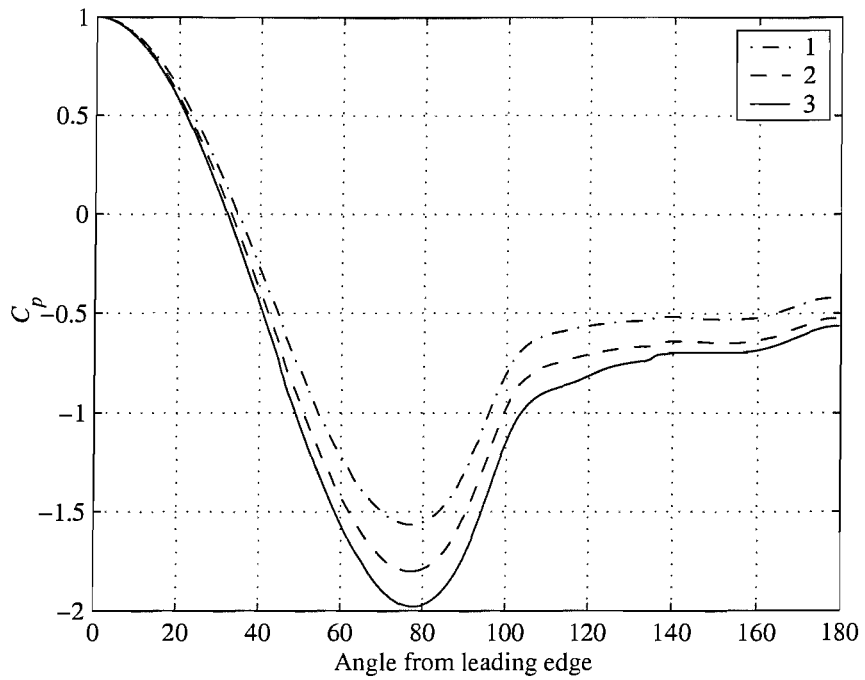

Figure 4.7: Pressure distribution around cylinder for different grid resolutions

the performance of the new DES model. The channel flow case showed that the boundary layer prediction is well handled by the Spalart-Allmaras model, which is the same as DES near the wall. The LES model failed to predict a turbulent boundary layer due to too coarse a grid resolution and the lack of a wall function in the LES model.

- A test of the boundary layer prediction on a grid with a refined mesh in the centre shows that the DES model has some difficulty in maintaining the boundary layer profile in the "grey area" between the RANS and LES modes.

- The two-dimensional cylinder case has shown that the Spalart-Allmaras model predicts the separation and pressure drag well if the near-wall grid spacing is sufficiently small.

Chapter 5

RANS modelling of the truncated cylinder

5.1 Introduction

The experiments on the truncated cylinder reported in Chapter 3 have provided a large amount of data on this particular flow. The flow has been found to consist of a number of different features with a high degree of unsteadiness in the wake region. The exact way in which some of these features interact is difficult to determine from experimental data which consists of a number of two-dimensional planes or surfaces. The three-dimensional flow features cannot be seen in these planes. This is one of the attractions of using computational fluid dynamics as it can solve the entire three-dimensional flow domain, allowing easier visualisation of complex flow structures. The drawback with CFD is that it can be difficult to obtain accurate results, or even to know whether or not they are accurate.

The motivations behind the numerical computations performed as part of this research are to assess the accuracy of various turbulence models by comparison with the experimental data already obtained, and to use these simulations to gain a better understanding of the flow field.

Although it was felt that LES-type methods were likely to be better able to simulate this sort of flow, a RANS model was run to provide a reference point. The RANS model used here was a simple two-equation model which is known to have limitations for this type of flow [45]. It is likely that more sophisticated RANS models such as the $k-\omega$ SST model [83] or a Reynolds stress model [84, 85] would produce better results than those used here.

All the numerical simulations were performed using the code described in Chapter 4. For the RANS modelling the k-ε model was used. This chapter will first describe the setup of the computational model, and will then compare the results with the experimental values. Most of the description of the computational model will also apply to the subsequent work on LES and DES, described in Chapters 6 and 7. The results will be presented starting with a look at certain key parameters such as attachment and separation points. The modelling of various features of

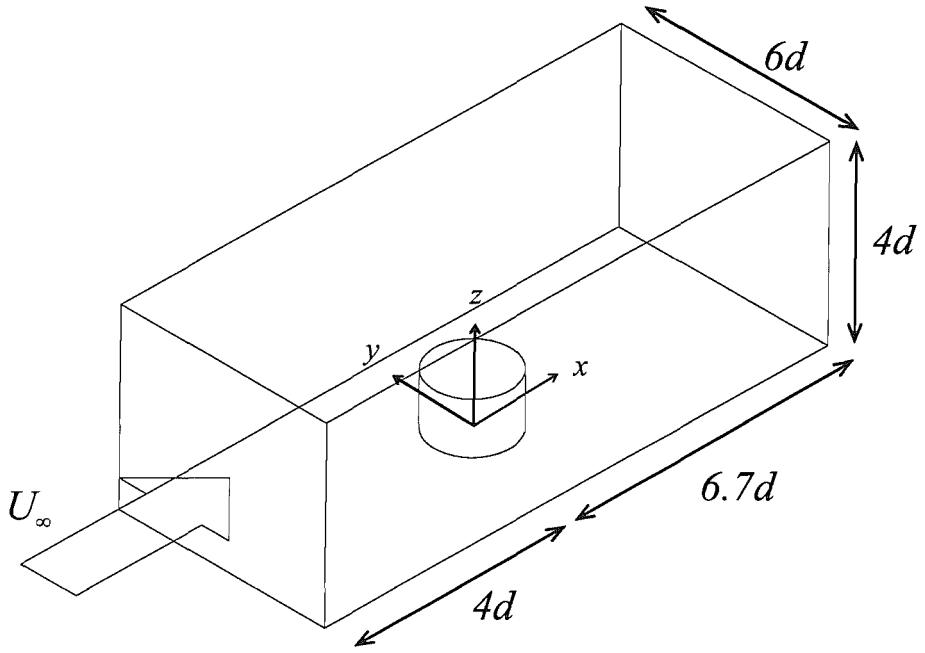

Figure 5.1: Dimensions of the computational domain

the flow will then be examined in more depth in subsequent sections.

5.2 Details of the computational model

The computational domain was designed to replicate the flow conditions in the wind tunnel as far as possible. To this end the dimensions of the domain matched the tunnel dimensions so that the blockage effects were the same. The length of the ground plane upstream of the cylinder was also the same, meaning that the boundary layer development was modelled.

The dimensions of the domain are shown in Fig. 5.1. The domain size was $4.0h$ upstream of the cylinder, $6.7h$ downstream, $6.0h$ laterally and $4.0h$ vertically. No-slip conditions were applied to the walls of the tunnel, although the grid was not fine enough on the side and top walls to resolve the boundary layers on these surfaces. A uniform velocity was applied to the inlet and a zero-gradient condition to the outlet.

The grids were composed of 32 structured blocks in a stacked O-grid format. The cells were clustered towards the walls of the cylinder and the floor of the tunnel as shown in Figure 2. Table 5.1 shows the number of cells in each dimension around the cylinder. The figures shown are the numbers of cells in the azimuthal and radial directions (N_c and N_r) and the number of cells along the span of the cylinder (N_h). The cell sizes normal to the walls of the cylinder and the floor (S_r and S_h) and the azimuthal spacing (S_c) are also given. An expanded version of this table can be found in Appendix E where full details of all the edge distributions

Table 5.1: Details of RANS/LES grids

Grid No.	1	2	3
N_c	228	284	360
N_r	60	76	95
N_h	30	38	48
S_c	0.0138	0.0111	0.0087
S_r	0.0007	0.0007	0.0007
S_h	0.002	0.002	0.002
Total cells	1,051,650	2,090,950	4,190,400

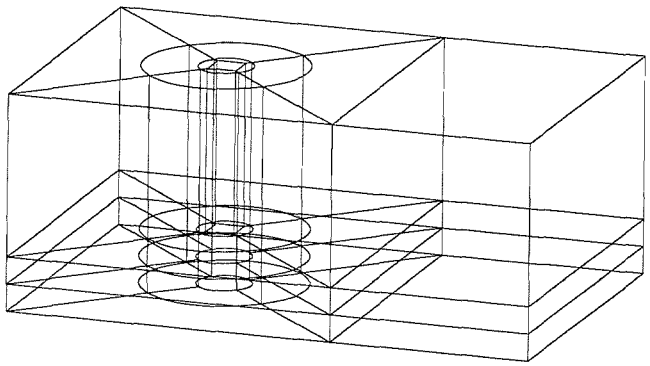

Figure 5.2: Diagram showing arrangement of blocks in the computational grid

are given. On the finest grid the cell size on the floor of the tunnel was $0.002d$ and on the cylinder walls $0.0007d$. The grid topology and mesh are shown in Figures 5.2 and 5.3.

The time-step was set at 0.005 units, normalised with velocity and diameter, which corresponds to a Courant number of less than 1 at the side of the cylinder in the high speed flow region on the crest of the cylinder. The simulations were run until the flow reached a steady state. It was found that 20000 time-steps or 100 non-dimensional time units was sufficient.

An important feature of the flow is the transition of the boundary layers from laminar to turbulent. Although the flow on the ground plane is mostly turbulent and so transition does not need to be considered, the flow on the upstream face of the cylinder is laminar up to the separation point. The RANS model as used here cannot account for transition and so the entire flow is modelled as turbulent. The solution for this would be a model which could take account of transition: either by explicitly setting it's location as in the Spalart-Allmaras model

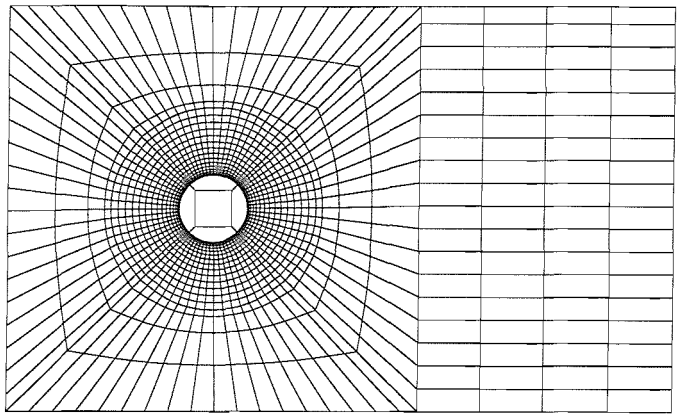

Figure 5.3: Representation of the computational grid (not all cells drawn)

Table 5.2: Key results of k-ε runs

Grid	1	2	3	Exp.
CPU time / time step (secs)	36	70	147	
Side separation, ϕ_s (degrees)	106.6	107.2	105.9	70
Upstream sep. from ground, X_{S2} (x/d)	-0.78	-0.79	-0.79	-0.78
Attachment on free-end, X_{RT} (x/d)	0.35	0.40	0.28	0.17
Attachment on ground downstream, X_{RF} (x/d)	2.1	2.1	2.1	1.6
Local C_D at $z/d = 0.5$	0.47	0.45	0.35	0.79

(4.2.3) or by incorporating a transition model such as the e^N model [86]. Work was started on the incorporation of the trip terms in the Spalart-Allmaras model into the code but there was insufficient time to resolve the problems which were encountered.

5.3 Results

5.3.1 Global flow parameters

An overview of the performance of the model for different grids can be obtained from Table 5.2 which shows the positions of separation on the cylinder side and on the ground plane upstream, as well as the attachment point on the ground downstream and the local drag coefficient at the mid-height.

Looking at the three $k-\varepsilon$ cases, it can be seen that there is little difference between the

three grids in terms of the separation and attachment positions, although all are significantly different to the experimental values. This is particularly evident in the separation from the side of the cylinder which is predicted much too far back. The primary reason for this is that in the experiment the boundary layer remained laminar up to separation, whereas the RANS model is fully turbulent. This represents a problem with the use of fully turbulent RANS methods in situations where there are some regions of laminar flow.

The length of the recirculation region behind the cylinder, X_R, is defined by the location of the stagnation point on the ground on $y/d = 0$. All three k-ε runs give $X_R = 2.1$, which is 34% greater than the experimental value. This is in accordance with the findings of Rodi et al. (1997) [46] for the surface mounted cube case, where the recirculation length was predicted to be 2.182 by the basic k-ε model compared to 1.6 in the experimental data. This was found to be due to the over-prediction of k in front of the leading edge of the top of the cube.

The predicted local drag coefficients are widely scattered. The curves in Figure 5.4, which show the pressure distribution at $z = 0.5$ for the different cases, indicate that the pressure on the forward part of the cylinder is well predicted by all, but the base pressure at the rear is not. Figure 5.5 shows the pressure coefficient around the cylinder at five heights for the $k-\varepsilon$ case, corresponding to those in Figure 3.25. The main difference is that the separation point is much further back than in the experimental case, causing the minimum pressure to be further back and also of greater magnitude. The sharp spike in the C_P curves at $\theta = 135$ degrees is due to a discontinuity in the curvature of the cylinder surface in the mesh. This was because the grid was constructed using spline curves on the four quarters of the cylinder with no means of matching the slope of these curves at the interfaces. After this problem was noticed the grid generator was modified to use arcs on these edges, so that the simulations reported in subsequent chapters do not suffer this problem. As the effect was localised it was not deemed necessary to repeat the calculations.

In view of the small differences between the three levels of grid refinement, the medium density grid was used for the subsequent analysis. The CPU time, storage requirements and post-processing time for the 4 million cell mesh were considered to be too great for further runs.

5.3.2 Horseshoe vortex

As has been seen from the experimental data, a vortex is formed at the junction of the cylinder with the ground plane, due to the pressure increase on the leading edge of the cylinder causing separation from the ground plane. This separation was seen to occur at $x/d = -0.78$, with the centre of the vortex located at $z/d = 0.04$.

Some of the key features of the flow as seen in the experiments were visualised using

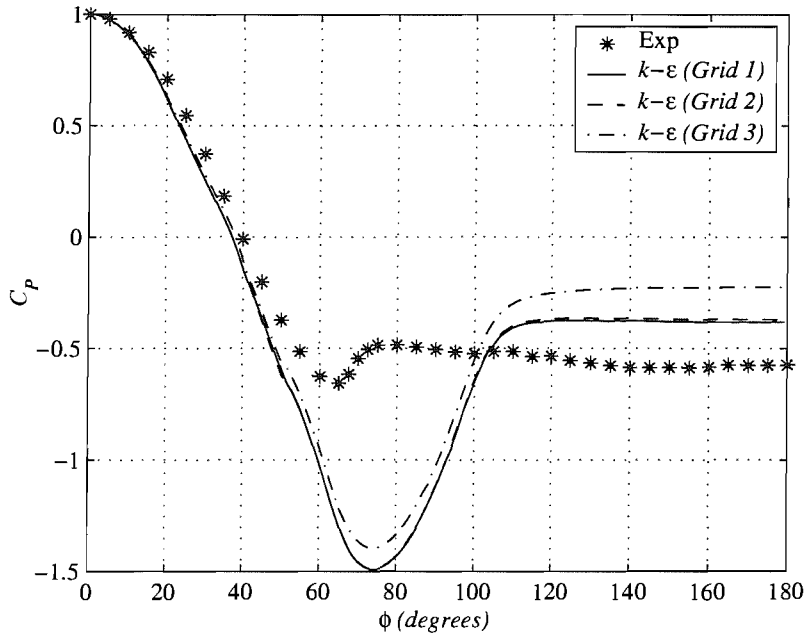

Figure 5.4: Plot of Cp around cylinder at $z/d = 0.5$ for different grids

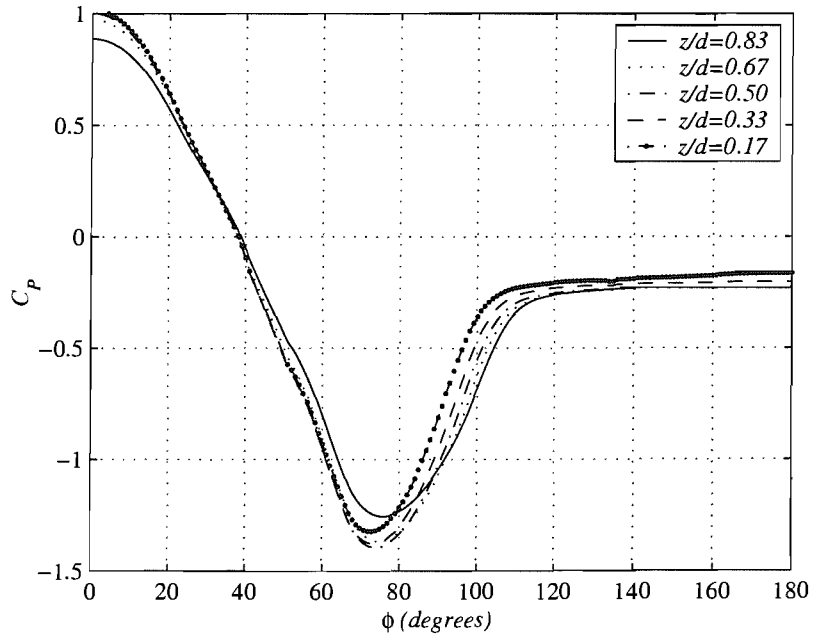

Figure 5.5: Plot of Cp around cylinder using $k - \varepsilon$ model (Grid 3)

oil-flow patterns on the surface of the floor and cylinder. These can be reproduced from the numerical data by calculating the surface restricted streamlines on the surface. This was carried out by the Fieldview visualisation package which was used for the analysis of the data [87]. This applies a grid of particles to the surface from which streamlines are computed based on the velocity gradient at the wall (as the velocity on the wall is assumed to be zero). Figure 5.6 shows the streamlines on the centre plane upstream of the cylinder for the k-ε run on the medium density grid. The separation from the ground is seen to occur at $x/d = -0.79$ which is close to the experimental value, within the error bounds of the PIV results. The centre of the vortex is at $z/d = 0.03$, slightly lower than the experimental location. This could perhaps be due to the slightly thinner boundary layer in the numerical models than in the experiments as seen in Figure 4.5.

Comparing the surface flow images in Figure 5.7, there is a significant difference between the simulated flow and the experimental one, in spite of the sections on the symmetry plane being very similar. In the numerical results the primary separation point is at $x/d = -0.79$, which coincides with the separation seen in the symmetry plane. In the experimental results however this position corresponds to the secondary separation, while the primary separation is further upstream at $x/d = -1.0$. In Chapter 3 it was suggested that these separation points were created by a vortex system very close to the ground beneath the primary vortex. It appears that the k-ε model fails to predict this flow very close to the wall, only predicting the primary vortex. This is perhaps not surprising as there were only two points below $z/d = 0.01$ where these vortices appear to occur. Moving downstream the line of the vortex on the ground does not diverge as the experimental one does but actually remains parallel to the x-axis. This may be a function of the late separation from the side of the cylinder.

5.3.3 Flow over the free end

The flow over the free end is characterised by a region of three-dimensional recirculating flow enclosed within the separation bubble. Streamwise vortices are also produced on the side edges of the cylinder. These streamwise vortices interact with the flow in the wake region and so it is important that they be predicted correctly.

Looking at Figure 5.8 which shows the surface flow patterns for the experimental and medium grid k-ε cases, it can immediately be seen that the k-ε model fails to capture the detail of the swirl patterns on the free-end. The attachment line which should be an arc is actually a straight line. The failure here is thought to be due to two things: the late separation could make a large difference to the flow over the free-end as the swirl patterns appear to draw fluid up from behind the separation line, but also the RANS model may not be capable of predicting what is essentially a boundary layer flow on the free-end with strong rotation.

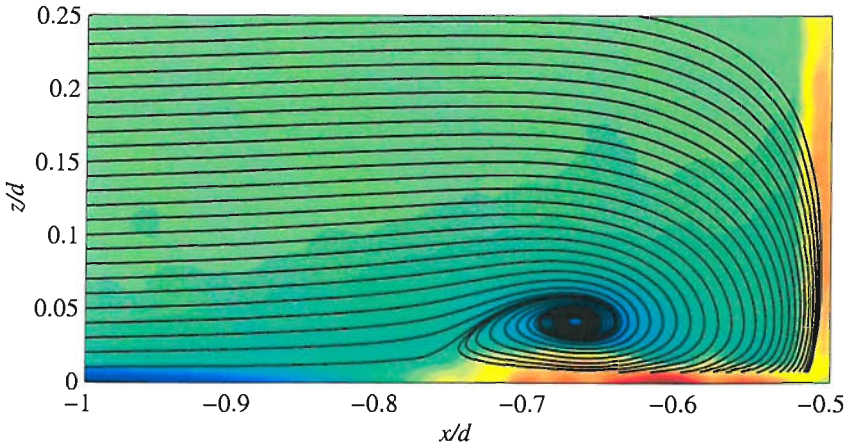

(a) Experimental

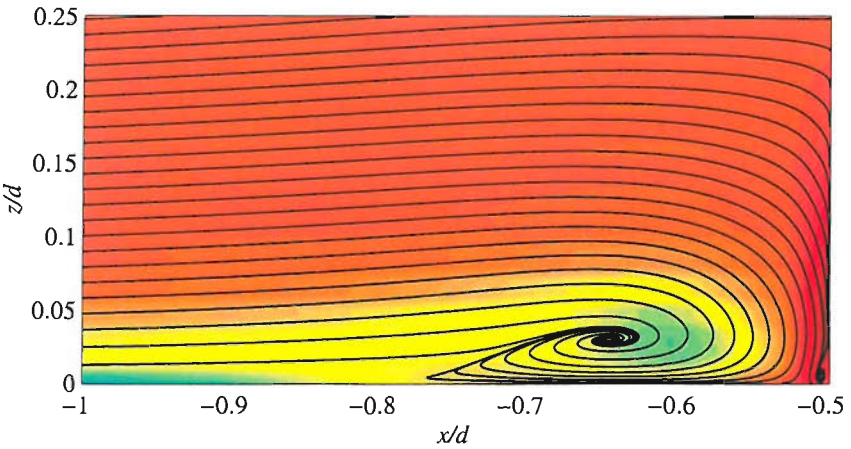

(b) $k-\varepsilon$

Figure 5.6: Velocity vectors and vorticity contours on centreline ($y/d = 0$) upstream of cylinder

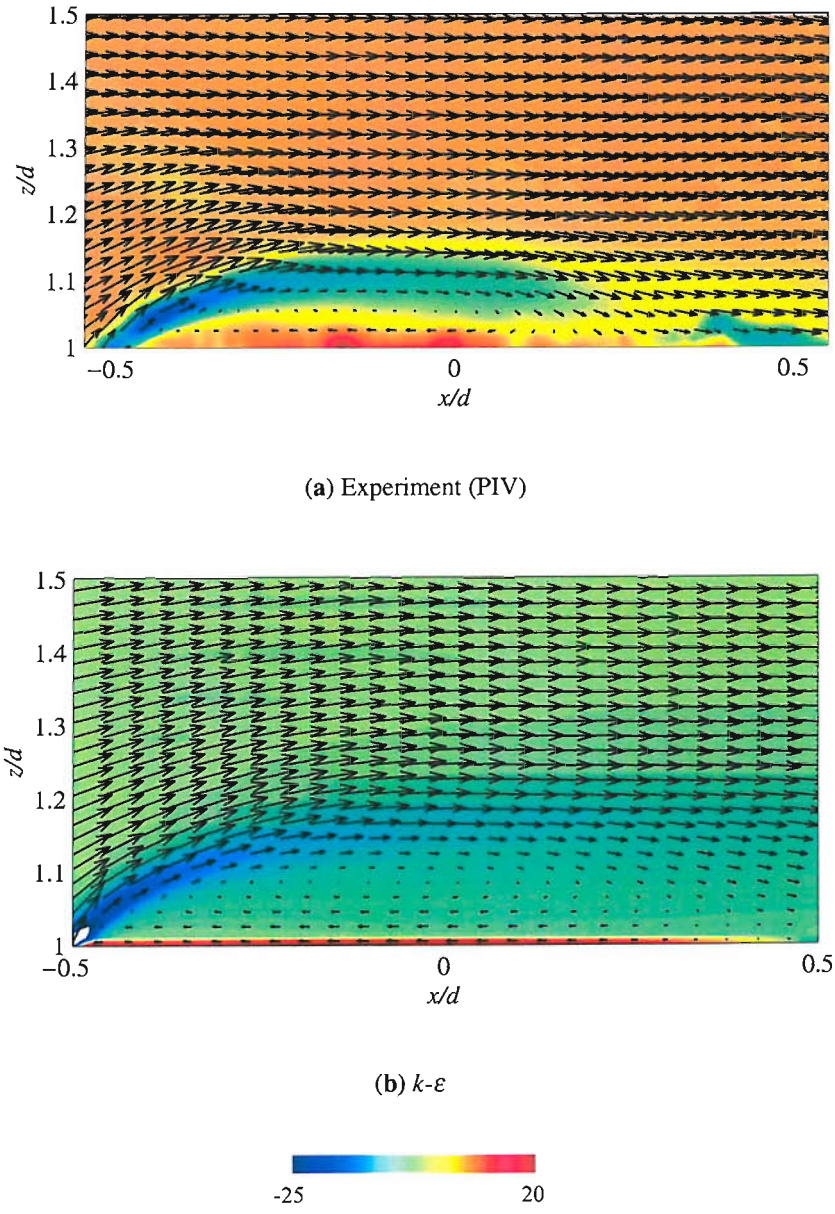

(a) Experiment (PIV)

(b) k-ε

Figure 5.9: Velocity vectors and vorticity contours on centreline ($y/d = 0$) on top cylinder

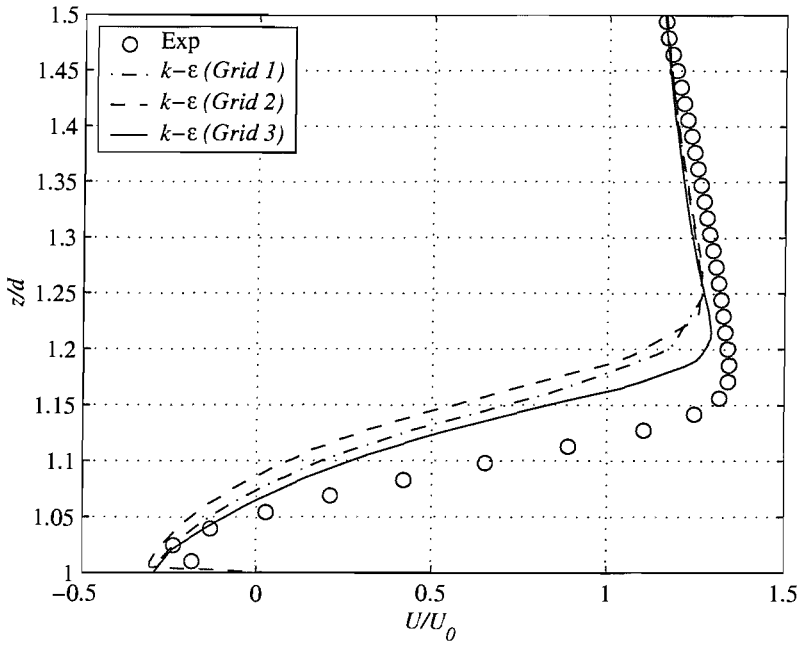

Figure 5.10: Plot of U velocity against z/d at $x/d = 0$

into line with the experiment. At this point the flow consists of two large counter-rotating vortices which create a strong downwash on the centreline. The turbulent kinetic energy, k, is significantly underpredicted by the model particularly in the centre of the recirculation region.

The vector plots in Figure 5.13 show the evolution of the streamwise vortex structures with x. These can be compared to the PIV planes in Figure 3.18. The qualitative agreement is quite good in that the areas of strong vorticity are in the correct locations. The form of the vortices is different to the experiments, largely because of the greater length of the recirculation region.

5.4 Conclusions

The flow around a finite-height cylinder of $h/d = 1$ has been computed using the Reynolds Averaged Navier Stokes equations with the k-ε turbulence model. Three different grid resolutions were tested, with the results on the medium one being considered sufficiently close to the fine mesh to be worth the halving of the computational time.

1. The main problem with this model is that the separation from the cylinder side is much too far back at 107 degrees.

2. The primary horseshoe vortex formed at the junction of the cylinder with the ground plane is well predicted by this model being very close to the measured vortex. However the surface flow pattern differs from the flow visualisation in not having a second separation line at $x/d = -1$.

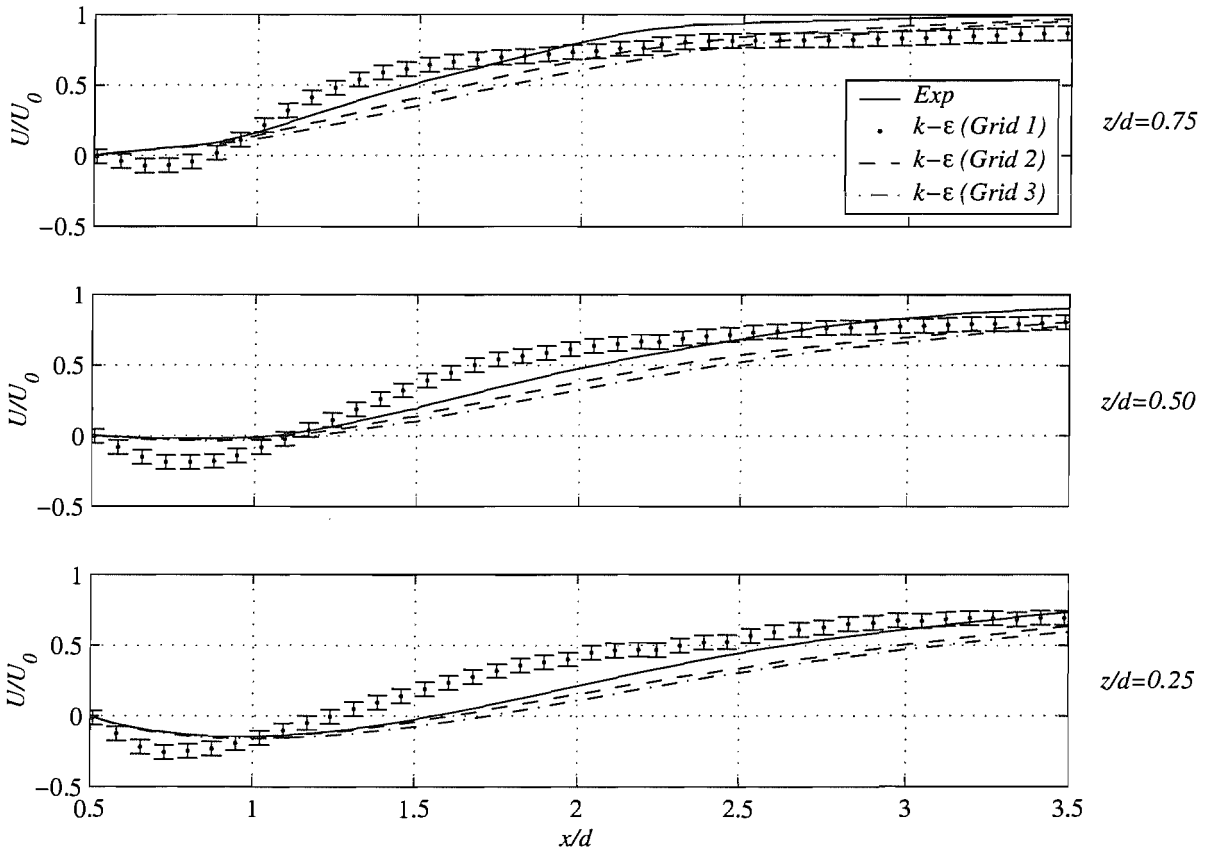

Figure 5.11: Comparison of U-velocity distribution along centreline in wake

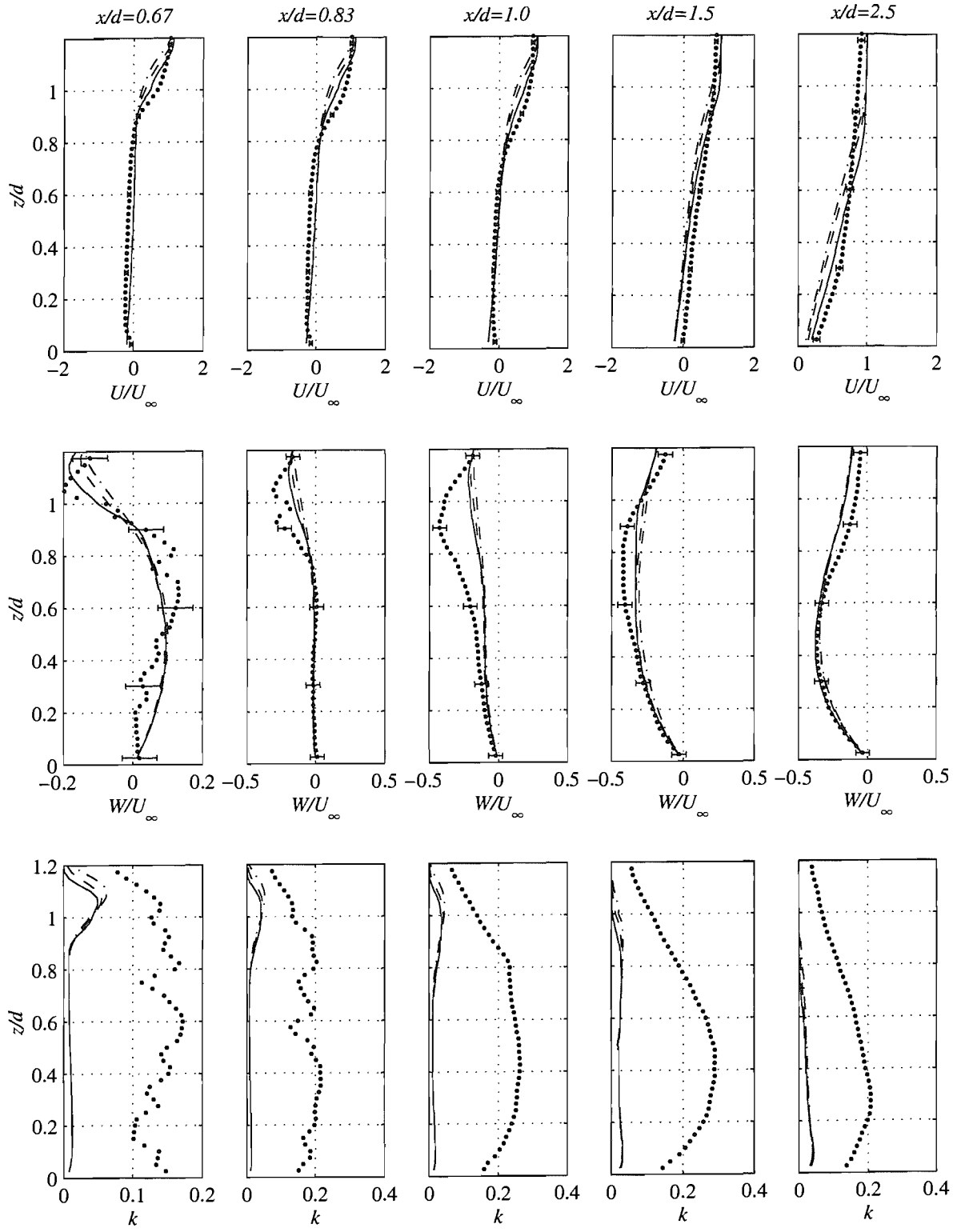

Figure 5.12: k-ε profiles of velocity and turbulent kinetic energy at $y/d = 0$ in wake region. + PIV measurements, −− k-ε grid 1, −· k-ε grid 2, − k-ε grid 3

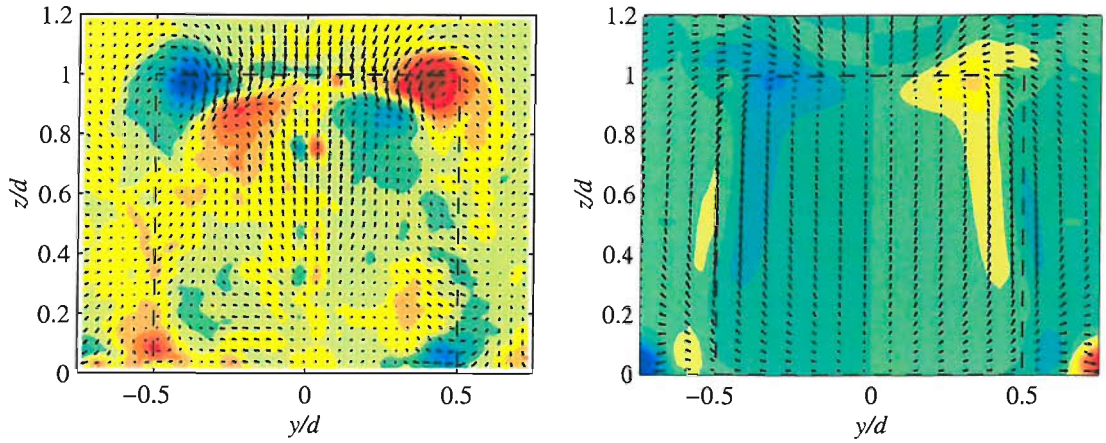

(a) $x/d = 0.67$ (PIV)

(b) $x/d = 0.67$ (k-ε)

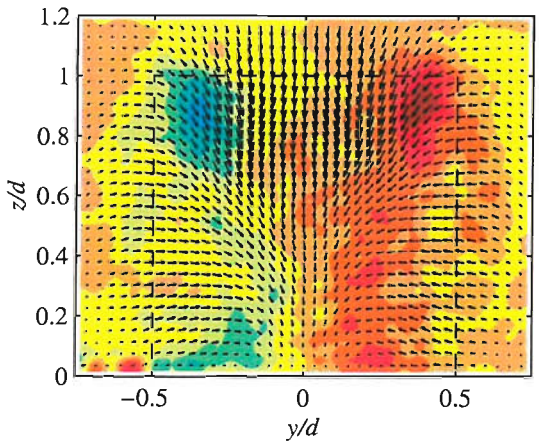

(c) $x/d = 1.0$ (PIV)

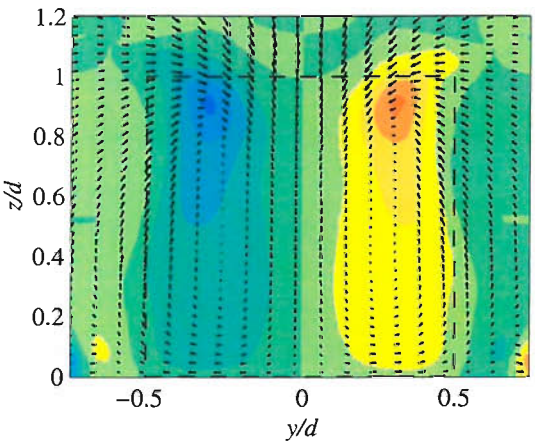

(d) $x/d = 1.0$ (k-ε)

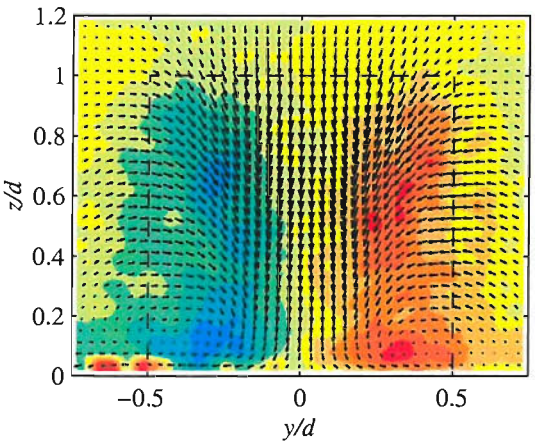

(e) $x/d = 1.5$ (PIV)

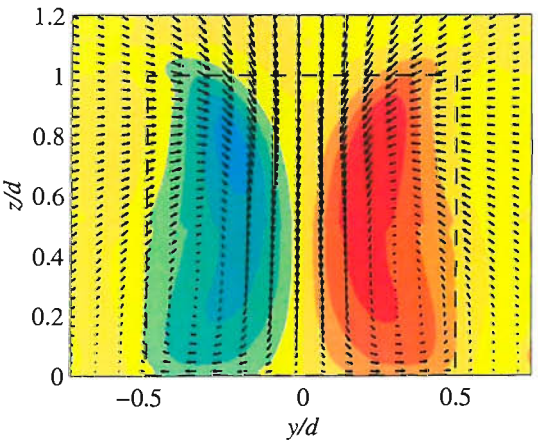

(f) $x/d = 1.5$ (k-ε)

Figure 5.13: Velocity vectors and vorticity contours from k-ε and PIV results

3. The recirculation bubble on the free-end of the cylinder is too high and long (by 34%), while the detail of the flow immediately adjacent to the top surface is not captured at all.

4. The separated flow region in the wake extends too far downstream which affects the velocity profiles in the wake.

5. Downstream of reattachment the two longitudinal vortices are fairly well predicted.

Chapter 6

LES simulations of the truncated cylinder

6.1 Introduction

Having carried out some basic RANS modelling of the flow over the low-aspect ratio cylinder, as reported in the previous chapter, it has been seen that the RANS model is capable of predicting the mean flow quite well in certain areas of the flow. If the mean flow is all that is required a better RANS model such as a $k-\omega$ SST model or a Reynolds stress model can be calibrated to give good results. However, as was seen from the PIV measurements the flow in this case is not at all steady, particularly in the wake where the turbulence intensities reach 30%, meaning that at any instant the flow is significantly different to the mean flow pattern. A RANS model will give no information about this instantaneous flow field.

As well as it being useful to be able to simulate the instantaneous flow features, in some situations it is likely that a more accurate mean flow pattern will be obtained by simulating the large scale turbulent features rather than by simply modelling them with a statistical model. In this case a technique such as Large Eddy Simulation (LES) or even Direct Numerical Simulation (DNS) will be required. These are both time-dependent simulation techniques which resolve the turbulent structures in the flow field. In the case of LES, only those structures larger than a certain size, normally dependent upon the grid size, will be resolved while all the smaller vortices are modelled with a statistical model. In DNS everything is resolved, requiring a grid resolution which is not currently achievable, particularly at the Reynolds number used in this study.

It was therefore decided to simulate the flow over the truncated cylinder using LES. Even if the mean flow prediction is not much better than a good RANS model, the extra detail on the turbulent structures in the flow should be valuable to the understanding of a particular flow. The objective of this part of the work was therefore to simulate the mean flow better than the RANS model and also to obtain greater understanding of the instantaneous flow features.

6.2 Details of the computational model

The LES simulations were run using the code described in Chapter 4. This was run in time-stepping mode using a three time-level implicit scheme. The second order upwind CLAM scheme was used for spatial discretisation of the momentum terms. The use of upwind schemes for LES is not generally recommended as the numerical diffusion acts as an extra viscosity which may damp out some of the smaller scale motions. Indeed some authors have used an upwind differencing scheme as an alternative to a subgrid model [88]. In general central differencing schemes are used for LES [46], but it was considered impractical to modify the code to employ this scheme. The SIMPLEC pressure correction scheme was employed. This is not the most efficient for time-stepping problems due to its requirement for a number of iterations at each time step. The PISO scheme was a possible alternative for time dependent solutions which does not require iteration, but an unresolved bug in the code meant that this scheme failed on multiblock grids with skewed boundaries as used in these cases. The inlet condition was the standard fixed inflow. This does not include any information about the free-stream turbulence level at the inlet which may introduce a source of error.

The LES simulations were run on grids 1 and 2, as described in the previous chapter, and detailed in Table 5.1. The finer mesh would have required double the CPU time to compute which was felt to be excessive. The only change to the grids was the use of arcs rather than spline curves to define the circular edges. One of the problems of numerical modelling is in the estimation of the error due to the spatial discretisation. With a laminar flow or RANS model the accuracy will improve with grid refinement as the discretisation errors will reduce. The required level of refinement can be judged by conducting a series of runs on progressively finer meshes until the difference in the solution becomes sufficiently small.

In the case of LES however the grid resolution also affects the range of length scales which are resolved compared to those which are modelled by the subgrid model. As the subgrid models are generally simple algebraic models, which are normally calibrated for isotropic turbulence, they will not perform well at modelling larger eddies in non-isotropic parts of the flow, such as bluff body wakes and shear layers. Provided that the grid is fine enough the majority of the energy containing scales can be resolved and so the subgrid model will have a limited role. If the grid is too coarse however, the subgrid model will be asked to model larger scale features than it is intended for. This ambiguity between the resolved and modelled scales adds another potential grid dependent error. If the flow is relatively simple and the required computational time is short enough a number of runs should be made to determine the effect of grid resolution. Unfortunately most LES simulations are computationally expensive and so it is impractical to perform many grid dependence tests. The two grids used in this study will give some insight into the grid dependence but it is not possible to say that the solution is fully grid independent.

A time step of 0.005 non-dimensional time units was used for all the simulations. While this leads to a maximum Courant number of 8 in a small number of cells above the cylinder, where the grid is rather stretched, it is less than 1 in the majority of the domain. A small number of outer iterations must be solved at each time step so that a converged solution is obtained. Five iterations were found to be sufficient, as the residuals did not reduce much further after this. The maximum number of inner iterations, that is iterations of the system of linear equations at each outer iteration, is also fixed. The fact that the CPU time doubles from the coarse grid to the fine grid indicates that the same number of inner iterations are being performed on each grid. This implies that the fine grid is not being converged as much as the coarser one as the matrix solver does not scale linearly with grid size. If the solution is not being fully converged at each time step there may be small errors in the flow field which will grow with time so that after 10000 time steps the instantaneous flow field will be wrong. Although not carried out in this work it would be desirable in future to compare the instantaneous flow fields after a long period with different parameters to ensure convergence.

Due to the unsteady nature of turbulent flows it is usual to describe the flow in terms of statistical quantities such as mean and root mean square velocities. These values can be readily compared to the results of experiments and of RANS models which only give the mean velocities. These statistical quantities can either be calculated by outputting data from the code at many time steps and post-processing it to obtain the statistics. For a large enough sample size this requires a large amount of storage, unless just a small subset of the flow domain is required. The alternative is to calculate the statistics within the code at every time step and to store these as separate variables. This increases the memory requirements of the code while running, but this is generally not a problem with current computers. This is the approach used in this work. Further details of the algorithm which was implemented by the author can be found in Appendix C.

6.3 Results

6.3.1 Global flow parameters

The results of the LES simulations on the two grids are summarised in Table 6.1. It can be seen that the separation point from the side of the cylinder is too far back by 13 or 11 degrees on the coarse and medium grids respectively. This is slightly surprising since the boundary layer in the LES simulations is laminar, which should result in early separation. The problem may be due to insufficient resolution of the boundary layer.

Looking at the separation from the ground plane it can be seen that this point is much too far forward, at $x/d = -1.38$ or $x/d = -1.45$ on the coarse and medium grids respectively. It

Table 6.1: Details of LES runs

Grid	1	2	Exp.
CPU time / time step (secs)	27	55	
Side separation, ϕ_s (degrees)	83.0	81.0	70
Primary sep. from ground, X_{S1} (x/d)	-1.38	-1.45	-1.0
Secondary sep. from ground, X_{S2} (x/d)	-1.00	-0.97	-0.78
Attachment on free-end, X_{RT} (x/d)	0.30	0.39	0.17
Attachment on ground downstream, X_{RF} (x/d)	2.6	2.1	1.6
Local C_D at $z/d = 0.5$	0.81	0.80	0.79

will be seen in the next section that there is actually a pair of horseshoe vortices. Again this is likely to be due to the laminar boundary layer on the ground plane, as was seen in the Section 4.4.2. A laminar boundary layer will undergo separation earlier than a turbulent one due to the reduced momentum near the wall.

The attachment point of the shear layer on the ground plane downstream of the cylinder is given at $x/d = 2.6$ and $x/d = 2.1$ on the two grids. This implies a strong dependence on the grid resolution in the shear layer and recirculation region. This is likely as the turbulence intensities are high in these areas. The flow is also strongly influenced by the geometry here which means that the subgrid model could be inadequate to model the effects of larger eddies if the grid is too coarse. Fröhlich et al. [35] also found a strong grid dependence in their simulations of a cylinder of $h/d = 2.5$. This was attributed to the sensitivity of the results on the simulation of transition in the shear layer just after separation.

The plots of C_P in Figure 6.1 show that the pressure on the surface of the cylinder is well predicted in the LES simulations. The point of minimum C_P is very close to the experimental one, while the local maximum or inflexion point just after separation is about 10 degrees further back. This is consistent with the separation line being 11 degrees further back. The base pressure is also close the experimental value. The results on the finer mesh are closer to the experimental results than the coarse mesh. The similarity in the pressure distribution is reflected in the drag coefficient which is 0.79 in the experiment and 0.80 for the LES on the fine mesh.

6.3.2 Horseshoe vortex

As has been seen from the flow parameters discussed in the preceding section, the horseshoe vortex extends too far forward in the LES simulations. Looking at the streamlines in the centre plane ($y/d = 0$) in Figure 6.3, it can be seen that there is in fact a pair of counter-rotating

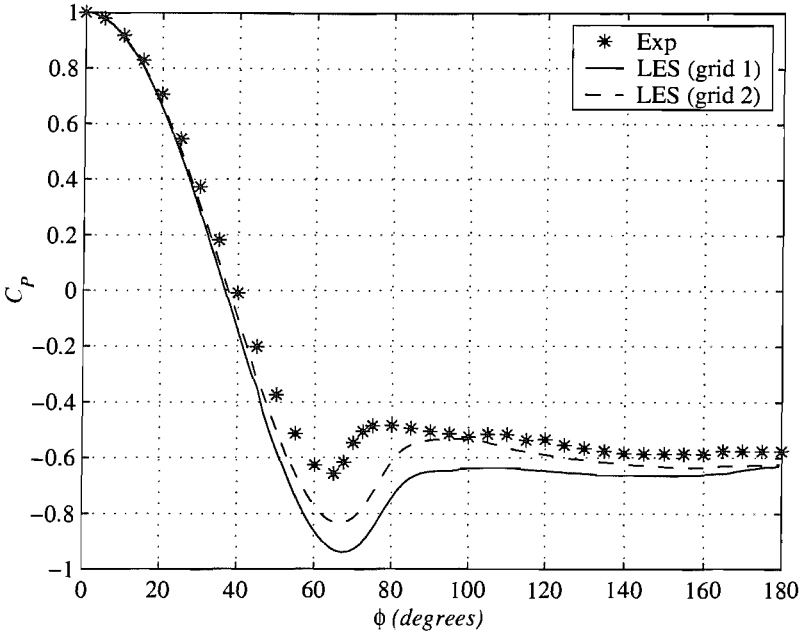

Figure 6.1: Plot of C_P around cylinder at $z/d = 0.5$

vortices upstream of the cylinder. This is reflected in the surface flow visualisation (Figure 6.2). This shows two separation lines in front of the cylinder. The centre of the inner vortex is also located further upstream than the single vortex in the experiment and in the k-ε results.

The failure to model this feature of the flow correctly is probably due to the poor resolution of the boundary layer on the tunnel floor as demonstrated in Section 4.4.2. This shows that the approaching boundary layer profile is closer to a laminar one than a turbulent profile. The separation behaviour would therefore be very different to the turbulent boundary layer. In fact according to Simpson [23] for a laminar boundary layer the number of primary vortices increases with Re_d with two vortices, as seen here, occurring at $Re_d < 1000$ and three vortices above $Re_d = 1000$. As the number of vortices increases due to the instability of the system at higher Re_d it is likely that the present computations only give two vortices due to the extra viscosity and fully boundary layer profile than the laminar case. The position of the upstream separation point is approximately $x/d = 1.7$ according to Ballio et al. [28] at $Re_{\delta^*} = 409$.

The separation line marking the inside edge of the horseshoe vortex, which wraps into the base of the arch vortices, shows good agreement with the experiment. The divergence angle of the separation line from the x-axis is 13.4 degrees compared to 15.5 degrees for the experiment.

6.3.3 Flow over the free end

It was seen in the previous chapter that the RANS model fails to capture the swirl patterns on the free-end of the cylinder. This could be attributed partially to the late separation from the cylinder side which alters the position of the upwash on to the free-end.

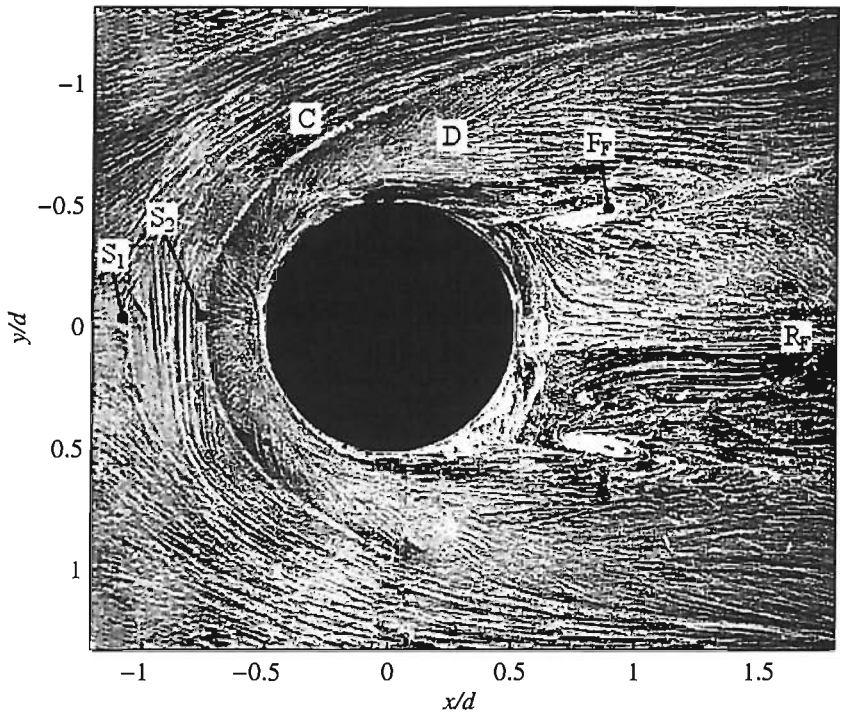

(a)

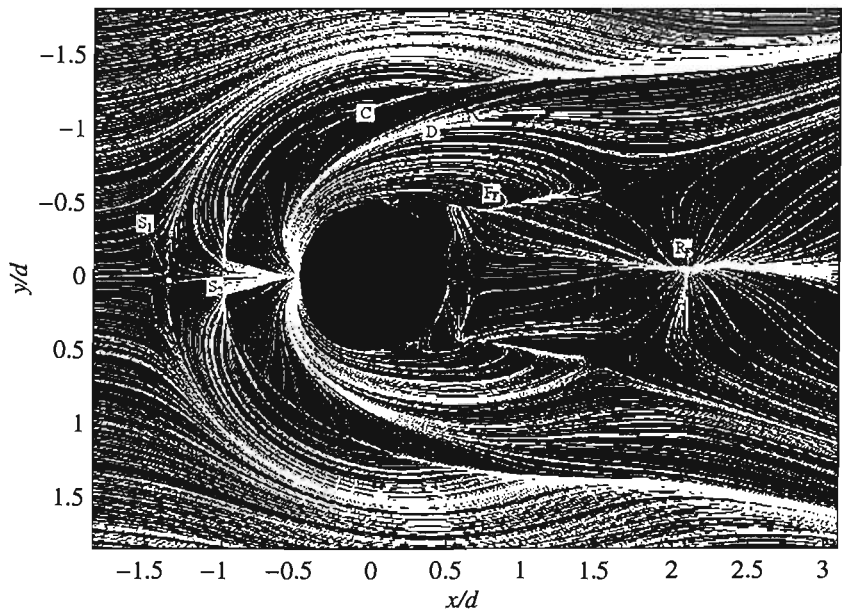

(b)

Figure 6.2: Surface flow visualisation on the ground plane (a) experimental, (b) LES (flow from left to right)

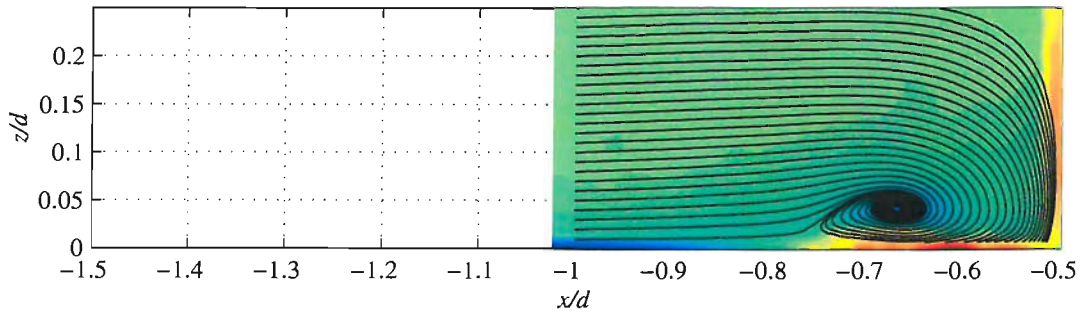

(a) Experimental

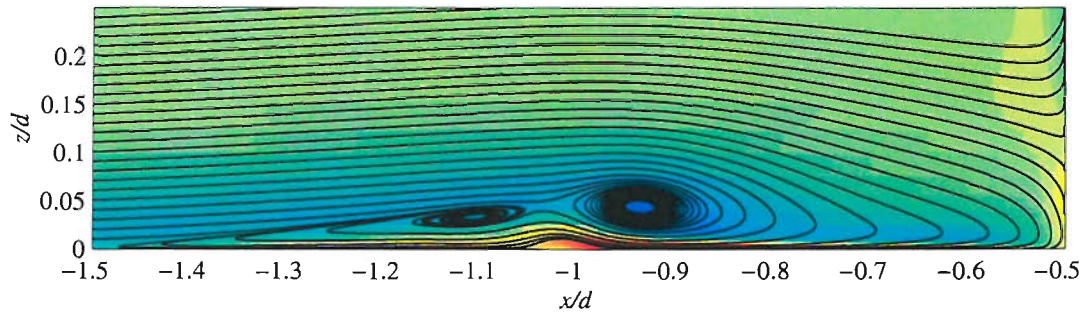

(b) LES

Figure 6.3: Velocity vectors and vorticity contours on centreline ($y/d = 0$) upstream of cylinder

Comparing the surface flow pattern in Figure 6.4, obtained from the LES simulation on grid 2, with the image from the experiment, it can be seen that the swirl patterns are very similar. The location of the vortex core is in the same position although it is difficult to judge from the experiment due to the accumulation of oil at this spot. Three saddle points can be seen towards the rear of the cylinder along the attachment line. The location of this line is not clear on the experimental picture. In the experiment there appears to be flow from the leading edge moving back as far as a separation point at $x/d \sim -0.4$, which must be due to a small vortex in front of and beneath the main recirculation. This does not appear in the LES results where all the flow is from the back of the cylinder.

Turning to the flow in the $y/d = 0$ plane above the free-end (Figure 6.5), the recirculation vortex predicted by the simulation is much larger than that measured by PIV. The centre is further downstream, resulting in a later attachment to the free-end. The centre of the vortex is located at $x/d = 0.3$ compared to $x/d = 0$ in the experiment. The attachment point is correspondingly far back, at $x/d = 0.4$ compared to $x/d = 0.25$ in the experimental case. In fact the coarser grid gives a shorter recirculation bubble than the finer mesh, giving attachment at $x/d = 0.3$.

Figure 6.6 is a plot of U against z/d at the centre of the free-end. It shows that on both grids the height of the recirculation vortex, to the point of maximum velocity, is overpredicted by a factor of 2. The velocity profile close to the surface of the cylinder is close to the experimental points on the finer mesh, with the correct maximum backflow velocity. The overprediction of the size of the recirculation region could be due to the lack of free-stream turbulence.

6.3.4 Wake region

The pool of oil which accumulated in the experiment masks the detail of the flow in this region but it seems to show the same flow pattern as the numerical results. This point appears to mark the base of the so-called "arch" vortex. The numerical results show the backflow from the attachment point being wrapped up into these vortices, which are also drawing fluid in from the shear layer to the side.

The reattachment point behind the cylinder is found to be at $x/d = 2.1$ on the finer grid. This is longer than in the experiment which can be related to the oversize recirculation region on the free-end, pushing the shear layer up. Figure 6.7 shows U against z/d for different heights above the ground. This shows that the backflow velocity is quite close to the experimental values but the streamwise extent of the reversed flow is too long. The velocity recovery downstream is slower than in the experiments.

More detail of the structure of the wake can be seen in Figures 6.8 to 6.10. Figure 6.8 shows profiles of U, W and k against z/d at different locations downstream on the centreline. V is

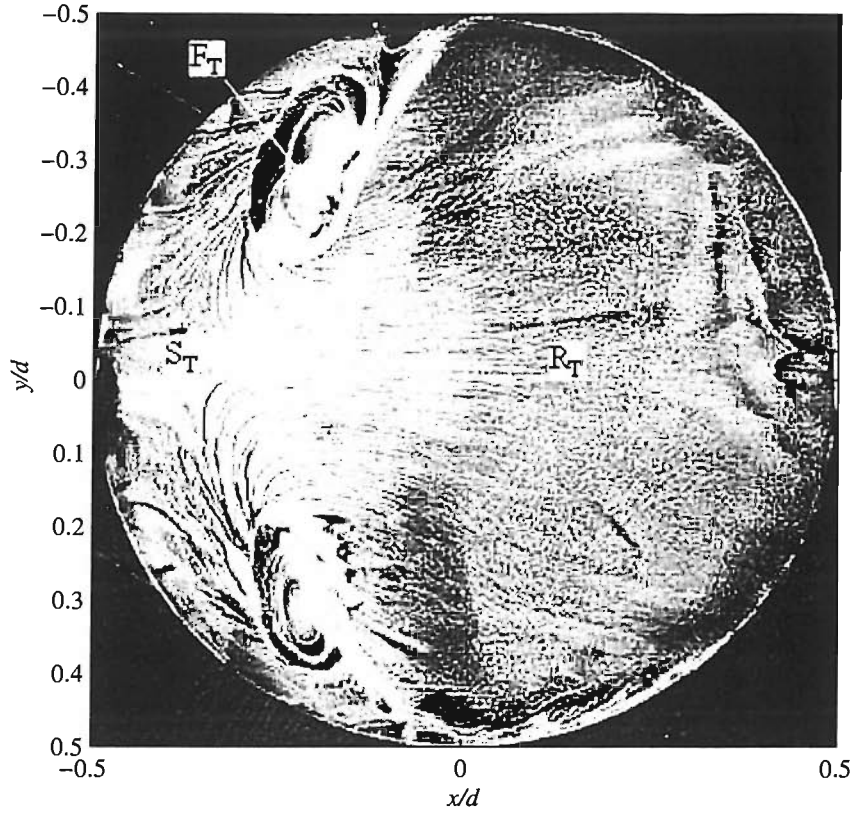

(a)

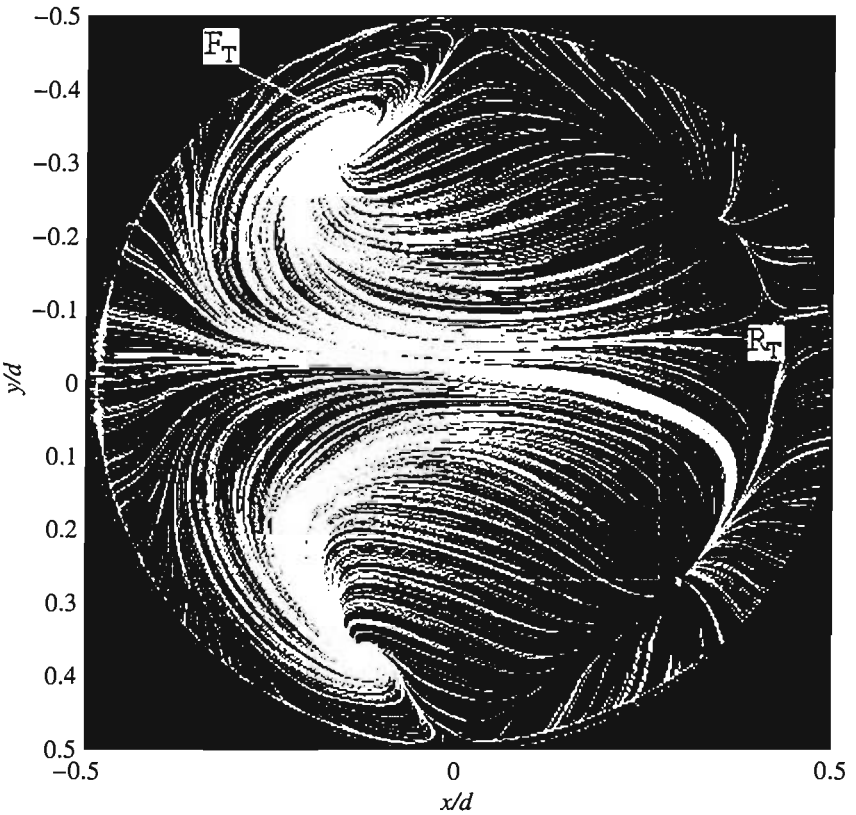

(b)

Figure 6.4: Surface flow visualisation on the free-end of the cylinder (a) experimental, (b) LES (flow from left to right)

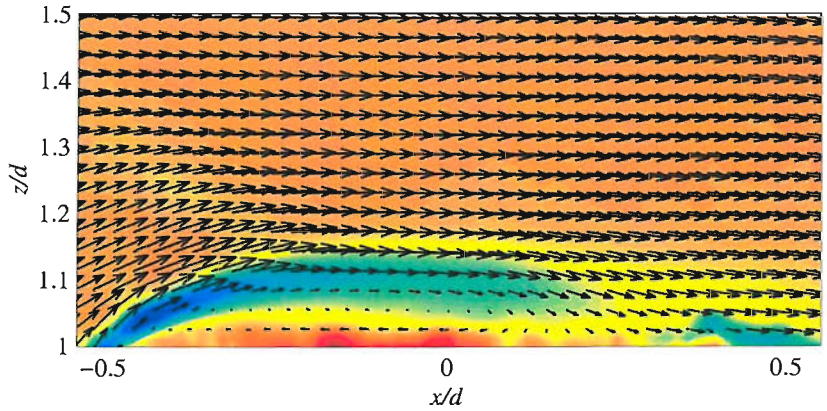

(a) Experiment (PIV)

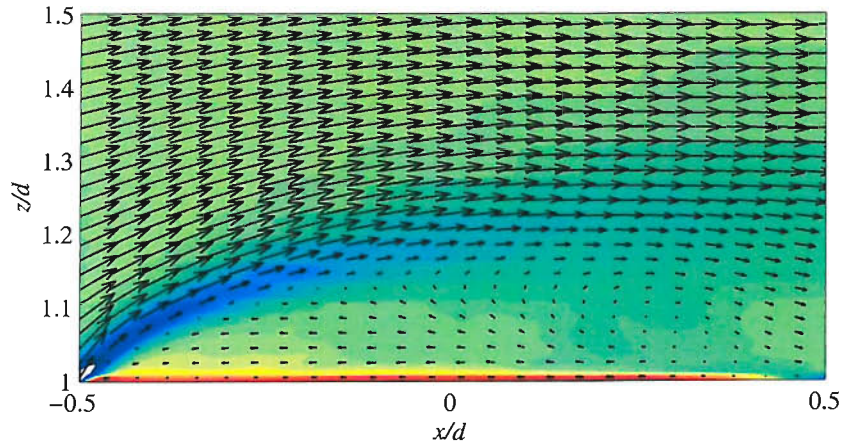

(b) LES

Figure 6.5: Velocity vectors and vorticity contours on centreline ($y/d = 0$) on top cylinder

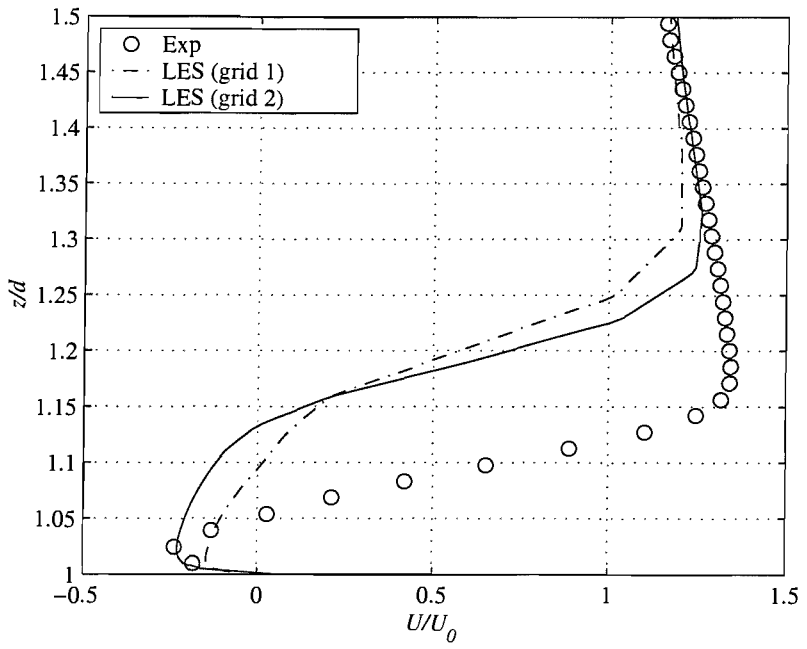

Figure 6.6: Plot of U velocity against z/d at $x/d = 0$

of course 0 on the centreline due to symmetry so is not plotted. The data is compared to the PIV measurements. The components of the Reynolds stress tensor, $u_i u_j$, are plotted at the same locations in Figures 6.9 and 6.10.

Looking first at the velocity profiles the U component towards the top is quite different to the experimental values as the shear layer is higher due to the larger recirculation region on the free-end of the cylinder. Further downstream the velocities tend to the free stream value. Towards the ground the flow is reversed further downstream due to the later attachment. The W component is mainly influenced by the downwash angle of the shear layer, which is shallower in the LES simulation than in the experiment. This means that the minimum W in the simulation is larger than in the experiment. Downstream of the attachment the velocities agree better with the experiment as the flow is dominated by the two streamwise vortices which are well predicted.

The turbulent kinetic energy is quite close to the experimental values except in the shear layer close downstream of the trailing edge where the simulation over-predicts k. Also at $x/d = 1.0$ there is a large discrepancy throughout, although at this location in the experiment the flow is approaching attachment. At the downstream location the agreement between the experimental and numerical results is remarkably good.

Turning now to the Reynolds stresses, $\overline{u'u'}$ is substantially overpredicted in the shear layer although the agreement is better in the lower half of the profile. $\overline{v'v'}$ is of the right order of magnitude close to the cylinder although the detail of the variation with height is not captured.

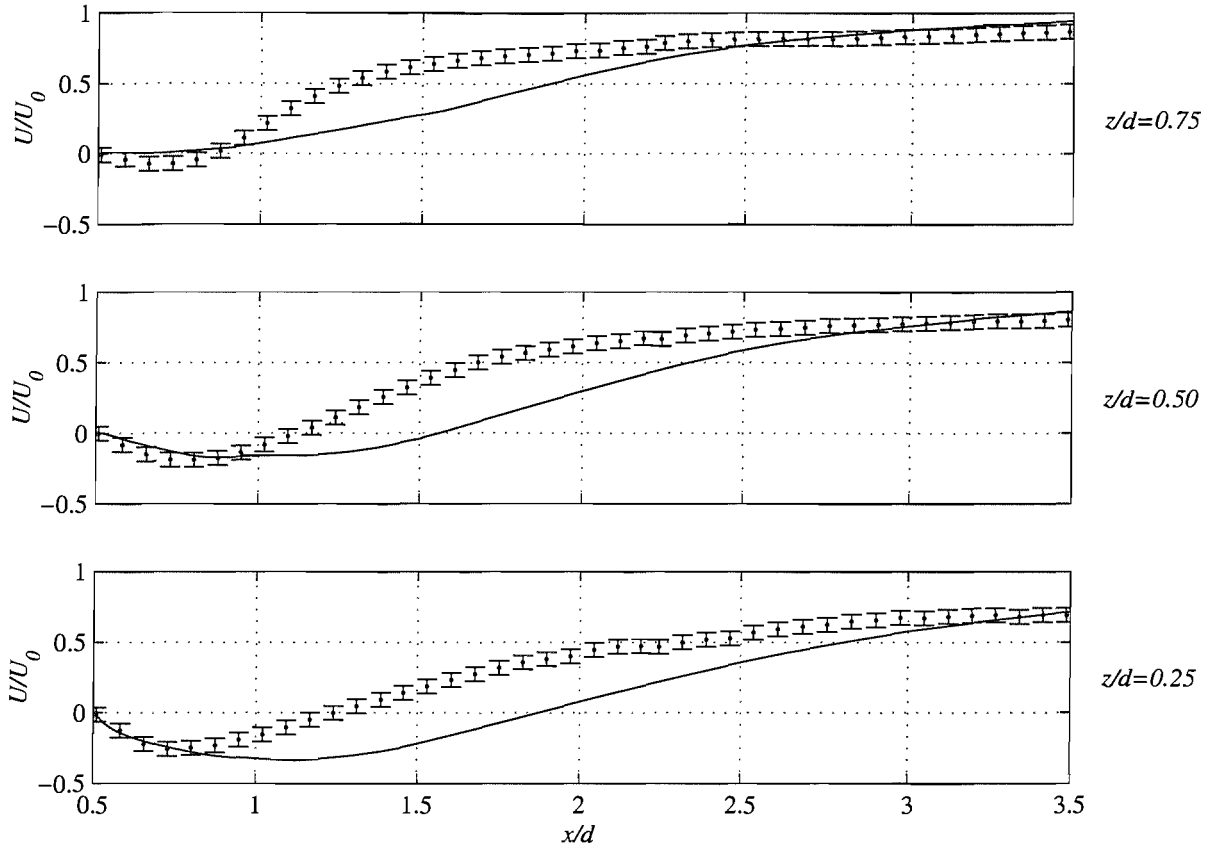

Figure 6.7: Comparison of U-velocity distribution along centreline in wake

Moving downstream to $x/d = 1.0$ the agreement becomes worse, only improving after attachment. $\overline{w'w'}$ seems to agree better with the experimental data than the other two normal stress components although the detail in the near wake region is not fully captured. Looking at the shear stresses, $\overline{u'w'}$ is affected by the position of the shear layer. The magnitude downstream is correct but upstream the peak is not clear. The $\overline{v'w'}$ component is small but the simulations do agree fairly well with the experiment. The experimental values are not very smooth suggesting that they may not be very accurate.

Figure 6.11 shows the evolution of the vortices in the transverse planes downstream. The vortices produced by the LES differ in location and strength from the experimental measurements. This could be related to the overprediction of the size of the recirculation region.

A plot of the power spectral density function of the U velocity, measured outside the wake near the top of the cylinder, from the LES results is given in 6.12. This shows that the LES predicts the shedding frequencies quite well compared to the hot-wire measurements from the experiments. The vortex shedding frequency predicted by the LES is in good agreement with the hot-wire measurements from the experiments, with a Strouhal number of 0.10 for the LES compared to 0.125 for the experiments.

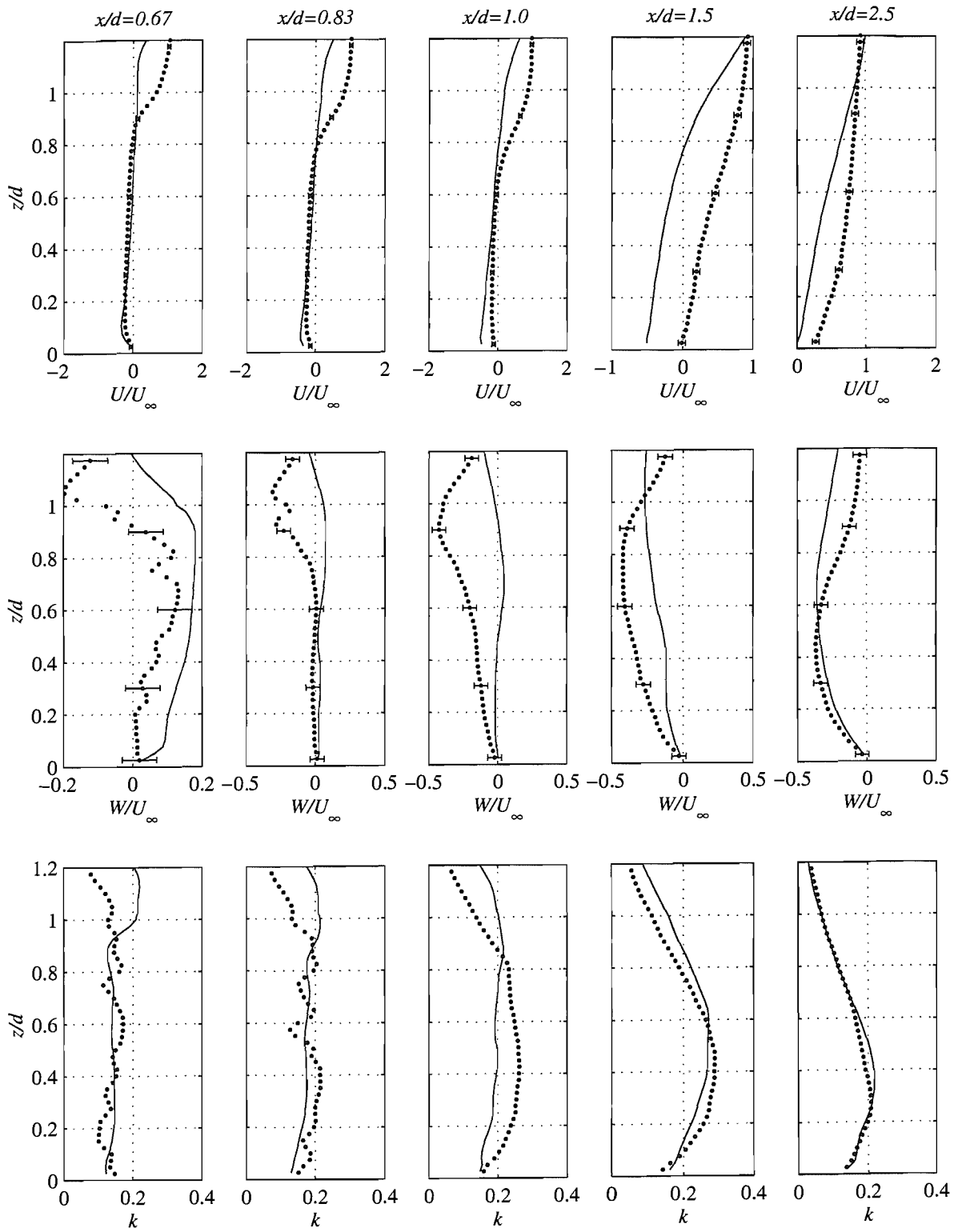

Figure 6.8: LES profiles of velocity and turbulent kinetic energy at $y/d = 0$ in wake region. + PIV measurements, - simulations

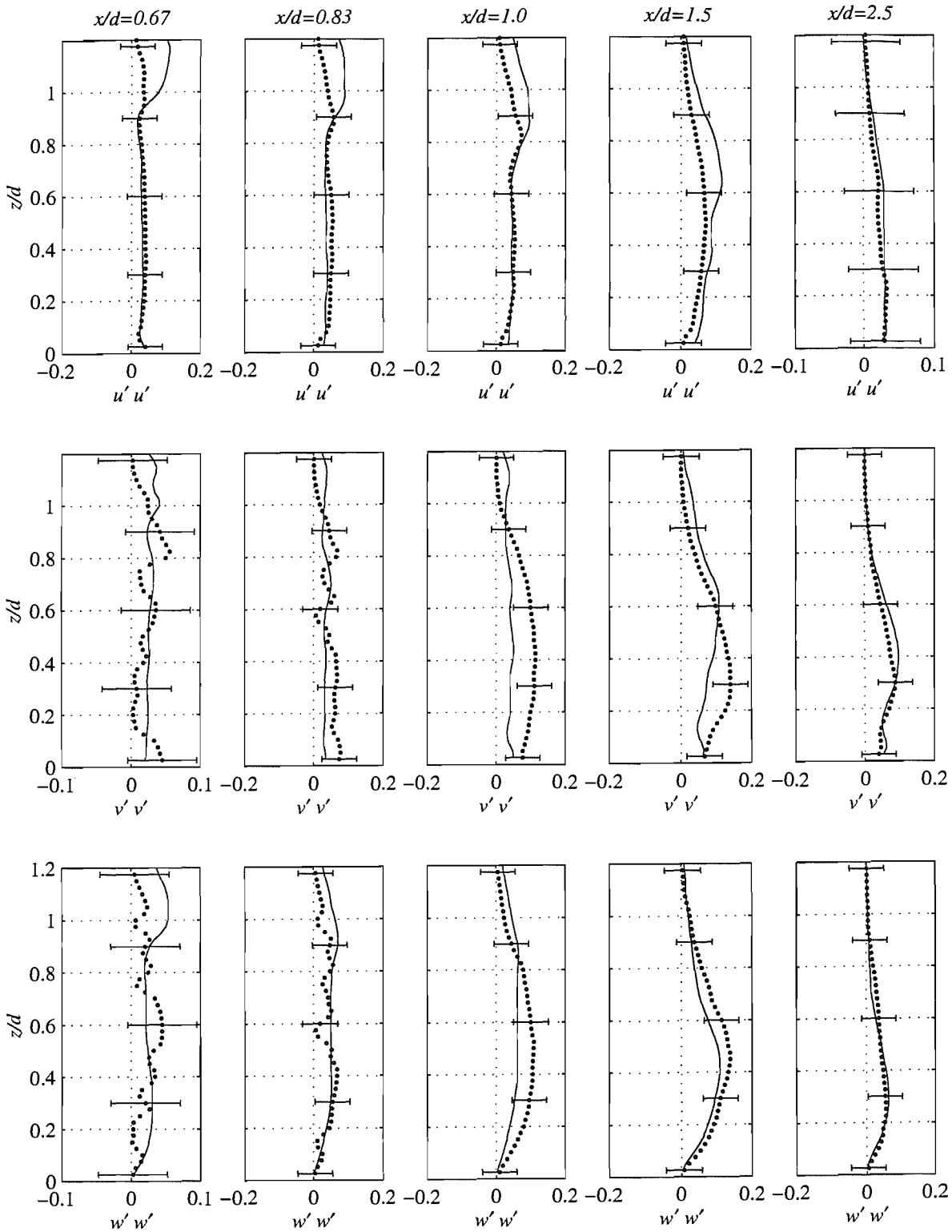

Figure 6.9: LES profiles of normal stresses at $y/d = 0$ in wake region. + PIV measurements, - simulations

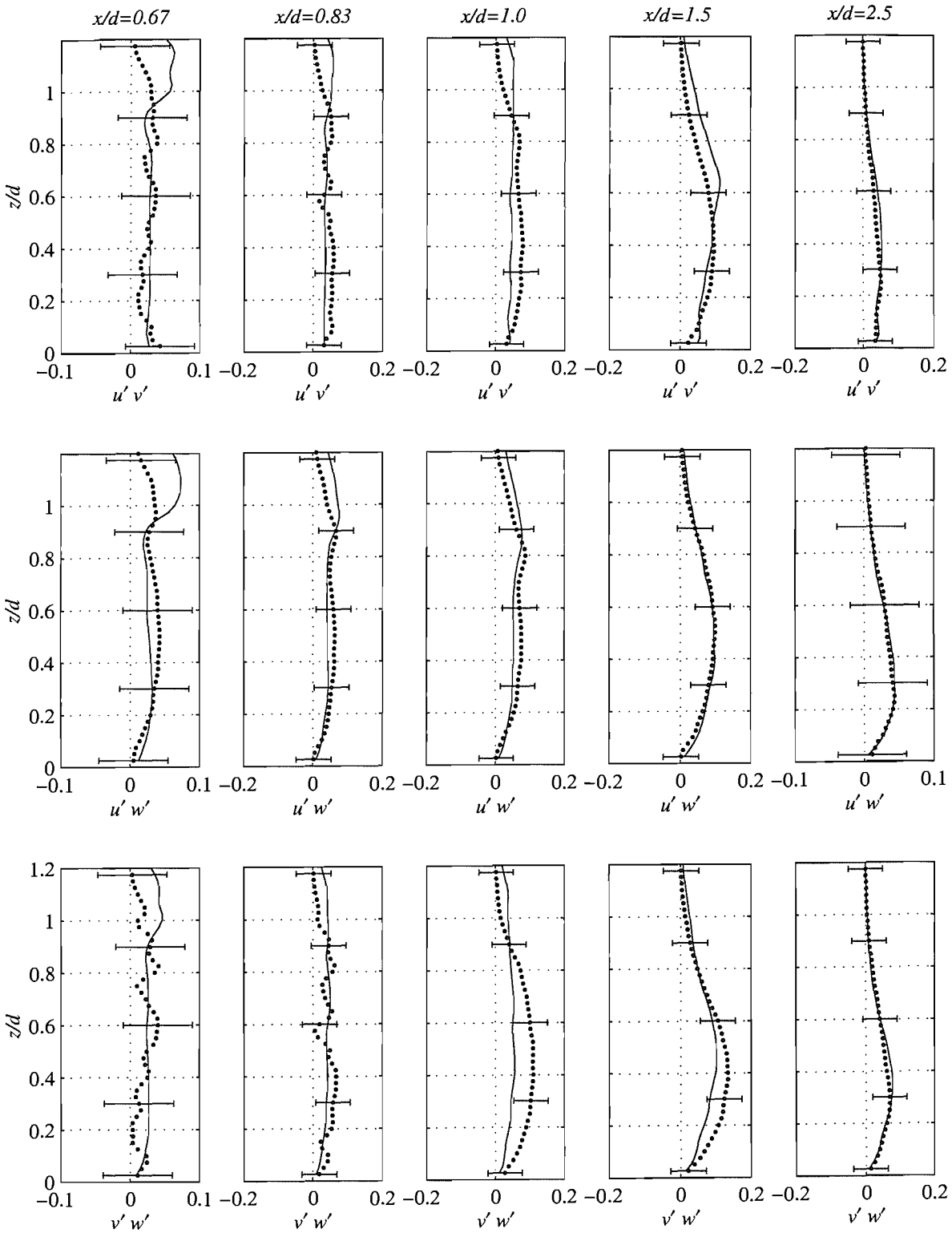

Figure 6.10: LES profiles of shear stresses at $y/d = 0$ in wake region. + PIV measurements, - simulations

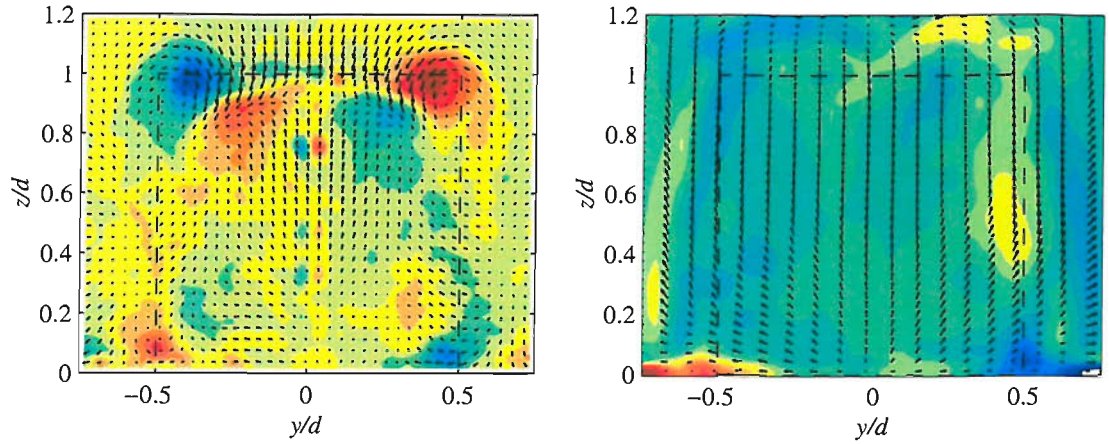

(a) $x/d = 0.67$ (PIV)

(b) $x/d = 0.67$ (LES)

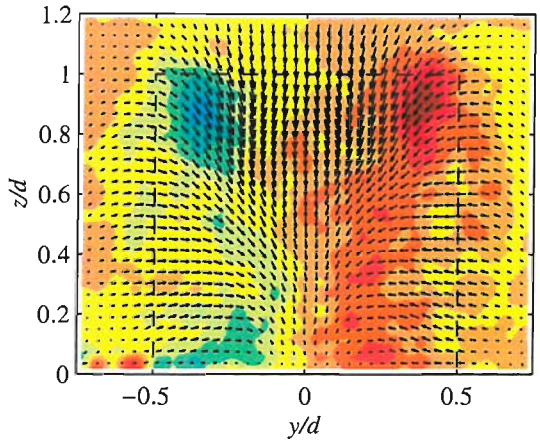

(c) $x/d = 1.0$ (PIV)

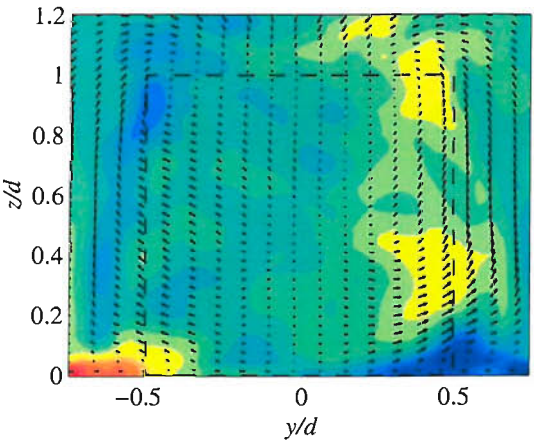

(d) $x/d = 1.0$ (LES)

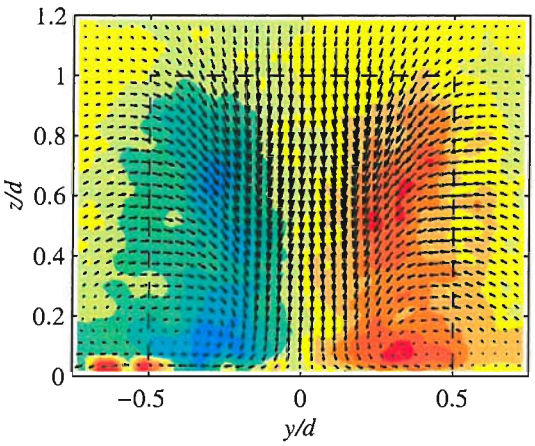

(e) $x/d = 1.5$ (PIV)

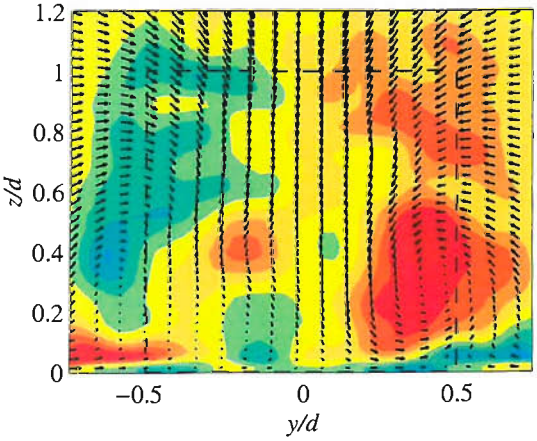

(f) $x/d = 1.5$ (LES)

Figure 6.11: Velocity vectors and vorticity contours from LES and PIV results

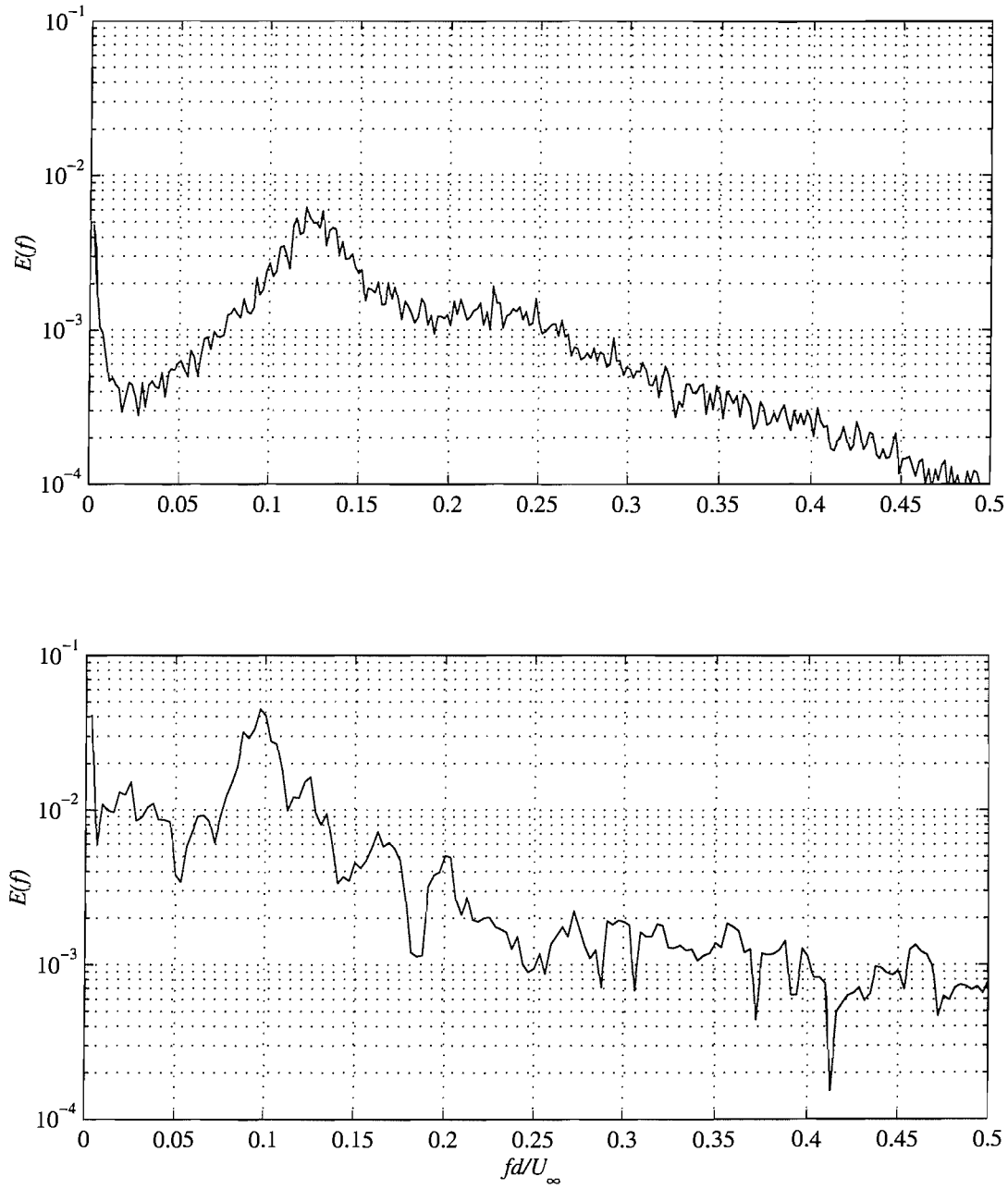

Figure 6.12: Power spectral density function of U-velocity from LES and experimental results at $x/d = 1.5$, $y/d = 1$, $z/d = 1$

6.4 Conclusions

LES simulations of the flow around the truncated cylinder were performed on two grids of different densities. The difference between the results on the two grids was substantial in some areas so the finer one was considered necessary. The results from this simulation have been compared to the experimental data, and to the RANS results. They show good agreement with the experiment in certain areas. The key findings are summarised below.

1. The main failing of the LES simulation was in the prediction of boundary layer on the ground plane upstream of the cylinder. This is due to the grid resolution being insufficient to fully resolve the turbulence scales in the boundary layer, and the lack of a wall function. This led to an incorrect modelling of the horseshoe vortex with the upstream vortex being too large. The separation point in front of the first vortex was over 3 times further upstream than the experimental measurement.

2. The flow on the surface of the free-end was found to agree well with the experiments as the boundary layer on this surface was correctly resolved. The shear layer above the free-end was too high with the attachment point being 33% too far back.

3. The velocity profiles in the wake region showed agreement with the experimental data in some areas away from the tip of the cylinder and became very good downstream of the attachment location. The Reynolds stresses also showed good agreement in some places. In general they were of the correct order of magnitude and generally had the right form.

4. The power spectral density function of the velocity in the wake agreed well with the experimental result indicating that the turbulent structures are being resolved fully down to small scales.

These findings suggest that although the values may not be accurate the structure of the mean and instantaneous flow fields are likely to be correct, and can therefore be used to learn more about the flow physics. This will be explored further in Chapter 8.

Chapter 7

DES simulations of the truncated cylinder

7.1 Introduction

The LES simulations reported in the previous chapter proved promising in terms of predicting the turbulent flow in the separation regions, although the actual accuracy was perhaps compromised by the grid resolution and numerical schemes used. Overall the LES simulations were better than the RANS k-ε results in all areas except the primary horseshoe vortex at the junction of the cylinder with the ground plane. This was felt to be due to the poor resolution of the boundary layer on the ground plane using LES. As it is quite common in high Reynolds number engineering flows, as found in the marine environment, to find large areas of turbulent attached boundary layers it is necessary to find a solution to this problem. One approach which is gaining popularity is the Detached Eddy Simulation method [73]. As described in Chapter 4, this is a technique which modifies a RANS model to act as an LES subgrid model in areas where the grid density is sufficient to resolve the energy containing scales. In practice this means that high Reynolds number boundary layers will be treated in RANS mode so that the velocity and turbulent kinetic energy profiles should be correctly predicted.

Due to its potential benefits for marine flow computations it was decided that a DES model should be implemented in the finite volume solver used previously in order to test its capabilities. The present flow was considered to be a good test case due to its wide variety of flow features. In particular it was hoped that the boundary layer on the ground plane would be better predicted than in the LES simulations, which might help the prediction of the horseshoe vortex. There are some areas of laminar boundary layers on the cylinder which would not be expected to be as well modelled as in the LES.

This chapter presents the results of a DES simulation on one grid, which was a modified version of the medium density grid used previously. In addition to the simulation at the usual

Reynolds number of 200000, to compare with the other simulations and most of the experimental data, another simulation was performed at $Re = 100000$ to see if the variations in the velocity spectra in the wake as seen in the experiments could be reproduced. The majority of this chapter will concentrate on the results at $Re = 200000$ and unless otherwise stated all data is at this Re.

7.2 Details of the computational model

The model used is the Spalart-Allmaras RANS model with the modified length scale as proposed by Spalart et al. [73]. The modification of the code to incorporate a DES model has been described in Chapter 4. As well as the description of the model and its implementation, that chapter describes some of the validation studies that were carried out, primarily to check the performance of the model in RANS mode. No attempts were made to run a full DES simulation of any other geometry due to time constraints. The truncated cylinder flow was thus the first case to be run using the DES model.

The grid used was initially the same as for the LES runs, i.e. Grid 2 in Table 7.1. Initial runs on this grid gave diverging solutions: a problem which was thought to be due to some large cell expansion ratios. This problem was particularly evident above the cylinder. The outer mesh is extruded from the mesh around the cylinder and another inner mesh is generated on the top of the cylinder which is extruded vertically. The outer mesh is very fine close to the edge of the cylinder in order to resolve the boundary layer on the cylinder, but the inner mesh on the top does not need to be so refined near the edge so there is a mismatch between the grids. At the top of the cylinder the inner mesh can be stretched so that it matches the boundary layer cell size. In Grids 1-3 the inner mesh was extruded straight to the top of the domain meaning that the same stretching of the cells occurred all the way up while the outer mesh was expanded to be uniform at the top of the domain. This led to some very large ratios between adjacent cell sizes which appeared to be the root of the solution divergence. To resolve this the inner grid spacing at the top of the domain was also made uniform so that the cells expanded away from the top of the cylinder.

Attention was also paid to the uniformity of the mesh in the wake region. There is a similar problem to the one described above due to the small z spacing to resolve the boundary layer on the top of the cylinder. The positions of the edges defining the blocks were moved so that at 1 diameter away from the cylinder the grid was nearly uniform in z in the wake region.

As a result of some of these changes the number of cells in the mesh was increased as shown in Table 7.1. In addition the wall normal spacing on the cylinder side was actually increased to 0.002 from 0.0007.

Table 7.1: Details of grids

Grid No.	2	4
N_c	284	324
N_r	76	72
N_h	38	52
S_c	0.0111	0.0098
S_r	0.0007	0.002
S_h	0.002	0.002
Total cells	2,090,950	2,760,960

7.3 Results

7.3.1 Global flow parameters

The key parameters characterising the flow field for the two Reynolds numbers are listed in Table 7.2. The separation from the side of the cylinder occurs at 83 or 84 degrees which is similar to the LES results. This is also close to the 80 degrees at which the flow separates when the boundary layer is tripped. As the flow in the DES simulation is assumed to be turbulent everywhere it is this value with which the results should be compared.

The extent of the primary horseshoe vortex, defined by the separation point, X_{S2}, on the ground plane upstream of the cylinder, is at $x/d = -1.0$ which is further forward than the measured position. This could be due to it being in the "grey area" between the RANS and DES modes where it has been seen that the boundary layer resolution suffers. It could also be due to weaknesses in the underlying Spalart-Allmaras turbulence model. At the lower Reynolds number the separation point is further forward.

The length of the recirculation region in the wake is characterised by the attachment point on the ground downstream of the body. This is predicted to be $x/d = 2.1$ which is exactly the same as the LES and k-ε results. This point is slightly further downstream at the lower Reynolds number.

Figure 7.1 shows the pressure distribution around the cylinder at $z/d = 0.5$. The shape of the distribution is correct but the minimum pressure is higher than in the experiment. The base pressure coefficient is half the measured value.

Table 7.2: Details of DES runs

Re	100000	200000	200000
Grid	4	4	Exp.
CPU time / time step (secs)	80	80	
Side separation, ϕ_s (degrees)	83.0	84.0	70
Primary sep. from ground, X_{S1} (x/d)	-1.17	-1.11	-1.0
Secondary sep. from ground, X_{S2} (x/d)	-0.92	-0.98	-0.78
Attachment on free-end, X_{RT} (x/d)	0.47	0.41	0.17
Attachment on ground downstream, X_{RF} (x/d)	2.2	2.1	1.6
Local C_D at $z/d = 0.5$	0.71	0.68	0.79

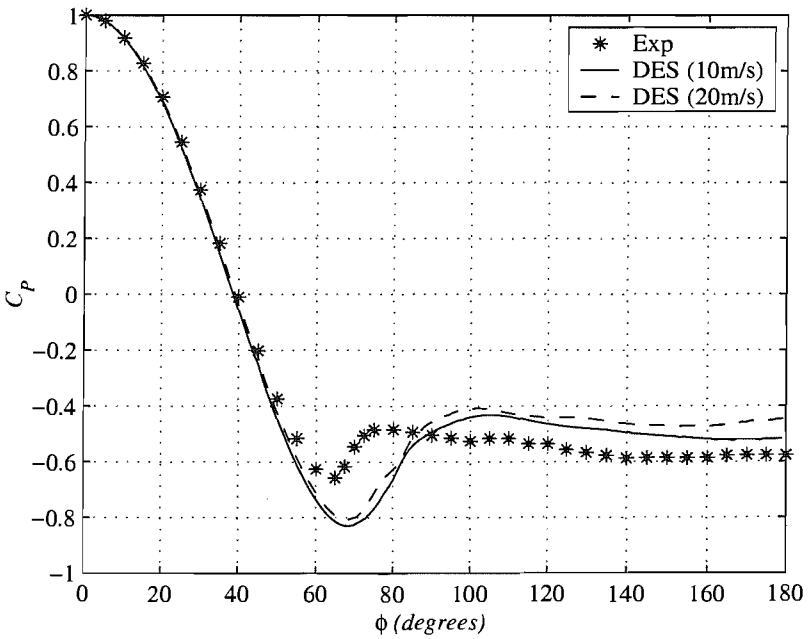

Figure 7.1: Plot of Cp around cylinder at $z/d = 0.5$

7.3.2 Horseshoe vortex

One of the motivations for trying the DES technique on this flow was that the LES was unable to resolve the boundary layer on the ground plane, which seemed to cause the horseshoe vortex to be incorrectly simulated. The DES method, acting as a RANS model on the boundary layer could be expected to perform as well as the k-ε model at capturing the shape of the primary horseshoe vortex.

In practice however, the DES simulation falls halfway between the LES and k-ε results. As shown by the primary separation position reported above the horseshoe vortex extends further forward than the one found in the experiment, but not as far as the LES one. In fact the simulations do show a two vortex system as is expected with the primary separation close to the experimental position. The main vortex however is too far upstream with $X_{S2} = -0.98$ compared to $X_{S2} = 0.78$. The streamlines on the $y/d = 0$ plane, in Figure 7.3, show that the vortex centre is further forward, and the stagnation point on the cylinder wall appears to be lower than in the PIV measurements. These results are an improvement over both the LES and the k-ε model in terms of the secondary vortices but not as good as the RANS at predicting the primary vortex size and shape. This may be due to the grey area between the RANS and LES modes of the DES model.

There is also uncertainty over the upstream boundary layer, due to the lack of experimental data with the model in position. Inaccuracies in the approaching boundary layer would affect the formation of the horseshoe vortex. Additional experimental data is therefore needed to be sure about the behaviour of the simulations in this area.

The surface flow patterns in Figure 7.2 clearly show the separation line at the leading edge of the horseshoe vortex. The flow pattern as the vortex trails downstream shows similar features to the experimental image in terms of the flow directions under the vortex. The differences are caused by the excessive length of the vortex. The separation line on the inside of the horseshoe vortex, marking the edge of the shear layer, diverges at an angle of 17.3 degrees compared to 15.5 degrees in the experimental flow.

7.3.3 Flow over the free end

The two main aspects which characterise the flow above the free-end of the cylinder are the vertical and streamwise extents of the recirculation bubble and the swirl patterns on the surface of the tip. It has been seen in the preceding chapters that the RANS model completely fails to resolve the detail of the swirls on the tip while the LES reproduces these patterns very well. This suggests that the simple no-slip boundary condition with no turbulence model is the best for this swirling boundary layer flow. It might be expected that the DES with its RANS component will damp out some of this motion. The extents of the recirculation bubble on the

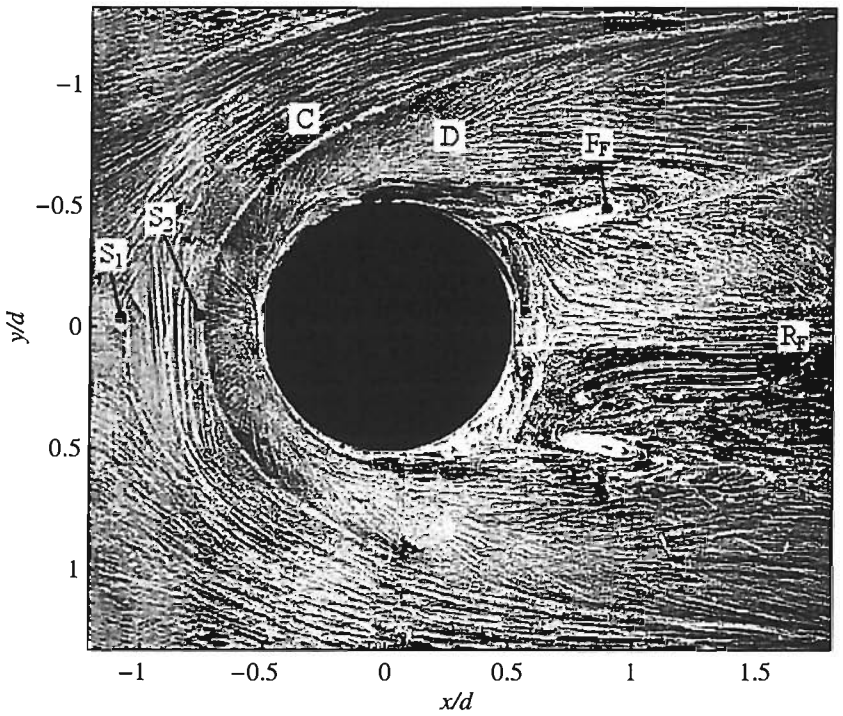

(a)

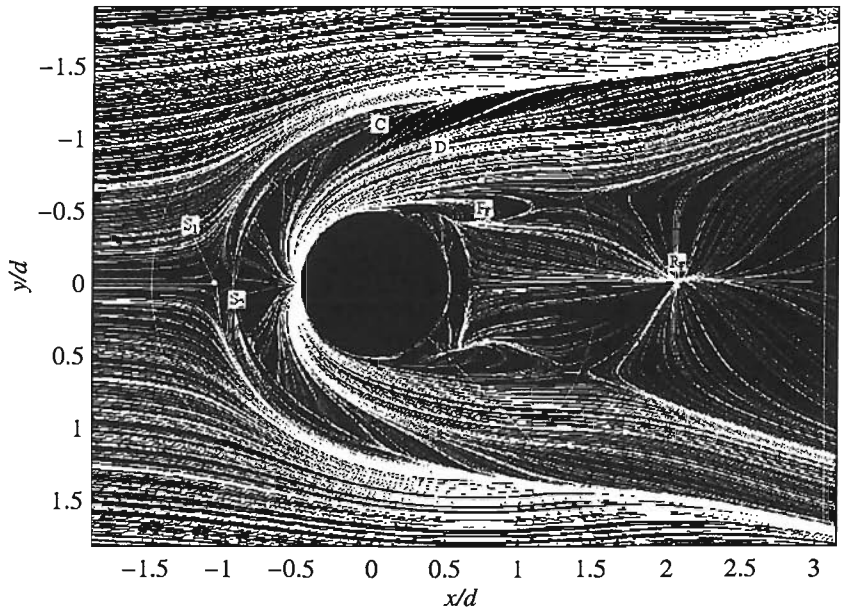

(b)

Figure 7.2: Surface flow visualisation on the ground plane (a) experimental, (b) DES (flow from left to right)

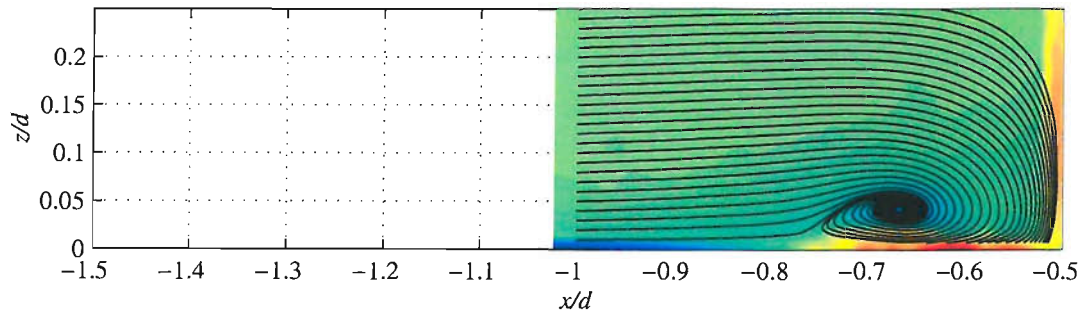

(a) Experimental

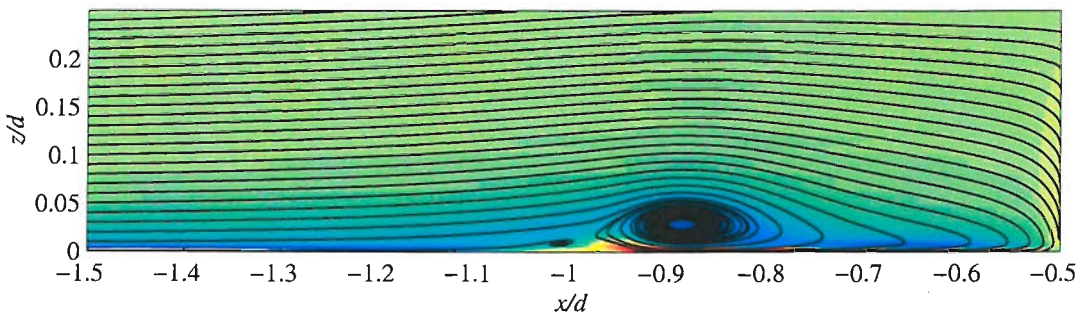

(b) DES

Figure 7.3: Velocity vectors and vorticity contours on centreline ($y/d = 0$) upstream of cylinder

centreplane are overpredicted by all models so far.

Looking at the surface flow patterns on the free-end, shown in Figure 7.4, as expected the swirl patterns are not completely captured, although the direction of the streamlines is correct. It is just the wrapping up of the vortex eye which is not resolved. The prediction of this flow feature is likely to depend strongly on the ability of the model to predict the boundary layer flow on the top surface of the cylinder. Due to the low speeds and strong pressure gradients in this region the nature of this boundary layer may be difficult to predict using RANS type models.

The flow pattern in the $y/d = 0$ plane (Figure 7.5) shows that the vortex extends too high above the cylinder in the same way as the previous simulations. Attachment occurs at $x/d = 0.41$ which is further back than the experiment. Figure 7.6 which plots U against z/d at $x/d = 0$ confirms that the peak velocity occurs 60% higher than in the experiment. The flow near the surface is faster with a thinner boundary layer. This is where the LES on Grid 2 performed well suggesting that the boundary layer prediction with the RANS model is incorrect for this area of the flow.

7.3.4 Wake region

With the separation point, at 84 degrees, and the attachment point on the ground downstream, at $x/d = 2.1$, being very close to the LES results on Grid 2, as reported in the previous chapter, one would expect the structure of the wake to be very similar to the LES. Looking first at the U velocity component in the streamwise direction in Figure 7.7 the numerical results can be seen to be much closer to the experimental values than the previous simulations, especially in the upper half of the wake. At the bottom, at $z/d = 0.25$, the length of the reversed flow is too long, corresponding to the later attachment on the ground.

Figures 7.8 to 7.10 show profiles of velocity components and Reynolds stresses with respect to z/d at various locations in the x/d direction. The profiles of U velocity are quite close to the experimental values except in the shear layer near the cylinder where the peak rise to the free-stream velocity is slower. The later attachment means that the flow near the ground is reversed for longer and is also stronger due to the flatter vortex. The W profiles follow the shape of the experimental curves but the maximum downwash is less due to the shallower angle of the shear layer. The agreement in the lower half of the profiles is quite good. Looking at the turbulent kinetic energy, it is of the right magnitude in the near wake except in the shear layer where it is overpredicted. This is similar to the LES results. Moving downstream the agreement becomes better.

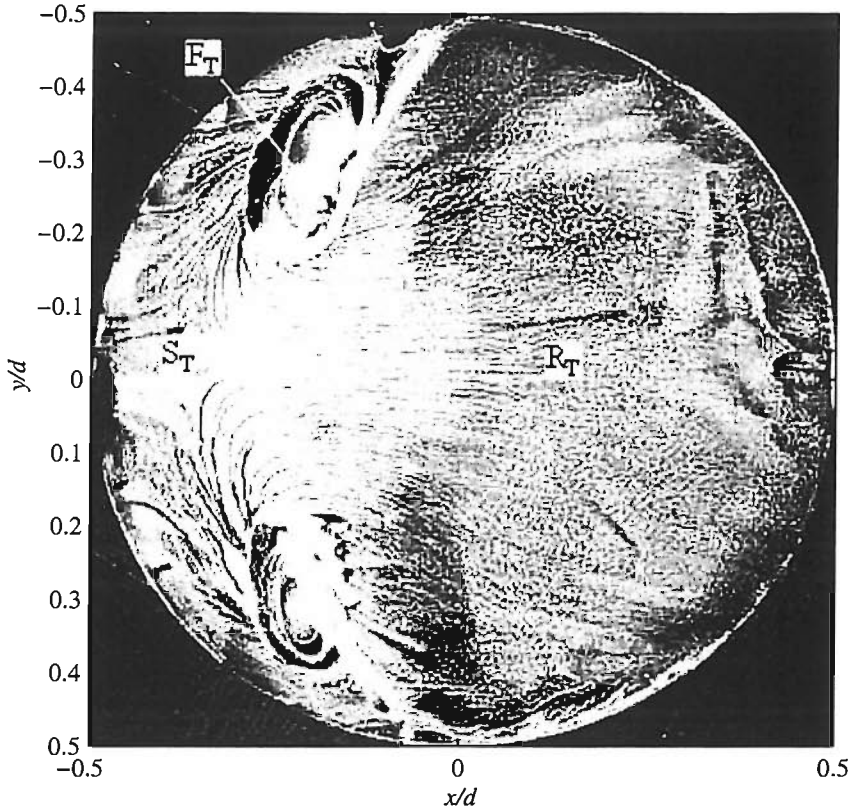

(a)

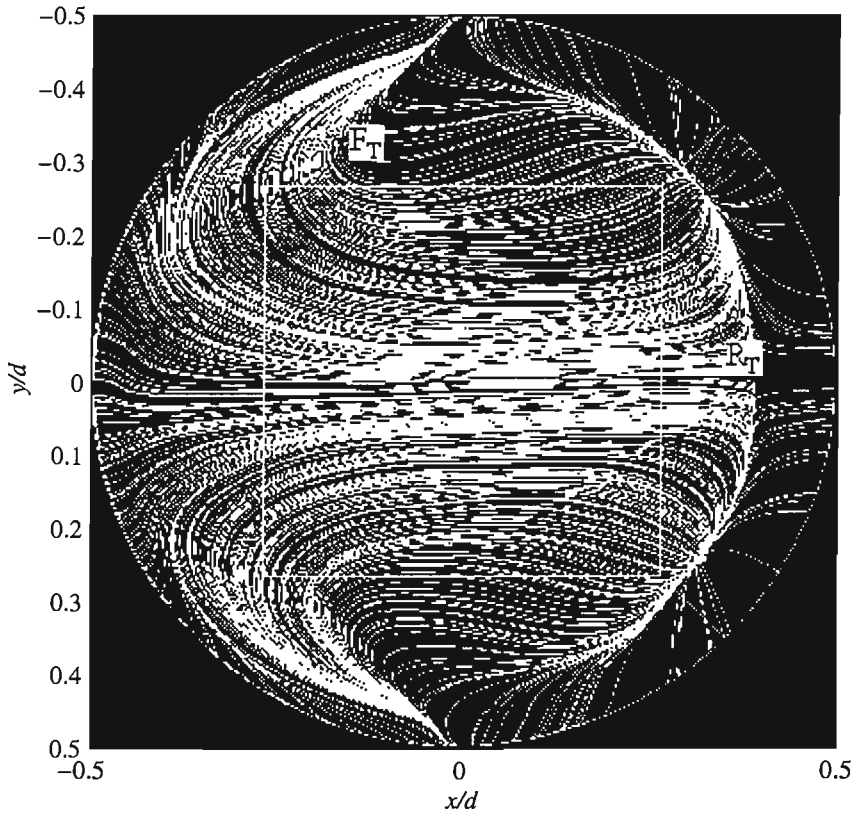

(b)

Figure 7.4: Surface flow visualisation on the free-end of the cylinder (a) experimental, (b) DES (flow from left to right)

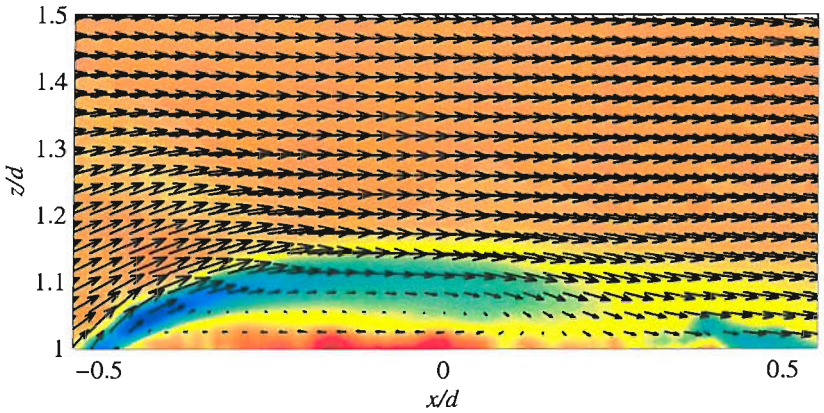

(a) Experiment (PIV)

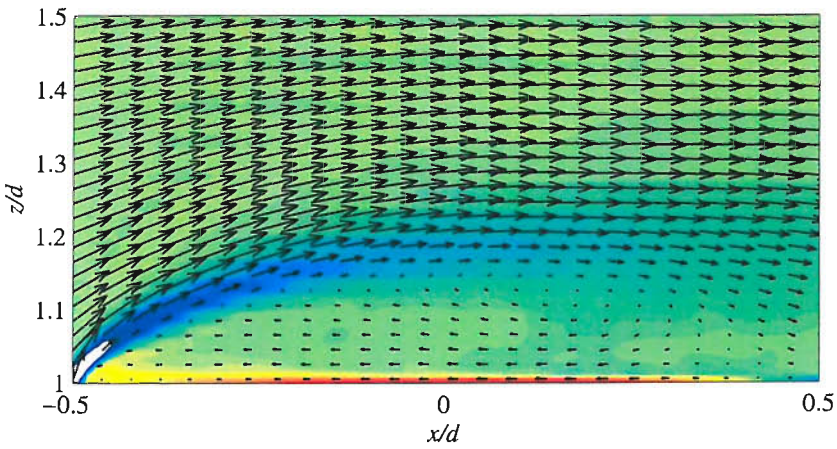

(b) DES

Figure 7.5: Velocity vectors and vorticity contours on centreline ($y/d = 0$) on top cylinder

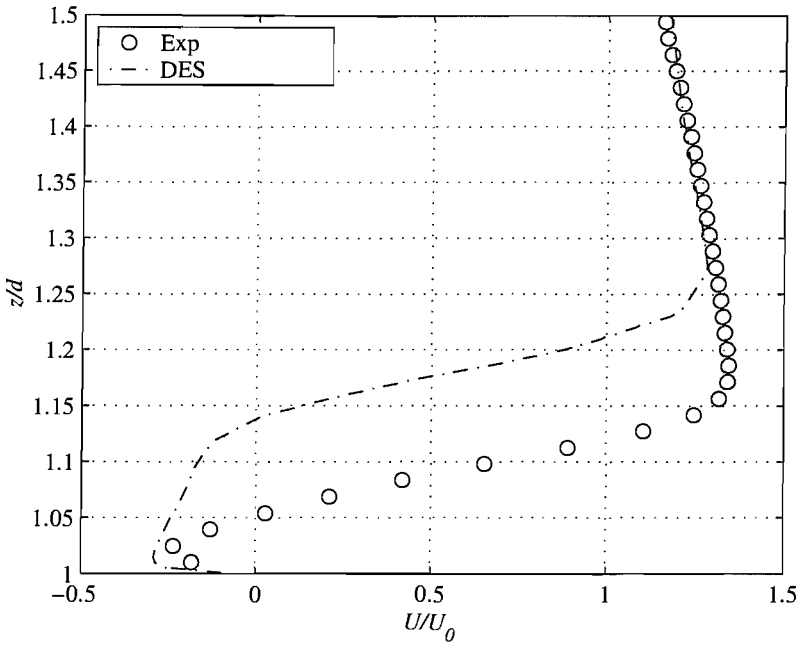

Figure 7.6: Plot of U velocity against z/d at $x/d = 0$

The Reynolds stresses show similar errors to the LES ones. In particular $\overline{u'u'}$ is overpredicted in the shear layer close to the cylinder, as is $\overline{w'w'}$. $\overline{v'v'}$ is underpredicted almost everywhere, until after attachment. The difference in the vertical location of the shear layer is evident from the profiles of $\overline{u'u'}$, which show the peak in the experimental values about $0.2d$ lower in the experiment than in the numerical results at $x/d = 0.83$ and $x/d = 1.0$. The $\overline{u'w'}$ shear stress agrees quite well with the experimental data with the peaks in the shear layer being very close. The $\overline{v'w'}$ term is much smaller (by about 10 times) and is perhaps not measured very accurately by the PIV. The smallness of this term is because there is little correlation between the v fluctuations which are caused by spanwise vortices, formed in the side shear layers, and the w fluctuations which are created by fluctuations in the shear layer over the top. The power spectral density function of the DES velocity output (Figure 7.12) shows no strong peak. There is a very broad peak between $0.1 < Str < 0.2$. Although a simulation was run at $10m/s$ to try to see the same effect as was seen in the hot-wire measurements, neither of the DES runs produced any discernible peak so the spectrum is not presented.

The vector plots in Figure 7.11 show reasonable agreement particularly downstream where the large streamwise vortices have formed. The tip vortices off the free-end are captured. In the same way as the previous simulations, the differences can be attributed to the longer recirculation region.

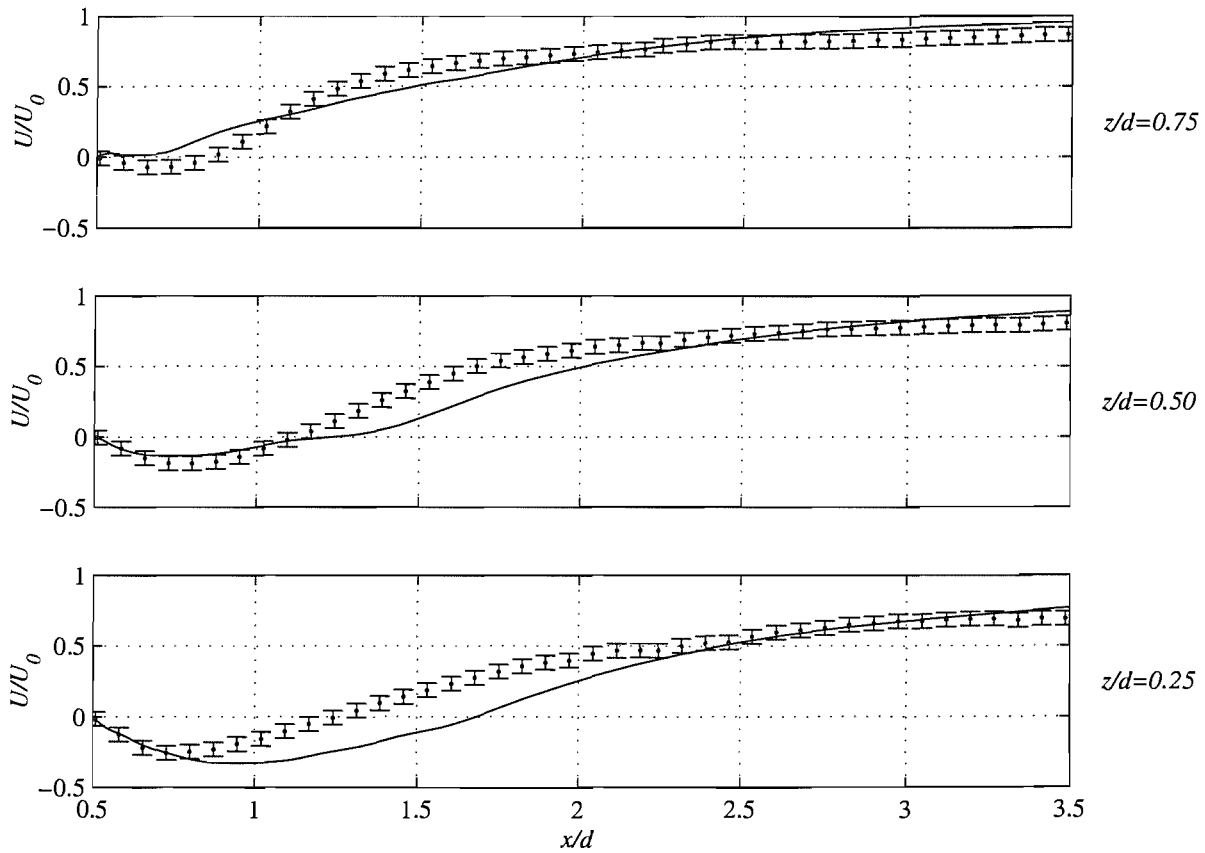

Figure 7.7: Comparison of U-velocity distribution along centreline in wake

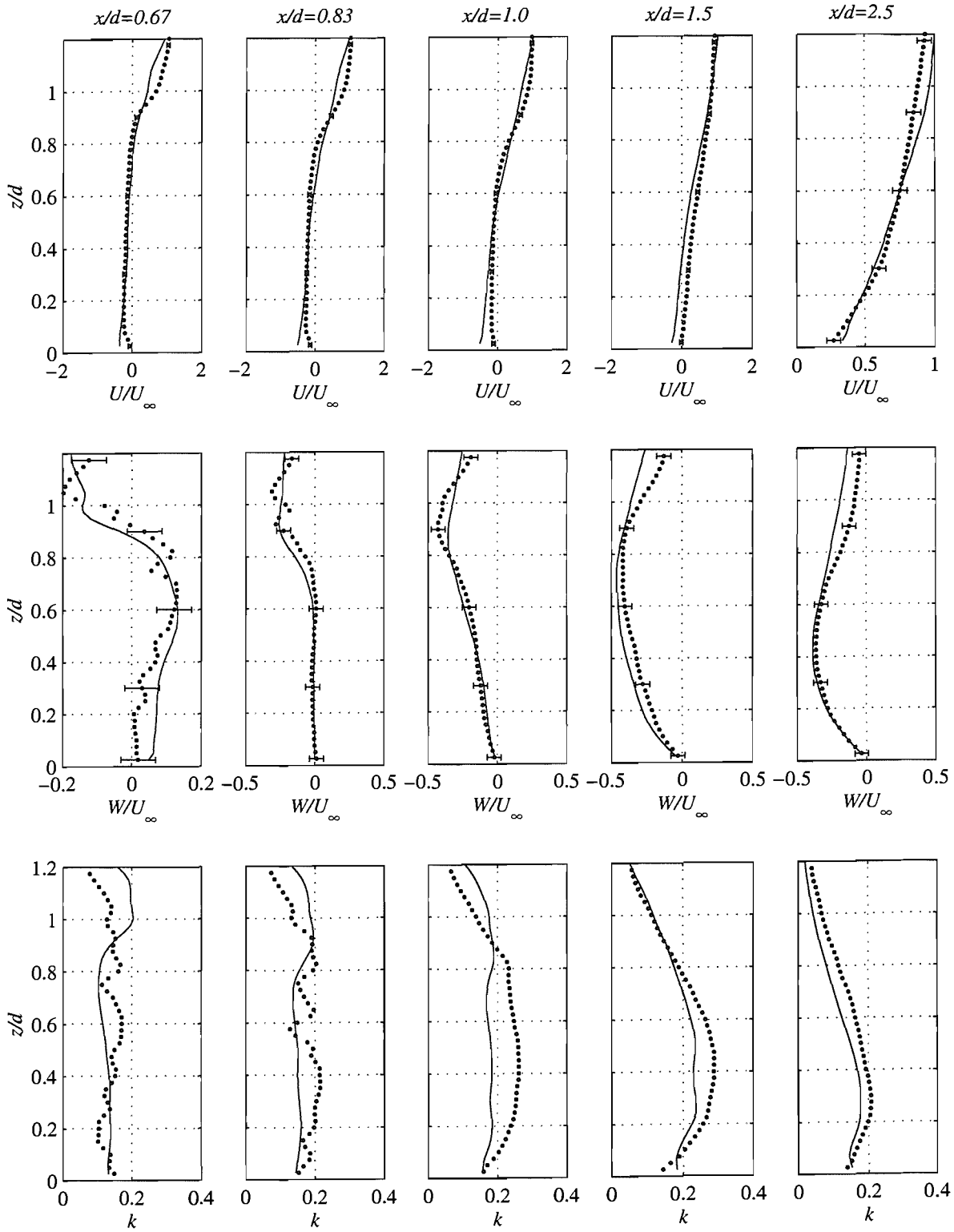

Figure 7.8: DES profiles of velocity and turbulent kinetic energy at $y/d = 0$ in wake region. + PIV measurements, - simulations

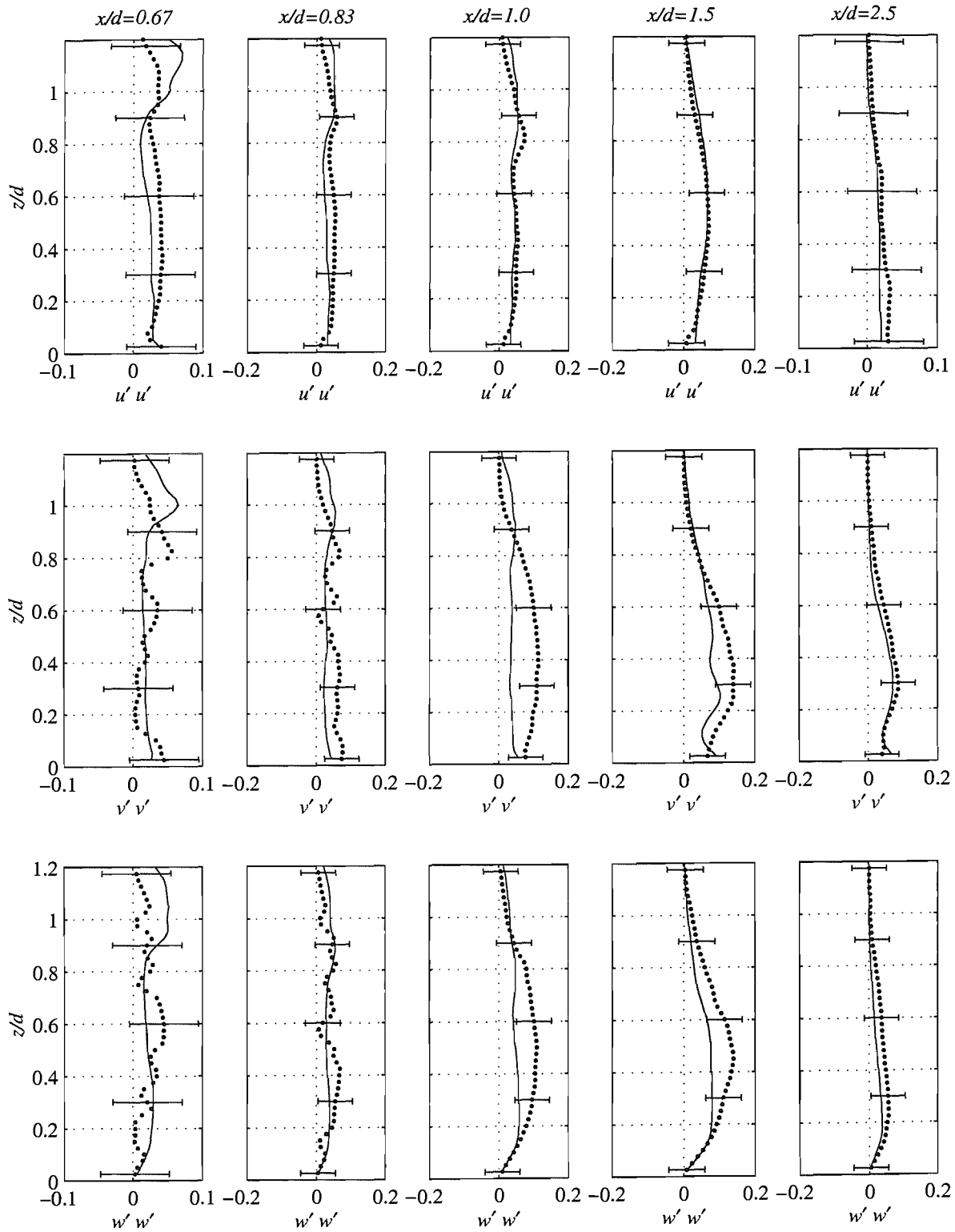

Figure 7.9: DES profiles of normal stresses at $y/d = 0$ in wake region. + PIV measurements, - simulations

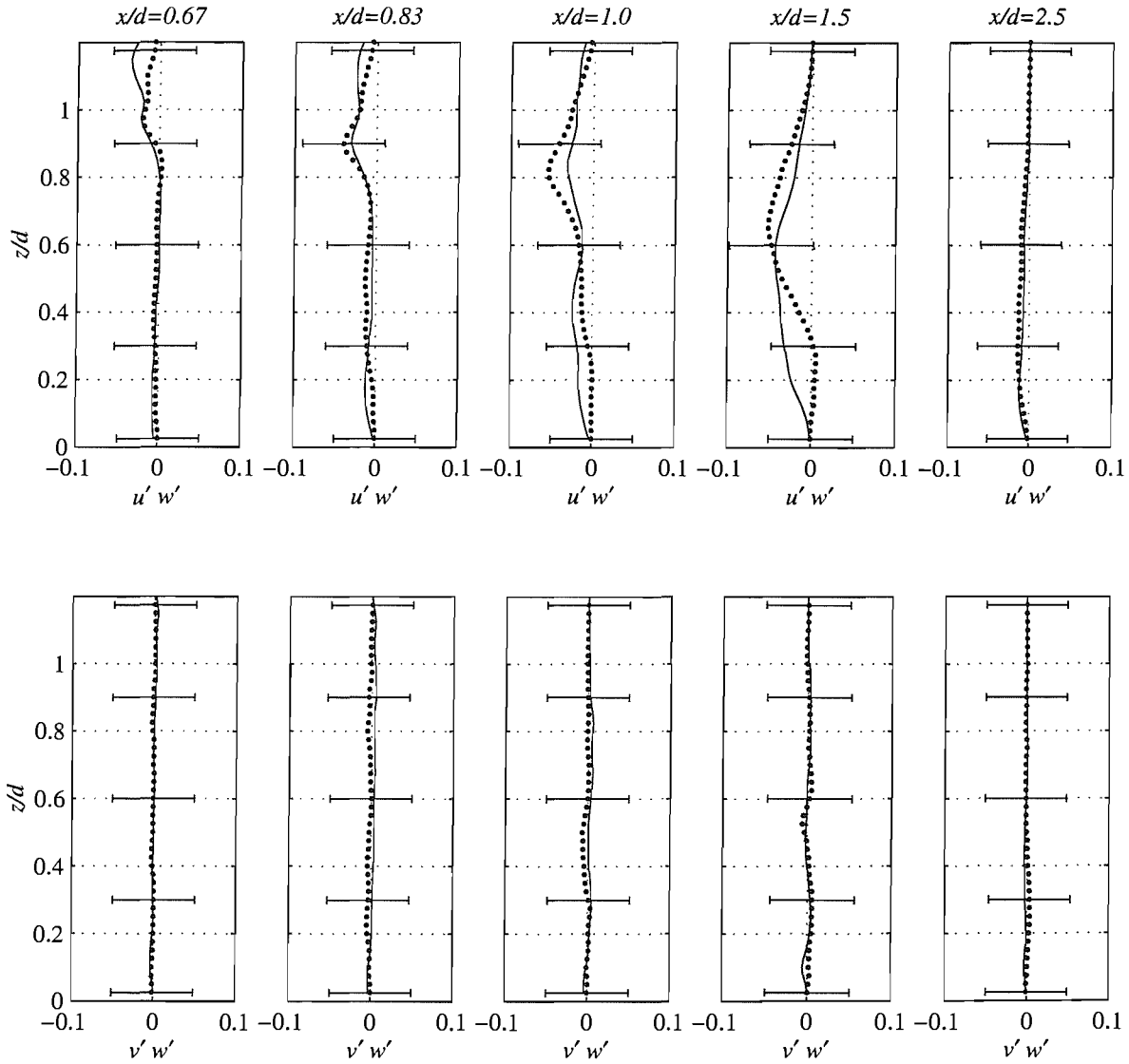

Figure 7.10: DES profiles of shear stresses at $y/d = 0$ in wake region. + PIV measurements, - simulations

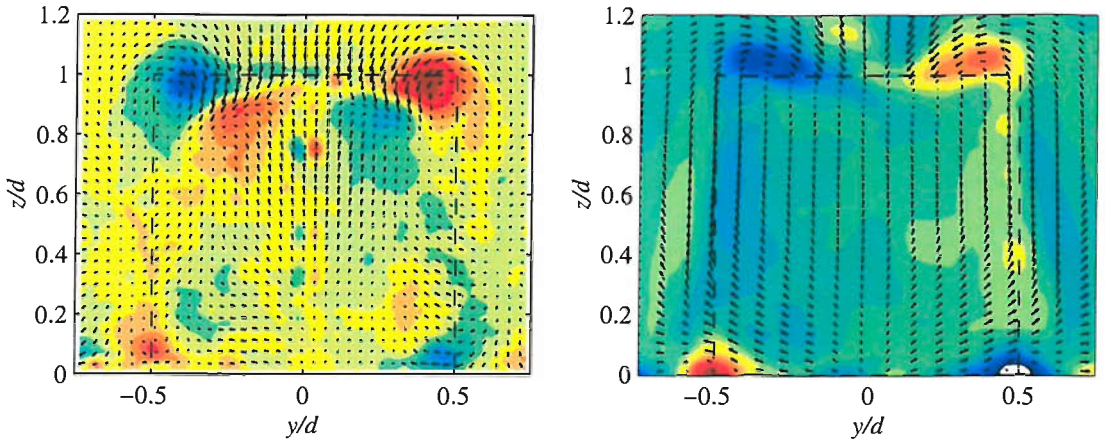

(a) $x/d = 0.67$ (PIV)

(b) $x/d = 0.67$ (DES)

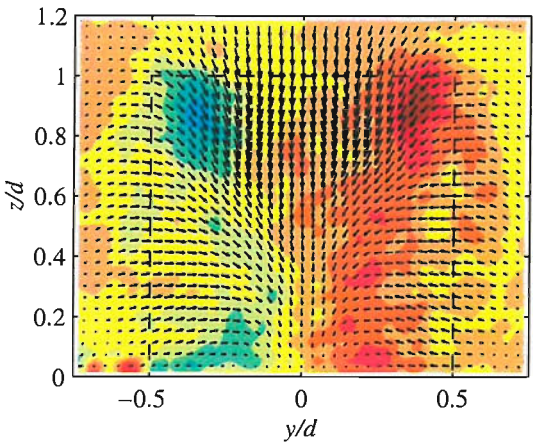

(c) $x/d = 1.0$ (PIV)

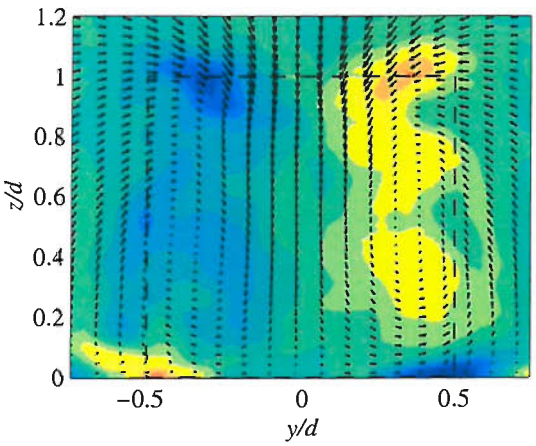

(d) $x/d = 1.0$ (DES)

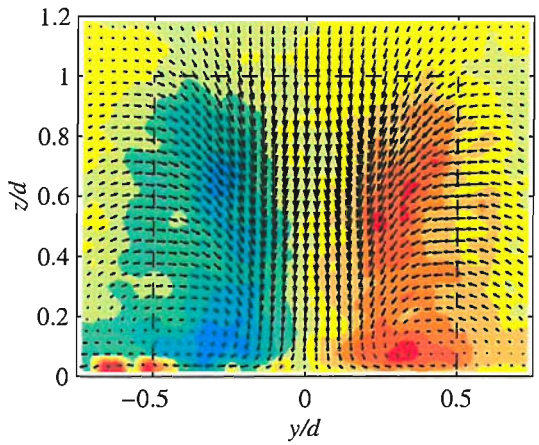

(e) $x/d = 1.5$ (PIV)

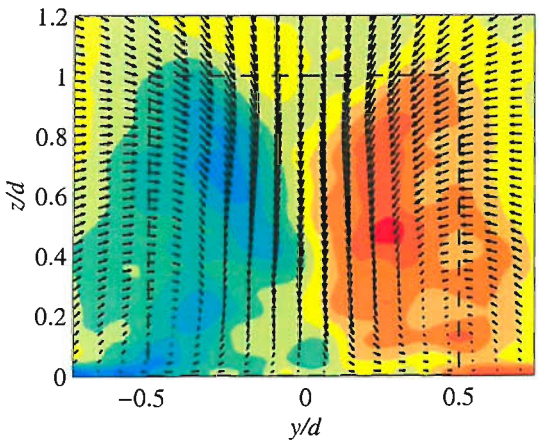

(f) $x/d = 1.5$ (DES)

Figure 7.11: Velocity vectors and vorticity contours from DES and PIV results

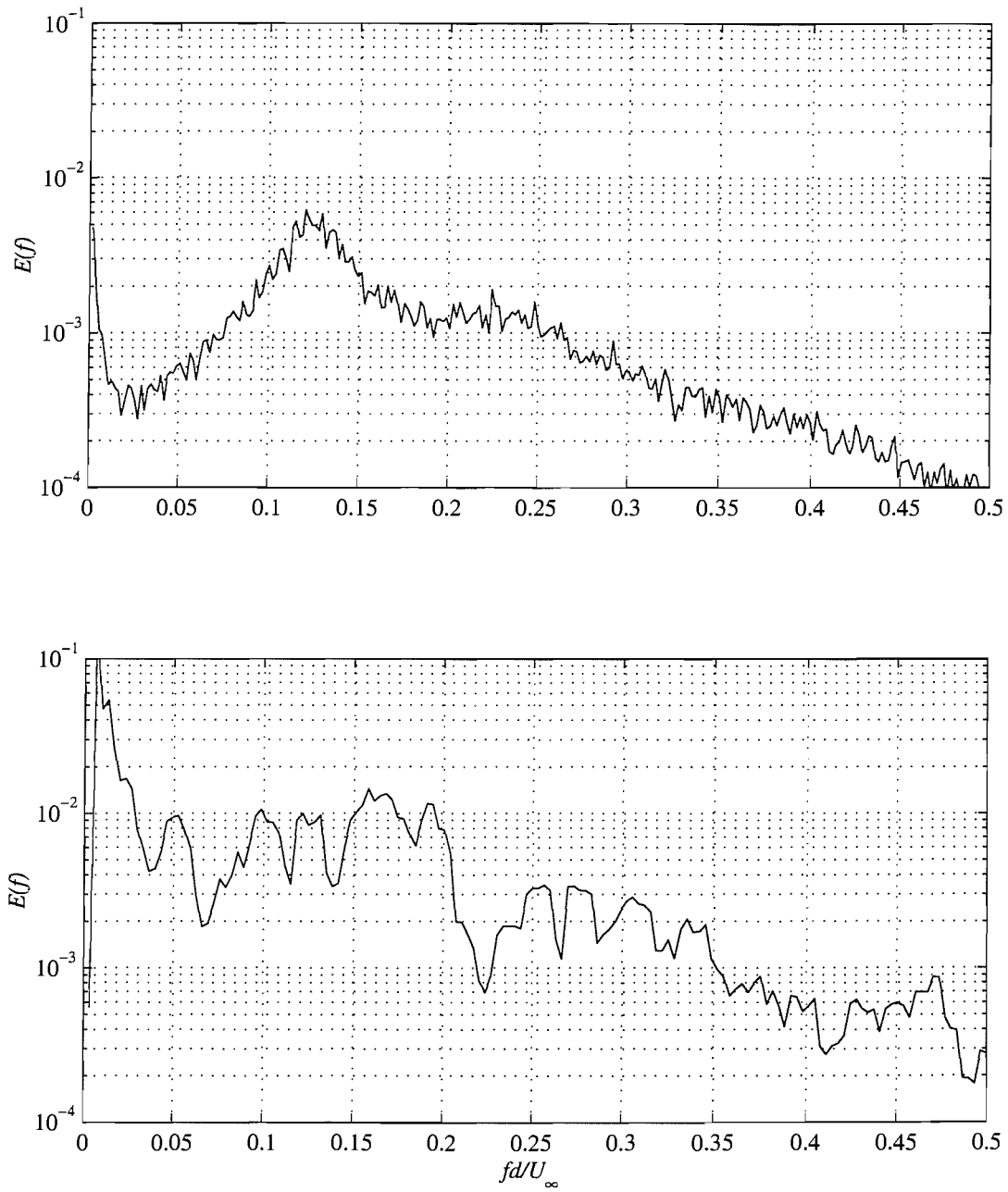

Figure 7.12: Power spectral density function of U-velocity from DES and experimental results at $x/d = 1.5$, $y/d = 1$, $z/d = 1$

7.4 Conclusions

Simulations of the truncated cylinder flow have been performed using the Detached Eddy Simulation method. This was hoped to give improved performance in the region of the ground plane where the LES was unable to resolve the boundary layer, while retaining the benefits of the LES in the separation region. In practice it was only slightly better than the LES at predicting the horseshoe vortex but it did match the LES in the separation region. The following summarises the main results.

1. The quality of the mesh was found to be very important to even get the code to run and so a lot of time was spent trying to improve it. In particular attention has to be paid to the cell expansion ratio which should not exceed 1.2.

2. While the boundary layer upstream was modelled correctly the primary separation from the ground was 22% too far upstream while the secondary separation was 71% too far upstream, resulting in the horseshoe vortex being stretched. This could be due to the switch from RANS to DES mode in the vicinity of the cylinder due to the refined grid. It has been shown that this area poses a problem as the turbulent viscosity due to the RANS/SGS model dies away before the turbulent fluctuations start to develop. Despite this problem the horseshoe vortex is still better than the LES model.

3. On the surface of the free-end the RANS modelling in the boundary layer causes a loss of detail of the swirl patterns in that region, although the general pattern is still visible. The recirculation bubble is again too large with attachment 36% too far back on the top of the cylinder.

4. The regions of separated flow, where the DES is functioning as an LES subgrid model, are very close to the LES results. In the wake region the DES appears to give better agreement with the velocity profiles, which could be due to the improved grid used for these computations. The Reynolds stresses though are perhaps slightly worse than the LES ones.

The similarities between the DES and LES in regions where the DES is operating in its LES mode are understandable as in both cases the grids seem to be fine enough to allow the resolution of most of the energy containing scales, so that the details of the subgrid scale model are not too important.

Chapter 8

Discussion and further analysis of results

8.1 Introduction

The preceding chapters have presented the results of experiments and numerical simulations of the flow over a truncated cylinder in a wind tunnel. The flow has been found to contain a number of complex three-dimensional flow features which are turbulent in nature. There are certain areas of the flow, particularly the free-end and the wake region where the flow physics is less well understood. Using a synthesis of the experimental data with the LES/DES results which contain details of the entire flow field it should be possible to gain understanding of the flow phenomena. This chapter will begin by addressing this challenge with an attempt to describe the flow physics of the horseshoe vortex system, the flow above the free-end and the flow in the wake region. It will then go on to discuss the strengths and weaknesses of the numerical models used in this work with reference to the characteristics of the flow. Finally the relevance of this work to the simulation of flows around ships will discussed.

As presented in Chapter 2 there have been a few other experiments on the configuration studied here. It is useful to compare the results obtained in the course of this work with some of the previous data, and while this has been done throughout the presentation of the results a summary is given here for clarity. This will highlight where the present work contributes to increased understanding of the flow.

The physical flow structures which occur in this flow are particularly complex and as such are difficult to fully appreciate using traditional experimental techniques and even RANS based numerical methods. This is partly due to the strong three-dimensionality of the flow which means that simple lines or planes of data do not necessarily give a true representation of the flow, but also due to the highly unsteady, turbulent nature of the flow. The mean flow pattern which is given by many experimental and computational techniques bears little relation to the actual flow at any instant. It is therefore revealing to look at the instantaneous flow structures

which can be seen with LES/DES simulations or PIV experiments.

The simulations presented above have been shown to be accurate in certain areas and do appear to contain most of the features of the real flow even if certain parameters do not match the experiments. It is therefore possible to use these results to obtain further insight into the flow physics of this configuration, in conjunction with the experimental data. Attention will be focussed on the horseshoe vortex system, the flow over the free-end and on the vortex shedding in the wake region as these are the least understood and the most difficult to investigate experimentally.

8.2 Further analysis of the flow physics

8.2.1 The horseshoe vortex system

The upstream flow and the horseshoe vortex are the areas for which the most literature is available, although these features have rarely been reported in conjunction with a low-aspect ratio cylinder. In fact providing the boundary layer thickness is much less than the cylinder height the horseshoe vortex should depend only on the diameter and upstream boundary layer characteristics. Most of the experiments on finite-height cylinders have had $\delta/d \approx 0.1$ as in this work, although some have been carried out with the cylinder completely immersed in the boundary layer [12]. None of these has reported details of the size and position of the horseshoe vortex although some appear to have done visualisations which should give this information.

The flow visualisation (Figure 3.4) corresponds to the topology proposed by Baker [27] for turbulent horseshoe vortices (Figure 2.2). This consists of a primary separation (S_1) of the oncoming boundary layer, at a distance X_{S1} from the centre of the cylinder. This is followed by a vortex (2) which terminates at the attachment line (A_1), at X_{A1} from the cylinder. Downstream of this point is a small reversed vortex (1') originating from the separation point S_2, at a distance X_{S2} from the cylinder centre. The line of accumulated pigment on the floor encircling the cylinder lies underneath vortex 1' and is created by the high shear in this region. The attachment and separation points are assumed to be at the up- and downstream edges of this band. Above this vortex is the primary vortex (1) which extends to the cylinder wall. There is a saddle point between these three vortices. Very close to the cylinder is another reversed vortex where the flow down the front of the cylinder separates.

The review of Ballio et al. [28] presents details of characteristics of laminar and turbulent horseshoe vortices around various obstacles. The position of the primary separation, X_{S1}, is shown to be independent of δ^*/d provided that $h/d \geq 1$. For $Re_{\delta^*} = 2600$ as we have here, $X_{S1} \approx 1.1$ ([27]). This is in agreement with the position measured from the surface flow visualisation. Similarly the longitudinal position of the centre of the vortex is given as being constant

in the range of $x/d = -0.65 \rightarrow -0.75$ according to Kubo and Takezawa [89]. The PIV results show the centre of the vortex at $x/d = -0.68$. The horseshoe vortex measured here is therefore consistent with the established data.

The number of vortices and separation lines present in the simulations, PIV measurements and flow visualisation is not always consistent. The surface flow visualisation shows a primary separation followed by an inner line marking a reattachment, according to the model of Baker [27]. This corresponds to a four-vortex system. In the PIV measurements however, only one large vortex is apparent. On closer inspection however it can be seen that the flow near the ground at the attachment point is in fact pointing towards the floor indicating the presence of vortices 1' and 2, although they are very thin (less than $0.01d$ in the z-dimension). It appears that other researchers have not seen these vortices in their measurements of velocity vectors in the symmetry plane.

Devenport and Simpson [29] presented LDA data on the symmetry plane upstream of a wing which give measurements to within $0.003d$ of the wall of the velocity. They suggest that the line of accumulated pigment is caused by the region of high shear under the primary vortex, and that there is no reseparation of the flow in front of the vortex. Instead they claim that a thin region of reversed flow is maintained all the way to the primary separation point. It is impossible to see clearly in their vector plot what the velocities are very close to the wall. The only other authors to have presented such a vector plot to the author's knowledge are Pierce and Tree [30] whose first measurement is at $z/d = 0.02$ and therefore would be above the two additional vortices. The reported separation point according to the LDA data is at $x/d = 0.9$ while the primary separation in the flow visualisation is at $x/d = -0.97$.

In the present simulations the k-ε model predicts the primary vortex in the right place with a single separation at $X_{S2} = -0.79$ and the vortex centre at $x/d = -0.65$, $z/d = 0.03$. In the surface flow patterns derived from this data there is no other line corresponding to the line of accumulated pigment. The LES does predict a four-vortex system although in this case the upstream vortex is quite large and the primary separation and reattachment are two far upstream. The surface flow pattern does have the saddle point at the primary separation and another line similar to the line of accumulated pigment. This line actually occurs at the reattachment point. The similarity of this pattern to the observed flow implies that the four-vortex topology is correct and that there is a thin vortex upstream of the primary one along with a vortex of opposite sign underneath the primary vortex as shown in Figure 8.1. The DES simulations are similar to the LES in that there are four-vortices although the proportions are different. The primary separation is closer to the experimental position while the primary vortex is too far upstream. There is still a thin vortex upstream of the reattachment point and a small recirculation beneath the primary vortex.

To summarise, the present investigation suggests that the flow on the upstream side of the

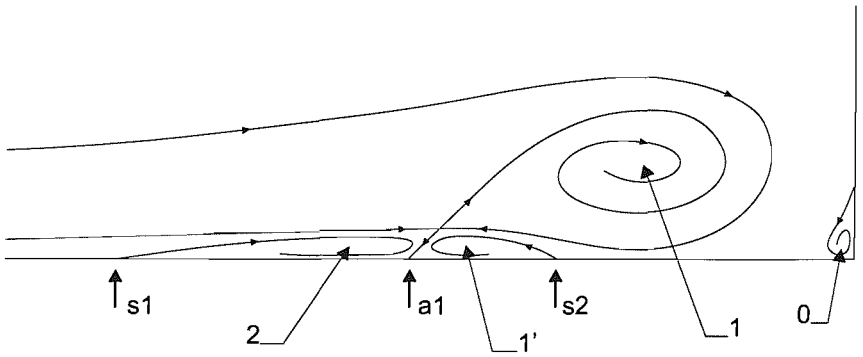

Figure 8.1: Topology of turbulent horseshoe vortex inferred from current work

cylinder consists of a four-vortex structure as proposed by Baker [27]. However, the upstream vortex (2) and the recirculation (1') are too thin to be resolved experimentally although the PIV measurements do show a tendency for the flow to turn towards the floor at the reattachment point. The LES and DES simulations support this hypothesis by producing surface flow patterns which are topologically the same as that observed in the experiment. It would be interesting to perform further computations of the flow in this region using a better RANS model, such as the k-ω model, which can resolve the flow very close to the wall given a fine enough mesh.

8.2.2 The free-end flow

So far in this work, the flow over the free-end has been seen in terms of the surface flow on the cylinder top and the velocities in the symmetry plane, $y/d = 0$. This is a rather simplified view of what is really a complex three-dimensional flow structure. In this section an attempt will be made to describe the structure of the flow in this region using both the experimental results and the numerical simulations. The mean flow will also be compared to the instantaneous flow pattern which will be seen to be very different.

The precise structure of the flow on the free-end of the cylinder appears to be a source of some debate with the two papers published on this topic presenting different interpretations of the flow physics. The first to attempt to describe the nature of this flow were Kawamura et al. [12] who used oil-flow visualisation on the free-end along with smoke visualisation of the flow in the symmetry plane to study the structure of the recirculation. They observed that the flow which separates from the leading edge reattaches to the free-end in the downstream half of the cylinder, depending on the aspect ratio. At $h/d = 1$ reattachment occurs at $x/d =$

$0.6 \rightarrow 0.7$. The form of the swirl patterns on the surface seems to become more rounded as the reattachment moves back and the recirculation bubble becomes larger, suggesting a relationship between the size of the recirculation vortex and the swirl patterns. They compare the flow pattern to the "mushroom" vortex described by Winkelman et al. [33] on a stalled aerofoil. This consists of the recirculation vortex in the centre of the foil attaching to the surface of the foil near the ends to create swirl patterns. In the context of the cylinder, the two swirl patterns on the surface are connected by a vortex passing through the symmetry plane.

This flow topology is questioned by a recent paper by Roh and Park [21] which presents visualisations of the flow on top of a cylinder of $h/d = 1.25$. They used both oil-flow visualisation on the free-end surface and smoke illuminated by a laser light sheet in various transverse planes on the top of the cylinder. The surface patterns are the same as those of Kawamura et al. and of the present study, consisting of two swirl patterns which they describe as the eyes of an owl's face. The smoke visualisation appears to show four streamwise vortex cores, seen as concentrations of smoke, along the free-end. The inner two of these appear to start near the swirl patterns on the free-end and progress downstream until they reach the trailing edge, where they descend to the surface and dissipate. They are still visible in the plane just downstream of the trailing edge though. The outer vortices are the tip vortices produced at the side edge of the cylinder by the upwash separating from the side. Based on this visualisation they propose that the eyes on the surface are the bases of streamwise trailing vortices which continue downstream, as shown in Figure 2.3. This is in contrast to the mushroom vortex of Kawamura et al..

Using the data from the experiments and simulations carried out for the current work the flow topology on the free-end can be investigated to determine which of the two proposals is correct. From the PIV measurements there are immediately two concerns with Roh and Park's hypothesis. Firstly the flow on the symmetry plane (Figure 3.15) does not match the streamlines that they have drawn for this plane as the flow reattaches at the saddle point on the symmetry plane at the rear. They have shown the flow separating at this point with no reattachment at all on the free-end, contrary to what they say elsewhere. Looking at the transverse plane the PIV results in Figure 3.16 show the two tip vortices but no inner streamwise vortex. No transverse PIV measurements were made on top of the cylinder as Roh and Park's paper had not been published when these measurements were made so further comparison with the experiments is not possible.

While the experimental data is limited in this region the numerical simulations should be able to provide valuable insight into the flow structure. It has been seen that both the LES and DES simulations capture the swirl patterns well, although the recirculation in the symmetry plane is too large, so the flow structure can be expected to be topologically correct. The best way to test where the vortices rising from the swirl patterns go to is to calculate the paths of

particles within this vortex. This was achieved using the Fieldview visualisation software which allows the user to place particles on a plane and then integrates through the flow-field, using a Runge-Kutta method, to obtain the paths which they would follow [87]. The result is shown in Figure 8.2 which shows the surface streamlines on the top of the cylinder with the vectors in the symmetry plane. The particles were placed on the streamlines leading into the swirl pattern and can be seen rising from the swirl pattern in a spiral motion and bending round towards the symmetry plane. On reaching the symmetry plane they are ejected into the shear layer in which they are convected downstream. The recirculation in the centreline is effectively mapped onto the surface of the cylinder through rotation and stretching. This view therefore supports the mushroom vortex hypothesis of Kawamura et al. rather than the streamwise vortices of Roh and Park.

This topology only occurs in the mean flow however, the instantaneous flow being much more chaotic. This is illustrated in Figure 8.3(a), which shows a vector plot on the symmetry plane at an instant of time, and in Figure 8.3(b), which shows three-dimensional isosurfaces of pressure on the top of the cylinder. It can be seen that the regions of low pressure correspond to the centres of the vortices seen in the vector plot. Within the recirculation region there are in fact three large scale structures at this instant. These appear to be instabilities in the shear layer which are growing as they are convected downstream from the leading edge. It is noticeable that the bases of the isosurface representations of the vortices are formed in the vicinity of the swirl patterns on the free-end.

8.2.3 The wake region

The recirculation region downstream of the cylinder has been said to consist of an "arch" vortex [16]. This connects the rolled up shear layers at the sides and the top. Due to the two sides being linked, the vortex shedding is symmetric rather than the antisymmetric von-Karman shedding seen behind a two-dimensional cylinder. In fact the vortex shedding is very weak with no dominant peak in the frequency spectrum as seen in Figures 3.21 to 3.24. This suggests that the flow is more chaotic, or turbulent, than the regular shedding from a two-dimensional cylinder. In this section the features of the mean flow will be discussed. The instantaneous flow will also be studied in an attempt to understand some of the physics of the turbulent wake.

In the time-averaged flow, the topology is that of an arch vortex sitting just downstream of the cylinder. The flow along the symmetry plane is characterised by the recirculation along the floor from the reattachment point to the back of the cylinder. This backflow rises up the back of the cylinder. Some of this fluid is swept out towards the sides of the cylinder where it either joins the tip vortex or rolls up to form a corner vortex at the base just behind the separation line. The shear layers roll up after separation to form the arch vortex. The base of this can be

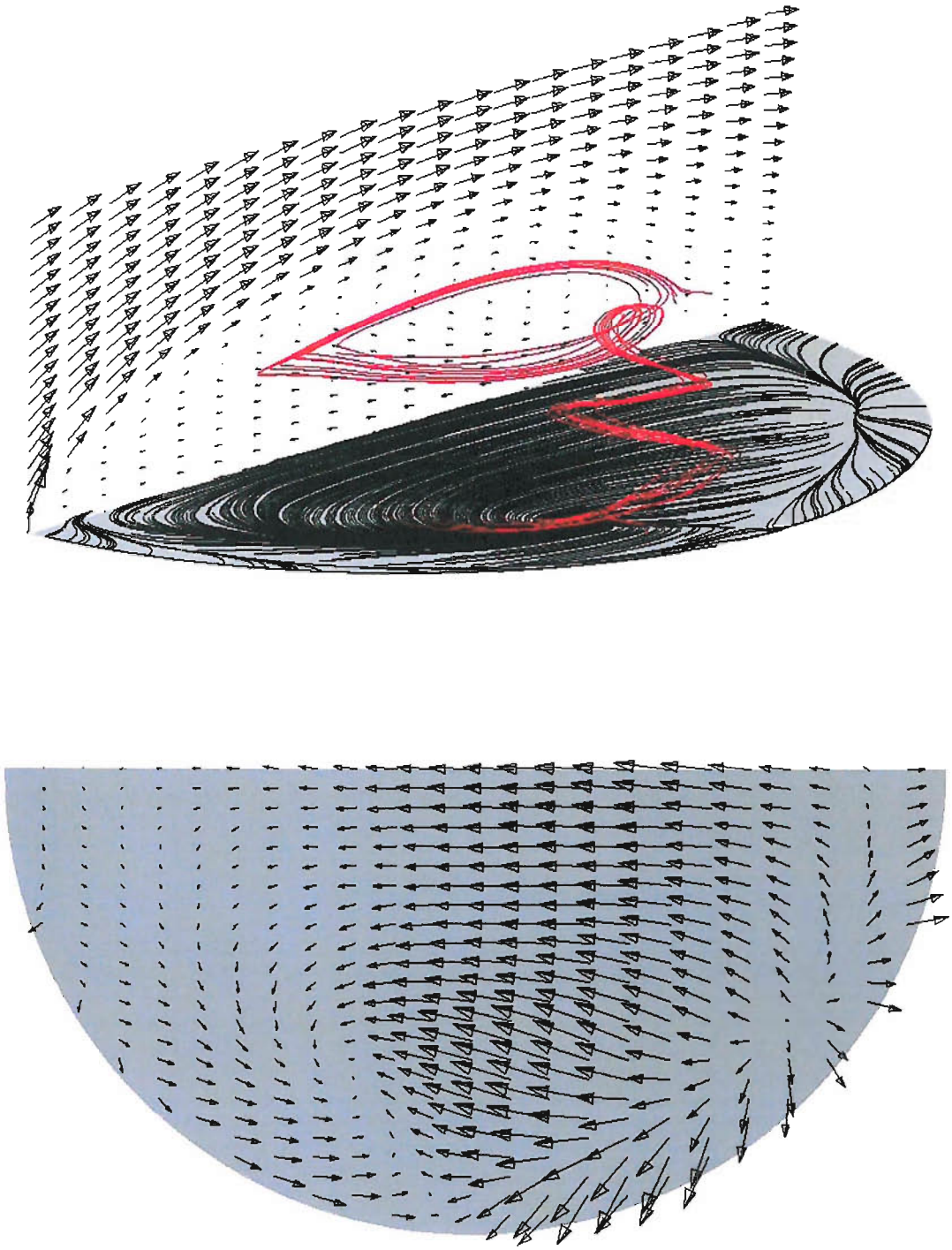

Figure 8.2: Vectors and particle paths on the free-end of the cylinder from DES results

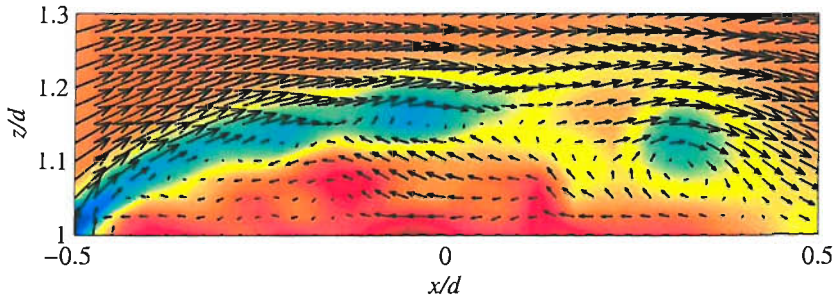

(a) Velocity vectors coloured by vorticity

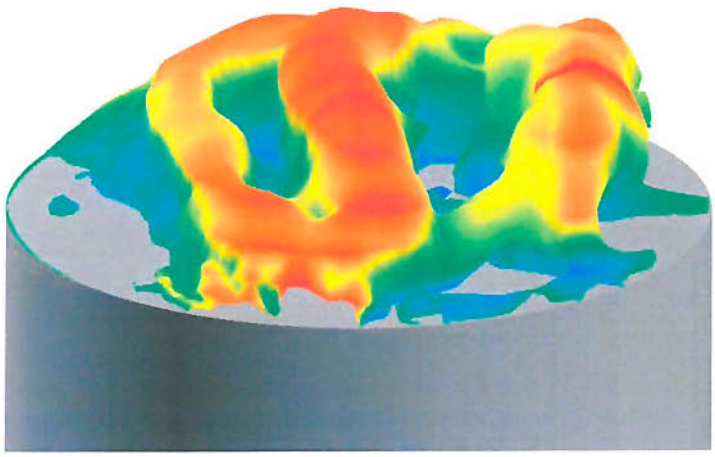

(b) Isosurfaces of pressure

Figure 8.3: An instantaneous realisation of the flow over the free-end, from the DES simulations. Displayed as vectors on the symmetry plane ($y/d = 0$) and isosurfaces of pressure

seen on the ground in the flow visualisation which shows the reversed flow along the ground being entrained into this vortex. The top of the arch can be seen in the PIV measurements on the symmetry plane just behind the top edge of the cylinder.

From the transverse PIV planes the evolution of the streamwise vortices can be seen. Close downstream of the cylinder there are four streamwise vortices visible. These are the two tip vortices and the two corner vortices at the base of the cylinder. Moving downstream the corner vortices disappear, but the tip vortices remain distinct to $x/d = 1$. At this point the downwash is strong, sweeping the tip vortices downwards. The shear layers also wrap up to form two large streamwise counter-rotating vortices in the wake. These trail a long way downstream, and are the main effect of the cylinder on the flow far downstream.

This idealised view of the flow structure only exists in the time-averaged flow. At any instant of time the flow consists of a large number of turbulent vortex structures. An example of this instantaneous flow is shown in Figure 8.4. This shows isosurfaces of pressure, corresponding to vortex structures, in the vicinity of the free-end and in the near-wake.

The initial vortex formation occurs at the separation at the side and at the leading edge of the free-end. The vortices at the side appear to be linked to the vortex at the leading edge. As these vortices are convected downstream they are broken apart towards the trailing edge of the cylinder. The upper part of the side vortex is entrained by the downwash from the top and is bent downstream. This action increases towards the reattachment location by which time the vortex is aligned in the streamwise direction and wraps around the other vortices to form the trailing streamwise vortex seen in the mean flow. These side vortices vary in size as some of them merge into one larger vortex. Some of them break near the top as they are skewed.

The vortices in the top shear layer also get aligned in the streamwise direction as they leave the recirculation region on the top of the cylinder. The outer ends seem to move downstream faster than the inside end. These wrap around the side vortices to form the streamwise mean-flow vortices.

Referring to the frequency spectra in Figures 3.20 to 3.23, there is a tendency for the peak to become more pronounced towards the tip of the cylinder. It seems possible that this peak corresponds to the frequency of the smaller structures seen in the shear layers, rather than the larger vortices. The smaller vortices seem to be more dominant near the upper corners while the side vortices around mid-height have a tendency to join together, giving a lower frequency. The fact that the peaks in the frequency spectra are broad is due to the random nature of the breaking and merging of these vortices.

The variation in the peak frequency with speed, shown in Figure 3.24, which shows that the peak Strouhal number halves at $U_\infty = 17.5$, is harder to explain. The implication is that the larger vortices are more dominant than the smaller ones at higher speeds. This seems surprising as the larger vortices might be expected to be less stable at high Reynolds number. Another

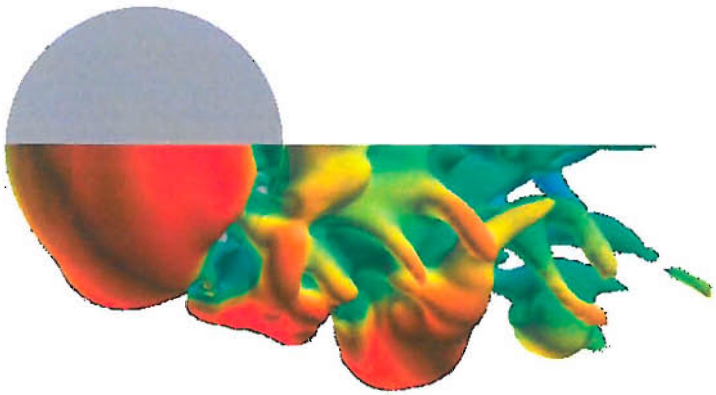

(a) Plan view

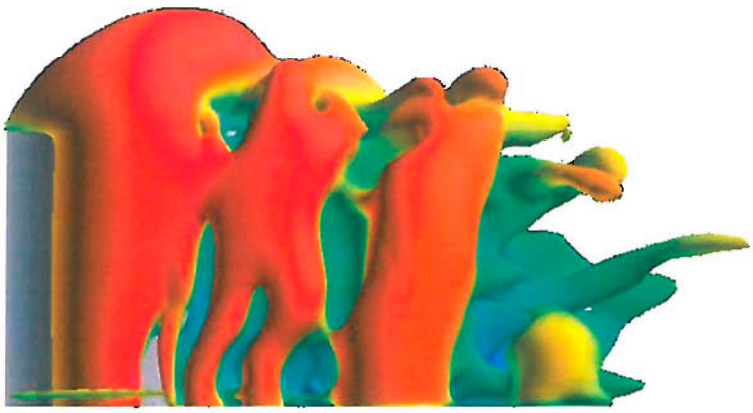

(b) Side view

Figure 8.4: Isosurface of pressure

possibility is that changes in the position of the shear layers and reattachment points with speed mean that the probe, which is at a fixed position, is in different part of the flow.

8.3 Appraisal of the numerical models

The flow that has been studied in this work is clearly a difficult one to solve using numerical methods due to the complex separated flows which interact with each other. In general the RANS computations using the standard k-ε turbulence model failed to predict the main features of the flow although in places good agreement with the experiments was achieved. In particular the structure of the flow over the free-end was not captured. The LES and DES simulations did capture the correct flow topology although the numerical values did not always match the experiments. In this section the successes and failures of each of the models will be assessed with reference to the knowledge of the flow physics detailed in the previous sections.

The first feature of interest is the horseshoe vortex system upstream of the cylinder. Although in the symmetry plane streamline traces it appears that the k-ε model correctly predicts the primary vortex, the surface flow pattern does not resemble the experimental one. As described above, the surface flow pattern is affected by the presence of the two additional vortices very close to the wall upstream of the primary vortex. The k-ε model fails to capture these secondary separations. It is well known [90] that the k-ε model is inaccurate in boundary layer flows, particularly in an adverse pressure gradient which could account for the failure to predict the separation in the near wall region. The k-ω model may be a better alternative in this situation as it can be integrated to the wall. The LES and DES do predict the right topology in terms of the number of vortices, but their size and position is wrong, especially with the LES model. The problem here is likely to be because of the poor prediction of the turbulent boundary layer on the floor. The LES in particular predicts an almost laminar boundary layer which will undergo separation much earlier than the turbulent one.

The models behave in a similar manner on the free-end: the k-ε model fails to capture the near wall structure, while the LES and DES predict the correct topology but overpredict the size of the recirculation region. It is possible that at the high Reynolds number used here the shear layer over the free-end undergoes transition immediately after separation which is not being captured by the LES due to insufficient grid resolution in this region. Earlier transition might cause the recirculation region to be shortened. This was commented on by Fröhlich et al. [35] who found a strong grid dependence in their solutions.

All the simulations overpredict the extents of the recirculation region behind the cylinder. This is apparent in the velocity profiles, and in the profiles of the Reynolds stresses. The k-ε model substantially underpredicts the turbulent kinetic energy in the wake which would contribute to a delayed reattachment. The LES and DES both give quite good agreement with

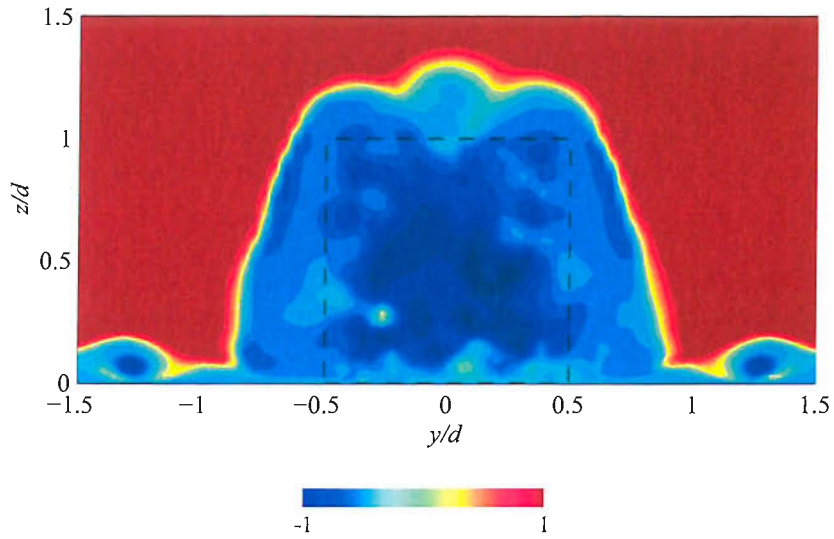

Figure 8.5: Contour plot of invariant of deformation tensor at $x/d = 1$

the magnitude of the measured stresses and turbulent kinetic energy even if they are shifted in space due to the different recirculation length. The flow can be seen to be anisotropic as $\overline{v'v'}$ and $\overline{w'w'}$ are about twice as large as $\overline{u'u'}$ on the centreline.

The likelihood of a turbulence model being able to predict a certain flow can be assessed by studying the nature of the deformation of the flow. Kim et al. [80] looked at the deformation of the flow around a prolate spheroid at an angle of attack as part of an investigation into turbulence modelling of this flow. They employed a normalised invariant of the deformation tensor Equation. 8.1, proposed by Hunt [91], to show the relative importance of strain, shear and rotation in the flow.

$$D = \frac{S_{ij}S_{ij} - \Omega_{ij}\Omega_{ij}}{S_{ij}S_{ij} + \Omega_{ij}\Omega_{ij}} \tag{8.1}$$

Here S_{ij} and Ω_{ij} are the strain and rotation tensors. In pure strain $D = 1$, in pure shear $D = 0$ and in pure rotation $D = -1$. Figure 8.5 shows the contours of this invariant in a transverse plane at $x/d = 1$ behind the cylinder, from the DES results. It shows that the outer flow away from the cylinder undergoes pure straining, while shear occurs in a thin layer around the cylinder. The wake region is dominated by rotational flow. The eddy-viscosity hypothesis makes the assumption that the turbulence is isotropic. However in complex flows such as the one considered here with streamline curvature this assumption is invalid [92].

The LES and DES simulations gave broadly similar results away from the boundary layer on the floor. The difference in the subgrid-scale model is rendered insignificant as the grid is fine enough for the modelled stresses, $2\nu_t S_{ij}$, to be much smaller than the resolved stresses, $-\overline{u_i u_j}$. Outside the boundary layers the modelled stresses are less than 1% of the resolved stresses.

8.4 Relevance to marine hydrodynamics

Flows around modern full-bodied ships such as tankers and bulk carriers are typified by the flow around the KVLCC2 hull form which was developed at the Korean Institute of Ships and Ocean Engineering [92] as a test case for numerical hydrodynamics. The flow in the propeller plane is of particular interest due to the interaction of the bilge vortex with the propeller. It was used in the Gothenburg 2000 workshop, where it was found that some RANS models were able to produce reasonable results. However, the anisotropic nature of the turbulence here means that two-equation RANS models have difficulty modelling the turbulent kinetic energy in the wake.

While many of the features found in the truncated cylinder flow have similarities with the flows found around the sterns of ships, there are certain differences. In particular the Reynolds number around large tankers is typically 10^9, four orders of magnitude greater than that considered here. There is a long length of attached flow along the hull with a turbulent boundary layer. This boundary layer interacts with the bilge vortex towards the stern to produce a region of unsteady turbulent flow. The turbulent kinetic energy in the propeller plane is lower than that found behind the truncated cylinder ($\sqrt{k} = 14\%U_\infty$ compared to $\sqrt{k} = 44\%U_\infty$) but is still large. The other difference is that the transverse normal stresses, $\overline{v'v'}$ and $\overline{w'w'}$ are around half of the streamwise stress $\overline{u'u'}$, whereas in the cylinder wake the streamwise stress is half the transverse stresses. However the flow is still anisotropic and therefore difficult for eddy-viscosity models to predict.

The larger scale structures in the flow in this region are likely to have a characteristic frequency of order 0.01Hz assuming that the non-dimensional frequency is of order 0.1 and that it scales with breadth and ship speed. This corresponds to a period of 100 seconds so the propeller could experience variations in inflow velocity lasting for long periods. It would therefore be useful to be able to simulate this flow as experiments are difficult to achieve at Reynolds numbers anywhere near the full-scale values.

Both the LES and DES results on the truncated cylinder geometry showed that while the agreement between the mean velocity and Reynolds stress profiles was not so good in the recirculating flow close to the cylinder, the results were quite good further downstream, where the flow is dominated by streamwise vortices. It is this part of the flow that probably has most in common with the flow around a ship's stern where the flow undergoes three-dimensional separation to create streamwise vortices but the dominant flow is still in the streamwise direction.

The main question to be resolved is whether the DES model will behave correctly as the grid is refined towards the stern. It has been seen that there is a grey area in the boundary layer modelling around this interface which can result in an under-resolved boundary layer and high levels of turbulent viscosity being carried into the DES region. DES has been used successfully

on a prolate spheroid geometry [43] which also has much in common with ship hulls.

It was beyond the scope of this thesis to perform DES simulations of the KVLCC2 flow, as it would have required too much time to complete. Some preliminary LES runs on an elongated (elliptical) cylinder were made, as reported in [93]. These show that the longitudinal vortices from the free-end of the cylinder become more dominant as the cylinder is stretched.

During the course of this work a set of measurements were made using PIV on the flow around a scale model of the KVLCC2 hullform in the wind tunnel. The aim of these being to look at the unsteady nature of the flow in the wake. These experiments are reported in Appendix F. The measurements do show that the bilge vortex seen in the mean flow is composed of unsteady smaller scale vortices but there are inaccuracies in the measurements which need to be addressed before final conclusions can be drawn.

8.5 Summary

This chapter has presented discussion and analysis of all the results obtained during the course of this study. Firstly the experimental and numerical results were studied to gain further insight into the physics of the flow in the three main areas - the horseshoe vortex system, the free-end flow and the near-wake region. The key findings are summarised as follows.

1. The horseshoe vortex system appears to follow the topology of Baker [25], but the two vortices next to the wall are very close to the wall and therefore are difficult to see in velocity measurements on the symmetry plane. This explains the apparent discrepancy between the surface flow visualisation and the velocity field in the symmetry plane which has been observed by some authors.

2. The mean flow on top of the free-end has been shown to consist of a single vortex connecting the two eyes visible in the surface flow patterns and passing through the recirculation vortex on the symmetry plane. This supports Kawamura et al.'s original hypothesis [12] but contradicts the more recent theory of Roh and Park [21].

3. The time-averaged structure of the near-wake region is seen to consist of an arch vortex immediately behind the cylinder. Further downstream the shear layers from the side and top wrap into a pair of streamwise vortices which trail downstream.

4. The instantaneous flow in the wake does not resemble the idealised mean flow. Vortices are formed from both the side and top shear layers which get twisted and broken near the top as they encounter the downwash flow. This results in smaller vortices wrapping around one another and becoming aligned with the stream.

An assessment of the strengths and weaknesses of the numerical models tested here has been presented, with the following conclusions.

1. The eddy-viscosity type RANS model is unlikely to be able to predict the flow well due to the large turbulent kinetic energy and anisotropic stresses. The high degree of rotation and shear in the flow will also present difficulties for the k-ε model.

2. The problem with predicting the upstream boundary layer with the LES and DES models is highlighted. This resulted in the poor prediction of the horseshoe vortex system.

3. The recirculation bubble over the free-end is over-predicted by all the models. This may be due to transition in the shear layer near the leading edge not being resolved fully.

The experience with the DES model gained on the truncated cylinder model suggests that this may be a suitable model for the simulation of turbulence in the stern region of tanker hulls.

1. It is shown that the cylinder flow has certain features in common with the flow in the propeller plane of the KVLCC2 tanker hull, notably the streamwise vortices, high turbulence intensities and anisotropic stresses.

2. It is estimated that the energy containing vortices in the wake will have time-scales of the order of 100s which could have an effect on the performance of the propeller and rudder. This is a motivation for the study of the turbulent flow in this region.

3. It is concluded that DES represents a viable option for the simulation of this flow.

Chapter 9

Conclusions

9.1 Overall

The principle aims of this research were to carry out a detailed experimental study of the flow around a truncated cylinder, to investigate the use of various simulation techniques to predict this flow, to investigate the flow physics of this flow, and to draw conclusions on the simulation of ship flows based on these findings. The aims as stated in Section 1.2 are addressed in turn below.

1. A set of experimental data, with known boundary conditions has been produced which will add to the somewhat sparse knowledge of the flow around low-aspect ratio cylinders. In particular the PIV results illustrate aspects of the flow that had previously been inferred from other sources, such as the recirculation on top of the free-end and the trailing longitudinal vortices. The data also provides a useful test case for CFD simulations as it contains a combination of features which will test most models.

2. An unsteady RANS computation was carried out using the $k-\varepsilon$ turbulence model but was found to perform poorly in the free-end region and in the recirculation region due to the anisotropic nature of the turbulence. Also a RANS method, even an unsteady one, does not capture the detail of the turbulence and simply gives the mean flow. There are many applications where this information is desirable. The prediction of the upstream flow on the ground plane and the horseshoe vortex was good however.

   Large-eddy simulations were performed and were found to perform well in the wake region, giving good resolution of the turbulent structures. This method cannot capture a turbulent boundary layer, such as that found on the ground plate, without very fine grid resolution, which would require an impractical number of cells. This resulted in the flow separating too far upstream on the ground plane.

In an effort to benefit from the advantages of both the RANS and LES methods, a DES model, based on the Spalart-Allmaras turbulence model, was implemented in the code. This model gave similar results to the LES in the separated flow regions. The upstream boundary layer was better predicted than with the LES model, as the model was working in RANS mode on the ground. However the separation upstream is still too early, perhaps because the model switches from RANS to LES modes in this region. The boundary layer in this situation is not correctly predicted because there are no turbulent fluctuations from upstream.

3. The LES and DES simulations have proved to be extremely valuable in aiding the understanding of the physical phenomena and structure of the flow, by providing full-field flow information at every instant. This is more than any current practical experimental technique would allow (holographic PIV being the only technique that can approach this state).

   The horseshoe vortex system has been shown to be a three vortex system as proposed by Baker, with two vortices very close to the ground, which are difficult to measure experimentally.

   The mean flow over the free-end has been shown to consist of a vortex looping over the top, anchored to the free-end in the forward quadrants, and visible on the surface as "eyes" in oil visualisation, and passing through the recirculation region visible in the vector planes on the centreline.

   In the wake, the LES/DES simulations have shown the existence of vortex structures on the inside of the shear layers at the sides and the top, which are shed downstream. The shear layers wrap up into trailing vortices downstream of the reattachment point.

4. The DES simulations have been seen to perform as well as the LES in the separated wake region, while the turbulent boundary layers are handled well if the model is operating in RANS mode. There is a region where the grid density changes from RANS to LES density where the turbulent fluctuations are delayed due to the turbulent viscosity from the RANS region upstream. This affects the shape of the boundary layer in this "grey" area. The tanker hull exhibits a large extent of attached turbulent boundary layer over most of the length of the hull, where the RANS model is sufficient. In the stern region the flow undergoes three-dimensional separation which would require an LES model to capture the turbulent structures. DES seems ideally suited to this flow.

9.2 Detailed

9.2.1 Flow features

The large amount of experimental and numerical data that has been obtained during the course of this work, has enabled a greater understanding of the physics of the flow over a low-aspect ratio cylinder. While many aspects of this flow had been studied experimentally there were gaps in the knowledge of certain areas. In particular the nature of the flow over the free-end and in the near-wake where traditional experimental techniques cannot capture the three-dimensional structure of the vortices. The use of the numerical simulations, with the experiments as a check on the accuracy, enables a much fuller picture of the flow to be developed. The key features which have been identified are summarised below.

1. A three vortex horseshoe system is formed at the junction of the cylinder with the ground plane. This is formed as the flow separates from the ground plane under the influence of an adverse pressure gradient due to the presence of the bluff body. The primary separation point is at $x/d = -1.0$ behind which a thin vortex is formed close to the ground. This reattaches at the start of the primary vortex at $x/d = -0.78$. Beneath the primary vortex there is a third very short vortex. There is a stagnation point on the upstream face of the cylinder at a height of $z/d = 0.4$. The mean location of the vortex centre is positioned at $x/d = -0.68$, $z/d = 0.04$ although it wanders through a distance $O(0.1d)$.

2. The flow on the cylinder side is laminar up to the separation point at 70 degrees from the leading edge. Tripping the boundary layer to turbulence with a wire upstream delays separation to 80 degrees. This is a much earlier separation than in the case of an infinite-height cylinder which separates at 80 degrees in the laminar case and 100 degrees when turbulent. The likely cause of this is the greater pressure recovery at the rear of the cylinder due to the downwash from the free-end which results in a higher pressure in the wake.

3. The flow separates at the leading edge at the top of the cylinder. A recirculation vortex is formed within this separated flow region which folds over the free-end. The bases of this vortex can be seen in the form of swirls in the forward half of cylinder top. Flow is drawn into these swirls from the sides of the cylinder from behind the separation line. The flow attaches to the top of the cylinder at $x/d = 0.17$ on the centreline. The attachment line can be seen curving forward on either side to the side separation point. A trailing longitudinal "tip" vortex originates behind the separation line.

4. In the near wake the shear layers at the sides and over the top wrap up to form vortices which are shed downstream. These do not have a strong periodicity in the manner of

a Von-Karman vortex street. The downwash tilts the vertical vortices downstream. The time-average of this flow gives the "arch" vortex described by other authors, and which is visible in the surface flow visualisation as two swirls on the ground behind the cylinder.

5. Further downstream the shear layers wrap up to form two counter-rotating longitudinal vortices which extend far downstream.

9.2.2 Experimental methods

A number of experimental methods were employed during this research. A number of conclusions can therefore be drawn on the use of these techniques for flows such as the one considered here.

1. The simplest tests which were made were also perhaps the most revealing in terms of the overall flow pattern. These were the oil flow visualisation tests to visualise the flow on the surfaces of the cylinder and the floor. It is strongly recommended that any set of experiments on a new flow should begin with this form of visualisation.

2. Particle image velocimetry (PIV) has proved to be extremely useful as a tool for measuring large areas of the flow. It gives the mean and instantaneous flow fields in a particular plane which give a larger set of data for validating a CFD code.

3. Hot-wire anemometry was useful for measuring the frequency content of the velocity signal outside the shear layers, but due to the three-dimensionality of the flow it could not be used to measure velocities within the near-wake.

4. The pressure transducers which were used proved problematic. Firstly mounting them in the model appeared to cause a slight distortion of the diaphragm which meant the supplied calibrations were incorrect. They therefore had to be calibrated *in situ* using previously measured pressures. The second problem was the fact that the transducers measured gauge pressure, that is the difference between the front and back of the transducer body. Since the back was inside the cylinder the pressure in the cylinder had to be measured. This was another possible source of error. The final results however agree well with other sources of data.

9.2.3 Numerical modelling

1. The flow on the ground plane was well modelled by the k-ε RANS model with the horseshoe vortex being very close to the measured one. The separation from the cylinder side was too far back which had an impact on the rest of the flow field. The intricate swirl patterns on the top of the cylinder were not captured at all.

2. The LES simulations failed to model the turbulent boundary layer on the ground plane. This resulted in the early separation from the ground and the formation of a double vortex system. A wall function may help with the boundary layer modelling.

3. The separation line on the cylinder side was close to the experimental one, but the recirculation regions both on the top and in the wake were too long. The reason for this is unclear. The flow pattern on the free-end is very similar to the experimental visualisation. The turbulence is resolved down to small scales as shown by the frequency spectra.

4. A DES model was implemented in the flow solver with the aim of benefitting from the advantages of the RANS and LES models. In practice DES did not perform as well as RANS on the ground plane, probably because of the grid density changes close to the cylinder. However, it did predict the right number of vortices whereas the k-ε model only showed one vortex. The prediction of the boundary layer upstream could not be verified as measurements were not made with the model in position.

5. The DES produced very similar results to the LES in the separated regions indicating that the grid is fine enough for the subgrid-scale model not to have much effect.

9.3 Recommendations for further work

While a great deal has been achieved in the course of this work, there remain a number of aspects of the truncated cylinder flow that could be studied further, both numerically and experimentally. This section lists the author's views on further investigation that could be carried out.

1. In order for the experimental data to be useful as a CFD validation case, more information is required on the flow upstream of the cylinder with the model in position. In particular, measurements should be made at the leading edge of the ground plate. This will allow a more representative inflow boundary condition to be applied. The development of the boundary layer under the influence of the adverse pressure gradient due to the model should also be measured.

2. One of the difficulties with modelling the flow around the truncated cylinder at the Reynolds number used here (2×10^5) is that there are regions of laminar and turbulent flow. The flow prior to separation on the cylinder is laminar, while the flow after separation and on the ground plane is turbulent. Standard RANS models assume that the flow is turbulent everywhere, resulting in the incorrect modelling of laminar separation. Some models have been developed to allow the turbulence to be tripped at a certain location.

There is such a model built in to the Spalart-Allmaras model which has been partially implemented in the code. It would be interesting to activate this or a similar transition model to account for the regions of laminar and turbulent flow.

3. All of the experiments so far carried out on finite-height cylinders have been in the sub-critical regime, that is with laminar separation. It would be very interesting and useful to many real-world applications to perform experiments at a higher Reynolds number with turbulent separation. The work presented here seems to suggest that the separation point does not move very far back, unlike a two-dimensional cylinder, with little change in the flow field. It would be useful to confirm this with more detailed experiments in the turbulent state.

4. The LES simulations have been shown to have limitations, particularly in the size of the separation bubble on the free-end and in the wake. This may be because either the free-stream turbulence is not represented or because some transition in the shear layers near separation is not being resolved. Reduced turbulence levels would delay reattachment.

5. The LES simulations fail to model the boundary layer on the ground plane upstream of the model. A wall-function should probably be employed here to improve the modelling of the boundary layer. This would need to be applied only to the ground plane and not the cylinder wall.

6. No attempt was made here to model the freestream turbulence at the inflow to the computational domain. It is possible that the LES simulations will be sensitive to this although the freestream turbulence intensity in the wind tunnel was only 0.3%. A turbulent inflow condition could be included in the code.

7. Much of the work in the literature on finite-height cylinders has been on the variation in the flow with changing aspect ratio with particular emphasis on the suppression of the Von-Karman vortex shedding at low aspect ratios. It would be interesting to extend the LES or DES simulations used here to higher aspect ratios to further the knowledge on this behaviour.

The above points have addressed the outstanding issues with the finite-height cylinder. The eventual target of this work is the turbulent flow in the stern region of ship hulls. The results of the cylinder simulations suggest that DES promises to allow the simulation of this flow and thus to give further insight into the nature of the flow in this region than is possible experimentally, particularly at full-scale Reynolds numbers. This could potentially open up a significant amount of research into the physics of this flow and its interaction with the propeller and rudder. Areas for further investigation are summarised below.

1. The PIV measurements in the wind tunnel carried out so far have shown considerable unsteadiness in the flow at the propeller plane. Some questions remain over the accuracy of the results, particularly the magnitude of the fluctuations and the shear stresses, which do not agree very well with the KRISO results. Further measurements could be made to try to improve these results and also to obtain data in more longitudinal planes to give the axial velocities. This could be supported by hot-wire anemometry. Areas of the experimental method where improvements could be made are detailed in Appendix F.

2. Detached-eddy simulations of the KVLCC hull should be performed. The results can be compared with both the PIV measurements and the original KRISO measurements. To run these simulations will require a lot of work on the grid to ensure that the cells are sufficiently fine in the stern region while not being stretched excessively. This is where unstructured grids are probably more suitable as they can be more easily fitted to a complex surface. It may prove to be more appropriate to use the commercial flow solver CFX-5.6, which includes a test version of DES, to perform these simulations.

3. Following on from the results of the previous two items, the effects of the turbulent wake on the propeller performance can be assessed. This could be done with any form of propeller model, from a potential flow panel code to an unsteady RANS or even DES simulation, with an unsteady inflow velocity profile taken from the previous results.

9.4 Closing remarks

The work presented in this thesis has attempted to provide a deeper understanding of a complex three-dimensional flow through the use of experiments and numerical simulations. While the simulations still have some limitations they do provide an excellent insight into the structure of the flow. It is clear that it is not yet possible to rely solely on numerical studies when accurate results are required but a combination of physical and numerical experiments is a powerful tool which offers the possibility to understand more complex flows. New experimental techniques such as PIV along with LES can provide a lot of information on the instantaneous flow field as well as the time-averaged one.

From the point of view of marine hydrodynamics it is hoped that techniques such as DES will enable the simulation of some of the high Reynolds number turbulent flows encountered in the marine environment, which are difficult to study in any other way.

Appendix A

Drawings of truncated cylinder model

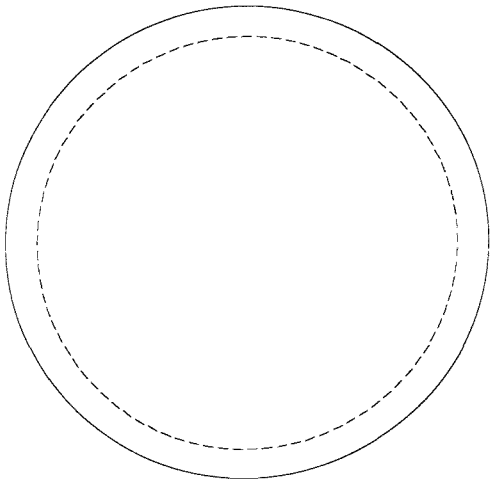

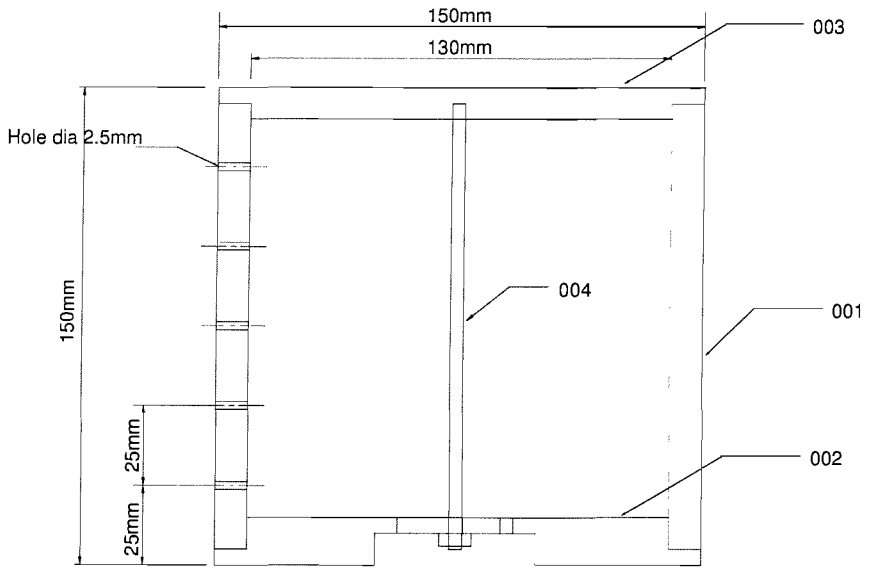

University of Southampton
School of Engineering Sciences

			TITLE: CYLINDER MODEL	
			DRAWN BY: R. PATTENDEN	DATE: 7/9/00
SIZE: A4	SCALE: 1:2	DWG NO. / FILE NAME: CYL-0001 / cylelev.skd	CHECKED	SHEET: 1 of 4

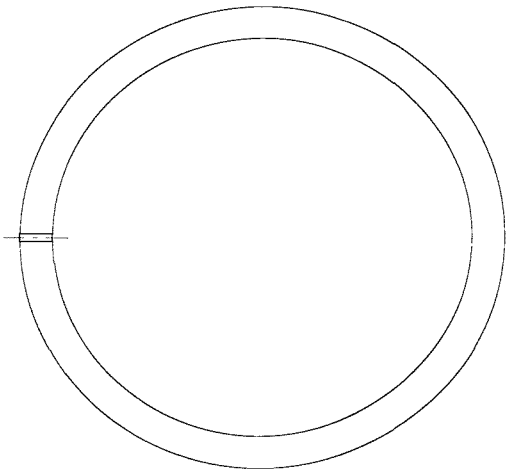

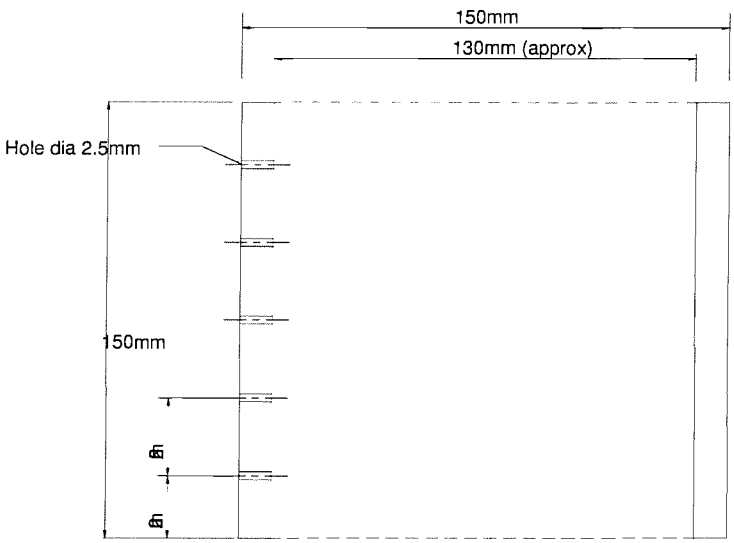

Material:

Aluminium tube 150mm OD
or 6" OD machined to 150mm
Thickness between 5-10mm

University of Southampton *School of Engineering Sciences*		TITLE: CYLINDER MODEL - PART 001	
		DRAWN BY: R. PATTENDEN	DATE: 7/9/00
SIZE: A4	SCALE: 1:2	DWG NO. / FILE NAME: CYL-001 / cyl001.skd	CHECKED
			SHEET: 2 of 4

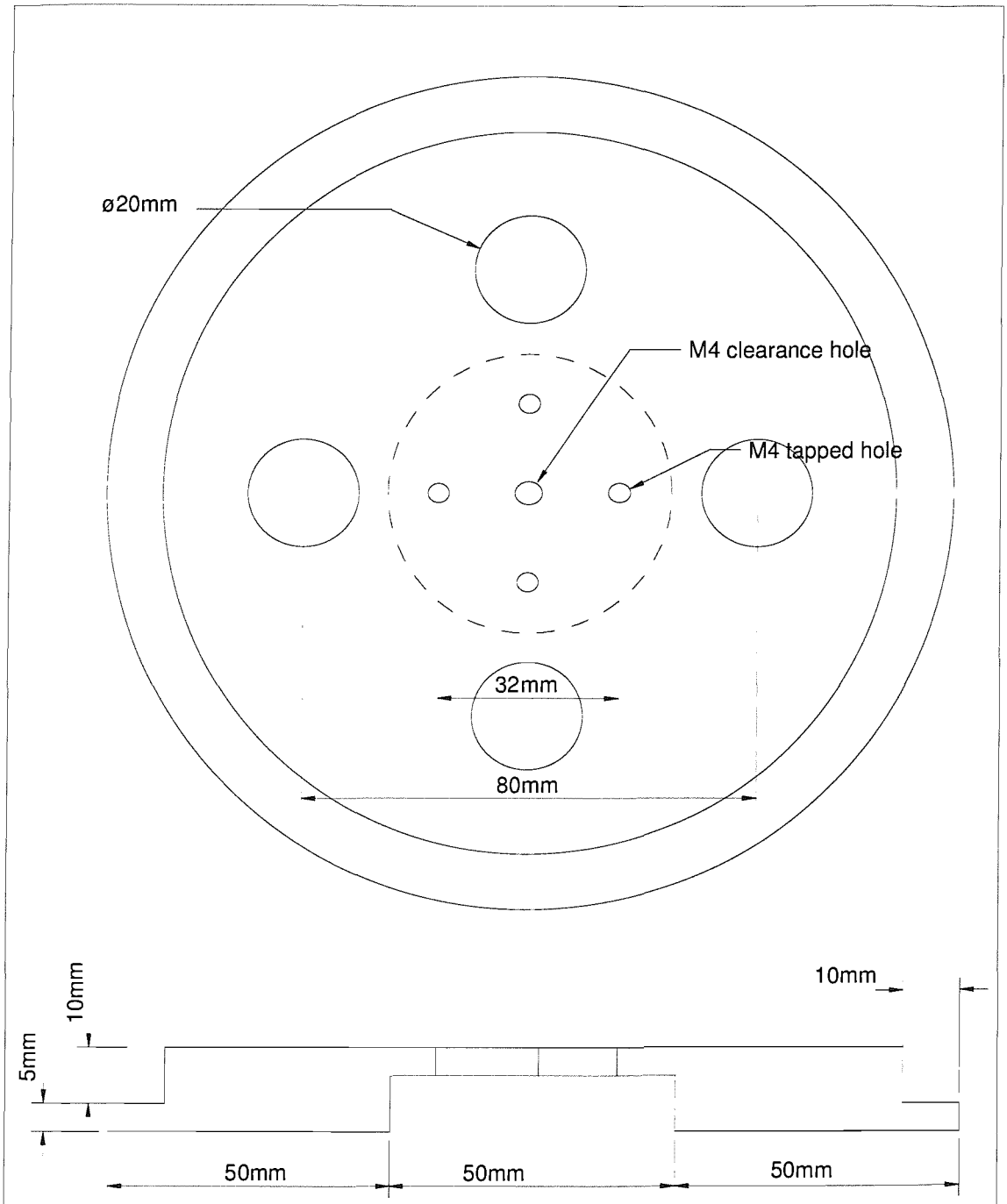

Material: Aluminium plate

University of Southampton *School of Engineering Sciences*		TITLE: CYLINDER MODEL - PART 002		
		DRAWN BY: R. PATTENDEN		DATE: 7/9/00
SIZE: A4	SCALE: 1:1	DWG NO. / FILE NAME: CYL-002 / cyl002.skd	CHECKED	SHEET: 3 of 4

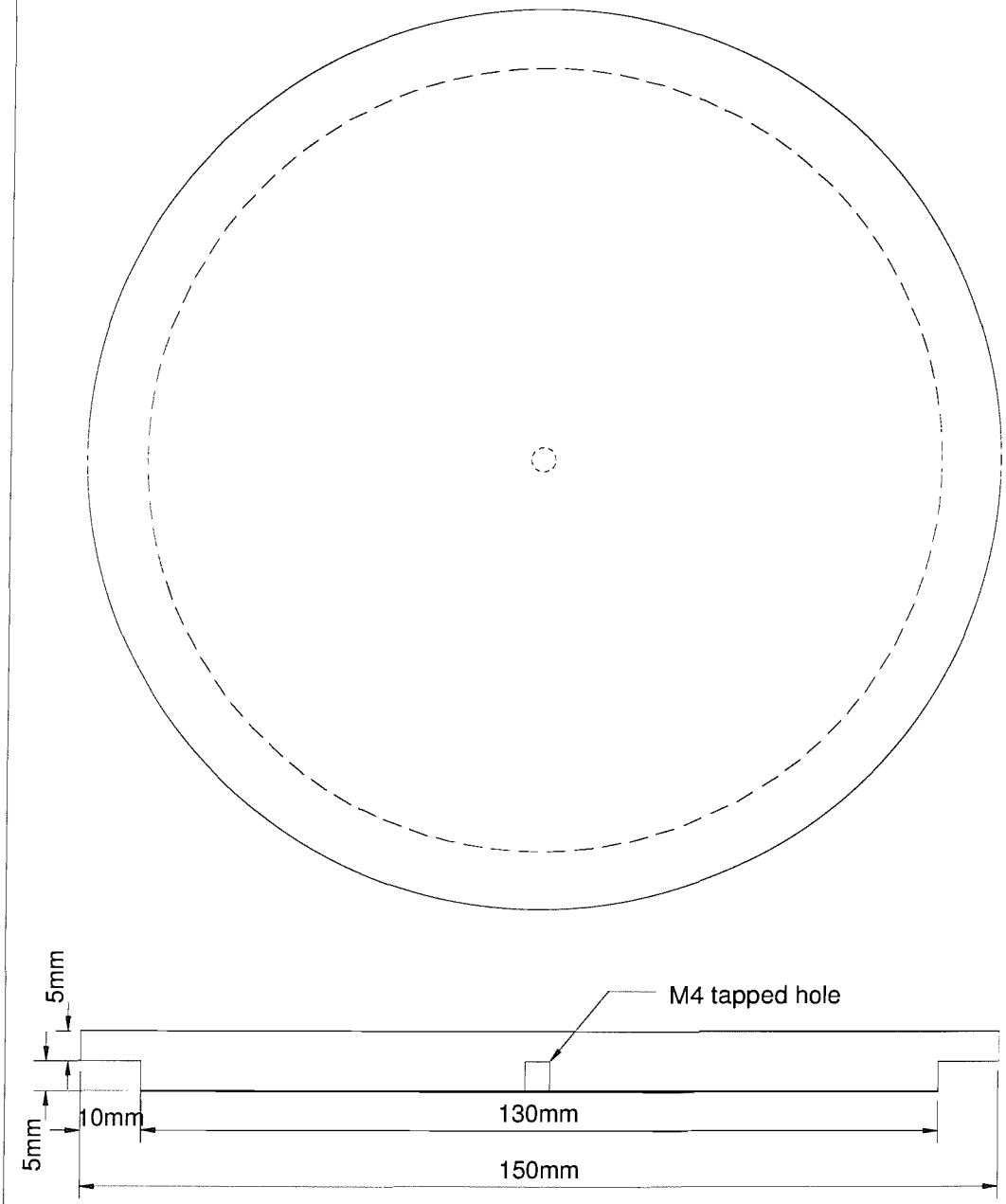

University of Southampton *School of Engineering Sciences*			TITLE CYLINDER MODEL - PART 003	
			DRAWN BY R. PATTENDEN	DATE 7/9/00
SIZE A4	SCALE 1:1	DWG NO. / FILE NAME CYL-003 / cyl003.skd	CHECKED	SHEET 4 of 4

Appendix B

Supplementary figures from the experiments

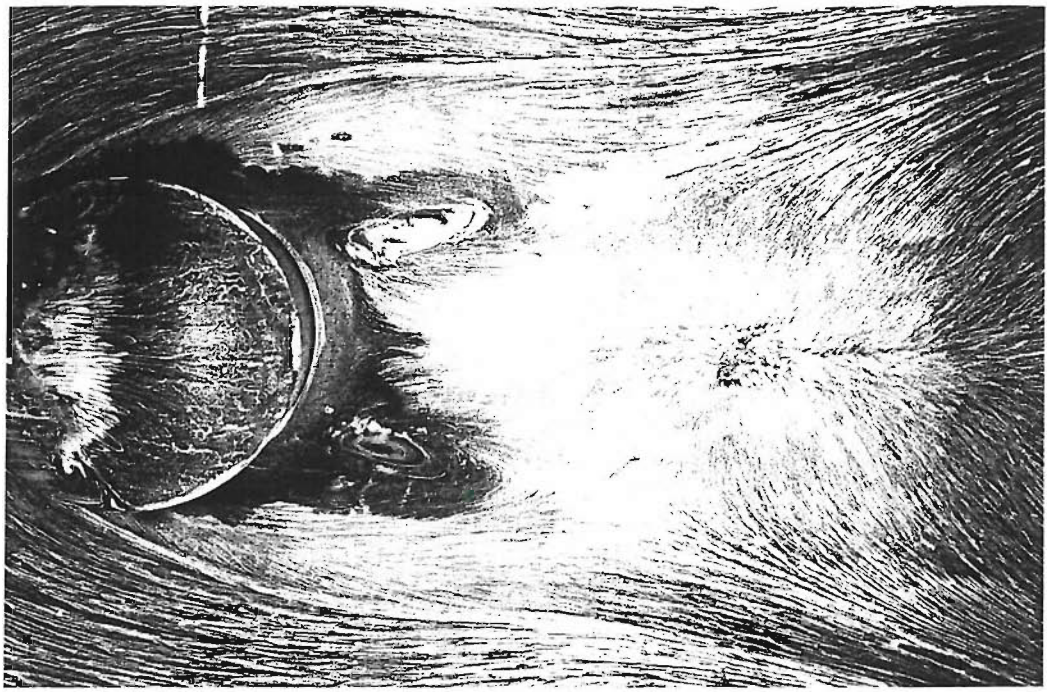

Figure B.1: Surface flow visualisation - floor of tunnel under recirculation bubble, $U_\infty = 20m/s$ (flow from left to right)

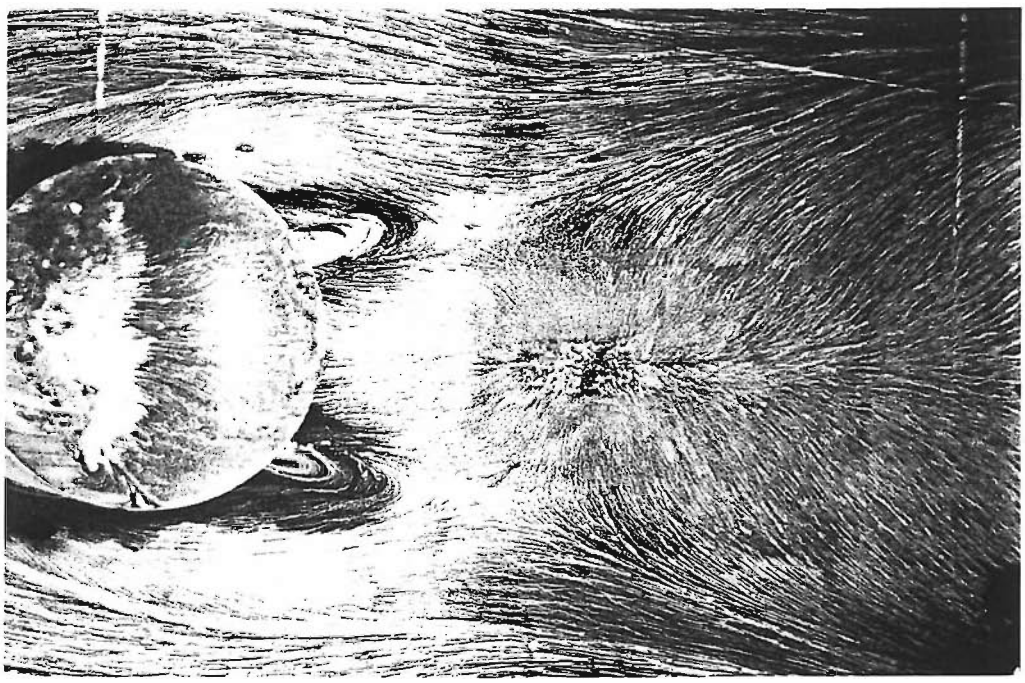

Figure B.2: Surface flow visualisation - floor of tunnel under recirculation bubble, $U_\infty = 20m/s$ (flow from left to right)

Figure B.3: Surface flow visualisation - flow under horseshoe vortex system, $U_\infty = 20m/s$ (flow from left to right)

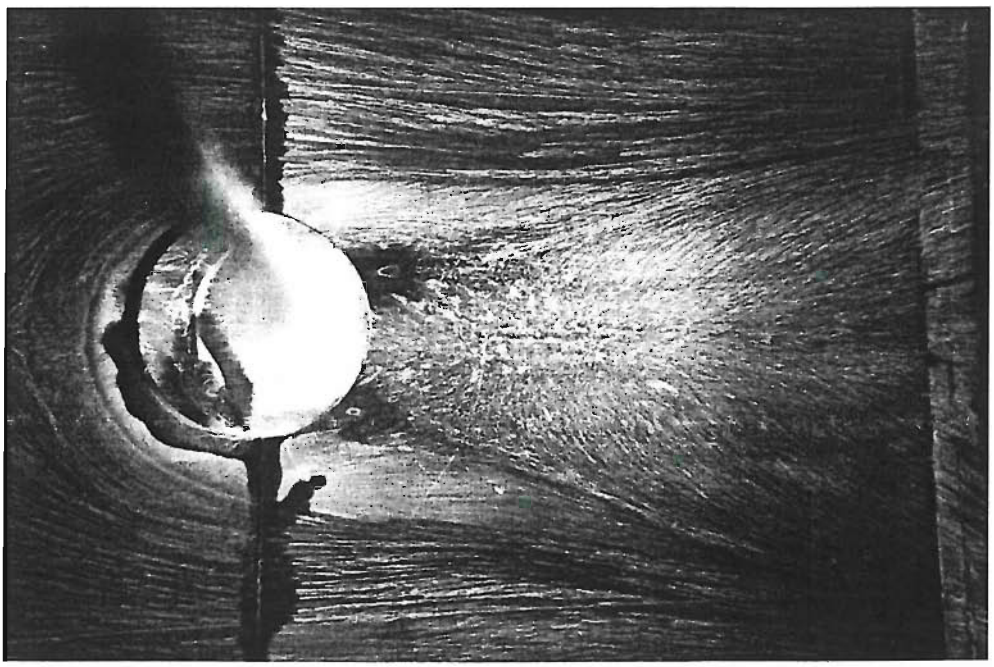

Figure B.4: Surface flow visualisation - floor of tunnel with tripped boundary layer, $U_\infty = 20m/s$ (flow from left to right)

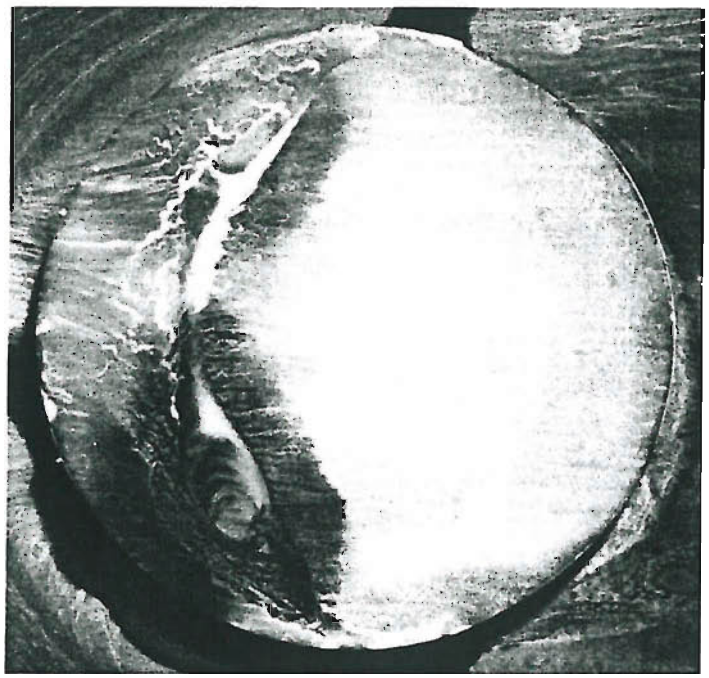

Figure B.5: Surface flow visualisation - top of cylinder with tripped boundary layer, $U_\infty = 20m/s$ (flow from left to right)

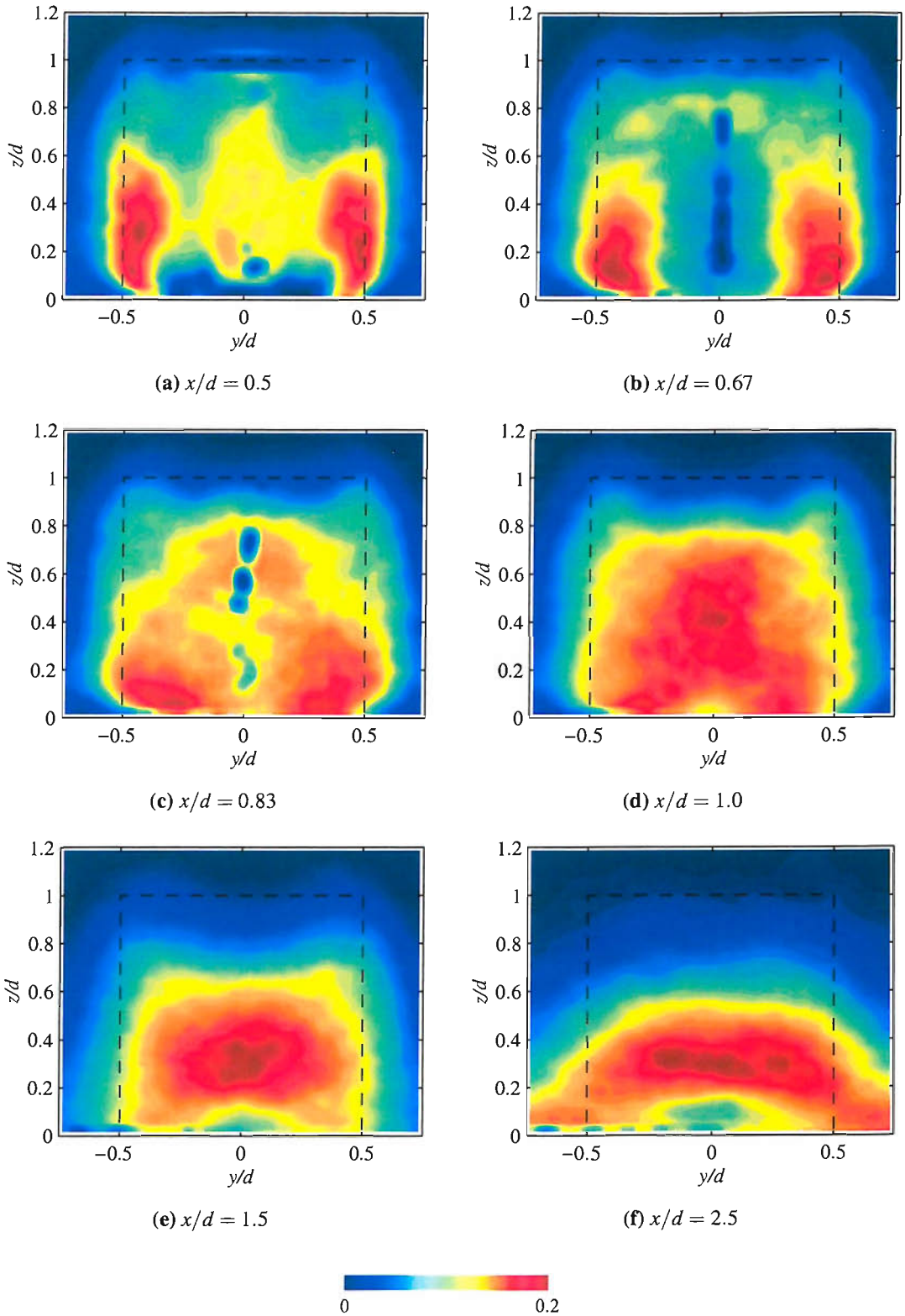

(a) $x/d = 0.5$

(b) $x/d = 0.67$

(c) $x/d = 0.83$

(d) $x/d = 1.0$

(e) $x/d = 1.5$

(f) $x/d = 2.5$

Figure B.6: Contours of vv from PIV measurements ($U_\infty = 20m/s$)

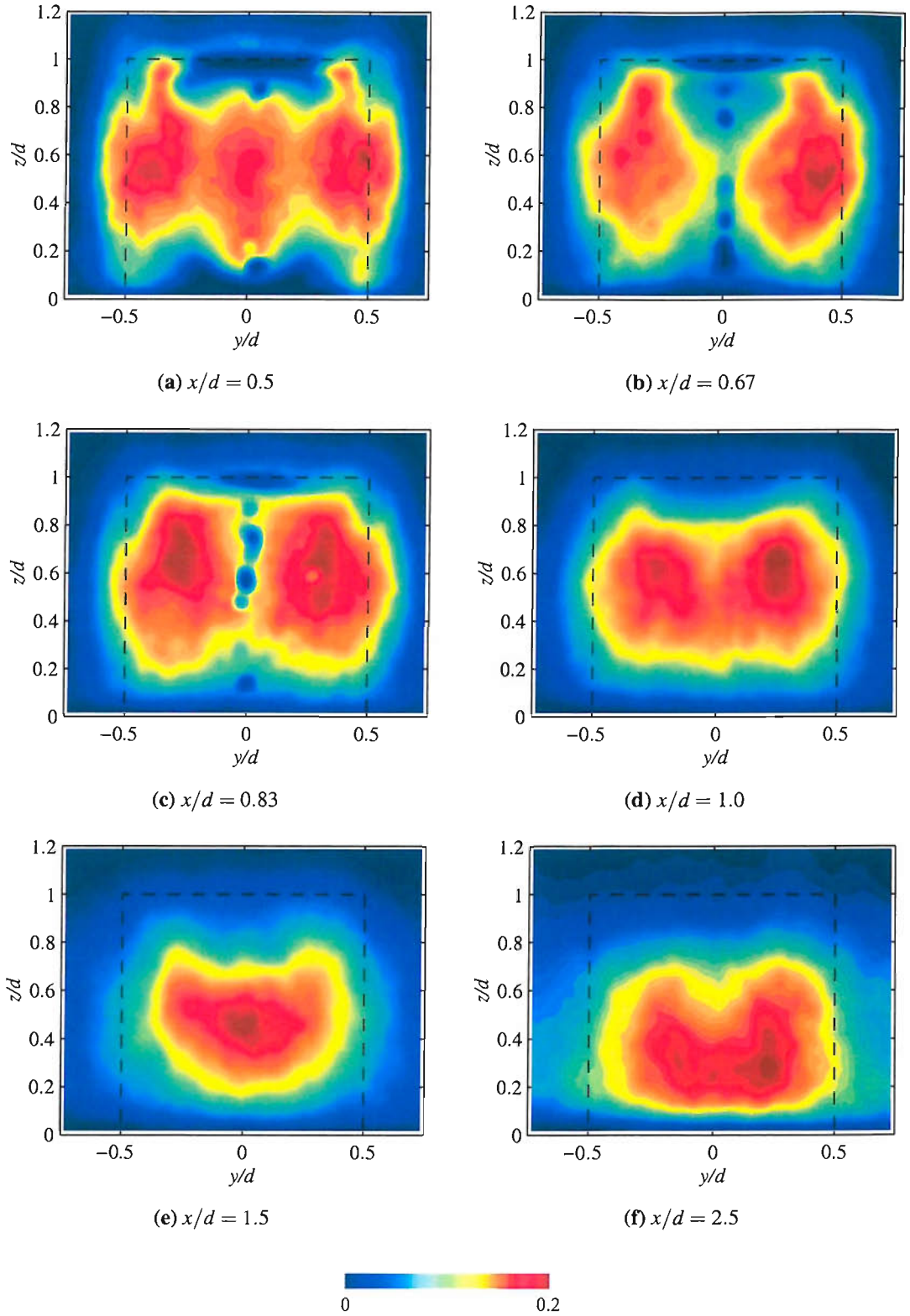

(a) $x/d = 0.5$

(b) $x/d = 0.67$

(c) $x/d = 0.83$

(d) $x/d = 1.0$

(e) $x/d = 1.5$

(f) $x/d = 2.5$

Figure B.7: Contours of *ww* from PIV measurements ($U_\infty = 20m/s$)

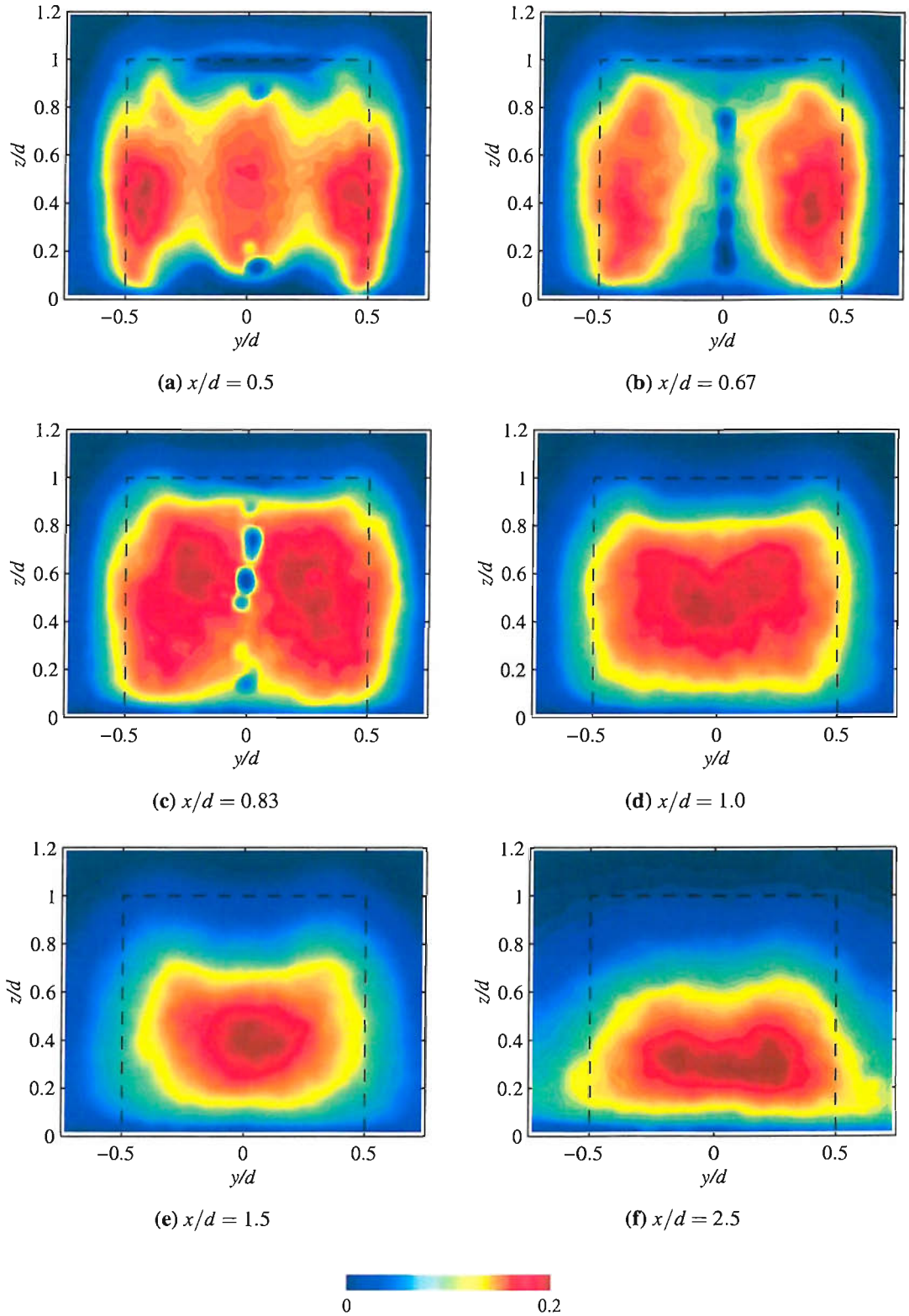

(a) $x/d = 0.5$

(b) $x/d = 0.67$

(c) $x/d = 0.83$

(d) $x/d = 1.0$

(e) $x/d = 1.5$

(f) $x/d = 2.5$

Figure B.8: Contours of vw from PIV measurements ($U_\infty = 20m/s$)

Appendix C

Changes made to Elmore

C.1 Introduction

This appendix describes the modifications that were made to the flow solver code, particularly for the implementation of Detached-Eddy Simulation (DES). The first section gives an overview of the steps that were necessary to achieve this, along with some of the errors that had to be traced in the code. The second section details the calculation of the length-scale $\tilde{d}$. Finally the calculation of the statistical quantities of the flow field such as mean velocities and Reynolds stress components is described.

C.2 Implementation of DES

As was shown in Section 4.2.6, Detached-Eddy Simulation is a method whereby a standard RANS model is modified such that the length-scale of turbulence employed in the equations can switch between two states [73]. The first is the standard length-scale used near walls or where the grid is not fine enough for LES. The second is a modified length-scale based on the cell size when the grid is fine enough for an LES solution. To date two RANS models have been subject to this treatment: the original DES used the Spalart-Allmaras one-equation model [38], and more recently the two-equation k-ω SST model has been adapted [74].

In this work the original Spalart-Allmaras version was used. In this model the length scale, l_{SA} is modified if the largest cell dimension is smaller than a certain fraction of the distance to the nearest wall.

$$\tilde{l}_{SA} \equiv \min\left(l_{SA}, C_{DES}\Delta\right) \tag{C.1}$$

where Δ is the largest dimension of the cell,

$$\Delta \equiv \max\left(\Delta x, \Delta y, \Delta z\right) \tag{C.2}$$

As the code already contained the Spalart-Allmaras RANS model it was necessary to apply the modification to the length scale, which is described in the next section. However it turned out that the existing code for the S-A model contained a number of errors and so a lengthy process of debugging was required before the simulations would run successfully. The following lists the main items that were changed to eliminate various crashes most of which were caused by variables in the model equations tending to infinity. The equations are presented in Chapter 4, Section 4.2.3.

1. The intermediate variable, r (Equation 4.13), is truncated to 10 as suggested in the original paper [38], as this term quickly becomes insignificant.

2. A check was added to stop ν_t becoming negative which occurred occasionally.

3. ν_t at the boundaries was set to $\mu/1000$ as suggested by Spalart [38].

4. r was found to cause occasional crashes when it became large and negative, so a check was added to keep it greater than -1000. The r^6 term in Equation 4.13 was becoming very large which was causing problems in Equation 4.12.

The last item was the most frustrating as it seemed to cause crashes almost at random and so was very difficult to trace. It was almost a year from starting work on DES to getting it fully working and capable of producing a solution.

C.3 Calculation of the DES length scale

The length scale in the standard Spalart-Allmaras model is equal to the distance of the cell to the nearest wall boundary. It is therefore necessary to calculate this at the start of the solution and to store it as a variable. In a general purpose flow solver designed to work on any grid it is necessary for each cell to loop through every wall face to search for the nearest one. To work in parallel on a multi-block grid the coordinates of all the wall faces have to be collated on each processor. This code had already been implemented but there were some errors in the looping which had to be resolved. Due to the number of loops required to find the nearest wall this process can take a long time - around 30 minutes for the truncated cylinder grid 4 used here. It was therefore decided to store the length scale to disk along with the other solution variables so that the solution could be restarted without having to recalculate the length scale.

In order to convert the length scale to the DES length scale the size of each cell must be calculated. In the curvilinear coordinate system, where ε, η, ζ are the grid coordinate axes and x, y, z are the cartesian coordinates, the cell size can be defined as the maximum of the edge

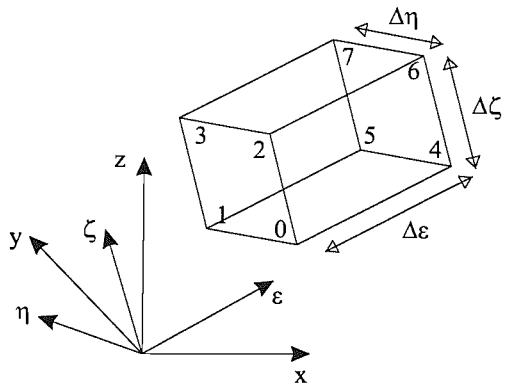

Figure C.1: Cell dimensions in curvilinear coordinate system

lengths along the grid axes ε, η, ζ (Figure C.1). To calculate this the x, y, z coordinates of the eight vertices of the cell are used as follows.

$$x_\varepsilon = 0.25 * (x_4 + x_5 + x_6 + x_7 - x_0 - x_1 - x_2 - x_3)$$
$$x_\eta = 0.25 * (x_1 + x_3 + x_5 + x_7 - x_0 - x_2 - x_4 - x_6)$$
$$x_\zeta = 0.25 * (x_2 + x_3 + x_6 + x_7 - x_0 - x_1 - x_4 - x_5)$$
$$y_\varepsilon = 0.25 * (y_4 + y_5 + y_6 + y_7 - y_0 - y_1 - y_2 - y_3)$$
$$y_\eta = 0.25 * (y_1 + y_3 + y_5 + y_7 - y_0 - y_2 - y_4 - y_6)$$
$$y_\zeta = 0.25 * (y_2 + y_3 + y_6 + y_7 - y_0 - y_1 - y_4 - y_5)$$
$$z_\varepsilon = 0.25 * (z_4 + z_5 + z_6 + z_7 - z_0 - z_1 - z_2 - z_3)$$
$$z_\eta = 0.25 * (z_1 + z_3 + z_5 + z_7 - z_0 - z_2 - z_4 - z_6)$$
$$z_\zeta = 0.25 * (z_2 + z_3 + z_6 + z_7 - z_0 - z_1 - z_4 - z_5)$$
$$\Delta\varepsilon = \left(x_\varepsilon^2 + y_\varepsilon^2 + z_\varepsilon^2\right)^{1/2}$$
$$\Delta\eta = \left(x_\eta^2 + y_\eta^2 + z_\eta^2\right)^{1/2}$$
$$\Delta\zeta = \left(x_\zeta^2 + y_\zeta^2 + z_\zeta^2\right)^{1/2}$$

The cell size is then equal to,

$$\Delta = \max(\Delta\varepsilon, \Delta\eta, \Delta\zeta)$$

and the length scale is determined by the larger of the cell size multiplied by a constant or the distance to the nearest wall as in Equation C.1.

C.4 Calculation of flow statistics

When carrying out large-eddy simulations the output from the solver will give a snapshot of the flow at that particular instant. However, in order to get an overall picture of the flow, and to compare the results with experimental flow measurements, it is also necessary to calculate statistical quantities describing the flow such as the mean and standard deviation of the velocity components. This can be achieved by periodically saving the solution after a certain number of time steps and then averaging this data. The problem with this method however is that the volume of data that needs to be stored becomes very large; for example one variable on a 2.6 million cell grid requires 12Mb of storage. Even making a very optimistic assumption that 100 samples are required for an accurate average means that over 1Gb of data has to be stored for each variable. The solution to this is to calculate the statistics while the solution is running.

There are then two ways of achieving this. Firstly the results could be saved to disk periodically and a separate program running in the background could process this and update the statistics. This method has the attraction of not requiring any modification to the solver code or any consequent increase in memory usage, but it would require another piece of software which would not be trivial. The alternative is to perform the calculation within the flow solver itself and store the statistical quantities as additional variables. While this would use more memory it has the advantage of using data at every time step without having to write to disk. The latter method was chosen for use in Elmore.

The statistical quantities required for a three dimensional flow are the means of the three velocity components and the components of the Reynolds stress tensor $\overline{u_i u_j}$. These are defined as follows where $\overline{uv}$ represents one of the Reynolds stress components.

$$\overline{U} = \frac{1}{T}\int_0^T U dt$$

$$\overline{uv} = \frac{1}{T}\int_0^T (U-\bar{U})(V-\bar{V})dt$$

or for the case of N discrete samples,

$$\overline{U} = \frac{1}{N}\sum_0^N U$$

$$\overline{uv} = \frac{1}{N}\sum_0^N (U-\bar{U})(V-\bar{V})$$

It follows that at a time step n, $\overline{U}$ and $\overline{uv}$ are given by,

$$\overline{U}_n = \frac{\overline{U}_{n-1}(n-1)+U_n}{n}$$

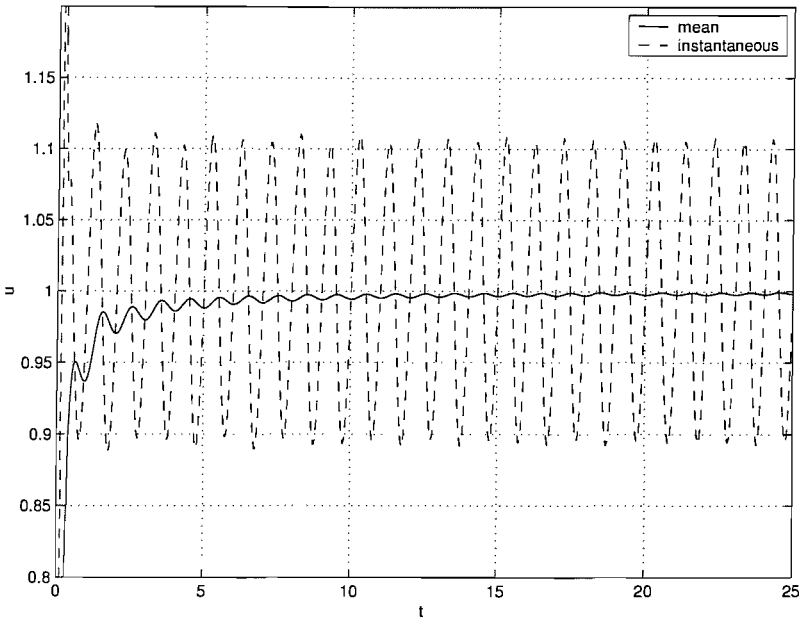

Figure C.2: Plot of the instantaneous and mean velocity against time for channel flow with oscillating inlet velocity

$$\overline{uv}_n = \frac{\overline{uv}_{n-1}(n-1) + (U_n - \bar{U}_n)(V_n - \bar{V}_n)}{n}$$

It is therefore necessary to store nine additional variables, $\overline{U}$, $\overline{V}$, $\overline{W}$, $\overline{uu}$, $\overline{vv}$, $\overline{ww}$, $\overline{uv}$, $\overline{uw}$ and $\overline{vw}$. These variables increase the memory requirement by 4%. The values are written to disk along with the all the other variables for post-processing or to restart the solution.

In order to check the implementation of these calculations a simple test case was used where an oscillating inflow velocity was applied to a channel flow. The inflow velocity was varied in a sine function of period, $T = 1.0$, amplitude, $a = 0.1$, and mean $\overline{U} = 1.0$. The instantaneous and mean velocity was recorded at a position downstream of the inlet as shown in figure C.2. The error in the mean is less than 0.5% after 10 oscillations, but this would be much less if the calculation of statistics was started after the initial transients in the solution.

Appendix D

Development of a dual-boot commodity computing cluster

D.1 Introduction

CFD codes have traditionally required large stand-alone supercomputers, such as the SGI Origin 2000 or CRAY TE4, to provide sufficient computational resources. These computers are extremely expensive both to purchase and to maintain, and so are often shared by a number of departments, which can be inconvenient when working to a deadline. While supercomputers have remained prohibitively expensive, desktop PCs have become cheaper and significantly more powerful and many are capable of running modest CFD jobs in a reasonable time. For more complex CFD tasks, however a single machine will run into limitations of memory and speed. Such jobs would normally be run in parallel on a multi-processor machine with it's attendant costs and inconveniences.

Recent advances in network technology and parallel computing software libraries such as MPI and PVM it is possible to connect many PC's together to run parallel jobs. The components required are standard off-the-shelf PC hardware and so the setup and maintenance costs can be significantly cheaper. They can be installed as a rack of machines without keyboards or monitors, which is a type of cluster commonly referred to as a "Beowulf" cluster. This type of cluster would be used in the same way as a traditional super-computer.

Many organisations would still consider this to be too expensive or inflexible. However, it is common for such groups to have large numbers of PC's sitting on people's desks, or in computer rooms in universities, which can remain idle for long periods outside working hours. It is therefore desirable to be able to utilise these idle resources instead of having to invest in dedicated hardware.

This philosophy has been applied to the network of workstations in the Department of

Ship Science. This network consists of 50 PCs in two rooms which are intended to provide students with access to office software as well as teaching them to use ship design software and programming techniques. Of course most of these PCs are idle overnight and at weekends and so there is a lot of waste of resources. In their daytime mode these PCs are running the Windows NT operating system as this is what most of the software required for teaching is intended for, however research computing is generally performed in a Unix environment and so it was decided to install the Linux operating system on the PCs to make a dual-boot system. Some effort was made to ensure the easy rebooting of the network from NT to Linux and vice-versa as described below.

D.2 Dual-boot system

A fundamental aspect of the cluster is the ability to switch a large number of machines from NT to Linux and vice-versa at certain times of the day. Normally, the machines would have to be rebooted manually, but this would obviously be very tedious to carry out regularly, and would restrict the operation to normal working hours. It was therefore desired to have a system whereby the machines could be rebooted from one operating system to the other remotely, at specified times.

Normally on dual-boot systems the user has to select which operating system to load when the machine boots up. This cannot be controlled remotely as there is no network connection at this stage. This means that it is necessary to somehow specify which operating system will be booted before shutting down the current system. This can be achieved by changing the active partition from which the boot sector will be loaded before shutdown.

The hard disk is organised into a number of partitions. There are two primary partitions which are both used by Windows NT (drives c and d), and an extended partition which contains two logical partitions on which Linux is installed (see D.1). The NT boot loader is installed in the boot sector of the first partition (hda1) and the Linux loader (LILO) is installed on the boot sector of the extended partition (hda3). A copy of the LILO boot sector is also stored as a file on the first partition so that it can be loaded by the NT boot loader. When the machine boots up the Master Boot Record on the hard disk looks at the partition table for the active partition and then loads the boot sector of that partition. If the first partition is active, the NT boot loader will start up, which gives the option of loading NT or Linux, using the copy of the LILO boot sector, defaulting to NT after 5s. If the third partition is marked as active LILO is started which also gives the choice between Linux and NT, but with Linux as the default.

The ability to switch the active partition and shutdown the PC is provided by a server program running on each machine, which listens on a TCP/IP port. This can be accessed through a web browser or a specific script to send the appropriate commands. A check is made

Table D.1: Details of the disk partitions on the workstations

Partition	Type	File system	Name
Partition 1	Primary	NT	hda1
Partition 2	Primary	NT	hda2
Partition 3	Extended	DOS	hda3
Partition 5	Logical	Linux	hda5
Partition 6	Logical	Linux swap	hda6

by the program that no user is logged in to the PC before it shuts down, to avoid the loss of data and inconvenience if someone is using the machine. The program also allows the interrogation of the machine to find out which system is currently running.

D.3 Performance of the cluster

The performance of the cluster has been tested by Law[94] using an Euler flow solver and a panel code. Some further tests have been carried out using a finite volume Navier-Stokes flow solver, called Elmore. These tests included testing the speed of a single machine with different numbers of computational cells (Figure D.1) and testing the parallel efficiency of the network using different numbers of processors for a constant number of cells (Figure D.2).

Figure D.1 shows the CPU time per iteration for different numbers of cells. As you would expect, the time scales linearly with the number of cells. Not shown on the graph however, is the sudden ten-fold increase in CPU time at 125000 cells due to the memory requirements exceeding the amount available and the subsequent use of the swap space. There is therefore a practical limit on the number of cells that each machine can solve at 100000 cells.

Figure D.2 is a plot of the speedup, defined as

$$\frac{\text{CPU time on 1 processor}}{\text{CPU time on N processors}}$$

against the number of processors (or blocks) used. This is shown for two grid sizes, 600000 cells and 900000 cells. For 600000 cells the speedup is not very great and in fact decreases above 20 blocks. This is likely to be due to the relatively large communications overhead compared to the amount of computational effort. For 900000 cells the speedup is more linear up to 30 blocks.

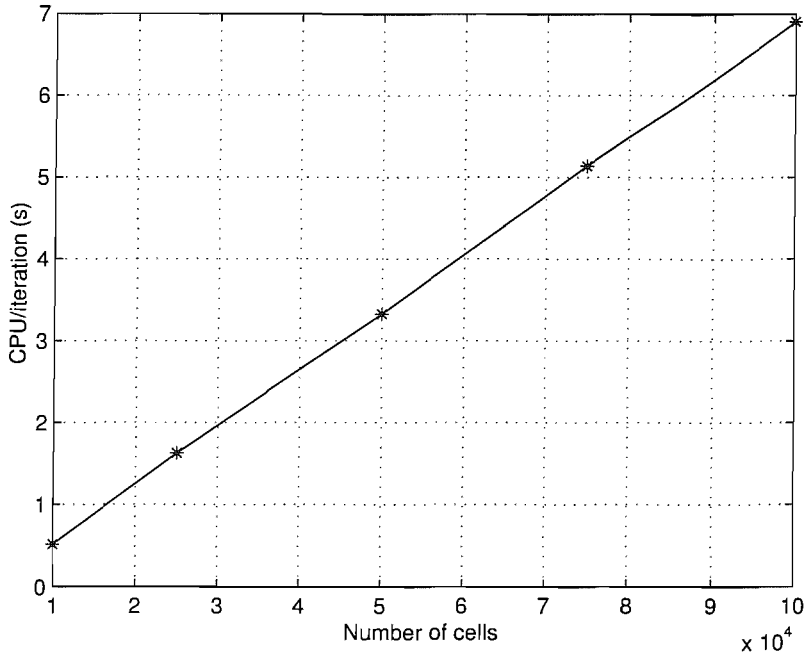

Figure D.1: Cluster performance running Elmore: CPU time per iteration against number of cells

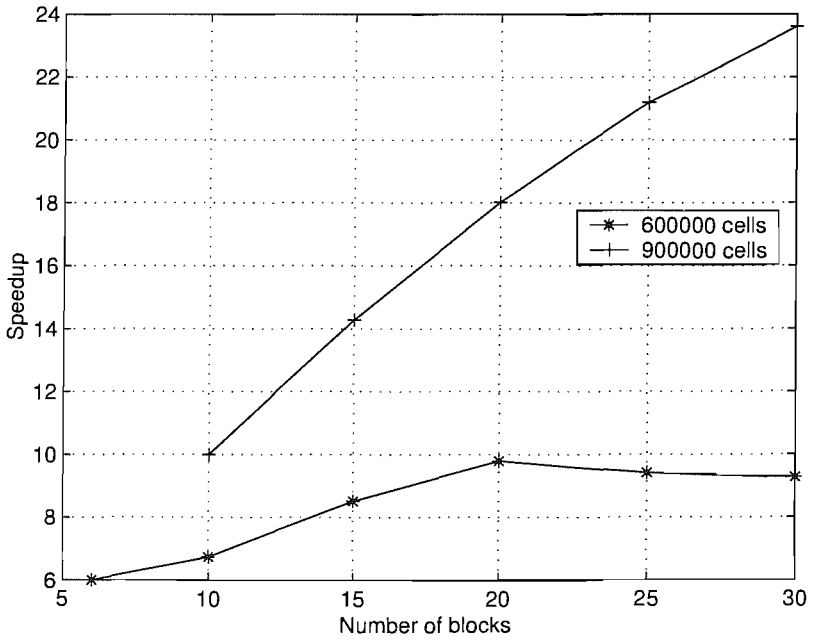

Figure D.2: Cluster performance running Elmore: speedup against number of blocks

Appendix E

Details of truncated cylinder grids

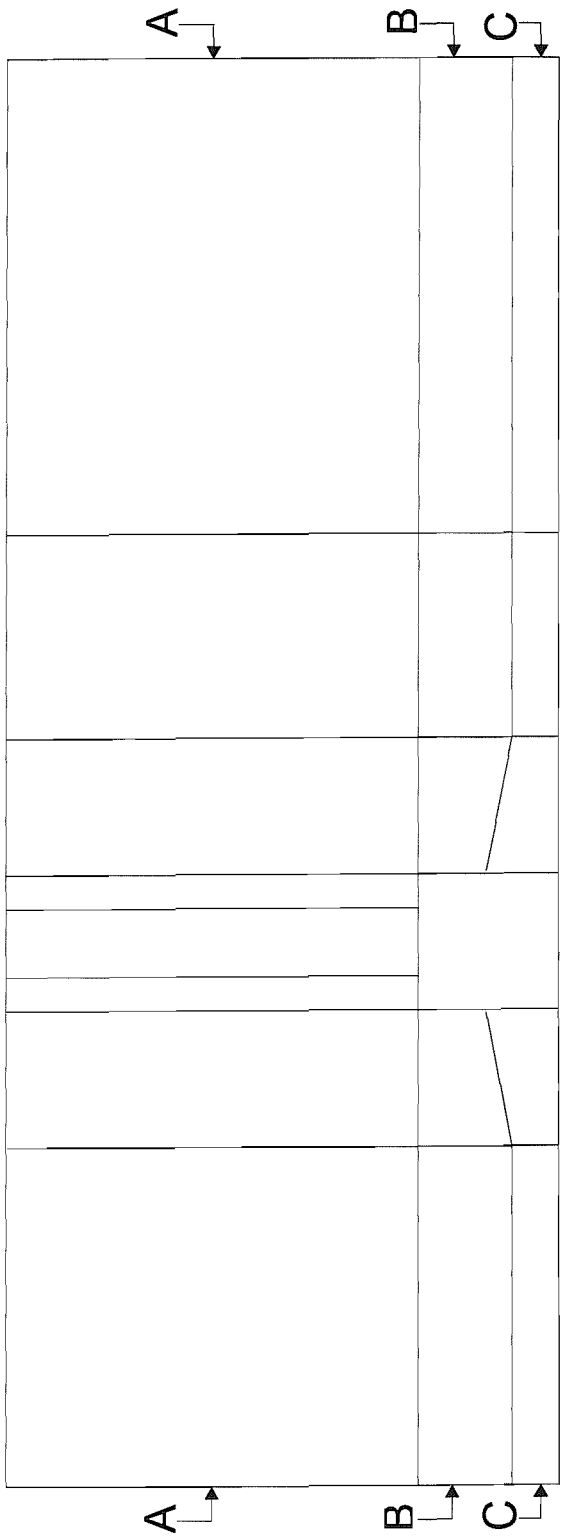

Figure E.1: Outline of block structure on $y/d = 0$

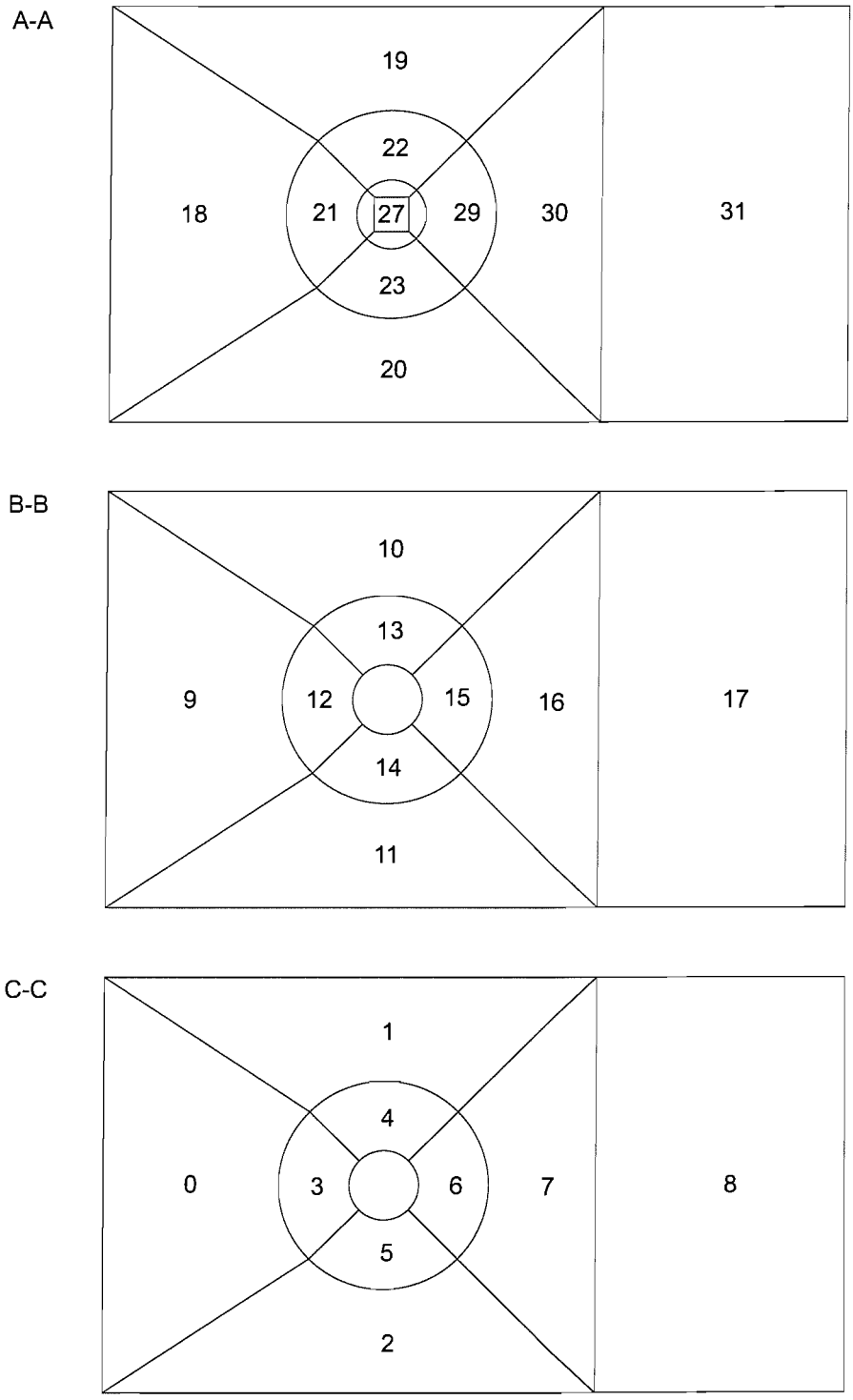

Figure E.2: Outline of block structure on horizontal planes as marked in Figure E.1 (Block numbers shown)

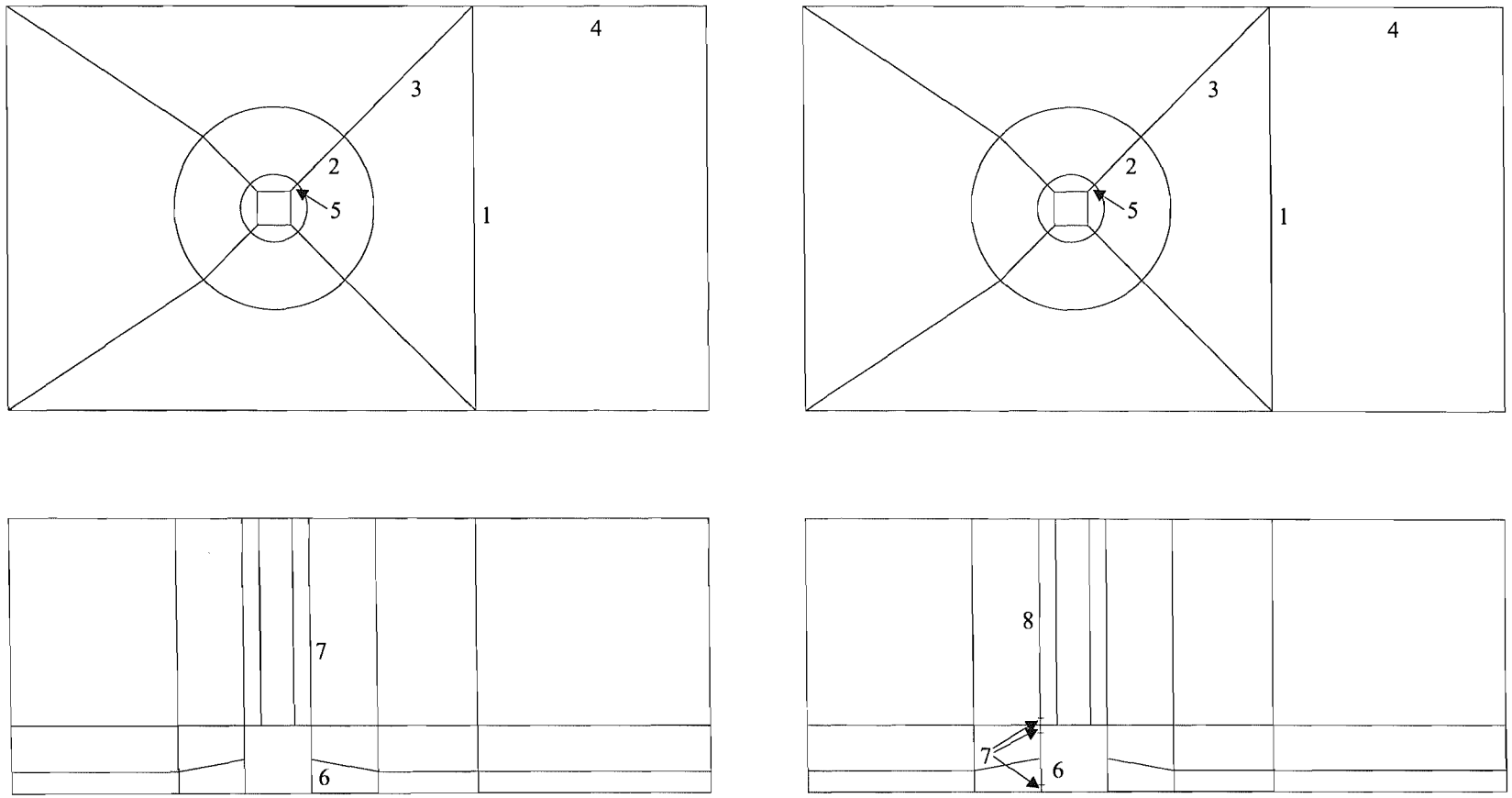

(a) Grids 1-3

(b) Grid 4

Figure E.3: Numbering of edges used in Table E.1

Table E.1: Details of grid parameters

		Edge no.							
Grid		1	2	3	4	5	6	7	8
1	N	58	48	14	14	14	16	31	
	p	1.0000	-3.9773	-1.6732	1.0000	1.0000	-3.0964	0.0013	
	q	1.0000	0.5913	0.8278	1.0000	1.0000	0.6745	3.3418	
	s_1	0.0138	0.0007	0.0333	0.2821	0.0095	0.0020	0.0020	
	s_2	0.0138	0.0333	0.3333	0.2821	0.0095	0.0533	0.3333	
2	N	72	61	17	17	17	20	39	
	p	1.0000	-2.2751	-0.0994	1.0000	1.0000	-1.4394	0.0089	
	q	1.0000	0.7552	1.7592	1.0000	1.0000	0.9181	3.4007	
	s_1	0.0111	0.0007	0.0267	0.2292	0.0077	0.0020	0.0020	
	s_2	0.0111	0.0267	0.3333	0.2292	0.0077	0.0433	0.2667	
3	N	91	76	21	21	21	25	49	
	p	1.0000	-0.2468	-0.0482	1.0000	1.0000	-1.7633	0.0101	
	q	1.0000	1.6817	1.7451	1.0000	1.0000	0.8279	3.2169	
	s_1	0.0087	0.0007	0.0267	0.1833	0.0061	0.0020	0.0020	
	s_2	0.0087	0.0267	0.2593	0.1833	0.0061	0.0333	0.2000	
4	N	81	54	17	17	30	15	11	29
	p	1.0000	-1.1629	-0.0561	1.0000	0.4192	0.2684	0.2542	0.2886
	q	1.0000	0.8660	1.8015	1.0000	2.3620	3.5272	1.5338	2.5106
	s_1	0.0098	0.0020	0.0300	0.2292	0.0020	0.0020	0.0200	0.0325
	s_2	0.0098	0.0300	0.3333	0.2292	0.0077	0.0200	0.0600	0.2000

Appendix F

PIV experiments on a KVLCC model

F.1 Introduction

The work described in the main part of this thesis describes the study of the flow over a finite-height, low aspect ratio cylinder mounted on a ground plane. One of the aims of this work was to investigate the numerical simulation of complex three-dimensional turbulent flow fields which are often found in the marine environment. One example of this is the flow around the stern of full-bodied ships such as tankers and bulk-carriers. These were the subject of a workshop on numerical ship hydrodynamics, held in Gothenburg in 2000 [95], for which the author was involved with the RANS simulations for the University of Southampton's contribution [96].

One of the test cases used at the workshop used the experimental data from the Korean Research Institute of Ships and Ocean Engineering (KRISO) on their KVLCC2 hull form [92]. They conducted experiments on the flow around the hull model both in a towing tank [97] and in a wind tunnel [98]. The towing tank experiments gave the elevation of the free-surface in a number of planes as well as mean velocities measured by a rake of pitot tubes. Of more interest to the current work however are the wind tunnel experiments where a X-wire probe was used to measure turbulence statistics in the near-wake of the hull. The flow in the propeller plane is of particular interest due to the interaction of the bilge vortex with the propeller. However, the anisotropic nature of the turbulence here means that two-equation RANS models have difficulty modelling the turbulent kinetic energy in the wake.

In order to investigate the turbulent flow in the propeller plane further, and to provide validation data for CFD simulations, it was decided to perform some PIV measurements on a model of the KVLCC2 hullform in the wind tunnel. A $\frac{1}{320}$ scale model was commissioned, made of hardwood. The model is divided longitudinally into three sections so that the parallel mid-body can be removed, and also allows for an extra piece to be added above the waterline

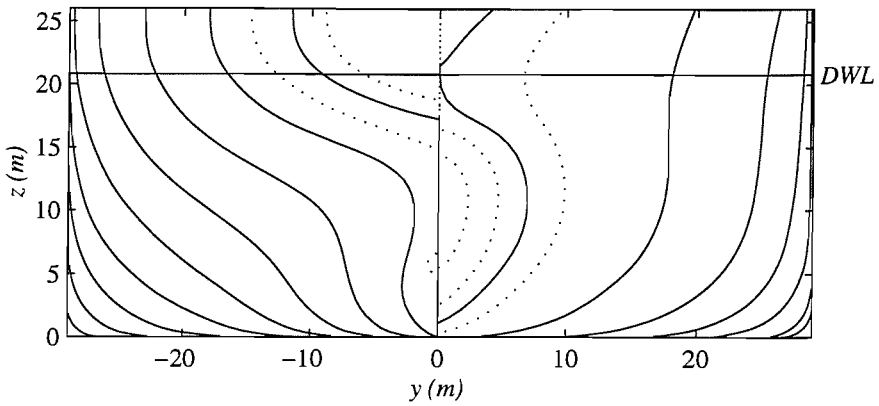

Figure F.1: Body plan of full-scale KVLCC2 hull

to increase the depth of the model. The sections are connected with dowel pins. The model was mounted on a ground plate in the wind tunnel in the same way as the cylinder described above. While this is not a strictly accurate representation of the real ship due to the presence of a boundary layer on the ground plate, the CFD model can be set to model this. It may also be the case that a double-body model as used in the KRISO tests does not give the same turbulence behaviour as the real ship. This is because the eddies are free to cross the whole wake rather than being constrained by the free-surface.

Particle image velocimetry (PIV) was used to obtain data on the flow in the propeller plane. The laser sheet was oriented in the y-z plane so that vectors of V and W were measured. The data was averaged over 500 samples. Figure 10 shows plots of velocity vectors with contours of vorticity, normalised by the maximum instantaneous vorticity magnitude. Only half of the plane was measured to enable greater resolution. The tests were run at a Reynolds number based on hull length of 1.3×10^6. The boundary layer on the surface of the hull was tripped using a roughness strip so the flow is fully turbulent.

F.2 Results

In the mean flow there are the longitudinal bilge vortices close to the hub of the propeller as found in [4]. However, as in the truncated cylinder flow these mean vortices appear very unsteady in nature revealing a chaotic instantaneous flow with many large-scale coherent structures. Only in the mean flow do these appear as the two counter-rotating vortices. This is similar to the flow found by Bearman [17], for the flow around a car. It is questionable whether the mean flow produced by a RANS calculation or even measured by time-averaging techniques is a valid picture of the flow for many applications. For example the flow over the propeller blades could be more influenced by this short time-scale flow pattern than by the mean flow. While this may not matter for the mean thrust characteristics it may be a factor in the simulation of

vibrations and pressure fluctuations.

The measurements taken in the propeller plane are shown in Figures F.2 to F.5. The current work is shown on the right with the KRISO data on the left. Looking first at the mean velocity field and the vorticity, it can be seen that the current measurements are close to the KRISO results, although the vortex is slightly smaller in the new data. The PIV measurements do not seem to capture as much detail of the flow close to the propeller hub, which could be due to reflections of the laser light sheet from the surface.

The turbulence levels are significantly different between the two cases, with the PIV results showing higher values towards the free-stream and not capturing the hook shape at all. This is perhaps due to errors in the high-speed flow where particles may have been crossing the light sheet too quickly.

F.3 Recommendations

To improve the accuracy of these experiments relative to the KRISO reference data, a number of factors should be looked at. Firstly, while the segmented model gives the opportunity to use different lengths and depths of the hull, to ensure a realistic flow the full length and correct draught model should be used. To represent the flow at the waterline most accurately an endplate should be used with as thin a boundary layer on it as possible. The experiments reported here used the same ground plate as the cylinder experiments, where the thickness of the boundary layer was not a problem. KRISO used a double-body model to eliminate the problem of a boundary layer here, but this could allow larger-scale turbulent structures spanning the full depth of the model which may be equally unrealistic. The most realistic solution would probably be a moving floor like the ones in the $7' \times 5'$ and $11' \times 8'$ wind tunnels which are used for car models, although the practicality of this might be limited by mounting difficulties. Assuming an endplate is used, it should be as short as possible to minimise boundary layer growth. A porous or slotted plate could be used to maintain a thin laminar boundary layer.

Although considerable efforts were made to reduce the scattered light from the laser where it hits the surface of the model, it still significantly affected the images near the surface, resulting in a loss of data close to the hull. This is probably made worse by the curvature of the hull. A transparent, perspex, model would probably be better from this point of view.

The timing of the laser flashes needs to be checked carefully to ensure that no particles are flowing through the beam between the flashes. This will affect the accuracy, particularly outside the hull in the high speed flow.

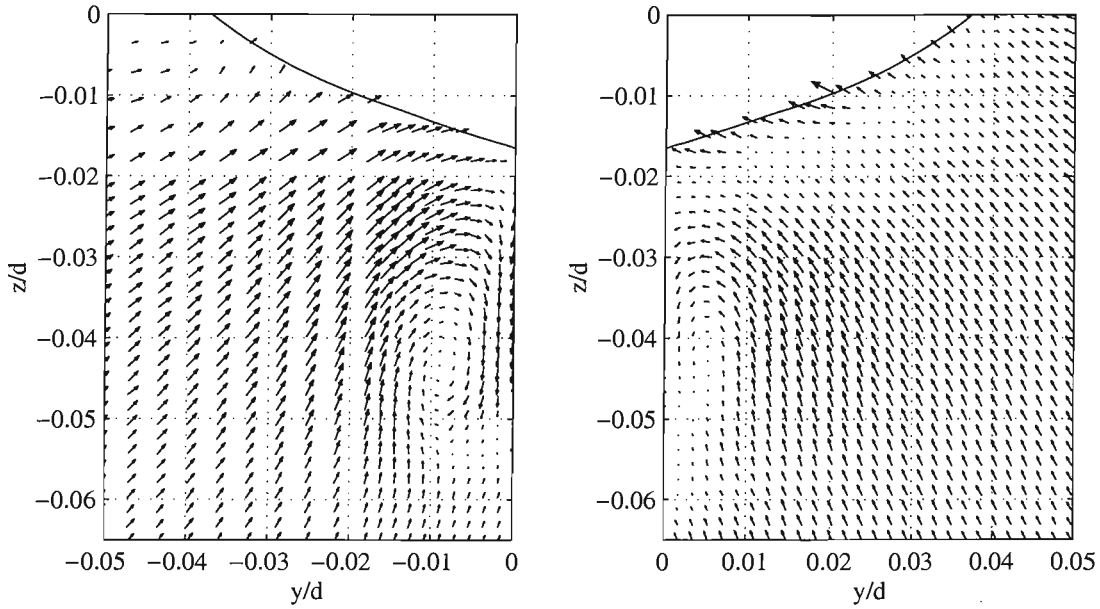

Figure F.2: Velocity vectors in the propeller plane (KRISO data - left, Current PIV - right

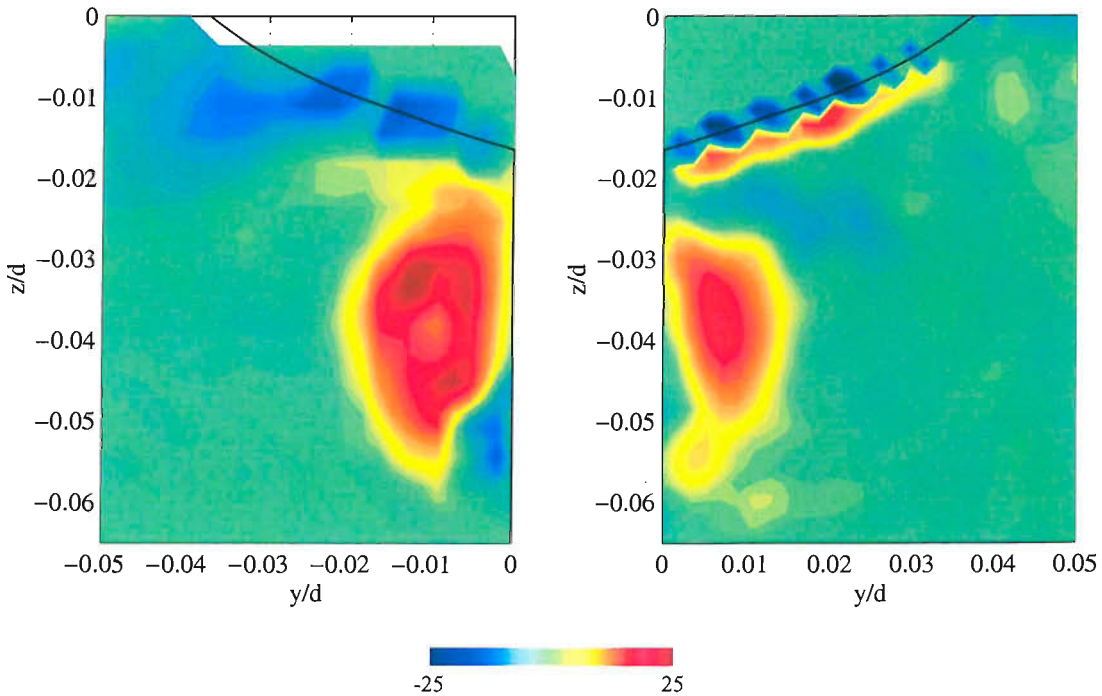

Figure F.3: Vorticity in the propeller plane (KRISO data - left, Current PIV - right

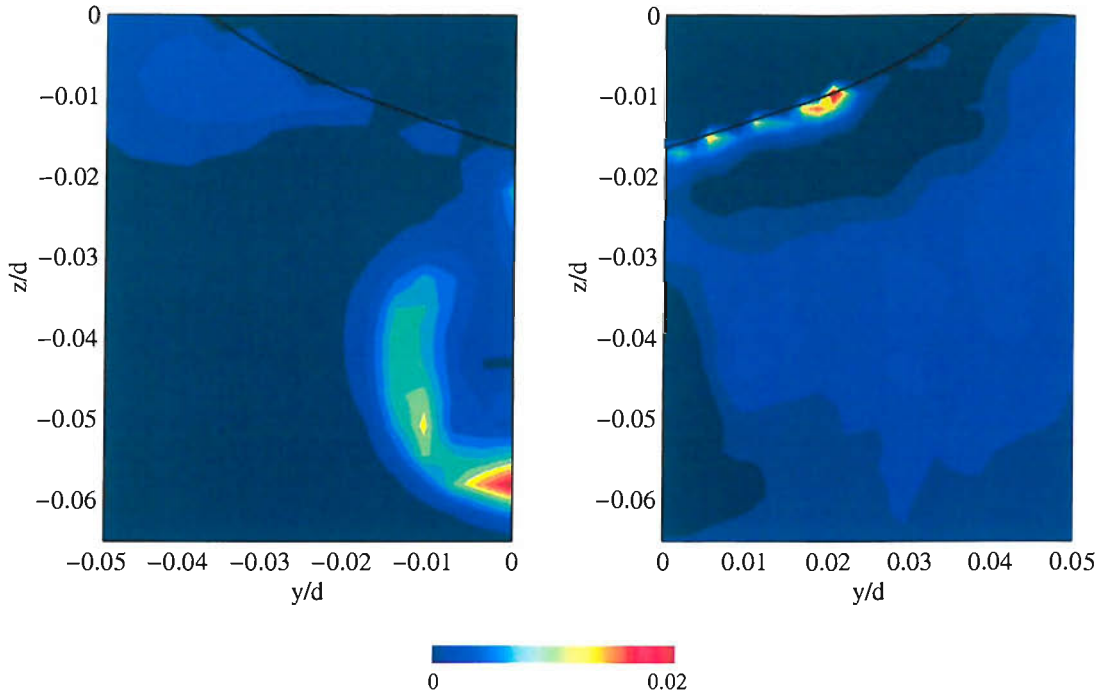

Figure F.4: $\overline{v'v'}$ in the propeller plane (KRISO data - left, Current PIV - right

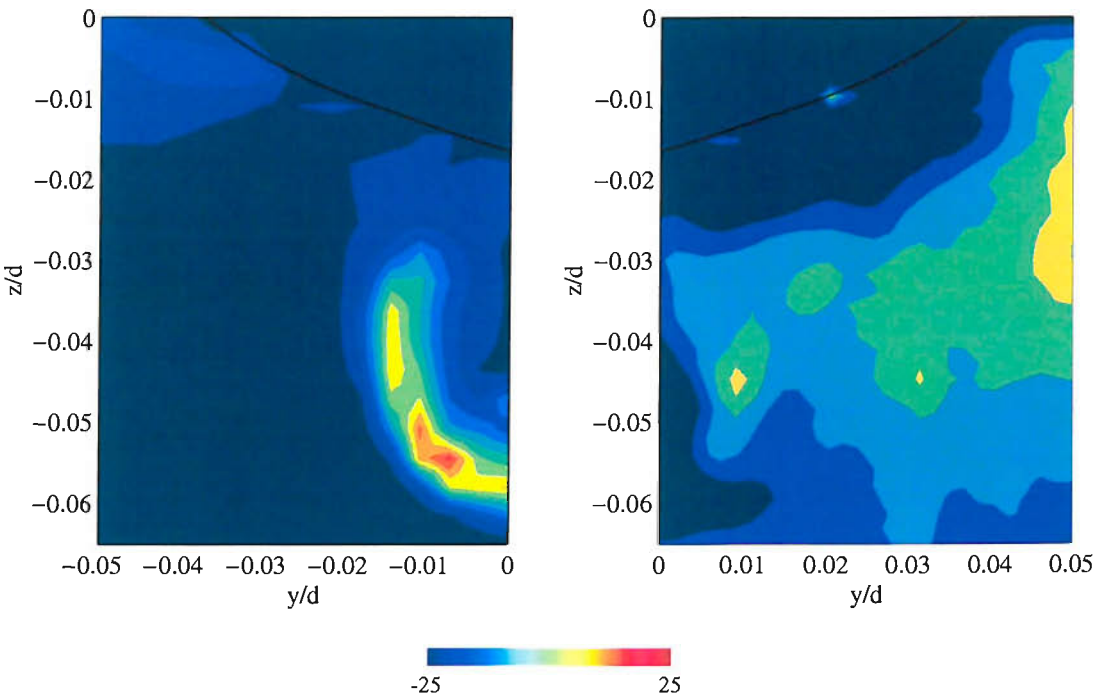

Figure F.5: $\overline{w'w'}$ in the propeller plane (KRISO data - left, Current PIV - right

References

[1] C.H.K. Williamson. Vortex dynamics in the cylinder wake. *Annual Review of Fluid Mechanics*, 28:477–539, 1996.

[2] M.M. Zdravkovich. *Flow around circular cylinders*, volume 1. Oxford University Press, 1997.

[3] T. Okamoto and M. Yagita. The experimental investigation on the flow past a circular cylinder of finite length. *Bulletin of Japan Soc. Mech. Eng.*, 16:805–814, 1973.

[4] Dj Farivar. Turbulent uniform flow around cylinders of finite length. *AIAA Journal*, 19:275–281, 1981.

[5] R.S. Sarode, S.L. Gai, and C.K. Ramesh. Flow around circular- and square-section models of finite height in a turbulent shear flow. *Journal of Wind Engineering and Industrial Aerodynamics*, 8:223, 1981.

[6] A. Slaouti and J.H. Gerrard. An experimental investigation of the end effects on the wake of a circular cylinder towed through water at low reynolds numbers. *Journal of Fluid Mechanics*, 112:297–314, 1981.

[7] S. Taniguchi, H. Sakamoto, and M. Arie. Flow around circular cylinders of finite height placed vertically in turbulent boundary layers. *Bulletin of the JSME*, 24(187):37–44, 1981.

[8] S. Taniguchi, H. Sakamoto, and M. Arie. Flow around a circular cylinder vertically mounted in a turbulent boundary layer. *Bulletin of the JSME*, 24(193):1130–1136, 1981.

[9] A. Ayoub and K. Karemcheti. An experiment on the flow past a finite circular cylinder at high subcritical and supercritical reynolds numbers. *Journal of Fluid Mechanics*, 118:1–26, 1982.

[10] S. Okamoto. Turbulent shear flow behind hemisphere-cylinder placed on a ground plane. In *Turbulent Shear Flows*, volume 3, pages 171–185. Springer-Verlag, 1982.

[11] H. Sakamoto and M. Arie. Vortex shedding from a rectangular prism and a circular cylinder placed vertically in a turbulent boundary layer. *Journal of Fluid Mechanics*, 126:147–165, 1983.

[12] T. Kawamura, M. Hiwada, T. Hibino, I. Mabuchi, and M. Kumuda. Cylinder height greater than turbulent boundary layer thickness - flow around a finite circular cylinder on a flat plate. *Bulletin of the JSME*, 27(232):2142–2151, 1984.

[13] V.K. Sin and R.M.C. So. Local force measurements on finite span cylinders in a cross-flow. *Trans. ASME, Journal of Fluids Engineering*, 109(2):136–143, June 1987.

[14] M. Baban and R.M.C. So. Aspect ratio effect on flow induced forces on circular cylinders in a cross-flow. *Experiments in Fluids*, 10(313-321), 1991.

[15] M. Baban and R.M.C. So. Recirculating flow behind and unsteady forces on finite-span circular-cylinders in a cross-flow. *Journal of Fluids and Structures*, 5(185-206), 1991.

[16] S. Okamoto and Y. Sunabashiri. Vortex shedding from a circular cylinder of finite length placed on a ground plane. *Trans. ASME, Journal of Fluids Engineering*, 114:512–521, December 1992.

[17] S.C. Luo, T.L. Gan, and Y.T. Chew. Uniform flow past one (or two in tandem) finite length circular cylinders. *Journal of Wind Engineering and Industrial Aerodynamics*, 59(1):69–93, January 1996.

[18] M. Kappler. *Experimentelle Untersuchung der Umströmung von Kreiszylinder mit ausgeprägt dreidimensionalen Effekten*. PhD thesis, Institute for Hydromechanics, University of Karlsruhe, 2002.

[19] C-W Park and S-J Lee. Free end effects on the near wake flow structure behind a finite circular cylinder. *Journal of Wind Engineering and Industrial Aerodynamics*, 88:231–246, 2000.

[20] C-W Park and S-J Lee. Flow structure around a finite circular cylinder embedded in various atmospheric boundary layers. *Fluid Dynamics Research*, 30:197–215, 2002.

[21] S.C. Roh and S.O. Park. Vortical flow over the free end surface of a finite circular cylinder mounted on a flat plate. *Experiments in Fluids*, 34:63–67, 2003.

[22] R. Martinuzzi and C. Tropea. The flow around surface-mounted, prismatic obstacles placed in a fully developed channel flow. *Trans. ASME, Journal of Fluids Engineering*, 115:85–92, 1993.

[23] R.L. Simpson. Junction flows. *Annual Review of Fluid Mechanics*, 33:415–443, 2001.

[24] M.R. Visbal. Structure of laminar juncture flows. *AIAA Journal*, 29(8):1273–1282, 1991.

[25] C.J. Baker. The laminar horseshoe vortex. *Journal of Fluid Mechanics*, 95(2):347–367, 1979.

[26] C.J. Baker. The oscillation of horseshoe vortex systems. *Trans. ASME, Journal of Fluids Engineering*, 113:489–495, 1991.

[27] C.J. Baker. The turbulent horseshoe vortex. *Journal of Wind Engineering and Industrial Aerodynamics*, 6:9–23, 1980.

[28] F. Ballio, C. Bettoni, and S. Franzetti. A survey of time-averaged characteristics of laminar and turbulent horseshoe vortices. *Trans. ASME, Journal of Fluids Engineering*, 120:233–242, 1998.

[29] W.J. Devenport and R.L. Simpson. Time-dependent and time-averaged turbulence structure near the nose of a wing-body junction. *Journal of Fluid Mechanics*, 210:23–55, 1990.

[30] F.J. Pierce and I.K. Tree. The mean flow structure on the symmetry plane of a turbulent junction vortex. *Trans. ASME, Journal of Fluids Engineering*, 112:16–22, 1990.

[31] W.A. Eckerle and L.S. Langston. Horseshoe vortex formation around a cylinder. *Trans. ASME, Journal of Fluids Engineering*, 109:278–285, 1987.

[32] B.M. Sumer, N. Christiansen, and J. Fredsœ. The horseshoe vortex and vortex shedding around a vertical wall-mounted cylinder exposed to waves. *Journal of Fluid Mechanics*, 332:41–70, 1997.

[33] A.E. Winkelmann and J.B. Barlow. Flowfield model for a rectangular planform wing beyond stall. *AIAA Journal*, 18:1006–1008, 1980.

[34] P.R. Spalart. Strategies for turbulence modelling and simulations. *International Journal of Heat and Fluid Flow*, 21:252–263, 2000.

[35] J. Fröhlich, W. Rodi, A. Dewan, and J.P. Fontes. Large-eddy simulation of the flow around the free end of a circular cylinder. In E. Hirschel, editor, *Notes on Numerical Fluid Mechanics*, volume 82. Springer, 2003.

[36] M. Kappler and W. Rodi. Visualisation of the flow past short circular cylinders with a free end. In *Proceedings of 4th International Colloquium on Bluff Body Aerodynamics and Applications*, pages 613–616, Bochum, 2000.

[37] A. Travin, M. Shur, M. Strelets, and P. Spalart. Detached-eddy simulations past a circular cylinder. *Flow, Turbulence and Combustion*, 63:293–313, 2000.

[38] P.R. Spalart and S.R. Allmaras. A one-equation turbulence model for aerodynamic flows. *La Recherche Aérospatiale*, 1:5–21, 1994.

[39] P.R. Spalart and M.Kh. Strelets. Mechanisms of transition and heat transfer in a separation bubble. *Journal of Fluid Mechanics*, 403:329–349, January 2000.

[40] M. Shur, P.R. Spalart, M. Strelets, and A. Travin. Detached-eddy simulation of an airfoil at high angle of attack. In *4th International Symposium on Engineering Turbulence Modelling and Measurements*, 1999.

[41] S. Morton, J. Forsythe, A. Mitchell, and D. Hajek. DES and RANS simulations of delta wing vortical flows. AIAA Paper 2002-0587, AIAA, 2002.

[42] G.S. Constantinescu and K.D. Squires. LES and DES investigations of turbulent flow over a sphere. AIAA Paper 2000-0540, AIAA, 1999.

[43] G.S. Constantinescu, H. Pasinato, Y-Q. Wang, and K.D. Squires. Numerical investigation of flow past a prolate spheroid. In *Aerospace Sciences Meeting*, Reno, Nevada, January 2002. AIAA.

[44] I.P. Castro and A.G. Robins. The flow around a surface-mounted cube in uniform and turbulent streams. *Journal of Fluid Mechanics*, 79(2):307–335, 1977.

[45] W. Rodi. Comparison of LES and RANS calculations of the flow around bluff bodies. *Journal of Wind Engineeringn and Industrial Aerodynamics*, 69-71:55–75, 1997.

[46] W. Rodi, J.H. Ferziger, M. Breuer, and Pourquié. Status of large-eddy simulation: results of a workshop. *Trans. ASME, Journal of Fluids Engineering*, 119:248–262, 1997.

[47] S. Murakami. Overview of turbulence models applied in CWE-1997. *Journal of Wind Engineering and Industrial Aerodynamics*, 74-76:1–24, 1998.

[48] N. Ives, D. Scott, R. Silva Fernandez de Ana, and M. Walker. Design and construction of an aerodynamic test facility. MEng Group Design Project Report, University of Southampton, Ship Science, 1999.

[49] C. Cant, E. Lait, N. Hankins, and R. Mason. The design, build and commissioning of an aerodynamic test facility. MEng Group Design Project Report, University of Southampton, School of Engineering Sciences, Ship Science, 2000.

[50] C.N.H. Lock. The interference of a wind tunnel on a symmetrical body. Technical Report 1275, British ARC, 1929.

[51] H.J. Allen and W.G. Vincenti. Wall interference in a two-dimensional-flow wind tunnel, with consideration for the effect of compressibility. Technical Report 782, NACA, 1944.

[52] G.S. West and C.J. Apelt. The effects of tunnel blockage and aspect ratio on the mean flow past a circular cylinder with Reynolds numbers between 10^4 and 10^5. *Journal of Fluid Mechanics*, 114:361–377, 1982.

[53] C. Farell, S. Carrasquel, O. Guven, and V.C. Patel. Effect of wind tunnel walls on the flow past circular cylinders and cooling tower models. *Trans ASME, Journal of Fluids Engineering*, 99:470–479, 1977.

[54] R.J. Adrian. Particle imaging techniques for experimental fluid mechanics. *Annual Review of Fluid Mechanics*, 23:261–304, 1991.

[55] M. Raffel, C.E. Willert, and J. Kompenhans. *Partical image velocimetry: a practical guide*. Experimental Fluid Mechanics. Springer-Verlag, 1998.

[56] S. Webb and I.P. Castro. PIV,LDA and HWA comparative measurements in various turbulent flows. To be published.

[57] I.P. Castro. Hot wire anemometry with the Newcastle, NSW bridges: Manual and accompanying notes for Southampton usage. Internal report, University of Southampton, November 2001.

[58] R.J. Moffat. Describing the uncertainties in experimental results. *Experimental Thermal and Fluid Science*, 1:3–17, 1988.

[59] A.F. Molland. The design, construction and calibration of a five-component strain gauge wind tunnel dynamometer. Ship Science Report 1/77, University of Southampton, November 1976.

[60] M. Tobak and D.J. Peake. Topology of 3-dimensional separated flows. *Annual Review of Fluid Mechanics*, 14:61–85, 1982.

[61] A.E. Perry and M.S. Chong. Interpretation of flow visualisation. In A.J. Smits and T.J. Lim, editors, *Flow Visualisation: Techniques and Examples*. Imperial College Press, 2000.

[62] P.S. Klebanoff and Z.W. Diehl. Some features of artificially thickened fully developed turbulent boundary layers with zero pressure gradient. NACA Report 1110, NACA, 1952.

[63] R.C. Pankhurst and D.W. Holder. *Wind-tunnel technique*. Pitman, 1952.

[64] J. Mathieu and J. Scott. *An introduction to turbulent flow*. Cambridge University Press, 2000.

[65] I.P. Castro. *An introduction to the digital analysis of stationary signals*. IOP, 1989.

[66] R.J. Pattenden, S.R. Turnock, and N.W. Bressloff. An experimental and computational study of three-dimensional unsteady flow features found behind a truncated cylinder. In *24th Symposium on Naval Hydrodynamics*, Fukuoka, Japan, 2002.

[67] G.K. Batchelor, editor. *An introduction to fluid dynamics*. Cambridge Univeristy Press, 1967.

[68] N.W. Bressloff. A parallel pressure implicit splitting of operators algorithm applied to flow at all speeds. *Int. Jnl of Numerical Methods in Fluids*, 36:497–518, 2001.

[69] J.H. Ferziger and M. Peric. *Computational methods for fluid dynamics*. Springer, 2nd edition, 1999.

[70] B.E. Launder and D.B. Spalding. The numerical computation of turbulent flows. *Computer Methods in Applied Mechanics and Engineering*, 3, 1974.

[71] O. Métais and M. Lesieur. Spectral large-eddy simulations of isotropic and stably-stratified turbulence. *Journal of Fluid Mechanics*, 239:157–94, 1992.

[72] U. Piomelli and E. Balaras. Wall-layer models for large-eddy simulations. *Annual Review of Fluid Mechanics*, 34:349–374, 2002.

[73] P.R. Spalart, W-H. Jou, M. Strelets, and S.R. Allmaras. Comments on the feasibility of LES for wings, and on a hybrid RANS/LES approach. In *Advances in DNS/LES, 1st AFOSR Int. Conf. on DNS/LES*, Columbus Oh., August 1997. Greyden Press.

[74] M. Strelets. Detached eddy simulation of massively separated flows. Technical Report 01-0879, AIAA, January 2000.

[75] N.V. Nikitin, F. Nicoud, B. Wasistho, K.D. Squires, and P.R. Spalart. An approach to wall modeling in large-eddy simulations. *Physics of Fluids*, 12(7):1629–1632, 2000.

[76] M. Shur, P.R. Spalart, M. Strelets, and A. Travin. Navier-stokes simulation of shedding turbulent flow past a circular cylinder and a cylinder with a backward splitter plate. In *3rd European CFD Conference*, Paris, September 1996.

[77] P.R. Spalart and M. Shur. On the sensitization of simple turbulence models to rotation and curvature. *Aerospace Science and Technology*, 1(5):297–302, 1997.

[78] B. Van Leer. Towards the ultimate conservative difference scheme. ii. monotonicity and conservation combined in a second order scheme. *Journal of Computational Physics*, 14:361–370, 1974.

[79] W.M.J. Batten. *Numerical predictions and experimental analysis of small clearance ratio Taylor-Couette flows*. PhD thesis, School of Engineering Sciences, University of Southampton, 2002.

[80] S.E. Kim, S.H. Rhee, and D. Cokljat. High-incidence and dynamic pitch-up maneuvering characteristics of a prolate spheroid - CFD validation. In *24th Symposium on Naval Hydrodynamics*, Fukuoka, Japan, 2002.

[81] P.R. Eisemann. A multi-surface method of co-ordinate generation. *Journal of Computational Physics*, 33:118–150, 1979.

[82] R.I. Issa. Solution of implicitly discretized fluid flow equations by operator-splitting. *Journal of Computational Physics*, 62:40–65, 1986.

[83] F.R. Menter. Two-equation eddy-viscosity turbulence models for engineering applications. *AIAA Journal*, 32(8):1598–1604, August 1994.

[84] B.E. Launder, G.J. Reece, and W. Rodi. Progress in the developments of a reynolds-stress turbulence closure. *Journal of Fluid Mechanics*, 68:537–566, 1975.

[85] C.G. Speziale, S. Sarkar, and T.B. Gatski. Modelling the pressure-strain correlation of turbulence: an invariant dynamical systems approach. *Journal of Fluid Mechanics*, 277:245–272, 1991.

[86] H.W. Stock and W. Haase. Navier-Sotkes computations with e^n transition prediction including transitional flow regions. *AIAA Journal*, 38(11):2059–2066, 2000.

[87] Intelligent Light. *Fieldview 8.0 Reference Manual*, 2001.

[88] T. Tamura, I. Ohta, and K. Kuwahara. On the reliability of two-dimensional simulation for unsteady flows around a cylinder-type structure. *Journal of Wind Engineering and Industrial Aerodynamics*, 35:275–298, 1990.

[89] K. Kubo and M. Takezawa. Experimental study on horseshoe vortex in the upstream front of cylindrical structure. In Kolkman et al., editor, *Modelling soil-water-structure interactions*, pages 117–126. Balkema, Rotterdam, 1988.

[90] D.C. Wilcox. *Turbulence modeling for CFD*. D.C.W. Industries, 2nd edition, 1998.

[91] J.C.R. Hunt. Development of computational modeling of turbulent flows. In Pironneau et al., editor, *Numerical Simulation of Unsteady Flows and Transition to Turbulence*. Cambridge University Press, 1992.

[92] S.B. Pope. *Turbulent Flows*. Cambridge University Press, 2000.

[93] S.H. Van, W.J. Kim, D.H. Yim, G.T. Kim, C.J. Lee, and J.Y Eom. Flow measurement around a 300K VLCC model. In *Proceedings of the Annual Spring Meeting, SNAK, Ulsan*, pages 185–188, 1998.

[94] R.J. Pattenden, S.R. Turnock, and N.W. Bressloff. Developments in the use of large-eddy simulation for ship hydrodynamics. In *CFD 2003: Computational fluid dynamics technology in ship hydrodynamics*, London, U.K., 2003. RINA.

[95] R.A. Law and S.R. Turnock. Utilising existing computational resources to create a commodity PC network suitable for fast CFD computation. In C.B. Jenssen, editor, *Parallel Computational Fluid Dynamics - Trends and Applications - Proceedings of the Parallel CFD 2000 Conference*, pages 115–122. Elsevier Science B.V., 2001.

[96] L. Larsson, F. Stern, and V Bertram, editors. *Gothenburg 2000: A Workshop on Numerical Ship Hydrodynamics*, Gothenburg, Sweden, 2000.

[97] S.R. Turnock, R.J. Pattenden, R. Pemberton, and S.J. Watson. Computation of viscous steady flow around the KRISO tanker (KVLCC2) hull form. In *Gothenburg 2000: A Workshop on Numerical Ship Hydrodynamics*, 2000.

[98] W.J. Kim, S.H. Van, and D.H. Kim. Measurement of flows around modern commercial ship models. *Experiments in Fluids*, 31:567–578, 2001.

[99] S.J. Lee, H.R. Kim, W.J. Kim, and S.H. Van. Wind tunnel tests on flow characteristics of the KRISO 3,600 TEU containership and 300K VLCC double-deck ship models. *Journal of Ship Research*, 47(1):24–38, 2003.